frontiers | Research Topics

Energy materials based novel solar thermal applications, 2nd edition

Edited by
Muhammad Amjad, Enio Pedone Bandarra Filho, Shafiq Ahmad, Fahid Riaz, Muhammad Abdul Qyyum, Yanwei Hu and Jabbar Gardy

Published in
Frontiers in Energy Research
Frontiers in Public Health
Frontiers in Environmental Science

ISSN 1664-8714
ISBN 978-2-8325-5165-3
DOI 10.3389/978-2-8325-5165-3

About Frontiers

Frontiers is more than just an open access publisher of scholarly articles: it is a pioneering approach to the world of academia, radically improving the way scholarly research is managed. The grand vision of Frontiers is a world where all people have an equal opportunity to seek, share and generate knowledge. Frontiers provides immediate and permanent online open access to all its publications, but this alone is not enough to realize our grand goals.

Frontiers journal series

The Frontiers journal series is a multi-tier and interdisciplinary set of open-access, online journals, promising a paradigm shift from the current review, selection and dissemination processes in academic publishing. All Frontiers journals are driven by researchers for researchers; therefore, they constitute a service to the scholarly community. At the same time, the *Frontiers journal series* operates on a revolutionary invention, the tiered publishing system, initially addressing specific communities of scholars, and gradually climbing up to broader public understanding, thus serving the interests of the lay society, too.

Dedication to quality

Each Frontiers article is a landmark of the highest quality, thanks to genuinely collaborative interactions between authors and review editors, who include some of the world's best academicians. Research must be certified by peers before entering a stream of knowledge that may eventually reach the public - and shape society; therefore, Frontiers only applies the most rigorous and unbiased reviews. Frontiers revolutionizes research publishing by freely delivering the most outstanding research, evaluated with no bias from both the academic and social point of view. By applying the most advanced information technologies, Frontiers is catapulting scholarly publishing into a new generation.

What are Frontiers Research Topics?

Frontiers Research Topics are very popular trademarks of the *Frontiers journals series*: they are collections of at least ten articles, all centered on a particular subject. With their unique mix of varied contributions from Original Research to Review Articles, Frontiers Research Topics unify the most influential researchers, the latest key findings and historical advances in a hot research area.

Find out more on how to host your own Frontiers Research Topic or contribute to one as an author by contacting the Frontiers editorial office: frontiersin.org/about/contact

Energy materials based novel solar thermal applications, 2nd edition

Topic editors

Muhammad Amjad — University of Engineering and Technology, Lahore, Pakistan
Enio Pedone Bandarra Filho — Federal University of Uberlandia, Brazil
Shafiq Ahmad — King Saud University, Saudi Arabia
Fahid Riaz — Abu Dhabi University, United Arab Emirates
Muhammad Abdul Qyyum — Sultan Qaboos University, Oman
Yanwei Hu — Harbin Institute of Technology, China
Jabbar Gardy — University of Leeds, United Kingdom

Citation

Amjad, M., Filho, E. P. B., Ahmad, S., Riaz, F., Qyyum, M. A., Hu, Y., Gardy, J., eds. (2024). *Energy materials based novel solar thermal applications, 2nd edition*. Lausanne: Frontiers Media SA. doi: 10.3389/978-2-8325-5165-3

Publisher's note: This is a 2nd edition due to an article retraction.

Table of contents

frontiers | Frontiers in Energy Research

TYPE Editorial
PUBLISHED 20 June 2023
DOI 10.3389/fenrg.2023.1230967

OPEN ACCESS

EDITED AND REVIEWED BY
Uwe Schröder,
University of Greifswald, Germany

*CORRESPONDENCE
Muhammad Amjad,
amjad9002@uet.edu.pk

RECEIVED 29 May 2023
ACCEPTED 14 June 2023
PUBLISHED 20 June 2023

CITATION
Amjad M, Bandarra Filho EP, Ahmad S, Riaz F, Qyyum MA, Hu Y and Gardy J (2023), Editorial: Energy materials based novel solar thermal applications. *Front. Energy Res.* 11:1230967. doi: 10.3389/fenrg.2023.1230967

Editorial: Energy materials based novel solar thermal applications

Muhammad Amjad[1,2]*, Enio Pedone Bandarra Filho[3], Shafiq Ahmad[4], Fahid Riaz[5], Muhammad Abdul Qyyum[6], Yanwei Hu[7] and Jabbar Gardy[8]

[1]Department of Mechanical Engineering, University of Engineering and Technology, Lahore, Pakistan, [2]Chair of Thermodynamics, School of Engineering and Design, Technical University of Munich, Garching, Germany, [3]School of Mechanical Engineering, Federal University of Uberlandia (UFU), Uberlandia, Brazil, [4]Department of Industrial Engineering, College of Engineering, King Saud University, Riyadh, Saudi Arabia, [5]Mechanical Engineering Department, Abu Dhabi University, Abu Dhabi, United Arab Emirates, [6]Petroleum and Chemical Engineering Department, College of Engineering, Sultan Qaboos University, Muscat, Oman, [7]School of Energy Science and Engineering, Harbin Institute of Technology, Harbin, China, [8]School of Chemical and Process Engineering, University of Leeds, Leeds, United Kingdom

KEYWORDS

solar PV, nanomaterials, AI in solar energy, heat transfer intensification, solar PVT, solar thermal collector, energy optimization

Editorial on the Research Topic
Energy materials based novel solar thermal applications

Introduction

With increasing apprehensions over global warming and environmental issues, the need to develop renewable energy is becoming more critical to secure our future energy needs. Solar energy is the most abundant source of energy and is easily accessible. However, making efficient use of solar energy is not an easy task. Energy materials, especially in their micro and nanoscale, have an excellent potential for absorbing, transferring, and storing solar energy when they are dispersed in an aqueous medium embedded on a surface. Various applications relevant to heat transfer, energy conversion, and storage have increasingly used nanoparticles due to their ability to absorb, store, and carry heat. However, successful deployment of materials in energy harvesting and storage applications must also consider some of the very fundamental challenges, including but not limited to sedimentation, entrainment, stability, and life of these potential energy materials. This Research Topic is designed to attract original research and review articles on AI based solar energy optimization, challenges, innovative applications and numerical studies in materials for energy capture, transfer, and storage to have a safe future in terms of solar energy utilization.

This Research Topic of 'Frontiers in Energy Research' has managed to attract and compile 11 high quality original research and review articles from passionate researchers and academicians from prestigious institutions in Australia, South Korea, China, Qatar, Pakistan, Korea, Saudi Arabia, Egypt, Oman, United Arab Emirates, Uganda, and Brazil. The guest editors are indebted to all the contributing authors to make this Research Topic successful. Figure 1

FIGURE 1
Integration of energy materials for novel solar thermal, PV and PVT applications.

Solar PV system evaluation and performance improvement

The integration of solar energy with the existing conventional electrical and thermal systems is revolutionizing to ensure the availability and augment the performance of the system to combat the exponentially increasing energy demands. Khan et al. proposed a systematic allocation of energy resources using the slice-based mechanism in a smart grid environment. This need-based approach is used to allocate energy resources not only helps save energy resources for future use but also improves the life of the power grid and is validated on real time conditions. Asim et al. presented an experimental validation of the numerical model used for the performance prediction of solar photovoltaic cells. They considered the varying and constant coefficients with the incident angle of the solar radiations in the energy balance equations to obtain the time-based electrical power of the solar cells. The model data of electrical power based on the optical-thermal model and classical thermal model was experimentally validated for the installed solar PV system.

The dust particles in the air keep accumulating on the surface of the PV panels and thus result in a reduction in their efficiency. Tamoor et al. investigated the impact of dust pollutants on the performance of PV systems and concluded that the efficiency of PV systems with dusty surfaces is reduced by up to 10.68% and must be taken care of while deciding the targets for solar electric power in the regions with higher levels of particulate matter.

Razzaq et al. explored that energy consumption in buildings can be reduced by 34% and the carbon footprints can be lessened by 32. 8 metric tons per year by retrofitting an existing building and integrating solar energy to make it a net zero energy building. An indirectly edited study by Khan et al. on exciting deep learning and ensemble learning mechanism for early detection of severe acute respiratory syndrome was published in a sister journal. Syed et al. conducted yet another interesting research to boost the photocatalytic efficiency of solar cells using carbon quantum dots to scatter the Sun radiations for higher current density.

Performance of solar thermal collectors

Solar thermal energy can be used more conveniently than solar electric energy and has even higher conversion efficiency. Using nanosized energy materials in solar thermal collectors has revolutionized this side of solar energy. Farhan et al. conducted an experimental investigation of a hybrid nanofluid based non-tracking compound parabolic solar collector. They explored that the collector efficiency can be enhanced up to 31.5% by suspending various energy materials of nanoscale and their hybrids at different volume concentrations and flow rates.

Ditta et al. interestingly integrated a solar thermal collector with the desiccant indirect evaporative system to produce a cooling effect for a dehumidified place. The integration resulted in a maximum efficiency of 56% at a maximum cooling capacity of the system at 4.6 kW. Rehman et al. outlined an inclusive review of the performance improvements of microchannel heat sinks through various techniques including the shapes of the microchannels, flow conditions, numerical methods, and the materials for the manufacturing of these channels.

Energy materials and photovoltaic-thermal hybrid systems

A solar photovoltaic system can be combined with a solar thermal system for an integrated performance gain. Such work is conducted by Usman et al. where they enhanced the efficiency of thermophotovoltaic (TPV) cells based on various design configurations by deploying existing photon recycling technologies. Using magnesium oxide as a spectral filter with a back surface reflector, they attained an efficiency of 35% of the TPV system at 2,200 K emitter temperature. Martins et al. exhibited an interesting numerical work on the integration of compound parabolic solar concentrators based hybrid photovoltaic-thermal (PVT) system to generate electricity during the day and night times combating the intermittency of solar energy. It was concluded that a backup of 1 h and 20 min can be set up for the hybrid cycle to generate 1,580 W power at 2,600 rpm and evaporation temperature of 80°C using R245fa as working fluid and urea-NaCl mixture for thermal energy storage in the absence of Sun.

Conclusion

Solar energy together with energy materials has enormous potential to meet exponentially increasing energy demands. This Research Topic sums up 11 high quality articles on emerging technologies to integrate solar energy into new and existing systems for augmented performance. The articles

present various technologies and applications of novel energy materials to harness solar energy for thermal and electric energy needs. Despite the high rated benefits of solar energy and nanomaterials, challenges like intermittency of solar potential, low efficiency of PV systems, high costs, and instability of the energy materials over prolonged times are to be taken care of for efficient deployment of solar energy.

Author contributions

All authors listed have made a substantial, direct, and intellectual contribution to the work and approved it for publication.

Conflict of interest

The authors declare that the research was conducted in the absence of any commercial or financial relationships that could be construed as a potential conflict of interest.

Publisher's note

frontiers | Frontiers in Energy Research

ORIGINAL RESEARCH
published: 15 June 2022
doi: 10.3389/fenrg.2022.922221

Efficient Power Grid Management Using Sliced-Based Mechanism for Systematic Allocation of Solar Energy Resources: A Conceptual Framework

Habib Ullah Khan[1]*, *Sulaiman Khan*[1] and *Shah Nazir*[2]

[1]Department of Accounting and Information Systems, College of Business and Economics, Qatar University, Doha, Qatar, [2]Department of Computer Science, University of Swabi, Swabi, Pakistan

OPEN ACCESS

Edited by:
Muhammad Amjad,
University of Engineering and Technology, Lahore, Pakistan

Reviewed by:
Astitva Kumar,
Delhi Technological University, India
Muhammad Ibrahim,
University of Science and Technology Beijing, China
Zia Ullah,
University of Engineering and Technology, Peshawar, Pakistan
Muhammad Adil,
University of Naples Parthenope, Italy

***Correspondence:**
Habib Ullah Khan
habib.khan@qu.edu.qa

Specialty section:
This article was submitted to Solar Energy, a section of the journal Frontiers in Energy Research

Received: 17 April 2022
Accepted: 05 May 2022
Published: 15 June 2022

Citation:
Khan HU, Khan S and Nazir S (2022) Efficient Power Grid Management Using Sliced-Based Mechanism for Systematic Allocation of Solar Energy Resources: A Conceptual Framework. Front. Energy Res. 10:922221. doi: 10.3389/fenrg.2022.922221

The over-population and the limited energy resources have puzzled the government and private organizations to think about the providence of non-stop energy resources to the industries, hospitals, smart homes, and shopping malls to ensure normal routine activities. To accept this challenge, some researchers put their efforts into generating energy from renewable energy resources (solar, fossil fuels, wind turbines, geothermal energy, and many others) to fulfill the needs of life. While some researchers worked on the efficient utilization of the available energy resources to save the energy for future generations. Inspiring from the second approach, this research work has proposed a systematic allocation of energy resources using the slice-based mechanism in a smart grid environment. This research framework using a hybrid model comprises long short-term memory (LSTM), and a support vector machine (SVM), where the LSTM classifies different energy requests (for allocation of energy resources) while the SVM accomplishes the statistical analysis (to estimate the number of solar energy resources allocated and for a specific interval of time). This need-based allocation of energy resources will not only assist in saving energy resources for future use, but will also improve the life of the power grid and other electric appliances (due to over-usage and burning). The applicability of this model is validated by testing it on a real-time scenario like slice failure conditions, slice overflow conditions, a huge number of requests, and alternate slice allocation conditions. Furthermore, the incoming request classification is also validated based on its accurate identification using a confusion matrix, varying number of hidden layers, accuracy, and time consumption. The outperformance of the selected based on these scenarios and validation metrics reflects the applicability of this framework. Moreover, this framework will assist in reducing overbilling charges and energy savage for future generations due to its need-based allocation of energy resources assignment capabilities.

Keywords: smart grids, power management, energy resources, sliced-based framework, systematic allocation

1 INTRODUCTION

Globally, the rapid economic development has endowed to an exponential increase in energy demands. The snippy evolution in world economies especially in the United States, China, and Europe is bound to increase energy consumption (Bórawski et al., 2019). The energy sector is followed as the prime caryatid of excrescence, development, and keenness of enterprises and new economies (European Commission Directorate-General for Energy, 2018). Around the world, 80% of the population uses electricity as a primary source of energy. Both government and non-government organizations contribute their full efforts to ensure non-interrupted power to their customers but the over-population, exponential growth in technologies, modern-day societies, and high reliance on electricity have baffled the researcher and power suppliers, in monitoring, managing, and analyzing the power grids to ensure non-stop power flow (Tian et al., 2021). The unavailability of sufficient incentives to upgrade the transmission infrastructure for example, in the US and Europe power cuts have become more frequent (Bruch et al., 2011). Achieving high energy security and environmental protection are the primary concern of an economy focused on sustainability. The non-uniform and unbalanced distribution of electric power mostly concludes with power outages and this power outage is among the key hurdles to sustainability. The power outage is divided into two different types of short-term power failure and long-term power failure. In the first failure form, the electricity mostly lasts part of an hour or for a few hours, but the long-term blackout ensues in enduring the electricity for days or even weeks (Tian et al., 2021).

Generally, we are facing bounded energy resources with more demands. Moreover, a high budget is required to produce energy from these limited resources. Keeping in view this critical problem the research community divided into two groups with different approaches 1) to identify new energy resources to meet the customers' needs and requirements, and 2) to efficiently utilize the available resources and develop an optimum power distribution model to provide need-based energy resources to the customers. This need-based distribution of resources not only assists in ensuring energy security and environmental protection but also improve the life of the available resources. The first group of researchers (those who decided to find alternate energy resources) presented new ideas such as Brockway et al. (2019) presented the use of fossil fuels as an alternate source of energy. They further explained that under many kismets it will remain the potent energy source to at least 2050. However, the extraction of useful energy from fossil fuels requires more energy and high incentives that resultantly make it more expensive for the customers and industrialists. Jurasz et al. (2020) accomplished a systematic analysis of the literature to perform a complementarity of the renewable energy sources. This research article provides chronological and spatial information about the extant and presented a complementarity concept of the extant. Panwar et al. (2011) and Sinsel et al. (2020) presented review articles to explain the use of renewable energy sources for environmental protection. Bórawski et al. (2019) suggested the use of biofuels as a renewable energy source for the European Union (EU). In this research article, the authors used descriptive and statistical analysis to detail the changes in bioenergy development in the EU. A. Kalogirou proposed a renewable energy source comprising solar collectors, geothermal energy, solar ponds, and photovoltaics for sea-water desalination (Kalogirou, 2005). Normally removal of salt from sea water requires high energy, so, the author presented a renewable source for sea-water desalination to bring this water into daily routine purposes like drinking, cooking, etc.

The key motivation behind the second approach (optimum utilization of the available resources) was cyber-attacks, meter reading errors, electricity theft, billing errors, fraud, and many other reasons. The unfair means and irregular distribution of the resources mostly result in providing more than enough resources to a group of people with no need, while limited energy resources to those (supposed to have more resources like industries, irrigation departments, etc.). In order to combat these challenges, some researchers like Colmenar-Santos et al. (2019) presented the concepts of smart grids to handle the issues like intermittency and the non-dispatchable nature of wind and solar energy production, but flexibility needs can migrate from generation to load, with the accretion of demand-side resources and storage technologies. A novel grid technique is suggested for the optimal integration of renewable resources and electric vehicles to increase penetration of renewable energy. Gu et al. (2020) presented a reliable fault ride mechanism to resist a large-scale disconnection of renewable energy plants due to grid faults. Lee and Lee presented an adaptive renewable energy mechanism for the base stations in the cellular networks to reduce energy consumption and provide high throughput with the help of traffic management and energy cooperation strategies (Lee and Lee, 2020). A network scheduling programming is used for the dispatching purposes between the on-grid and renewable energy resources in the base stations, while Lu et al. (2020) used stochastic programming for the optimal dispatch of on-grid and renewable energy resources. Rahbar et al. (2015) developed a real-time offline energy storage management framework for the renewable energy sources in the microgrid. Shah performed feasibility of six renewable energy sources including geothermal, municipal solid waste, biomass, wind, solar, and micro-hydro to develop a secure and renewable hydrogen-based energy source in Pakistan (Shah, 2020). The hydrogen-based energy source will enhance energy security and decrease hazardous emissions. The applicability of this renewable energy source was evaluated using Fuzzy Delphi, environmental data envelopment analysis (DEA), and fuzzy analytical hierarchy process (FAHP).

With the emergence of smart homes and integration of intelligent IoT-based smart devices, numerous automated appliances are nowadays available in every smart home architecture. These devices include a lighting system, colling and an air-conditioning system, efficient heating and

ventilation system, and many others. These devices on one side make our life easier but on the other side, it requires more energy to operate and resultantly it ends up with overbilling and high costs. So, significant attention is required in terms of energy efficiency. Moreover, the energy management of the poly-generation system or micro-generation has always been very complex. Keeping the balance between demands and production is always considered as a hectic job for the research community. To combat these challenges Hadi et al. (2020) proposed an efficient demand response algorithm to resist the intermittency problem by providing a continuous power supply to the customers. Han et al. (2014) developed a smart home energy management system using ZigBee and PLC technologies. In this research article, they perform energy estimation scheduling to reduce energy costs. O'Malley et al. (2020) reviewed the multi-carrier energy systems (MCESs) for future low carbon energy systems using electrification and very high variable renewable energy penetrations. Based on their review assessments they concluded that MCESs are more efficient and flexible to deploy on a large- and small-scale network level but are more complex to control and manage. These systems are classified using strong association in computation and planning throughout multiple energy vectors and/or sectors to provide reliable, cost-effective energy services to end users/customers with minimal impact on the environment.

To meet the high climate protection and resource efficiency, the development of a sustainable smart grid design is required to present a need-based allocation of energy resources to stop the waste of energy resources. This hypothetical model contains a sliced mechanism to provide energy resources to the appliances in smart homes. This hypothetical model uses LSTM and SVM classifiers, where the LSTM performs the identification of different energy requests (devices requesting energy resources) while the SVM classifiers perform the statistical analysis to calculate the time allocation of energy resources and relieving of energy resources. Based on the energy consumption and requirements, this hypothetical model divides the appliances into different categories. It allocates energy resources based on the information including season, weather, and priority-based allocation of resources (like if it is hot then more power for the fridge, water pumps, and air conditioning system, while if it is winter then more power to heaters and other heating appliances). The rest of the study is organized by explaining the most recent and relevant research work reported in **section 2** of the study. **Section 3** details the hypothetical model along with a full description and algorithm. **Section 4** evaluates the proposed hypothetical model based on some critical analysis followed by the conclusion and recommendations in **section 5** of the study.

2 RELATED WORK

Energy crises in the world have gained significant attention from the research community to think about the reduction of the energy resources in different areas. The abundance of integrated devices in the market and the installation of more appliances in smart homes have exponentially increased the energy consumption in the last few years (Han et al., 2014). Renewable energy sources and energy saving are alternate solutions for addressing the energy problems of smart residents. Power generation and consumption must be simultaneously considered for saving energy cost problems. The exponential increase in energy consumption, the diminution of non-renewable energy resources, the CO2 emanations resulting from energy production, and the affiliated global warming have become critical concerns worldwide, that drive the creation of new solutions for energy management and consumption. Tipantuña and Hesselbach presented an adaptive architecture for efficient energy utilization for both renewable and non-renewable energy sources (Tipantuña and Hesselbach, 2020). They suggested software-defined networking (SDN) and network functions virtualization (NFV) technologies enable and promote the primary use of energy from renewable sources. Khan et al. (2021a) proposed a smart appliances control system for the smart resident environment using the mobile application. A CNN-based hybrid solution is proposed for object identification and control purposes. Kumar et al. (2022a); Kumar et al. (2022b) suggested a hybrid model for proficient energy management using a grey wolf optimizer. Primarily, their work focuses on achieving energy from renewable energy resources and performing size optimization with reduced costs and increased productivity for the end-users.

To ensure the semipermanent development of human society, standards like energy saving and smart utilization have been encouraged by many researchers in the last few years, but above all, the need for low or zero-carbon emission sources, like renewable energy sources, have been bolstered (Int. Energy Agency Birol, 2013). Thus, green energy from renewable resources like wind and solar, in power grids has egressed as an environmentally friendly, important, and sustainable substitute to fulfill the current and future energy demands. However, the wavering nature of renewable sources due to environmental and geographical conditions may cause imbalance or instability when incorporated into the generation-consumption ecosystem (Carrasco et al., 2006). Moreover, the ineffective use of the limited energy generated has resulted in the development of different architectures such as Demand-Response (DR) systems that are capable of utilizing the available energy resources efficiently (Medina et al., 2010). This architecture comprises a set of actions and requests swapped between the energy consumer and the supplier that is accomplished using agreements, and aims to promote consumer involvement in energy management by granting the modification of consumption based on availability (Medina et al., 2010). The use of DR systems is encouraged among the consumers by offering reduced electricity bills or free-use electricity periods (Basmadjian et al., 2013; Basmadjian et al., 2018). The DR architecture can be implemented by integrating advanced ICT technology, such as data centers (Ghatikar, 2012).

Algorithms using deep learning (DL) architectures can convert simple features into more complex and abstract features automatically and are capable of solving practical problems by combining these

TABLE 1 | Different DL-based model used in smart grid management.

DL-based models	Research problem addressed	Application and characteristic evaluation
Stacked AE	Wang et al. (2018) suggested stacked auto-encoder for cyber-attacks on smart grids. Barbeiro et al. (2014) exploited AE model for state estimation in distribution grids.	AE models are designed to accurately accumulate the nonstationary and nonlinear features of data relevant to the electric load. These feature vectors are then applied to electric load forecasting to improve the accuracy of the grid which ultimately results in a narrower width of state variables. The probability in the form of forecasting errors is calculated using the Gaussian distribution parameter.
DeepCoin	Ferrag and Maglaras, (2020) proposed a DL-based blockchain-driven energy exchange framework for smart grids to counter intrusion attacks. Hasankhani et al. (2021) accomplished a systematic evaluation to assess the literature for evaluating the future of blockchain-driven applications in the domains of smart grids and safe energy transmissions.	This model exploits two different schemes, a blockchain-driven system, and a DL-based system. The blockchain-driven system comprises five stages: assemble stage, agreement stage, producing a block stage and consensus-making stage, and view change stage. It integrates a novel reliable peer-to-peer energy system using a practical Byzantine fault tolerance algorithm to achieve prominent results. To hinder smart grid attacks, this model makes secures each block with hash functions and short signatures.
Bayesian deep learning	Yang et al. (2020) suggested Bayesian DL-based design instead of the probabilistic load forecasting (PLF) model to ensure high reliability and efficient energy transmission in a smart grid.	Exponential increases in deploying smart meters in millions of households results in a drastic amount of individual electricity consumption. To counter this problem the Bayesian DL model provides a cluster-based pooling scheme primarily implemented to boost data diversity and volume for the framework.

features. Resultantly, DL has gained significant research interest in diverse domains. Since the Parousia of DL technology in 2013, DL architectures such as deep neural network (DNN) and deep belief network (DBN) have been suggested for fault diagnosing in mechanical systems. Using the recent literature as evidence, we concluded that the four DL algorithms based on CNN, DNN, Automatic Encoder (AE), and LSTM are extensively proposed in the fields of energy resource allocation and dis-connection as depicted in **Table 1**. The corresponding network model structures of these DNN models are shown in **Figure 1**.

The CNN architecture contains one or more convolutional and pooling layers, merged with a fully connected layer. These models outperformed in processing images and natural language databases, which can highly minimize the number of parameters used in the training process (Khan et al., 2019). On the other side, the CNN model is time-consuming in both the simulation and learning process. Also, its architecture is highly complicated and difficult to implement. The DNN architectures comprise at least one hidden layer trained by back-propagation and gradient descent functions. In the DNN models when we add a greater number of hidden layers it yields more abstract features that ultimately result in over-fitting problems. Auto encoder (AE) is an unsupervised training model that efficiently performs in compressing data, and thus it is often followed in data denoising and reducing visual-based data dimensions. The encouraging aspect of using the AE model is its ability to choose the suitable extended model using the actual processing data as an argument. But the capability to process only one type of data is considered the discouraging aspect of AE-based models. LSTM is a derived form of recursive neural network, capable of learning long distance dependent data. It contains multiple cells associated in series with each other, where every "cell" is framed by an input gate, an output gate, a forgetting gate, and a state unit. Strong sequence data modeling is the prominent tool of this architecture. Furthermore, the gradient fading problems can also be addressed using the output and forgetting gates. The unavailability of sufficient data (for training purposes) results in overfitting conditions and it is followed as the discouraging aspect of the LSTM models.

For achieving optimum resource utilization and traffic control, the researchers proposed sliced-based solutions for different research problems such as Khan et al. (2021b); Khan et al. (2022) suggested a sliced design for network communication systems to efficiently control the congestion and network traffic. They proposed a convolution neural network (CNN) for classification purposes, while LSTM and SVM for statistical analysis. This statistical analysis was aimed to calculate the traffic status to counter slice overflow or failure conditions. Thantharate et al. (2019) proposed a deep slice model for internet security and efficient communication in a 5^{th} generation network. Bideh et al. (2020) suggested Message Queue Telemetry Transport (MQTT) and Constraint Application Protocol (CoAP) for calculating energy consumption to secure lightweight IoT protocols. Requeno et al. (2012) proposed a sliced model to perform phylogenetic analysis to validate the biological properties of phylogenies. After studying the literature, it was concluded that there is no sliced-based framework suggested for the efficient allocation of energy resources. To counter this problem, this research work presents a smart grid design for optimum energy resource allocation using a slice-based deep learning model. This model uses LSTM and a support vector machine (hybrid architecture), where the LSTM performs the time-based allocation of resources while SVM will perform the statistical analysis to identify the need-based allocation of energy resources. This slice-based mechanism will not assure the non-stop energy resources, but it will minimize the over-billing charges of the customers. In addition, it will have low chances to cable damage or failure of overall grids.

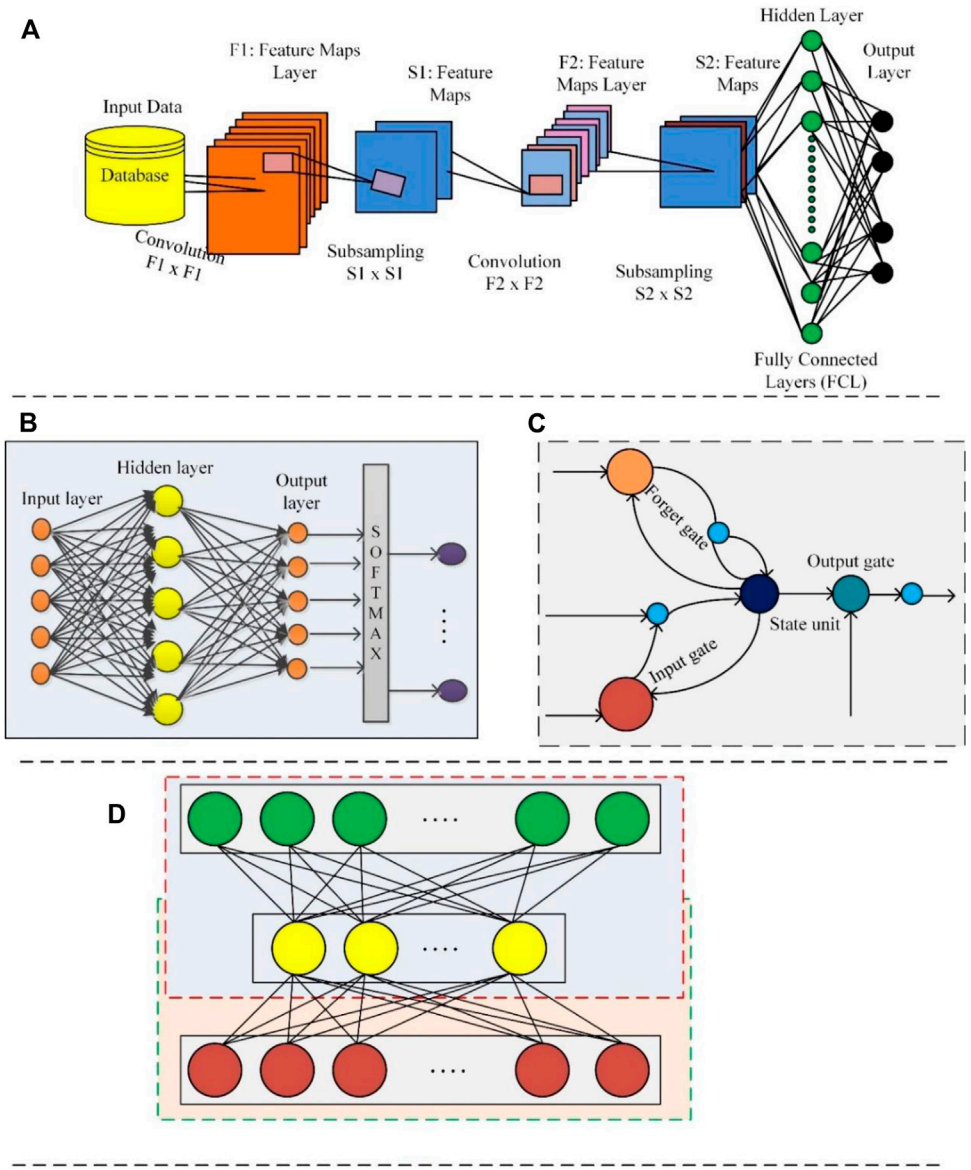

FIGURE 1 | Typical architectures of **(A)** CNN model, **(B)** DNN model, **(C)** LSTM, and **(D)** auto encoder.

3 PROPOSED CONCEPTUAL FRAMEWORK

A conceptual framework is developed in this research work for the development of a smart grid design that works by implementing a sliced-based approach to allocate energy resources to smart home appliances. The conceptual frameworks are proposed for numerous research problems like Sampaio and González proposed a conceptual design for Photovoltaic solar energy (Sampaio and González, 2017). They performed a systematic analysis by selecting different parameters like current market values, cost and technologies proposed different ways of obtaining energy resources, advantages, and disadvantages, and implications. Azar and Menassa presented a conceptual design for energy estimation in a smart building using the agent-based framework (Azar and Menassa, 2010). Chung et al. (2017) suggested a conceptual design for evaluating the security of available energy resources in South Korea. They performed a systematic evaluation of different energy resources like coal, oil, nuclear, natural gas, and renewable energy resources. They mainly focused on indexes of supply reliability, environmental sustainability, electricity production cost, and technology complementarity. Sadeq et al. (2022) presented a conceptual framework using a wireless sensor network integrated with MAC protocol (WSN-MAC) to achieve high energy consumption for the IoT devices.

Based on the literature evidence, a conceptual framework is presented in this research work for the efficient allocation of energy resources in smart homes. The proposed conceptual

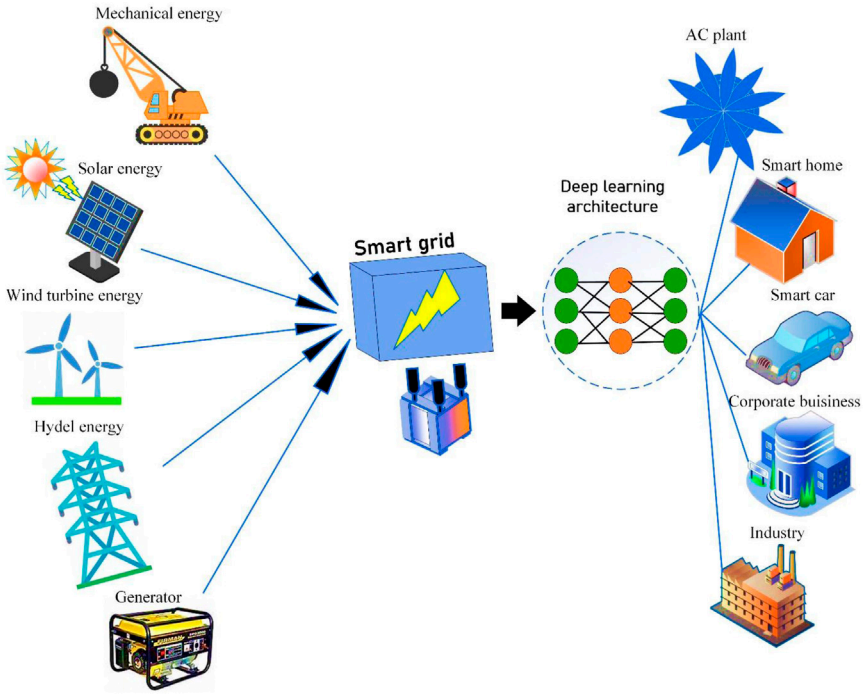

FIGURE 2 | Proposed conceptual framework.

framework is depicted in **Figure 2**. Generally, this framework is divided into three main sections. The input section (incoming energy from different electrical and mechanical sources including solar panels, hydel powers, mechanical systems, generators, and other renewable energy resources), the smart grid (the overall input energy is provided to the smart grid to perform a systematic allocation of energy resources using the artificial intelligence-based design), and the different systems and devices that consume energy resources. These consumers can be of type smart homes, industries, banking systems, air-conditioning plants, universities, and many others. The artificial intelligence-based design uses a hybrid design comprising LSTM and SVM classifiers and identification models. The SVM performs the statistical analysis to identify the need for resources to accomplish a certain task. This need-based allocation of resources will not only save energy resources for future use, but also keeps different valuable appliances from burning due to overload or overuse conditions. After identifying the requirement of resources, the LSTM model calculates the timely allocation of energy resources. Also, this model is capable of assigning priority-based allocation of energy resources. For example, in hard weather conditions (summer) the priority will be assigned to the water pump and other water evacuation systems (because it is more difficult to have time without water). On the side, if it is winter, then energy resources will be assigned to those appliances that keep the room temperature constant for living beings.

In the literature, the SVM classifier is extensively suggested for the classification of linear and non-linear problems (Khan et al., 2021c). Promising results can be generated by carefully choosing the quadratic function that solely depends on the regularization parameter. Kernel-based functions are a handy tool in the regularization process. Different kernel functions like radial-based function (RBF) kernel, polynomial-based kernel, sigmoid, and linear kernels are handy tools to consider.

- Linear-based Kernel – $H(u, v) = u \times v$
- Sigmoid-based Kernel – $H(u, v) = \tanh\langle \beta_0 uv + \beta_1 \rangle$
- RBF-based Kernel – $H(u, v) = e^{(-\gamma \|u-v\|^2)}$
- Polynomial Kernel – $H(u, v) = [(u \times v) + 1]^d$

The letters d, β_0, β_1, and γ are the metrics that can be estimated empirically with the help of **Eq. 1**.

$$f(x) = W^T \theta x + v \tag{1}$$

where $w \in R$ and $b \in R$ and $\theta(x)$ depicts a feature vector.

The motivation behind the use of the SVM classifier is its easy implementation, the providence of accurate results during a limited span of time, and operationally smartness. The transformation function is implemented with the help of a non-linear operator $\theta(x)$ to convert inputs a_u, b_u into a high dimensional space. The optimum hyper-place is depicted in **Eq. 2** below.

$$f(x) = sgn\Big(\sum b_u x_u M(a_u, a) + y \Big) \tag{2}$$

where $M(a_u, a) = e^{(-\gamma \|a_u - a\|^2)}$ is the kernel function using RBF, and this overall sgn (.) represents the sign function.

TABLE 2 | Description of the database used for simulation purposes (Candanedo, 2017).

S. No	Parameters	Description	S. No	Parameters	Description
1.	Total number of instances	19735	2.	Number of Web hits	185122
3.	Type of entries in the database	Time series, multivariate	4.	Entries type	Real-time (date, time)
5.	Number of features	29	6.	Attribute information	Appliances, energy use in Wh, temperature, humidity, etc.

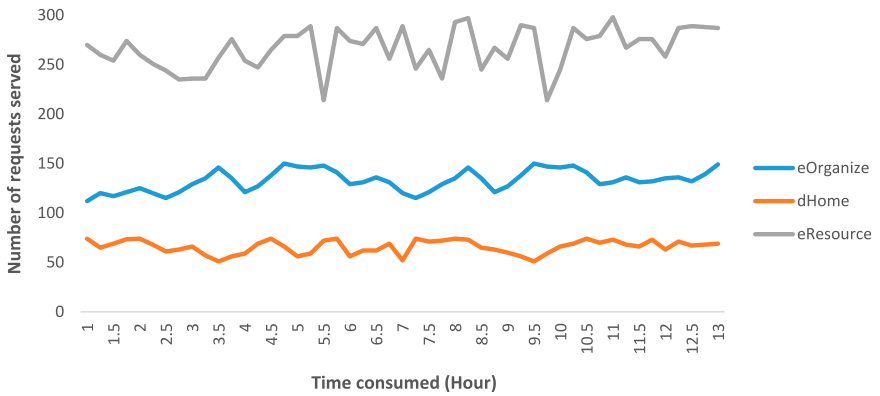

FIGURE 3 | Number of energy requests served.

Algorithm 1. Algorithm for the proposed hybrid energy framework is mentioned below.

Algorithm: To develop need-based energy resource allocation model using slicing mechanism

Input: Energy from different sources (mechanical energy plant, hydel power plant, solar plant, wind turbine plant, and so on)
Output: Need-based allocation of energy resources to different devices (air conditioning plant, industry, smart homes, smart cars, etc.

Start
Step 1: *initialize eResouce as a vector of length x* /* represents available energy resources
initialize dHome as a vector of length x /* represents home devices
initialize eOrganiz as a vector of length x /* represents different organizations/commercial devices
initialize mSlice as a vector of length x /* mSlice represents "master Slice"
Step 2: *initialize validate = 0* /*to check the availability of a certain energy vector
Step 3: *initiate energy resource request based on different input types, req*

for *i = 1 … x* ***do***

// *to control load balancing in different energy resource slices*
$s1 = eResource_x/sizeof(eResource) \times 100$ /* counts the % age utilization eResource slice
$s2 = dHome_x/sizeof(dHome) \times 100$ /* counts the % age utilization dHome slice
$s3 = eOrganize_x/sizeof(eOrganize) \times 100$ /* counts the % age utilization eOrganize slice
$s4 = eSlice_x/sizeof(eSlice) \times 100$ /* counts the % age utilization master slice

if *(validate)*
if *(high throughput && s1 < =93%)* /* above 95% is considered as overloading
$eResource_x = req_i$ /* high energy consuming resources will be assigned to eResource vector
ElseIf *((reliability && low latency) && s2 <=95%)*
$dHome_x = req_i$
ElseIf *((low throughput && high density) && s3 <=95%)*
$eOrganize_x = req_i$
Else
$mSlice_x = req_i$ /* if slice usage exceeds 95% new energy request must be allocated to mSlice
Else
$mFile_x = req_i$ /* during the slice failure the requests will be automatically assigned to mSlice
End if

End for

To validate the proposed conceptual model, home appliances database[1] developed by the U.S. Department of Commerce is freely available for simulation and experimental work. Candanedo et al. (2017) used this database for identifying the energy use of different appliances using data-driven predictive models. They have used four different classification models including SVM with the radical kernel, multiple linear regression, random forest, and gradient boosting machines (GSM). The description of this database is detailed in **Table 2**. The data is accumulated for a time interval ranging from 10 min to about 4.5 months.

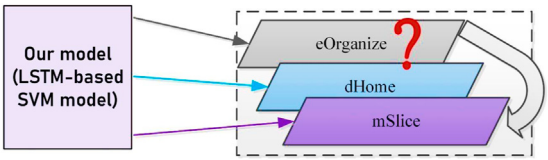

FIGURE 4 | Load overloading error in eOrganize slice and automatic allocation of requests to mSlice.

After training and testing our model with this real-time time, the following results are generated depicted in **Figure 3**. It represents the number of appliances requested for energy resources and served (resources allocated during a time interval of 13 h). From **Figure 3**, it is concluded that sufficient resources are assigned to home appliances and commercial-based devices and there are no overloading or slice failure conditions. In other words, there are enough resources left to serve the new incoming requests.

This model is validated for overloading conditions (requesting more than enough energy resources). The overloading condition is depicted in **Figure 4**, where the eOrganize requests for energy resources more than a slice can cover (>95%), then in this case the

[1]https://archive.ics.uci.edu/ml/datasets/Appliances+energy+prediction

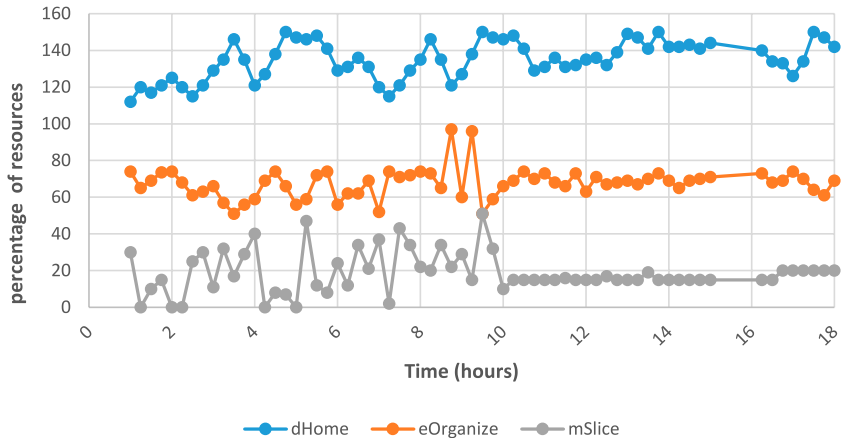

FIGURE 5 | Automatic allocation of mSlice to eOrgnaize requests after overloading conditions.

TABLE 3 | Performance evaluation of different techniques using different performance parameters.

Techniques	Recall	Precision	F1-score	Accuracy	AUC
particle swarm optimization	0.72	0.76	0.81	0.82	0.86
grey wolf optimization	0.74	0.81	0.85	0.87	0.89
Conv1D Net	0.76	0.78	0.81	0.82	0.83
Proposed model	0.96	0.87	0.87	0.86	0.95

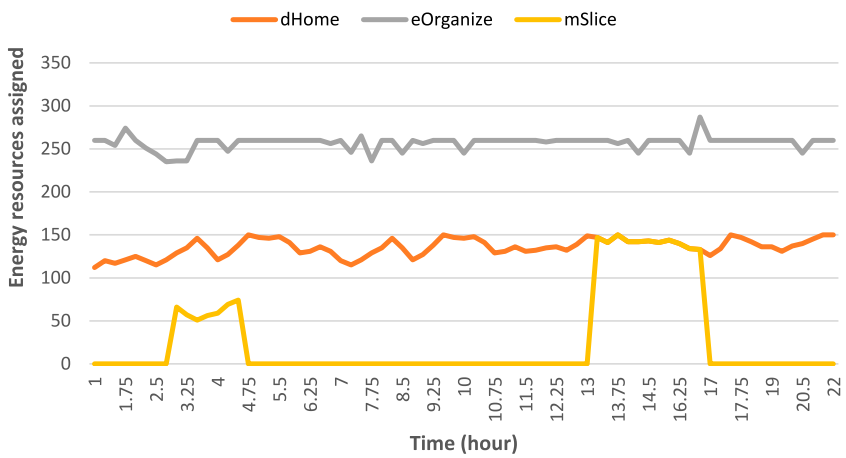

FIGURE 6 | mSlice automatic allocation during slice failure conditions.

energy resources are automatically assigned from the reserved energy resources (mSlice) to handle any unwanted situation like overloading or slice failure conditions. The proposed model is capable of assigning mSlice to the newly incoming energy requests and also assigns the mSlice to the currently available requests as depicted in **Figure 4**.

After overloading conditions, the automatic allocation of resources allocation is depicted in **Figure 5**. These results are generated for a period of 18 h. From **Figure 5**, it is concluded that at 9:30 and 9:45 h an overloading condition arises. When the model predicts these conditions, the new energy requests are automatically directed to mSlice (master slice) for allocation of sufficient energy requests.

4 RESULTS AND DISCUSSIONS

The applicability of the proposed sliced-based energy resource allocation model is validated using different scenarios and performance validation metrics. The scenarios include slice

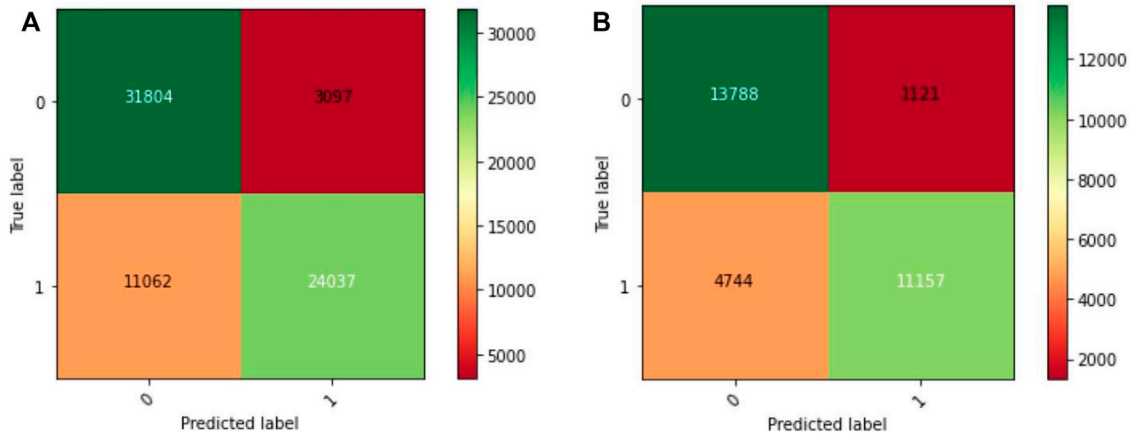

FIGURE 7 | Confusion matrix for the proposed framework **(A)** for training set, **(B)** for test set.

failure conditions and many energy requests. While performance metrics include accurate request identification capabilities based on precision, accuracy, and accurate time slot assignment. Moreover, the simulation time required and identification using a varying number of hidden layers are also used as evaluating strategies in this research work.

4.1 Energy Slice Failure Condition

The selected research model is assessed for the slice failure condition. The applicability of the proposed hybrid model is tested based on its accurate slice failure identification and accurate assignment of the mSlice (master slice). Based on the simulated results depicted in **Figure 6**, our hybrid model accurately assigned the master slice (mslice) in case of slice failure conditions.

In **Figure 6**, a slice failure condition occurs in the dHome slice (home appliances slice) during the period of 2 h and 15 min during the time interval 2:30 to 4:45, while another slice failure condition occurred for a period of 5 h during the interval 1:00 p.m. to 5:00 p.m. The proposed hybrid model automatically detects this slice failure condition and allocated the master slice to provide a non-stop energy resource to the ongoing requests. This automatic alternate slice allocation reflects the high applicability of this need-based energy resource allocation framework. And after slice recovery, the dHome slice is then automatically assigned back to the ongoing operations. In other words, there is no energy loss or operation loss condition occurred during this handover/slice-exchange process.

4.2 Alternate Slice Allocation

The proposed model is also validated for a high number of energy requests (utilization of an energy slice of more than 95%). In this case, the new devices from both the dHome slice and eOrganize slice are automatically routed to the mSlice. This automatic redirection assists in controlling the devices' requests in peak hours' conditions like the summer season (when there is more attention required for the ventilation and cooling systems).

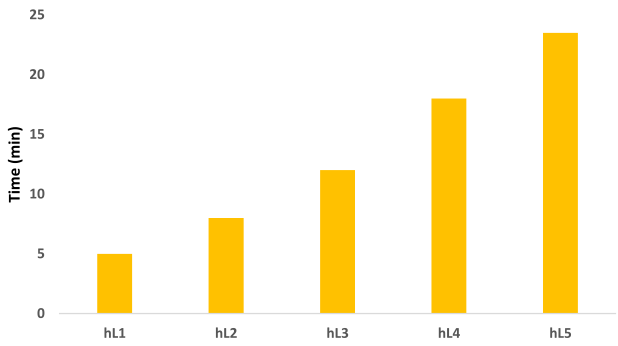

FIGURE 8 | Hidden layers-based performance validation using time consumption as a key metric.

4.3 Accurate Incoming Requests Classification

The proposed research framework is also avouched for the classification of incoming requests based on energy resources requirements (low energy resources consuming devices or high energy resources consuming devices. In other words, the incoming requests are from factories or industries (that mostly require non-stop high energy resources) or the home appliances (smart cars, smart doors, other home appliances) that typically require small energy resources. To avouch the performance of the proposed hybrid model confusion matrix, time consumption using a different number of hidden layers, precision, and accuracy are used. The experimental results are detailed below.

Figure 7 depicts the identification rate of the proposed framework using a confusion matrix as a validation parameter. The small false-positive values depict the applicability of the proposed model in the targeted research domain.

This framework is also evaluated using a varying number of hidden layers (hL) and corresponding time consumption. The low time consumption during the classification process depicts the applicability of the proposed hybrid framework. In our case, we used hidden layers (starting from one hidden layer). The corresponding results are depicted in **Figure 8**. These simulation results are generated on a core-i7 laptop. From **Figure 8**, it is observed that increases in hL resultantly increase the time consumption in the energy requests classification. If the proposed framework is trained using a GPU-based system, then the time consumption will be reduced to a number of seconds instead of minutes.

Applicability of the proposed hybrid model is also validated using different classification and recognition models including particle swarm optimization technique, grey wolf optimization, and convolution 1dimensional network (Conv 1D Net). For validation purposes, different performance metrics including recall, accuracy, precision, and area under the curve (AUC) are used. Based on the performance values it was concluded that our model outperformed by generating optimum classification and recognition results. During the experimental results, it was concluded that particle swarm optimization and grey wolf optimization techniques are shallow architectures. Shallow architectures performed well in binary classification problems, while failing in multi-class problems. In our case, we have a multi-class problem (including six different classes).

5 CONCLUSION

Globally, the actual energy consumption is more than the available current energy reservoirs. The daily-based infrastructure development with a high speed and exponential increase in world population is another prominent challenges to these available energy reservoirs. The research community, the public, and private organizations put their part by exploring new energy resources from solar, fossil fuels, wind turbines, geothermal energy, and many others to meet the current and future energy demands. But the non-planned energy distribution mechanism concludes with non-optimum results in the form of non-stop energy providence to different sectors (industries, smart homes, etc.). An efficient and need-based resource allocation framework is required for the providence of energy resources so that the misuse and waste of energy resources must be stopped. To combat this critical problem this research work presents a sliced-based energy providence mechanism using a hybrid model consisting of LSTM and SVM classifiers. This hybrid model can classify incoming energy requests and provides energy resources based on their requirements. In the sliced approach, the low and high energy consumption devices are divided into different slices. This sliced-based division assist not only helps in evaluating the incoming requests, but it also assists in estimating the currently available resources to fulfill the number of future energy requests they can serve.

The SVM classifier performs the statistical analysis to handle overloading and slice-failure conditions. Also, it ensures the timely allocation of energy resources. The applicability of this framework is analyzed using a real-time database and different slice failure conditions (alternate slice allocation during slice failure or overflow conditions). Other performance metrics include confusion matrix, accuracy, and time consumption. Based on the performance results, our framework outperformed not only in generating optimum classification results and providing need-based energy resources, but it also saves energy resources for future generations.

DATA AVAILABILITY STATEMENT

The original contributions presented in the study are included in the article/Supplementary Material; further inquiries can be directed to the corresponding author.

AUTHOR CONTRIBUTIONS

Leading the research, introduction, L. Reivew, Discussion, Analysis, HK The methodology by SK Discussion and conclusion by SN.

FUNDING

The publication was supported by Qatar National Library and Qatar University Internal Grant QUHI-CBE-21/22-1.

REFERENCES

Azar, E., and Menassa, C. (2010). "A Conceptual Framework to Energy Estimation in Buildings Using Agent Based Modeling," in Proceedings of the 2010 Winter Simulation Conference, 3145–3156. doi:10.1109/wsc.2010.5679007

Barbeiro, P. N. P., Krstulovic, J., Teixeira, H., Pereira, J., Soares, F. J., and Iria, J. P. (2014). "State Estimation in Distribution Smart Grids Using Autoencoders," in 2014 IEEE 8th International Power Engineering and Optimization Conference (PEOCO2014), 358–363.

Basmadjian, R., Botero, J. F., Giuliani, G., Hesselbach, X., Klingert, S., and De Meer, H. (2018). Making Data Centers Fit for Demand Response: Introducing GreenSDA and GreenSLA Contracts. *IEEE Trans. Smart Grid* 9, 3453–3464. doi:10.1109/tsg.2016.2632526

Basmadjian, R., Lovasz, G., Beck, M., Meer, H. D., Hesselbach-Serra, X., Botero, J. F., et al. (2013). "A Generic Architecture for Demand Response: The ALL4Green Approach," in 2013 International Conference on Cloud and Green Computing, 464–471. doi:10.1109/cgc.2013.79

Bideh, P. N., Sönnerup, J., and Hell, M. (2020). "Energy Consumption for Securing Lightweight IoT Protocols," in presented at the Proceedings of the 10th International Conference on the Internet of Things, Malmö, Sweden. doi:10.1145/3410992.3411008

Bórawski, P., Bełdycka-Bórawska, A., Szymańska, E. J., Jankowski, K. J., Dubis, B., and Dunn, J. W. (2019). Development of Renewable Energy Sources Market and Biofuels in the European Union. *J. Clean. Prod.* 228, 467–484. doi:10.1016/j.jclepro.2019.04.242

Brockway, P. E., Owen, A., Brand-Correa, L. I., and Hardt, L. (2019). Estimation of Global Final-Stage Energy-Return-On-Investment for Fossil Fuels with Comparison to Renewable Energy Sources. *Nat. Energy* 4, 612–621. doi:10.1038/s41560-019-0425-z

Bruch, M., Munch, V., Aichinger, M., Kuhn, M., Weymann, M., and Schmid, G. (2011). "Power Blackout Risks. Risk Management Options. Emerging Risk Initiative—Position Paper," in *CRO Forum*.

Candanedo, L. (2017). Appliances Energy Prediction Data Set. UCI Machine Learning Repository. *Accessed from*.https://www.archive.ics.uci.edu/ml/datasets/Appliances+energy+prediction

Candanedo, L. M., Feldheim, V., and Deramaix, D. (2017). Data Driven Prediction Models of Energy Use of Appliances in a Low-Energy House. *Energy Build.* 140, 81–97. doi:10.1016/j.enbuild.2017.01.083

Carrasco, J. M., Franquelo, L. G., Bialasiewicz, J. T., Galvan, E., PortilloGuisado, R. C., Prats, M. A. M., et al. (2006). Power-Electronic Systems for the Grid Integration of Renewable Energy Sources: A Survey. *IEEE Trans. Ind. Electron.* 53, 1002–1016. doi:10.1109/tie.2006.878356

Chung, W.-S., Kim, S.-S., Moon, K.-H., Lim, C.-Y., and Yun, S.-W. (2017). A Conceptual Framework for Energy Security Evaluation of Power Sources in South Korea. *Energy* 137, 1066–1074. doi:10.1016/j.energy.2017.03.108

Colmenar-Santos, A., Muñoz-Gómez, A.-M., Rosales-Asensio, E., and López-Rey, Á. (2019). Electric Vehicle Charging Strategy to Support Renewable Energy Sources in Europe 2050 Low-Carbon Scenario. *Energy* 183, 61–74. doi:10.1016/j.energy.2019.06.118

European Commission Directorate-General for Energy (2018). EU Energy in Figures : Statistical Pocketbook 2018: Publications Office. Available at https://www.data.europa.eu/doi/10.2833/279113.

Ferrag, M. A., and Maglaras, L. (2020). DeepCoin: A Novel Deep Learning and Blockchain-Based Energy Exchange Framework for Smart Grids. *IEEE Trans. Eng. Manage.* 67, 1285–1297. doi:10.1109/tem.2019.2922936

Ghatikar, G. (2012). *Demand Response Opportunities and Enabling Technologies for Data Centers: Findings from Field Studies*. Lawrence Berkeley National Laboratory powered by California library.

Gu, Y., Huang, Y., Wu, Q., Li, C., Zhao, H., and Zhan, Y. (2020). Isolation and Protection of the Motor-Generator Pair System for Fault Ride-Through of Renewable Energy Generation Systems. *IEEE Access* 8, 13251–13258. doi:10.1109/access.2020.2965773

Hadi, A. A., Silva, C. A. S., Hossain, E., and Challoo, R. (2020). Algorithm for Demand Response to Maximize the Penetration of Renewable Energy. *IEEE Access* 8, 55279–55288. doi:10.1109/access.2020.2981877

Han, J., Choi, C.-s., Park, W.-k., Lee, I., and Kim, S.-h. (2014). Smart Home Energy Management System Including Renewable Energy Based on ZigBee and PLC. *IEEE Trans. Consum. Electron.* 60, 198–202. doi:10.1109/tce.2014.6851994

Hasankhani, A., Mehdi Hakimi, S., Bisheh-Niasar, M., Shafie-khah, M., and Asadolahi, H. (2021). Blockchain Technology in the Future Smart Grids: A Comprehensive Review and Frameworks. *Int. J. Electr. Power & Energy Syst.* 129, 106811. doi:10.1016/j.ijepes.2021.106811

Int. Energy Agency, Birol, F. (2013). World Energy Outlook 2013, IEA. Available at https://www.iea.org/reports/world-energy-outlook-2013.

Jurasz, J., Canales, F. A., Kies, A., Guezgouz, M., and Beluco, A. (2020). A Review on the Complementarity of Renewable Energy Sources: Concept, Metrics, Application and Future Research Directions. *Sol. Energy* 195, 703–724. doi:10.1016/j.solener.2019.11.087

Kalogirou, S. (2005). Seawater Desalination Using Renewable Energy Sources. *Prog. Energy Combust. Sci.* 31, 242–281. doi:10.1016/j.pecs.2005.03.001

Khan, S., Ali, H., Ullah, Z., Minallah, N., Maqsood, S., and Hafeez, A. (2019). *KNN and ANN-Based Recognition of Handwritten Pashto Letters Using Zoning Features*.

Khan, S., Hussain, A., Nazir, S., Khan, F., Oad, A., and Alshehr, M. D. (2021a). Efficient and Reliable Hybrid Deep Learning-Enabled Model for Congestion Control in 5G/6G Networks. *Comput. Commun*, 31–40. doi:10.1016/j.comcom.2021.11.001

Khan, S., Khan, S., Ali, Y., Khalid, M., Ullah, Z., and Mumtaz, S. (2022). Highly Accurate and Reliable Wireless Network Slicing in 5th Generation Networks: A Hybrid Deep Learning Approach. *J. Netw. Syst. Manag.* 30, 29. doi:10.1007/s10922-021-09636-2

Khan, S., Nazir, S., Ullah Khan, H., and Hussain, A. (2021b). Pashto Characters Recognition Using Multi-Class Enabled Support Vector Machine. *Comput. Mater. \& Contin.* 67, 2831–2844. doi:10.32604/cmc.2021.015054

Khan, S., Nazir, S., and Ullah Khan, H. (2021c). Smart Object Detection and Home Appliances Control System in Smart Cities. *Comput. Mater. \& Contin.* 67, 895–915. doi:10.32604/cmc.2021.013878

Kumar, A., Rizwan, M., and Nangia, U. (2022). A Hybrid Optimization Technique for Proficient Energy Management in Smart Grid Environment. *Int. J. Hydrogen Energy* 47, 5564–5576. doi:10.1016/j.ijhydene.2021.11.188

Kumar, A., Rizwan, M., and Nangia, U. (2022). A New Approach to Design and Optimize Sizing of Hybrid Microgrids in Deregulated Electricity Environment. *CSEE J. Power Energy Syst.* 8, 569–579. doi:10.17775/CSEEJPES.2020.03200

Lee, H.-S., and Lee, J.-W. (2020). Adaptive Traffic Management and Energy Cooperation in Renewable-Energy-Powered Cellular Networks. *IEEE Syst. J.* 14, 132–143. doi:10.1109/jsyst.2018.2890281

Lu, R., Ding, T., Qin, B., Ma, J., Fang, X., and Dong, Z. (2020). Multi-Stage Stochastic Programming to Joint Economic Dispatch for Energy and Reserve with Uncertain Renewable Energy. *IEEE Trans. Sustain. Energy* 11, 1140–1151. doi:10.1109/tste.2019.2918269

Medina, J., Muller, N., and Roytelman, I. (2010). Demand Response and Distribution Grid Operations: Opportunities and Challenges. *IEEE Trans. Smart Grid* 1, 193–198. doi:10.1109/tsg.2010.2050156

O'Malley, M. J., Anwar, M. B., Heinen, S., Kober, T., McCalley, J., McPherson, M., et al. (2020). Multicarrier Energy Systems: Shaping Our Energy Future. *Proc. IEEE* 108, 1437–1456.

Panwar, N. L., Kaushik, S. C., and Kothari, S. (2011). Role of Renewable Energy Sources in Environmental Protection: A Review. *Renew. Sustain. Energy Rev.* 15, 1513–1524. doi:10.1016/j.rser.2010.11.037

Rahbar, K., Xu, J., and Zhang, R. (2015). Real-Time Energy Storage Management for Renewable Integration in Microgrid: An Off-Line Optimization Approach. *IEEE Trans. Smart Grid* 6, 124–134. doi:10.1109/tsg.2014.2359004

Requeno, J. I., Blanco, R., de Miguel Casado, G., and Colom, J. M. (2012). "Sliced Model Checking for Phylogenetic Analysis," in 6th International Conference on Practical Applications of Computational Biology & Bioinformatics, Berlin, Heidelberg, 95–103. doi:10.1007/978-3-642-28839-5_11

Sadeq, A. S., Hassan, R., Sallehudin, H., Aman, A. H. M., and Ibrahim, A. H. (2022). Conceptual Framework for Future WSN-MAC Protocol to Achieve Energy Consumption Enhancement. *Sensors* 22, 2129. doi:10.3390/s22062129

Sampaio, P. G. V., and González, M. O. A. (2017). Photovoltaic Solar Energy: Conceptual Framework. *Renew. Sustain. Energy Rev.* 74, 590–601. doi:10.1016/j.rser.2017.02.081

Shah, S. A. A. (2020). Feasibility Study of Renewable Energy Sources for Developing the Hydrogen Economy in Pakistan. *Int. J. Hydrogen Energy* 45, 15841–15854. doi:10.1016/j.ijhydene.2019.09.153

Sinsel, S. R., Riemke, R. L., and Hoffmann, V. H. (2020). Challenges and Solution Technologies for the Integration of Variable Renewable Energy Sources-A Review. *Renew. Energy* 145, 2271–2285. doi:10.1016/j.renene.2019.06.147

Thantharate, A., Paropkari, R., Walunj, V., and Beard, C. (2019). "DeepSlice: A Deep Learning Approach towards an Efficient and Reliable Network Slicing in 5G Networks," in 2019 IEEE 10th Annual Ubiquitous Computing, Electronics & Mobile Communication Conference (UEMCON), 0762–0767. doi:10.1109/uemcon47517.2019.8993066

Tian, Y., Wang, Q., Guo, Z., Zhao, H., Khan, S., Mao, W., et al. (2021). A Hybrid Deep Learning and Ensemble Learning Mechanism for Damaged Power Line Detection in Smart Grids. *Soft Comput.* 1, 1–9. doi:10.1007/s00500-021-06482-x

Tipantuña, C., and Hesselbach, X. (2020). NFV/SDN Enabled Architecture for Efficient Adaptive Management of Renewable and Non-renewable Energy. *IEEE Open J. Commun. Soc.* 1, 357–380. doi:10.1109/OJCOMS.2020.2984982

Wang, H., Ruan, J., Wang, G., Zhou, B., Liu, Y., Fu, X., et al. (2018). Deep Learning-Based Interval State Estimation of AC Smart Grids against Sparse Cyber Attacks. *IEEE Trans. Ind. Inf.* 14, 4766–4778. doi:10.1109/tii.2018.2804669

Yang, Y., Li, W., Gulliver, T. A., and Li, S. (2020). Bayesian Deep Learning-Based Probabilistic Load Forecasting in Smart Grids. *IEEE Trans. Ind. Inf.* 16, 4703–4713. doi:10.1109/tii.2019.2942353

Conflict of Interest: The authors declare that the research was conducted in the absence of any commercial or financial relationships that could be construed as a potential conflict of interest.

Publisher's Note: All claims expressed in this article are solely those of the authors and do not necessarily represent those of their affiliated organizations, or those of the publisher, the editors, and the reviewers. Any product that may be evaluated in this article, or claim that may be made by its manufacturer, is not guaranteed or endorsed by the publisher.

frontiers | Frontiers in Energy Research

ORIGINAL RESEARCH
published: 22 June 2022
doi: 10.3389/fenrg.2022.873322

Experimental Validation of a Numerical Model to Predict the Performance of Solar PV Cells

Muhammad Asim[1], *Muhammad Usman*[1], *Jafar Hussain*[1], *Muhammad Farooq*[1], *Muhammad Irfan Naseer*[1], *Yasser Fouad*[2], *M.A. Mujtaba*[1]* *and Fahad Awjah Almehmadi*[2]

[1]*Department of Mechanical Engineering, University of Engineering and Technology, Lahore, Pakistan,* [2]*Department of Applied Mechanical Engineering, College of Applied Engineering, Muzahimiyah Branch, King Saud University, Riyadh, Saudi Arabia*

The models designed to evaluate the performance of photovoltaic (PV) cells depend on classical thermal principles with the use of constant optical coefficients (reflectance, absorbance, and transmittance). However, these optical coefficients depend on incident angle actually and, hence, are a function of the inclination and orientation of the PV panel along with the geographical location and time of the day. In this study, varying coefficients (optical thermal model) and constant coefficient (classical thermal model) with incident angle in the energy balance equations followed by experimental validation were considered. First, the incident angle of direct radiation on the PV panel was determined with the help of astronomic simplified calculations, and second, the optical coefficients were evaluated by using principles of classical electromagnetic theory. Third, the energy balance equations were expressed in the form of differential equations and solved numerically by the Runge–Kutta method to obtain the electrical power as a function of time. Finally, electrical power produced by the optical–thermal model and classical thermal model was validated against experimental data for the solar PV system installed at the Central Station, Punjab Emergency Service. The results show that there is significant agreement between the classical thermal model and experimentally produced electricity throughout the year which validates the modeling.

Keywords: renewable energy, solar radiations, solar panels, photovoltaics, numerical study

OPEN ACCESS

Edited by:
Enio Pedone Bandarra Filho, Federal University of Uberlandia, Brazil

Reviewed by:
Gleyzer Martins, Federal University of Uberlandia, Brazil
Daniel Dall'Onder Dos Santos, Federal University of Uberlandia, Brazil
Luz Elena Chenche, Federal University of Rio de Janeiro, Brazil

***Correspondence:**
M.A. Mujtaba
m.mujtaba@uet.edu.pk

Specialty section:
This article was submitted to Solar Energy, a section of the journal Frontiers in Energy Research

Received: *10 February 2022*
Accepted: *04 May 2022*
Published: *22 June 2022*

Citation:
Asim M, Usman M, Hussain J, Farooq M, Naseer MI, Fouad Y, Mujtaba MA and Almehmadi FA (2022) Experimental Validation of a Numerical Model to Predict the Performance of Solar PV Cells. Front. Energy Res. 10:873322. doi: 10.3389/fenrg.2022.873322

1 INTRODUCTION

The importance of energy in the development of human beings cannot be denied. Even some experts used consumption of energy to assess the economic development (Rafindadi and Ozturk, 2015; Rafindadi and Ozturk, 2016; Rafindadi and Ozturk, 2017; Rafindadi and Mika'Ilu, 2019). The recent developments in all areas and inventions during the last century have caused a substantial increase in the consumption of energy, mainly from sources of fossil fuels. This intensification of fossil fuel consumption is the primary cause of contaminated and greenhouse gaseous emissions, including CO_2 as a major component causing the severe environmental impact (Rafindadi, 2016a; Rafindadi, 2016b; Al-Dhaifallah et al., 2018; Nassef et al., 2018a; Nassef et al., 2019b; Mohamed et al., 2019). The shrinking of fossil fuel reserves and increasing prices have led to the search for non-pollutant, cheap, environment-friendly, and sustainable energy alternatives for replacement (Neves et al., 2018; Rafindadi et al., 2018; Ren et al., 2018; Rezk et al., 2019). Consequently, more attention by experts was paid on renewable energy sources (RESs) because they are cheaper, environment-

friendly, easily accessible, and more importantly sustainable when compared to fossil fuels (Diab et al., 2015; Gomaa et al., 2018; Khan et al., 2018; Tahir et al., 2021). That is why, managements are urged to modify their interests and directions to RESs such as solar energy, wind energy, geothermal heat, hydropower, tidal energy, and biofuels (Ghenai and Janajreh, 2016; Mohamed et al., 2017; Abdelkareem et al., 2018; Abdelkareem et al., 2019; Inayat et al., 2019; Sayed et al., 2019). Simultaneously, a lot of efforts have been put to minimize the energy consumption with optimum usage of the existing resources. Cuce et al. (2019) proved that low/zero energy building may be developed effectively by a biometric strategy which is an operational approach, and a 15.7% reduction in annual energy consumption with the usage of an atrium in a small house was reported by Sher et al. (2019). Furthermore, a rapid growth was seen in the development of fuel-cells and photovoltaic (PV) modules as emergent technologies for collecting energy which then was launched very successfully in the market (Nassef et al., 2019a; Poompavai and Kowsalya, 2019; Ghenai et al., 2020).

Solar energy is available in abundant form and it is a sustainable, clean, and promising energy source for electricity generation. It is believed by many researchers that solar energy will replace fossil fuels in a very short time because of non-polluting and maintenance-free resource that is implementable with ease in numerous applications (Shukla et al., 2016a). The generation of solar photovoltaic (PV) power is one of the major applications. Moreover, the world is showing attention toward hybrid systems of photovoltaic and thermal energy, which is also an advancement toward pollution-free environment. The solar photovoltaic systems being the cheapest ones than other renewable energy resources are widely used as integrated systems with other electricity production systems. Solar energy using PV cells is an extensively used technology for electricity production in numerous countries around the world. Solar energy becomes the ultimate choice, particularly with the persistent variation in supply by grid electricity (Zeyringer et al., 2015). There are numerous arrangements of photovoltaic systems in use: stand-alone photovoltaic systems are also called off-grid PV systems, and grid-connected PV systems are also called on-grid PV systems (Menconi et al., 2016).

The addition of a PV system into a well-designed building can allow self-production of electricity (Shukla et al., 2017), and the system can support the electricity-grid by supplying surplus electricity produced, particularly in the peak demand season of summer because of the usage of air conditioners (Lau et al., 2016). This will also support in the reduction of weather and ecological effects. However, for feasibility of a solar PV system, there must be sufficient solar irradiance during the complete year. The performance of a PV solar system strongly depends on many factors of the environment such as solar irradiance, humidity, wind speed, and temperature (Shukla et al., 2016b). For uninterrupted supply throughout the year, it is very important that a PV system must be properly installed with optimal dimensions. This needs a comprehensive study for the selection of the best choice, the most effective and at very economical cost. In addition, the PV solar system is categorized with different performance constraints such as energy yield, ambient temperature, and performance ratio. There are many studies available in the literature on performance investigation of the PV system. The forecasting of solar data is an important tool for the prediction of output parameters of PV commercial projects (Tahir et al., 2020). Khatib et al. (2013) demonstrated that the highest output of PV solar systems is highly dependent on meteorological parameters such as solar radiation, wind speed, humidity in air, and temperature. So, keeping in view the significance, it is highly recommended to conduct a comprehensive investigation at many sites for suitable selection. The modeling and feasibility of a PV solar system at the selected location are to be evaluated before actual execution. The evaluation can easily be worked on many software available in the market, and the results are very useful for the selection of the best suited model for executing the same in the field.

This study aims to predict the performance of solar PV cells with experimental validation of numerical models for performance evaluation of solar PV cells. Moreover, a comparison of electricity generation is also performed between variable optical coefficients (obtained at different geographical locations, orientation of solar cells, and inclination of variable 1 m^2 of the PV panel) and constant optical coefficients to evaluate the effect of varying optical coefficients on the performance of the PV panel. The novelty of this study lies in the investigation of the impact of climate conditions on Jhang city (31.2781^o N and 72.3317^o E) in Pakistan. There are four seasons in Pakistan throughout the year, and the climate keeps changing due to seasonal behavior. Pakistan has been selected as the location for this research work, and it is divided into different regions according to climatic conditions (Nicol et al., 1999). The methodology adopted and the outcomes of this study can be used by researchers, experts, and policy-makers.

2 DATA COLLECTION

The solar irradiation and weather data were collected from Pakistan Metrological Department, Lahore for a period of 2 years (2016–2018) for Jhang, Pakistan (Sharma and Goel, 2017). In the present analysis, the monthly average data were used to predict the performance of the PV panel in Jhang, Pakistan for a period of 1 year (2016–17) as presented in **Figures 1A,B**.

2.1 Experimental Data

The experimental data were collected from a solar PV system which was installed at the Central Station, Punjab Emergency Service, Rescue 1122, Faisalabad Road, Jhang. The monthly variations in energy production by the installed solar PV system are shown in **Figure 2**. It is observed that a solar PV system generates a maximum and minimum amount of energy in May (16.63 kWh) and December (7.80 kWh), respectively, because of the amount of solar irradiance falling on the surface of the cell.

3 MATERIALS AND METHODS

3.1 Numerical Modeling

In the present study, a numerical model was developed on MATLAB using differential equations and the Runge-Kutta

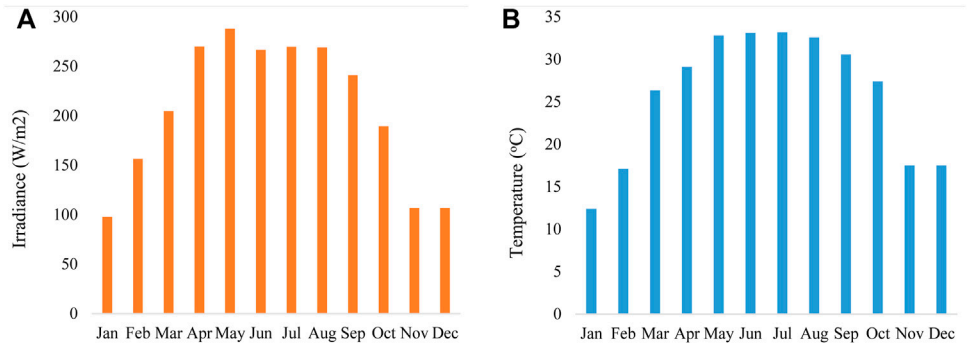

FIGURE 1 | One-year (2016–17) solar and weather data for Jhang, Pakistan. **(A)** Monthly average global horizontal irradiance. **(B)** Monthly average dry bulb temperature.

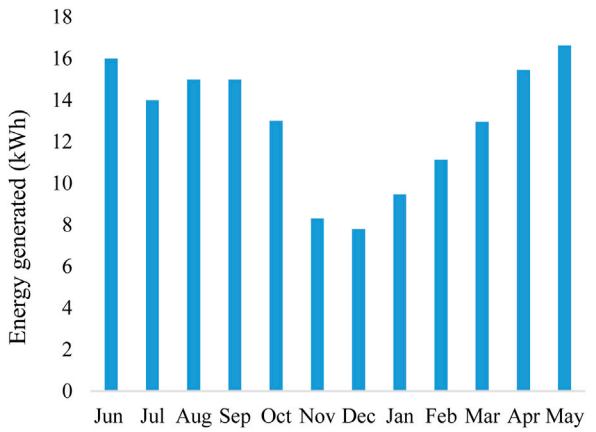

FIGURE 2 | Actual PV energy production from June 2016 to May 2017.

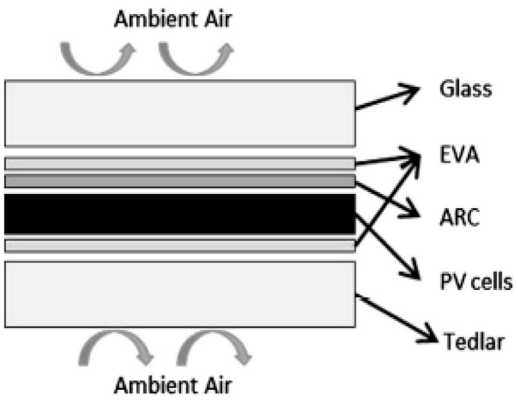

FIGURE 3 | Six layers of a modeled PV cell.

method to describe the energy production by a standard configured PV cell.

To make the analysis simpler and easier, the following assumptions were taken into account.

- Unpolarized incident and diffused solar radiations
- Uniform temperature inside each layer of the PV cell
- Zero heat capacity for ARC (antireflection coating) and silicon layer
- Negligible side thermal exchanges of the PV cell
- Natural convection heat transfer

Since the solar PV panel consists of five different layers (exterior glass, ethylene vinyl acetate, antireflexive coating, PV cells, and Tedlar) as presented in **Figure 3**, the energy balance equations were developed considering the conduction and convection heat transfer between layers and with the surrounding. As the facet effects of rims of PV cells were not considered; therefore, it is most effective to consider the unit surface area of the cell. The differential equations were explicated in the form of temperature change of the layers beyond regular time assuming the isothermal conditions in each layer.

The energy balance equation for each layer can be represented as **Eq. 1**.

$$\rho_i e_i C_i \frac{dT_i}{dt} = \sum energy\ exchange. \tag{1}$$

In **Eq. 1**, i represents the number of that layer for which the energy exchange is being analyzed, and it varies between 1 and 6. The energy exchange is the heat transfer between different layers of PV cells and with the surrounding air.

3.1.1 Energy Balance for the Exterior Glass

The energy balance for the exterior glass of a solar PV cell can be represented by **Eq. 2**.

$$\rho_{glass} e_{glass} C_{glass} \frac{dT_{glass}}{dt} = Absorbtion_{glass} - Conduction_{glass-EVA1} - Convection_{glass} - Radiation_{glass}, \tag{2}$$

where $Absorbtion_{glass}$ represents the sun rays absorbed by the glass and can be calculated by **Eq. 3**.

$$Absorption_{glass} = \alpha_{glass} * I_{incident}, \tag{3}$$

$K_{glass\_EVA1}/e_{glass\_EVA1}$:

$$Conduction_{glass\_EVA1} = \frac{K_{glass-EVA1}}{e_{glass-EVA1}}\left(T_{glass} - T_{EVA1}\right). \quad (4)$$

In **Eq. 4**, the term $K_{glass-EVA1}$ and $e_{glass-EVA1}$ epitomize the thermal conductivity of the medium across the layers and traveled distance by flux, respectively. As represented, each layer *via* a factor placed within the layer's center and each layer temperature is supposed to be unvarying, the resistance of conduction is given as **Eq. 5**.

$$\frac{e_{glass-EVA1}}{K_{glass-EVA1}} = \frac{e_{glass}}{2K_{glass}} + \frac{e_{EVA}}{2K_{EVA}}. \quad (5)$$

It is assumed here that the temperature gradient between the two faces of the interface is zero.

In this research, we consider the natural convection between the layer of glass and surrounding air only, written as **Eq. 6**.

$$Convection_{glass} = h_{glass,free}*\left(T_{glass} - T_{amb}\right). \quad (6)$$

For the sake of simplicity of the calculations, the minor temperature difference between the surface externally and the middle of the glass was ignored in comparison to the temperature difference $T_{glass} - T_{amb}$.

The free convective coefficient of exchange is expressed by Holman (Edalati et al., 2015).

$$h_{glass,free} = 1.31*\left(T_{glass} - T_{amb}\right)^{1/3}. \quad (7)$$

Radiation heat transfer through a long route is given by Stefan–Boltzmann regulation [46].

$$Radiation_{glass} = \varepsilon_{glass} * F_{glass,sky} * \sigma * \left(T^4_{glass} - T^4_{sky}\right) + \varepsilon_{glass}* F_{glass,ground}* \sigma* \left(T^4_{glass} - T^4_{ground}\right), \quad (8)$$

It is assumed here that both the sky and ground react as blackbodies in **Eq. 8**. It needs to be well-known that for middle IR (λ= 7–14 μm), ε_{glass} is nearly 1.

As it is evident that the PV panel is not completely open to the ground and the sky, for this reason, the radiation contacts between the sky and the panel and between the ground and the solar panel need to be in agreement with the use of the sky view factors F_{sky} and the ground view factor F_{ground}. F_{sky} is described as the hemispherical portion of the unhindered sky, and the same is considered with the use of the analogical method of Nusselt (Rakovec et al., 2011).

$$F_{glass,sky} = \frac{1}{2}\left(1 + \cos(s)\right). \quad (9)$$

In **Eq. 9**, s is the panel inclination. Ground-view factor is calculated from **Eq. 10**.

$$F_{glass,ground} = \frac{1}{2}\left(1 + \cos(s)\right), \quad (10)$$

$$Convection_{glass} = \varepsilon_{glass}* \sigma* T^4_{glass} - \varepsilon_{glass}* \frac{1}{2}\left(1 + \cos(s)\right)* \sigma* T^4_{sky} - \varepsilon_{glass}* \frac{1}{2}\left(1 + \cos(s)\right)*\sigma* T^4_{ground}. \quad (11)$$

For the temperature of the sky T_{sky}, in the available works, there are many terms that were deduced for approximating it (Notton, Cristofari et al., 2005). In this research study, the formulation was developed by Schott (1985).

$$T_{sky} = T_{amb} - 20K. \quad (12)$$

The temperature of the ground is assumed to be equal to ambient temperature (Schott, 1985).

3.1.2 Energy Balance for Upper EVA (EVA 1)

The energy balance for the ethylene vinyl acetate (EVA) first layer of the PV panel can be represented by **Eq. 13**.

$$\rho_{EVA}e_{EVA}C_{EVA}\frac{dT_{EVA1}}{dt} = Absorbtion_{EVA1} + Conduction_{glass-EVA1} - Conduction_{EVA1-ARC}. \quad (13)$$

The term related to absorption expresses that the EVA layer has absorbed the energy as the radiation has been absorbed through the surface of the glass and can be calculated by **Eq. 14**.

$$Absorption_{EVA1} = \alpha_{EVA} * \tau_{glass}* I_{incident}. \quad (14)$$

The conduction between the ARC and EVA is expressed as given in **Eq. 15** and **Eq. (16)**.

$$Conduction_{EVA1-ARC} = \frac{K_{EVA1-ARC}}{e_{EVA1-ARC}}\left(T_{EVA1} - T_{ARC}\right), \quad (15)$$

$$\frac{e_{EVA1-ARC}}{K_{EVA1-ARC}} = \frac{e_{EVA1}}{2K_{EVA1}} + \frac{e_{ARC}}{2K_{ARC}}. \quad (16)$$

3.1.3 Energy Balance for the ARC Layer

The anti–reflection coating layer is used to avoid the reflection process of solar rays in solar cells to increase their output and can be represented by **Eq. 17**.

$$\rho_{ARC}e_{ARC}C_{ARC}\frac{dT_{ARC}}{dt} = Absorbtion_{ARC} + Conduction_{EVA1-ARC} - Conduction_{ARC-Si}. \quad (17)$$

The rays absorbed and conducted by the ARC layer can be calculated by **Eq. 18** and **Eq. (19)**, respectively.

$$Absorption_{ARC} = \alpha_{ARC} * \tau_{glass}* \tau_{EVA}* I_{incident}, \quad (18)$$

$$Conduction_{ARC-Si} = \frac{K_{ARC-Si}}{e_{ARC-Si}}\left(T_{ARC} - T_{Si}\right), \quad (19)$$

$$\frac{e_{ARC-Si}}{K_{ARC-Si}} = \frac{e_{ARC}}{2K_{ARC}} + \frac{e_{Si}}{2K_{Si}}. \quad (20)$$

3.1.4 Energy Balance for the Semiconductor Layer

The energy balance for the semiconductor layer of the PV panel can be represented by **Eq. 21**

$$\rho_{Si}e_{Si}C_{Si}\frac{dT_{Si}}{dt} = Absorbtion_{Si} + Conduction_{ARC-Si} - Conduction_{Si-EVA2} - P_{elec}, \quad (21)$$

$$Absorption_{Si} = \alpha_{Si} * \tau_{ARC} * \tau_{glass} * \tau_{EVA} * I_{incident}, \quad (22)$$

$$Conduction_{ARC-Si} = \frac{K_{Si-EVA2}}{e_{Si-EVA2}} (T_{Si} - T_{EVA2})$$

$$\frac{e_{Si-EVA2}}{K_{Si-EVA2}} = \frac{e_{Si}}{2K_{Si}} + \frac{e_{EVA2}}{2K_{EVA2}}. \quad (23)$$

The electricity is defined as the efficiency function of the panel and irradiance striking on the silicon layer, **Eq. 24**.

$$P_{elec} = \tau_{glass} * \tau_{EVA} * \tau_{ARC} * I_{incident} * \eta. \quad (24)$$

The efficiency of the panel varies with the changes in the temperature and with the incident radiations and may be described by the subsequent expression (Evans, 1981), **Eq. 25**.

$$\eta = \eta_{STC} * \left(1 + \beta_0 * (T_{Si} - 298) + \gamma_o * \mathrm{Log}\left(\tau_{glass} * \tau_{EVA} * \tau_{ARC} \text{-} I_{incident}\right)\right). \quad (25)$$

In **Eq. 25**, β_0 is the coefficient of temperature, γ_0 is the coefficient of solar radiation, and η_{STC} is the efficiency of the panel at standard conditions. The PV panel characteristics used in this research work are standard efficiency (0.125), temperature coefficient (0.004 K^{-1}), and coefficient of solar radiation ($W^{-1}m^2$); these characteristic values are available in Ref. (Schott, 1985).

3.1.5 Energy Balance for the Back-EVA Layer (EVA 2)

The silicon layer absorbs most irradiance, so solar irradiance absorption in the Tedlar layer and EVA-2 is neglected. The energy balance for the back-EVA layer can be represented by **Eq. 26**, and conduction through this layer can be calculated using **Eq. 27**.

$$\rho_{EVA2} e_{EVA2} C_{EVA2} \frac{dT_{EVA2}}{dt} = Conduction_{Si-EVA2} - Conduction_{EVA2-Tedlar}, \quad (26)$$

$$Conduction_{EVA2-Tedlar} = \frac{K_{EVA2-Tedlar}}{e_{EVA2-Tedlar}} (T_{EVA2} - T_{Tedlar}), \quad (27)$$

$$\frac{e_{EVA2-Tedlar}}{K_{EVA2-Tedlar}} = \frac{e_{EVA2}}{2K_{EVA2}} + \frac{e_{Tedlar}}{2K_{Tedlar}}. \quad (28)$$

3.1.6 Equation for Tedlar-Based Back Sheet

$$\rho_{Tedlar} e_{Tedlar} C_{Tedlar} \frac{dT_{Tedlar}}{dt} = Conduction_{EVA2-Tedlar} - Convection_{Tedlar} - Radiation_{Tedlar}. \quad (29)$$

Only natural convection by temperature difference is considered for the Tedlar layer and environment on the same pattern of the front glass layer.

$$Convection_{Tedlar} = h_{Tedlar,free} * (T_{Tedlar} - T_{amb}), \quad (30)$$

$$h_{Tedlar,free} = 1.31 * (T_{Tedlar} - T_{amb})^{1/3}. \quad (31)$$

Exchange of the irradiance for the Tedlar layer and view factors are expressed by using the previous approach as **Eq. 32**.

$$Radiation_{Tedlar} = \varepsilon_{Tedlar} * F_{Tedlar,sky} * \sigma * \left(T_{Tedlar}^4 - T_{sky}^4\right) + \varepsilon_{Tedlar} * F_{Tedlar,ground} * \sigma * \left(T_{Tedlar}^4 - T_{ground}^4\right), \quad (32)$$

$$F_{Tedlar,sky} = \frac{1}{2} (1 + \cos(\pi - s)) \text{ and}$$

$$F_{Tedlar,ground} = \frac{1}{2} (1 + \cos(\pi - s)). \quad (33)$$

The properties of the material constituting the layers are mentioned in **Table 1**, taken From Refs. (Armstrong and Hurley, 2010; Sharma and Goel, 2017).

3.2 Optical Phenomena and Optical Coefficients

Solar flux propagation through the solar panel is analyzed by calculating the reflection, absorption, and transmission in every layer of the panel as shown in **Figure 4**. As the solar radiation moves through the front surface of the glass, a portion of the radiation is reflected, and the other portion infiltrates and passes through the glass. As the irradiance passes through the glass, some of the irradiances are passed through the glass, whereas some are captured by it. The irradiance which has the capability to pass through the boundary of glass reaches to the lower boundary of the glass, and from there it is transferred to the next medium. In general, constant values of optical coefficients are used for evaluating the PV models. However, these coefficients are not constant and depend upon a number of parameters including the incident angle. The constant optical coefficients for different materials used in this study are presented in **Table 1**. The optical constant coefficients correspond to conditions in which the angle of incidence of irradiance is zero ($\theta = 0$).

3.2.1 Incident Angle Calculations

Solar radiation's incident angle is defined as the angle of incident irradiance which it makes perpendicular to the surface of the panel at the point where radiation strikes.

The following astronomic formula is used for estimating the cosine of the incident angle (θ) at every fraction of the time in the entire day (Beckman and Duffie, 1974), **Eq. 34**.

$$\cos\theta = \sin\delta * \sin l * \cos S + \cos\delta * \sin l * \sin S * \cos\varphi * \cos\omega - \sin\delta * \cos l * \sin S * \cos\varphi \quad \cos\delta * \cos l * \cos S * \cos\omega + \cos\delta * \sin S * \sin\varphi * \sin\omega, \quad (34)$$

The δ is the declination of the sun, l represents the latitude, ω is used for the hour angle, s shows the inclination angle, and φ is here for the PV panel azimuthal angle.

The declination of the sun (δ) fluctuates every day of the whole year (J), and in spring it is zero. In the literature, there are many

TABLE 1 | Material properties, optical properties, and constant optical coefficients for different materials of PV panels.

Material of the panel	Material properties			Optical properties [61]			Constant optical coefficients		
	Thermal conductivity ($Wm^{-1}K^{-1}$)	Density (Kgm^{-3})	Specific heat capacity ($JKg^{-1}K^{-1}$)	Emissivity	Absorption coefficient (m^{-1})	Refractive index	Material reflectance	Material transmittance	Material absorbance
Glass	1.8	2700	750	0.9	4.41	1.52	0.040	0.950	0.010
EVA	0.35	960	2090	-	54.9	1.45	0.000	0.970	0.030
ARC	32	2400	691	-	120	2.30	0.030	0.970	0.000
Silicon	49	2300	836	-	$1.10*10^6$	3.69	0.070	0.000	0.930
Tedlar	0.35	1370	1760	0.9	-	-	-	-	-

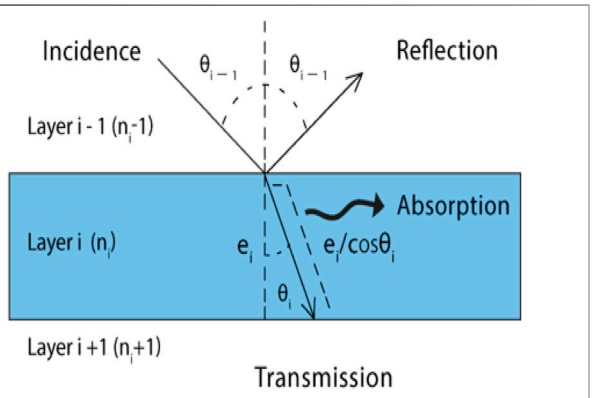

FIGURE 4 | Optical phenomenon of irradiance.

formulae deduced for this cause, but in this research study, **Eq. 35** was used.

$$\delta = 0.38 + \sin\left(\frac{2\pi J'}{365.24} - 1.395\right) + 0.37\sin\left(\frac{4\pi J'}{365.24} - 1.457\right). \tag{35}$$

The time equation E is the development of the meantime as compared to the sun time. The "Institut de mécanique celeste et de calcul des ephemerides" (IMCCE) prints every 12 months the "Guide des données astronomiques" (Le Lay, 2021), which may be used to give the maximum accurate formulation for the equation of time for the period 1900–2100 with minimal error. This complicated formula simplified for length 2013–2023 is deduced to **Eq. 36**. The equation of time is widely used in different applications regarding solar energy (sundials and similar devices). Different machines such as solar trackers and heliostats move in a pattern that is influenced by the time equation to obtain maximum output.

$$E = 7.5*\sin\left(\frac{2\pi J'}{365.24} - 0.03\right) + 9.9*\sin\left(\frac{4\pi J'}{365.24} + 0.35\right). \tag{36}$$

3.2.2 Transmittance, Reflectance, and Absorbance Calculation

The angle of refraction is derived by the Snell–Descartes regulation as **Eq. 37**.

$$\theta_i = \arcsin\left(\frac{n_{i-1}}{n_i} \times \sin\theta_{i-1}\right). \tag{37}$$

After calculating these angles, the fraction of reflectance on the layer may be evaluated by Fresnel's formula. The reflectance corresponding to perpendicular and parallel separation is assumed by the following equations (Lu and Yao 2007).

$$r_i^{-} = \frac{sin^2(\theta_{i-1} - \theta_i)}{sin^2(\theta_{i-1} - \theta_i)}, \tag{38}$$

$$r_i^{''} = \frac{tan^2(\theta_{i-1} - \theta_i)}{tan^2(\theta_{i-1} - \theta_i)}, \tag{39}$$

$$r_i = \frac{r_i^{''} - r_i^{-}}{2}. \tag{40}$$

Thus, the fraction of irradiance propagating over the layer i is given by **Eq. 41**.

$$t_i = 1 - r_i. \tag{41}$$

The transmitted portion keeps moving through the medium and is continuously absorbed. The Beer–Lambert law is used to express this attenuation:

$$\varnothing = \varnothing_0 \times e^{-a \times l}, \tag{42}$$

In **Eq. 42**, a is the absorption coefficient, which is also called as linear attenuation coefficient and is restrained in m^{-1}. This coefficient is material type–dependent and changes with the change in wavelength. L is the measurement of traveled distance that the solar radiation covers as it passes over the material and is expressed as

$$L = e_i/\cos\theta_i. \tag{43}$$

The transmittance of solar irradiation in the layer i is given as **Eq. 44**.

$$\tau_i = (1 - r_i) \times \exp\left(-\alpha_i \times \frac{e_i}{cos\theta_i}\right). \tag{44}$$

The absorbed irradiance fraction in the ith layer is derived by the conservation of energy.

$$r_i + \tau_i + \alpha_i = 1$$
$$\alpha_i = (1 - r_i) \times \left(1 - \exp - \alpha_i \times \frac{e_i}{cos\theta_i}\right). \tag{45}$$

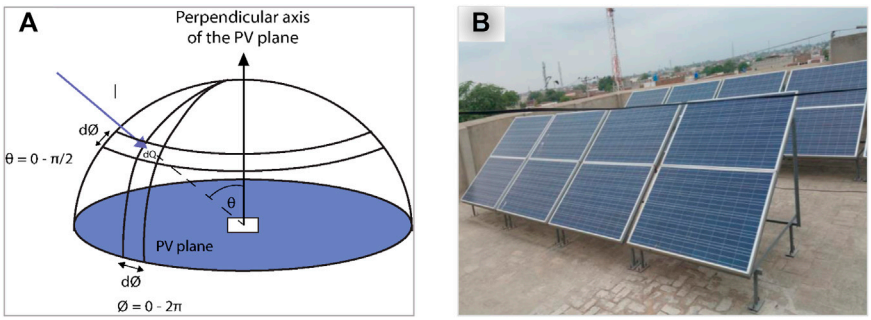

FIGURE 5 | (A) Representation of isotropic diffuse irradiance. **(B)** Site panel location.

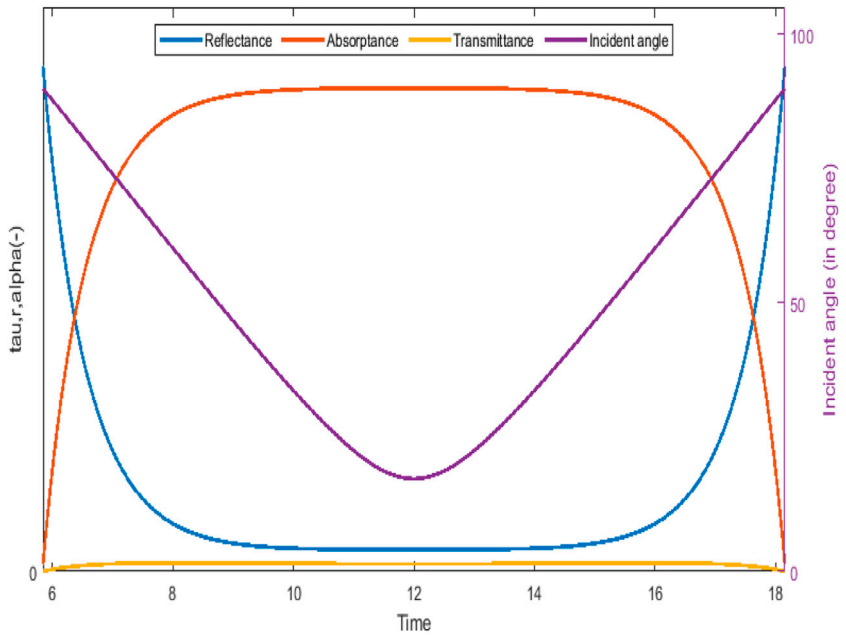

FIGURE 6 | Incident angle variation resulting in change in optical coefficients of a glass PV panel (July).

Numerous models are available in the literature regarding several reflections (Lu and Yao 2007). The ending result for the evaluation of reflectance was obtained by the addition of countless series. Only the first term was considered for the sake of simplicity. A lower value of the absorption in comparison to the actual, in the occasion of numerous reflections, was calculated, though this additional absorbed energy is very less (less than 0.2% of the total energy which also reflects).

For the intention of optical coefficients, information on panel material properties including the absorption coefficient 1) and the refractive index (n) is also required along with the incident and refractive angles. The value of the refractive indexes was taken as a constant in many studies (Lu and Yao, 2007). In this research study, the constant values from the research of Krauter and Hanitsch were used. However, the refractive indexes of the material change along with the wavelength of radiation (Mertin, Hody-Le Caer et al., 2014).

The coefficient of absorption was calculated by averaging the absorption spectrum A(λ) over the solar spectrum S(λ) (Santbergen and van Zolingen, 2008), **Eq. 46**.

$$\alpha = \frac{\int A(\lambda) \times S(\lambda) \times d\lambda}{\int S(\lambda) \times d\lambda}. \tag{46}$$

The averaged coefficients of absorption obtained and values of refractive indexes from the literature of the selected materials are given in **Table 1**.

3.2.3 Diffuse and Direct Irradiance

Until this part of the research, the incident irradiance arriving at an angle θ is used for the development of all formulas, but in

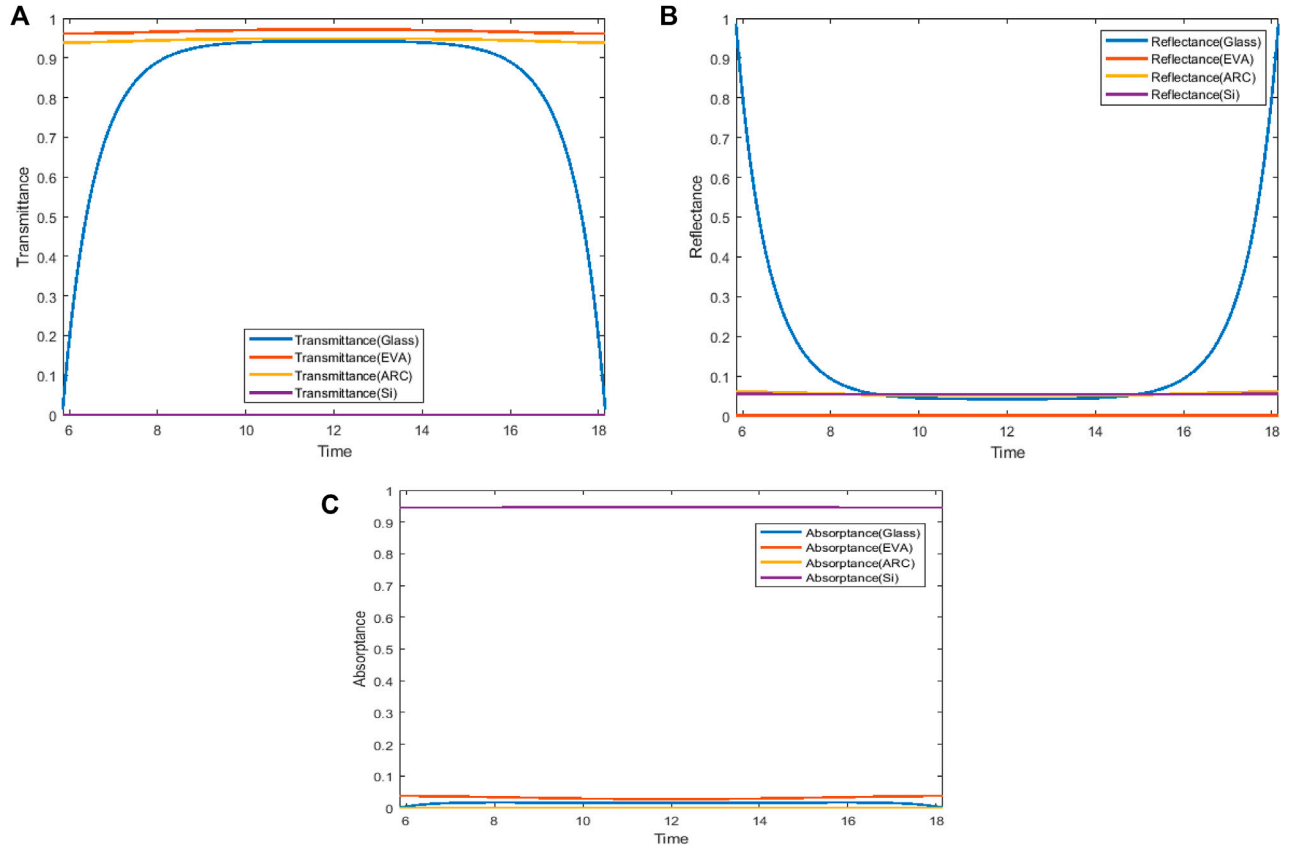

FIGURE 7 | Optical coefficient (transmittance) variation of different layers: ARC, glass, EVA, and silicon (July). **(A)** Transmittance, **(B)** reflectance, and **(C)** absorbance.

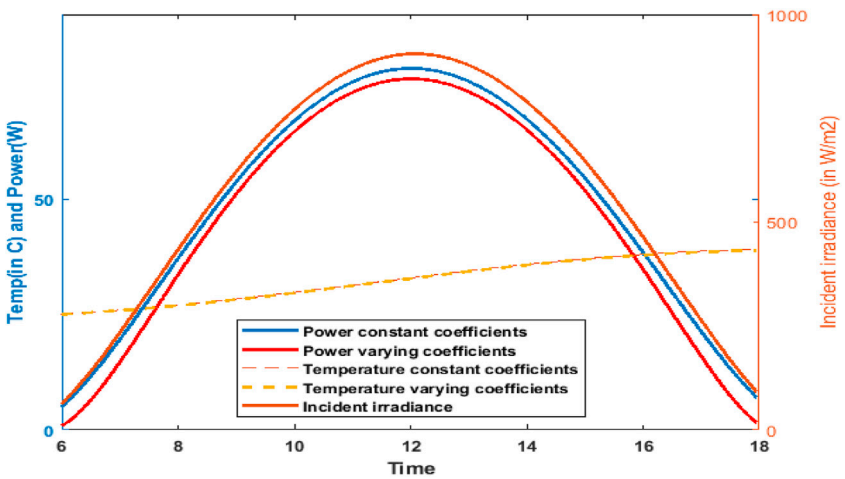

FIGURE 8 | Calculated the electrical power with constant and varying optical coefficients (July).

actuality, the latter consists of a direct and a diffuse component, **Eq. 47**.

$$I_{globalincident} = I_{directincident} + I_{diffuseincident}. \quad (47)$$

The optical coefficients for direct irradiance reaching an angle of incidence θ for different layers can easily be considered with all formulations, which were established

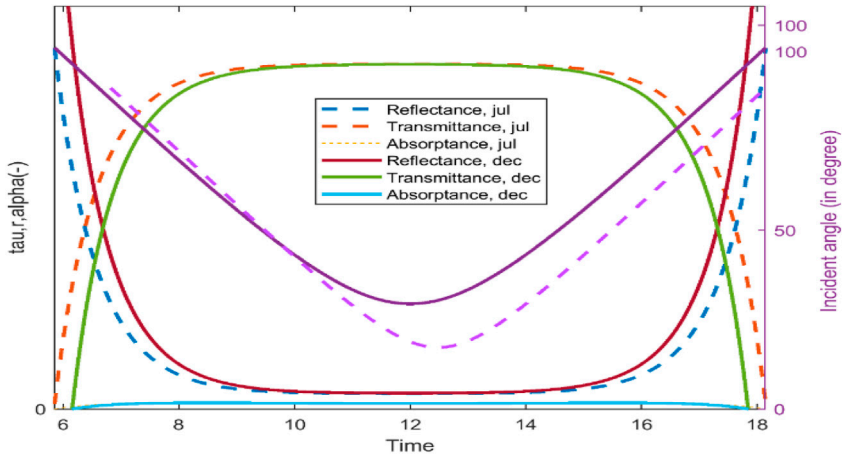

FIGURE 9 | Incident angle variation and of the optical coefficients of glass (July and December).

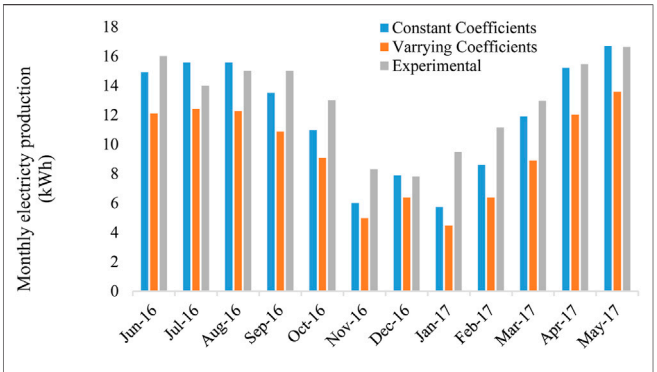

FIGURE 10 | Month-wise production of electricity of two models of constant and varying optical coefficients in comparison with experimental production.

in prior sections. It is pertinent to mention here that incident angles of diffuse irradiance range from 0° to 90°. For evaluation of coefficients, the values matching to the differential solid angle dΩ were analyzed after which integration to get the values over the whole hemisphere was carried out, as shown in **Figure 5A**. The PV solar system installed at the Central Station, Punjab Emergency Service, Rescue 1122, Faisalabad Road, Jhang (31.2781° N and 72.3317° E) is shown in **Figure 5B**.

4 RESULTS AND DISCUSSION

To validate the effects of optical phenomena in the prediction of electricity production by the PV panel, numerous cases with a range of changes were considered for many geographical locations, orientation, and inclination of 1 m^2 of the PV panel. Optical coefficient variation was evaluated in every case. The generation of electricity was calculated and compared to the results of constant optical coefficients.

4.1 Optimum Configuration (Inclination 38°; Orientation 0°) of the PV Panel

The variation in angle of incidence of direction radiations and its effect for three optical coefficients of the glass material for a particular day in July in Jhang, Pakistan is shown in **Figure 6**. The PV panel slopes at an angle of 38° and is positioned to the south properly in the current case. The incident angle of the radiation varies significantly at some points of the day, resulting in the variation of the three optical coefficients properly. This variation in optical coefficients is further prominent at the time of daylight and at the end of the day in the evening, while these optical coefficients are very much regular between 10:00 AM and 2:00 PM. Furthermore, the reflectance trend with the variation in the incident angle is matching, while the absorbance and transmittance angle have the opposite tendency in comparison to incident angle.

The optical phenomena of the glass layer are of most relevance than other layers for different layers of the PV cell, and the variations of three optical coefficients are so small that it can be neglected, as shown in **Figures 7A–C**. The temperature variation of the silicon layer and energy generated was calculated by varying and constant coefficients and irradiance which are incident of the silicon layer, as shown by **Figure 8**. The power produced which was calculated using a constant coefficient is more than that when using varying coefficients, and both curves are asymmetric with a variation on the left of the curve. It is clear that the power produced by the PV panel is less at noon when the temperature is maximum than morning for the same solar flux. The reason for this is that the panels are exposed to the sun throughout the day and absorb heat which raises the temperature of the panels and lowers the efficiency of the conversion of solar energy to electricity. It can also be seen by the comparison of two models that the difference in morning and evening is more considerable due to the large difference between the coefficients of models in these periods of the day. The same tendency has been observed when the same calculations were carried out for all months of a year. The incident angle of

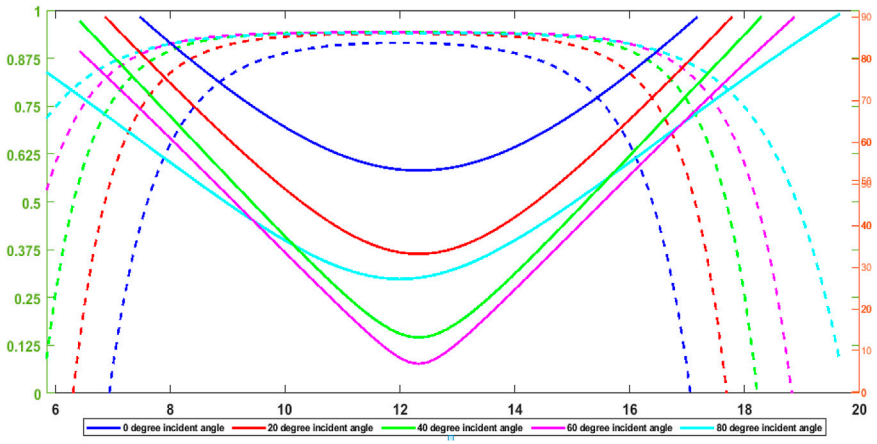

FIGURE 11 | Incident angle variation and the glass transmittance because of a range of angle of inclination (°) (December).

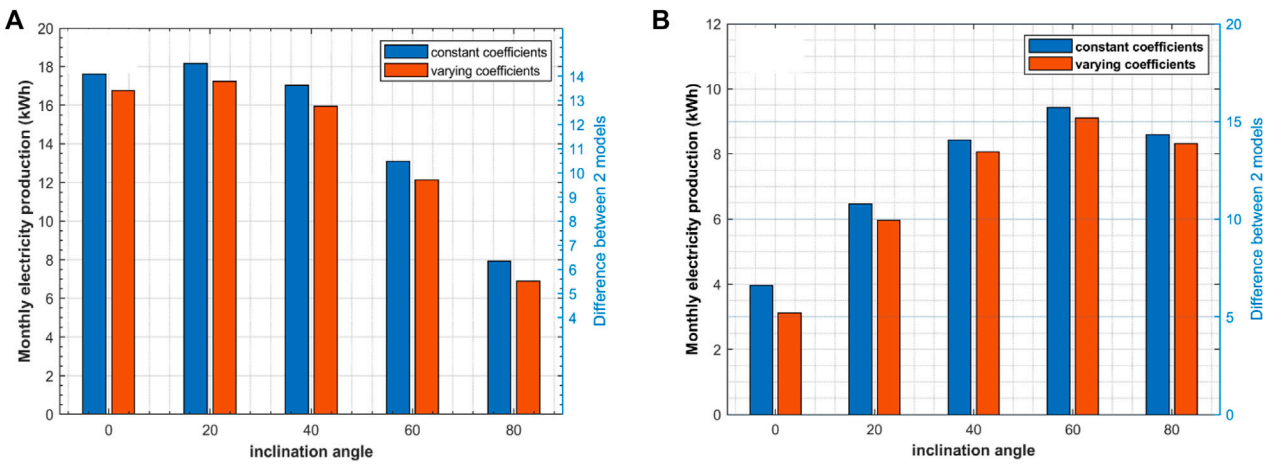

FIGURE 12 | Month-wise production of electricity with two models (classical and optical) and with an angle of inclination changing from 0° to 80° for **(A)** June and **(B)** December.

radiation changes more in the month July than the month of December as shown in **Figure 9**. Furthermore, the minimum angle in the month of July is less than that in the month of December. Hence, the transmittance and absorbance are higher in the month of July when compared to December, and the reflectance is higher in December, but this difference is minimal around noon.

Figure 10 depicts that there is significant agreement between the classical thermal model and experimentally produced electricity throughout the year which validates the modeling. The difference between electricity generation between the optical thermal model and the experimental model is higher than the difference between the classical and experimental models. The values of deviations are lower between the classical model's results and experimental data when compared to the optical model's results and experimental data. The mean percentage difference of monthly electricity production between the classical model and experimental data is noted as 12.4%, whereas for the optical model, it is observed as 28.2%. The highest error in monthly electricity production for both the models against experimental data occurred in the month of January-2017, whereas the lowest occurred in the month of May-2017 (July-2016) for the classical model (optical model) against experimental data. So, it can be inferred that the classic thermal model shows better performance as it more closely exhibits the results compared with experimental results. The classical thermal model may be used for estimating the power production at a typical geographical location and hence may facilitate the engineers for solar power projects. A uniform gap in electricity production between the classical thermal model and optical thermal model was observed throughout the year, which substantiates that a relationship exists between these two models. The classical thermal model presents better results than the optical model because the classical thermal model consists of constant

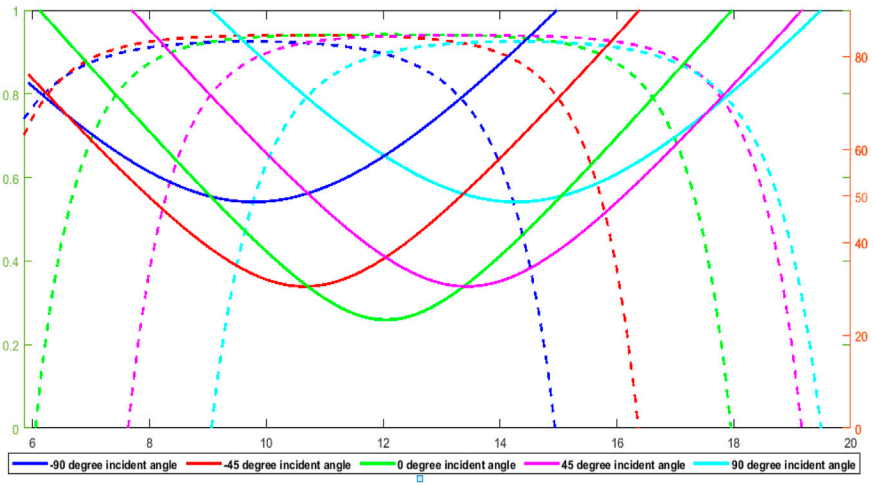

FIGURE 13 | Incident angle variation and the transmittance in the result of different azimuth angles (°) (December).

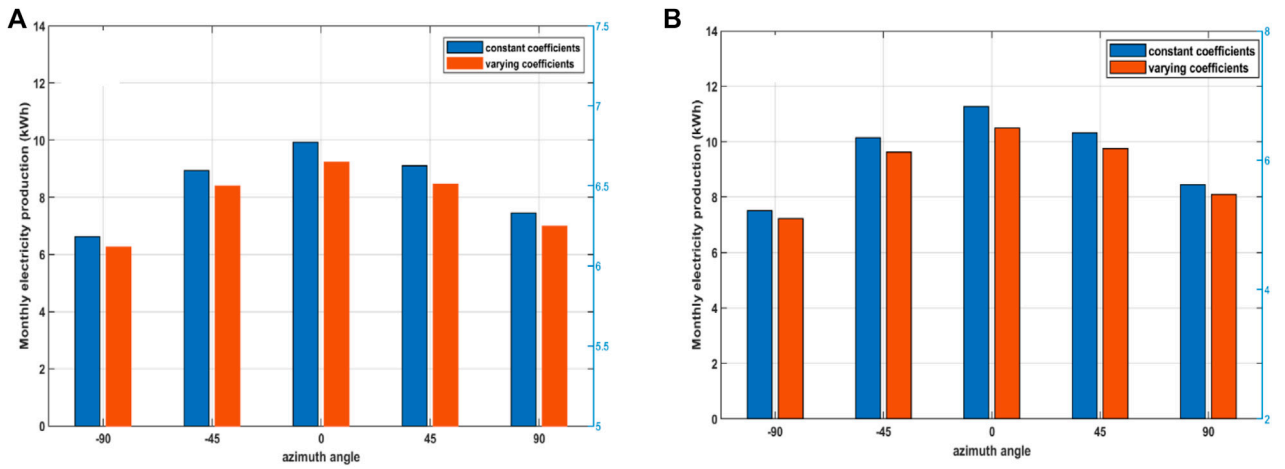

FIGURE 14 | Month-wise production of electricity corresponding to varying and constant optical coefficients models and with changing azimuth angle (- 90° to 90°) for **(A)** March and **(B)** September.

coefficients, whereas the optical model has variable coefficients. The variation in coefficient brings inaccuracy in the model, and it becomes difficult for the model to predict accurate behavior of the output parameter.

4.2 Incidence Angle Variation With Numerous Inclinations and Optimum Orientation (0°) of the PV Panel

The variation in incidence angle and in optical coefficients and the power generated with several angles of inclinations changing from 0° to 80° were studied in this study. The incidence angle normally reduces by increasing the inclination angle as shown in **Figure 11**. However, the distinction is only sizeable for lower angles (between 0° and 20°).

The electricity production for numerous month simulations in the year has been carried out. **Figures 12A,B** show the production of electricity at some time of June and December consistent with the exclusive angle of inclination, respectively. The changes in electricity production for the months of December and March are identical to those for the months of June and September. The difference among the models is considerable for smaller angles of inclination for the month of December, whereas the difference is accountable for larger inclination angles for the month of June. The angle of incidence has been valued a long way from 0° in those instances as shown in **Figure 11**, and the coefficients for the classical thermal model were evaluated with a 0° value of the incident angle. As a result, a considerable difference has been observed between the two models.

4.3 Different Orientations of the PV Panel with an Inclination of 38°

The configuration of the panel at different angles of azimuth was checked; south-west (−45° and 45°) and west (−90° and 90°), east (−90° and 90°), south-east (−45° and 45°), and south (0°); the results are shown in **Figure 13**. In addition, greater value is obtained if the PV panel is orientated toward the south, and the bigger the angle of inclination and curves of transmittance, the smaller the angle of inclination within the noon is (while their radiance is at very best level). Hence, the orientation of the south is best to collect maximum solar flux at some stage in the year. **Figures 14A,B** show month-wise production of electricity corresponding to varying and constant optical coefficients models and with changing azimuth angle (−90° to 90°) in March and September, respectively. It can be observed that the difference in electricity production by the two models normally increases as the panel moves away from the south.

5 CONCLUSION

This research work aims to develop theoretical models for performance evaluation of the photovoltaic (PV) system on the basis of classical thermal principles which uses constant values of optical coefficients (reflectance, transmittance, and absorbance). However, these coefficients, in fact, depend on the incident angle of the radiations approaching the PV panel and, therefore, are a function of the inclination and orientation along with the geographical position and time. The constant coefficient (classical thermal model) and the varying coefficient (optical thermal model) with an incident angle in the energy balance equations followed by experimental validation were considered in this study.

The comparison of electricity produced by both the optical–thermal and classical thermal models and experimentally assessed by the PV system installed in Jhang, Pakistan allows concluding that.

- There is significant agreement between the classical thermal model and experimentally produced electricity throughout the year which validates the modeling.
- The difference in electricity production between the optical–thermal model and experimental model is more as compared to the classical thermal model and experimental model, so it is inferred that the classic thermal model more closely shows a practical system. The reason for the accuracy of the classical model lies in constant coefficients as with constant or average coefficients, the errors become lower than varying coefficients.
- Comparison of variable and constant optical coefficients shows that the PV panel performs better with constant optical coefficients, and the difference of electricity production by the two models normally increases as the panel moves away from the south.
- The classical thermal model may be used for estimating the power production at a typical geographical location and hence may facilitate the engineers for solar power projects.
- A uniform gap in electricity production between the classical thermal model and optical thermal model was observed throughout the year, which clearly indicates that there exists a relationship between these two models.

The performance of the PV panel is evaluated by two models, that is, classical thermal model and optical thermal model and then validated experimentally, concluding that the classical thermal model is more accurate in evaluating the power output for the district Jhang in Pakistan, but there may be variations in other parts of the world due to different input parameters. For additional examination, these models should be pragmatic to other environmental concerns. Furthermore, the panel performance must be evaluated now with appreciative conditions to evaluate energy efficiency. The methodology adopted in this study can be used to evaluate the performance of PV panels according to solar conditions of other regions in the world.

DATA AVAILABILITY STATEMENT

The raw data supporting the conclusion of this article will be made available by the authors, without undue reservation.

AUTHOR CONTRIBUTIONS

MA (writing, experimentation, and conceptualization), MU (methodology and formal analysis), JH (writing—review and editing), MF (writing—review and editing), MN (data curation), MM (formal analysis, writing—review, and editing), FA (writing—review and editing, funding acquisition), and YF (writing—review and editing).

FUNDING

The authors extend their appreciation to the Researchers Supporting Project number (RSP2022R515), King Saud University, Riyadh, Saudi Arabia for funding this research work.

REFERENCES

Abdelkareem, M. A., El Haj Assad, M., Sayed, E. T., and Soudan, B. (2018). Recent Progress in the Use of Renewable Energy Sources to Power Water Desalination Plants. *Desalination* 435, 97–113. doi:10.1016/j.desal.2017.11.018

Abdelkareem, M. A., Tanveer, W. H., Sayed, E. T., Assad, M. E. H., Allagui, A., and Cha, S. W. (2019). On the Technical Challenges Affecting the Performance of Direct Internal Reforming Biogas Solid Oxide Fuel Cells. *Renew. Sustain. Energy Rev.* 101, 361–375. doi:10.1016/j.rser.2018.10.025

Al-Dhaifallah, M., Nassef, A. M., Rezk, H., and Nisar, K. S. (2018). Optimal Parameter Design of Fractional Order Control Based INC-MPPT for PV System. *Sol. Energy* 159, 650–664. doi:10.1016/j.solener.2017.11.040

Armstrong, S., and Hurley, W. (2010). A Thermal Model for Photovoltaic Panels under Varying Atmospheric Conditions. *Appl. Energy Eng.* 30 (11-12), 1488–1495. doi:10.1016/j.applthermaleng.2010.03.012

Beckman, W. A., and Duffie, J. A. (1974). *Solar Energy Thermal Processes*. Creset.

Cuce, E., Nachan, Z., Cuce, P. M., Sher, F., and Neighbour, G. B. (2019). Strategies for Ideal Indoor Environments towards Low/zero Carbon Buildings through a Biomimetic Approach. *Int. J. Ambient Energy* 40 (1), 86–95. doi:10.1080/01430750.2017.1372807

Diab, F., Lan, H., Zhang, L., and Ali, S. (2015). An Environmentally-Friendly Tourist Village in Egypt Based on a Hybrid Renewable Energy System--Part One: What Is the Optimum City? *Energies* 8 (7), 6926–6944. doi:10.3390/en8076926

Edalati, S., Ameri, M., and Iranmanesh, M. (2015). Comparative Performance Investigation of Mono- and Poly-Crystalline Silicon Photovoltaic Modules for Use in Grid-Connected Photovoltaic Systems in Dry Climates. *Appl. Energy* 160, 255–265. doi:10.1016/j.apenergy.2015.09.064

Evans, D. L. (1981). Simplified Method for Predicting Photovoltaic Array Output. *Sol. Energy* 27 (6), 555–560. doi:10.1016/0038-092x(81)90051-7

Ghenai, C., and Janajreh, I. (2016). Design of Solar-Biomass Hybrid Microgrid System in Sharjah. *Energy Procedia* 103, 357–362. doi:10.1016/j.egypro.2016.11.299

Ghenai, C., Salameh, T., and Merabet, A. (2020). Technico-economic Analysis of off Grid Solar PV/Fuel Cell Energy System for Residential Community in Desert Region. *Int. J. Hydrogen Energy* 45 (20), 11460–11470. doi:10.1016/j.ijhydene.2018.05.110

Gomaa, M., Mustafa, R., Rezk, H., Al-Dhaifallah, M., and Al-Salaymeh, A. (2018). Sizing Methodology of a Multi-Mirror Solar Concentrated Hybrid PV/thermal System. *Energies* 11 (12), 3276. doi:10.3390/en11123276

Inayat, A., Nassef, A. M., Rezk, H., Sayed, E. T., Abdelkareem, M. A., and Olabi, A. G. (2019). Fuzzy Modeling and Parameters Optimization for the Enhancement of Biodiesel Production from Waste Frying Oil over Montmorillonite Clay K-30. *Sci. Total Environ.* 666, 821–827. doi:10.1016/j.scitotenv.2019.02.321

Khan, M., Zeb, K., Sathishkumar, P., Rao, S., Gopi, C., and Kim, H.-J. (2018). A Novel Off-Grid Optimal Hybrid Energy System for Rural Electrification of Tanzania Using a Closed Loop Cooled Solar System. *Energies* 11 (4), 905. doi:10.3390/en11040905

Khatib, T., Mohamed, A., and Sopian, K. (2013). A Review of Photovoltaic Systems Size Optimization Techniques. *Renew. Sustain. Energy Rev.* 22, 454–465. doi:10.1016/j.rser.2013.02.023

Lau, K. Y., Muhamad, N. A., Arief, Y. Z., Tan, C. W., and Yatim, A. H. M. (2016). Grid-connected Photovoltaic Systems for Malaysian Residential Sector: Effects of Component Costs, Feed-In Tariffs, and Carbon Taxes. *Energy* 102, 65–82. doi:10.1016/j.energy.2016.02.064

Le Lay, C. (2021). *L'annuaire du Bureau des Longitudes et la Diffusion Scientifique : Enjeux et Controverses (1795-1870)*. L'Annuaire du Bureau des longitudes. (1795-1932).

Lu, Z. H., and Yao, Q. (2007). Energy Analysis of Silicon Solar Cell Modules Based on an Optical Model for Arbitrary Layers. *Sol. Energy* 81 (5), 636–647. doi:10.1016/j.solener.2006.08.014

Menconi, M. E., dell'Anna, S., Scarlato, A., and Grohmann, D. (2016). Energy Sovereignty in Italian Inner Areas: Off-Grid Renewable Solutions for Isolated Systems and Rural Buildings. *Renew. Energy* 93, 14–26. doi:10.1016/j.renene.2016.02.034

Mertin, S., Hody-Le Caër, V., Joly, M., Mack, I., Oelhafen, P., Scartezzini, J.-L., et al. (2014). Reactively Sputtered Coatings on Architectural Glazing for Coloured Active Solar Thermal Façades. *Energy Build.* 68, 764–770. doi:10.1016/j.enbuild.2012.12.030

Mohamed, H. O., Obaid, M., Sayed, E. T., Abdelkareem, M. A., Park, M., Liu, Y., et al. (2017). Graphite Sheets as High-Performance Low-Cost Anodes for Microbial Fuel Cells Using Real Food Wastewater. *Chem. Eng. Technol.* 40 (12), 2243–2250. doi:10.1002/ceat.201700058

Mohamed, M. A., Zaki Diab, A. A., and Rezk, H. (2019). Partial Shading Mitigation of PV Systems via Different Meta-Heuristic Techniques. *Renew. Energy* 130, 1159–1175. doi:10.1016/j.renene.2018.08.077

Nassef, A. M., Fathy, A., Sayed, E. T., Abdelkareem, M. A., Rezk, H., Tanveer, W. H., et al. (2019a). Maximizing SOFC Performance through Optimal Parameters Identification by Modern Optimization Algorithms. *Renew. Energy* 138, 458–464. doi:10.1016/j.renene.2019.01.072

Nassef, A. M., Sayed, E. T., Rezk, H., Abdelkareem, M. A., Rodriguez, C., and Olabi, A. G. (2019b). Fuzzy-modeling with Particle Swarm Optimization for Enhancing the Production of Biodiesel from MicroalgaEnergy Sources, Part A: Recovery, Utilization. *Energy Sources, Part A Recovery, Util. Environ. Eff.* 41 (17), 2094–2103. doi:10.1080/15567036.2018.1549171

Neves, D., Pina, A., and Silva, C. A. (2018). Comparison of Different Demand Response Optimization Goals on an Isolated Microgrid. *Sustain. Energy Technol. Assessments* 30, 209–215. doi:10.1016/j.seta.2018.10.006

Nicol, J. F., Raja, I. A., Allaudin, A., and Jamy, G. N. (1999). Climatic Variations in Comfortable Temperatures: the Pakistan Projects. *Energy Build.* 30 (3), 261–279. doi:10.1016/s0378-7788(99)00011-0

Notton, G., Cristofari, C., Mattei, M., and Poggi, P. (2005). Modelling of a Double-Glass Photovoltaic Module Using Finite Differences. *Appl. Therm. Eng.* 25 (17-18), 2854–2877. doi:10.1016/j.applthermaleng.2005.02.008

Poompavai, T., and Kowsalya, M. (2019). Control and Energy Management Strategies Applied for Solar Photovoltaic and Wind Energy Fed Water Pumping System: A Review. *Renew. Sustain. Energy Rev.* 107, 108–122. doi:10.1016/j.rser.2019.02.023

Rafindadi, A. A. (2016a). Does the Need for Economic Growth Influence Energy Consumption and CO_2 Emissions in Nigeria? Evidence from the Innovation Accounting Test. *Renew. Sustain. Energy Rev.* 62, 1209–1225. doi:10.1016/j.rser.2016.05.028

Rafindadi, A. A., and Mika'Ilu, A. S. (2019). Sustainable Energy Consumption and Capital Formation: Empirical Evidence from the Developed Financial Market of the United Kingdom. *Sustain. Energy Technol. Assessments* 35, 265–277. doi:10.1016/j.seta.2019.07.007

Rafindadi, A. A., Muye, I. M., and Kaita, R. A. (2018). The Effects of FDI and Energy Consumption on Environmental Pollution in Predominantly Resource-Based Economies of the GCC. *Sustain. Energy Technol. Assessments* 25, 126–137. doi:10.1016/j.seta.2017.12.008

Rafindadi, A. A., and Ozturk, I. (2016). Effects of Financial Development, Economic Growth and Trade on Electricity Consumption: Evidence from Post-fukushima Japan. *Renew. Sustain. Energy Rev.* 54, 1073–1084. doi:10.1016/j.rser.2015.10.023

Rafindadi, A. A., and Ozturk, I. (2017). Impacts of Renewable Energy Consumption on the German Economic Growth: Evidence from Combined Cointegration Test. *Renew. Sustain. Energy Rev.* 75, 1130–1141. doi:10.1016/j.rser.2016.11.093

Rafindadi, A. A., and Ozturk, I. (2015). Natural Gas Consumption and Economic Growth Nexus: Is the 10th Malaysian Plan Attainable within the Limits of its Resource? *Renew. Sustain. Energy Rev.* 49, 1221–1232. doi:10.1016/j.rser.2015.05.007

Rafindadi, A. A. (2016b). Revisiting the Concept of Environmental Kuznets Curve in Period of Energy Disaster and Deteriorating Income: Empirical Evidence from Japan. *Energy Policy* 94, 274–284. doi:10.1016/j.enpol.2016.03.040

Rakovec, J., Zakšek, K., Brecl, K., Kastelec, D., and Topič, M. (2011). Orientation and Tilt Dependence of a Fixed PV Array Energy Yield Based on Measurements of Solar Energy and Ground Albedo–A Case Study of Slovenia. *Energy Manag. Syst.*, 145

Ren, R., Han, X., Zhang, H., Lin, H., Zhao, J., Zheng, Y., et al. (2018). High Yield Bio-Oil Production by Hydrothermal Liquefaction of a Hydrocarbon-Rich Microalgae and Biocrude Upgrading. *Carbon Resour. Convers.* 1 (2), 153–159. doi:10.1016/j.crcon.2018.07.008

Rezk, H., Nassef, A. M., Inayat, A., Sayed, E. T., Shahbaz, M., and Olabi, A. G. (2019). Improving the Environmental Impact of Palm Kernel Shell through

Maximizing its Production of Hydrogen and Syngas Using Advanced Artificial Intelligence. *Sci. Total Environ.* 658, 1150–1160. doi:10.1016/j.scitotenv.2018.12.284

Santbergen, R., and van Zolingen, R. J. C. (2008). The Absorption Factor of Crystalline Silicon PV Cells: A Numerical and Experimental Study. *Sol. Energy Mater. Sol. Cells* 92 (4), 432–444. doi:10.1016/j.solmat.2007.10.005

Sayed, E. T., Eisa, T., Mohamed, H. O., Abdelkareem, M. A., Allagui, A., Alawadhi, H., et al. (2019). Direct Urea Fuel Cells: Challenges and Opportunities. *J. Power Sources* 417, 159–175. doi:10.1016/j.jpowsour.2018.12.024

Schott, T. (1985). Operation Temperatures of Pv Modules: a Theoretical and Experimental Approach. *EC Photovolt. Sol. energy Conf.* 6.

Sharma, R., and Goel, S. (2017). Performance Analysis of a 11.2 kWp Roof Top Grid-Connected PV System in Eastern India. *Energy Rep.* 3, 76–84. doi:10.1016/j.egyr.2017.05.001

Sher, F., Kawai, A., Güleç, F., and Sadiq, H. (2019). Sustainable Energy Saving Alternatives in Small Buildings. *Sustain. Energy Technol. Assessments* 32, 92–99. doi:10.1016/j.seta.2019.02.003

Shukla, A. K., Sudhakar, K., and Baredar, P. (2016a). A Comprehensive Review on Design of Building Integrated Photovoltaic System. *Energy Build.* 128, 99–110. doi:10.1016/j.enbuild.2016.06.077

Shukla, A. K., Sudhakar, K., and Baredar, P. (2016b). Exergetic Assessment of BIPV Module Using Parametric and Photonic Energy Methods: a Review. *Energy Build.* 119, 62–73. doi:10.1016/j.enbuild.2016.03.022

Shukla, A. K., Sudhakar, K., and Baredar, P. (2017). Recent Advancement in BIPV Product Technologies: A Review. *Energy Build.* 140, 188–195. doi:10.1016/j.enbuild.2017.02.015

Tahir, Z. u. R., Asim, M., Azhar, M., Moeenuddin, G., and Farooq, M. (2021). Correcting Solar Radiation from Reanalysis and Analysis Datasets with Systematic and Seasonal Variations. *Case Stud. Therm. Eng.* 25, 100933. doi:10.1016/j.csite.2021.100933

Tahir, Z. u. R., Azhar, M., Blanc, P., Asim, M., Imran, S., Hayat, N., et al. (2020). The Evaluation of Reanalysis and Analysis Products of Solar Radiation for Sindh Province, Pakistan. *Renew. Energy* 145, 347–362. doi:10.1016/j.renene.2019.04.107

Zeyringer, M., Pachauri, S., Schmid, E., Schmidt, J., Worrell, E., and Morawetz, U. B. (2015). Analyzing Grid Extension and Stand-Alone Photovoltaic Systems for the Cost-Effective Electrification of Kenya. *Energy Sustain. Dev.* 25, 75–86. doi:10.1016/j.esd.2015.01.003

Conflict of Interest: The authors declare that the research was conducted in the absence of any commercial or financial relationships that could be construed as a potential conflict of interest.

Publisher's Note: All claims expressed in this article are solely those of the authors and do not necessarily represent those of their affiliated organizations, or those of the publisher, the editors, and the reviewers. Any product that may be evaluated in this article, or claim that may be made by its manufacturer, is not guaranteed or endorsed by the publisher.

NOMENCLATURE

Abbreviations

A Absorption coefficient (m^{-1})

C Specific heat $Jkg^{-1}K^{-1}$

e Thickness of the layer m

E Time equation h

F View factor Pa

h Convective heat transfer coefficient $Wm^{-2}K^{-1}$

H True local solar time H

H_1 Local time H

ΔH_1 Time lag between the UTC and the given time zone h

ΔHg Time lag because of longitudinal variations within the time zone h

I Solar irradiance (Wm^{-2})

J The day of the year ——

K Thermal conductivity $Wm^{-1}K^{-1}$

L Latitude (°)Traveling distance by irradiance through material M

L Latitude (°)Traveling distance by irradiance through material M

n Refractive index ——

P Output electrical power W

r Material reflectance Wm^{-2}

S Greek symbol inclination angle of the PV panel (°)

T Temperature K

α Absorbance ——

βo Temperature coefficient K^{-1}

γ Coefficient of solar radiation ——

δ Sun's declination (°)

ε Material emissivity ——

η Efficiency ——

Θ Incident angle (°)

λ Wavelength M

t Time s

φ Azimuthal angle (°)

phi ——

ρ Density Kgm^{-3}

σ Stefan–Boltzmann constant $Wm^{-2}K^{-4}$

τ Transmittance ___

φ Azimuthal angle (°)

ω Hour angle (°)

frontiers | Frontiers in Public Health

ORIGINAL RESEARCH
published: 08 July 2022
doi: 10.3389/fpubh.2022.875971

A Novel Deep Learning and Ensemble Learning Mechanism for Delta-Type COVID-19 Detection

Habib Ullah Khan[1]*, *Sulaiman Khan*[1] and *Shah Nazir*[2]

[1] Department of Accounting and Information Systems, College of Business and Economics, Doha, Qatar, [2] Department of Computer Science, University of Swabi, Swabi, Pakistan

Recently, the novel coronavirus disease 2019 (COVID-19) has posed many challenges to the research community by presenting grievous severe acute respiratory syndrome coronavirus 2 (SARS-CoV-2) that results in a huge number of mortalities and high morbidities worldwide. Furthermore, the symptoms-based variations in virus type add new challenges for the research and practitioners to combat. COVID-19-infected patients comprise trenchant radiographic visual features, including dry cough, fever, dyspnea, fatigue, etc. Chest X-ray is considered a simple and non-invasive clinical adjutant that performs a key role in the identification of these ocular responses related to COVID-19 infection. Nevertheless, the defined availability of proficient radiologists to understand the X-ray images and the elusive aspects of disease radiographic replies to remnant the biggest bottlenecks in manual diagnosis. To address these issues, the proposed research study presents a hybrid deep learning model for the accurate diagnosing of Delta-type COVID-19 infection using X-ray images. This hybrid model comprises visual geometry group 16 (VGG16) and a support vector machine (SVM), where the VGG16 is accustomed to the identification process, while the SVM is used for the severity-based analysis of the infected people. An overall accuracy rate of 97.37% is recorded for the assumed model. Other performance metrics such as the area under the curve (AUC), precision, F-score, misclassification rate, and confusion matrix are used for validation and analysis purposes. Finally, the applicability of the presumed model is assimilated with other relevant techniques. The high identification rates shine the applicability of the formulated hybrid model in the targeted research domain.

Keywords: hybrid deep learning, Delta-type COVID-19, VGG16, ensemble learning technique, AI

OPEN ACCESS

Edited by:
Muhammad Amjad, University of Engineering and Technology, Lahore, Pakistan

Reviewed by:
Gaurav Dhiman, Government Bikram College of Commerce Patiala, India
Juliana Gomes, Federal University of Pernambuco, Brazil

***Correspondence:**
Habib Ullah Khan
habib.khan@qu.edu.qa

Specialty section:
This article was submitted to Digital Public Health, a section of the journal Frontiers in Public Health

Received: *14 February 2022*
Accepted: *13 June 2022*
Published: *08 July 2022*

Citation:
Khan HU, Khan S and Nazir S (2022) A Novel Deep Learning and Ensemble Learning Mechanism for Delta-Type COVID-19 Detection. Front. Public Health 10:875971. doi: 10.3389/fpubh.2022.875971

INTRODUCTION

Globally, the COVID-19 pandemic continues to have catastrophic effects on human lives. According to the WHO reports, about 4.8 million people died due to this outbreak and more than 19 million people were infected by this pandemic (1). To combat this outbreak, researchers around the world presented novel-based models for the identification of this outbreak's symptoms. But, the regional-based varying symptoms and emergence of a new type of virus (COVID-19 type) pose daunting challenges for the researchers to counter. The recrudescence of the new Delta COVID-19 virus swirled the researchers and practitioners due to its high resistance against human mutants and high death rates in a short period. After analyzing the integrating capabilities and achieving

satisfactory results laterally for numerous research problems, the researchers and practitioners suggested artificial intelligence (AI)- and machine learning (ML)-based models for the detection of COVID-19. Keeping in view the reality that AI techniques and models have left no stone unturned, Togaçar et al. (2) suggested a deep learning model for the identification of COVID-19 with the help of Social Mimic Optimization and structured chest X-ray images based on fuzzy color and stacking techniques. Alazab et al. (3) suggested a deep learning technique for the recognition of COVID-19 infection.

Ismail and Sengür assumed deep learning models for the prediction of COVID-19 detection (4). Chang et al. (5) presented deep learning for diagnosing COVID-19 infection using chest X-ray images. Karhan and Akal presented a convolutional neural network (CNN)-based architecture for the identification of COVID-19 using X-ray images (6). Their model consists of a residual network (ResNet) for classification and recognition purposes. A recognition rate of 78% is recorded for their model, which reflects high misclassification rates. This high misclassification shows that this model classifies 22% of normal persons as COVID-19-infected patients. Khan et al. (7) presented a three-dimensional (3D) deep learning model for diagnosing COVID-19 using CT images. Their model consists of 3D-ResNets, 3D-DenseNets, C3D, I3D, and a long-term recurrent convolutional network (LRCN). They performed their analysis of two different datasets (CC-19 and COVID-CT). Keeping in view the shortage of PCR kits and colossal demands, Anwar and Zakir proposed reverse transcriptase-PCR (RT-PCR) for identifying the COVID-19 infection using deep learning (8). For evaluating the performance of their model, they used three different strategies with varying learning rates: (1) limiting the learning rate when the model performance stops increasing (reduce on the plateau), (2) constant learning rate, and (3) cyclic learning rate. A diagnosing rate of 89.7% is recorded for their model.

After evaluating the extant, it was realized that almost every automatic diagnosing model is affected by low recognition rates, high simulation time, complexities, or requires more data to train (data hunger architectures), and many others. Keeping in view these issues in mind, a hybrid model is presented in this study for accurately addressing these problems and performing timely diagnosing and identification tasks. The technical contribution of the proposed research study includes:

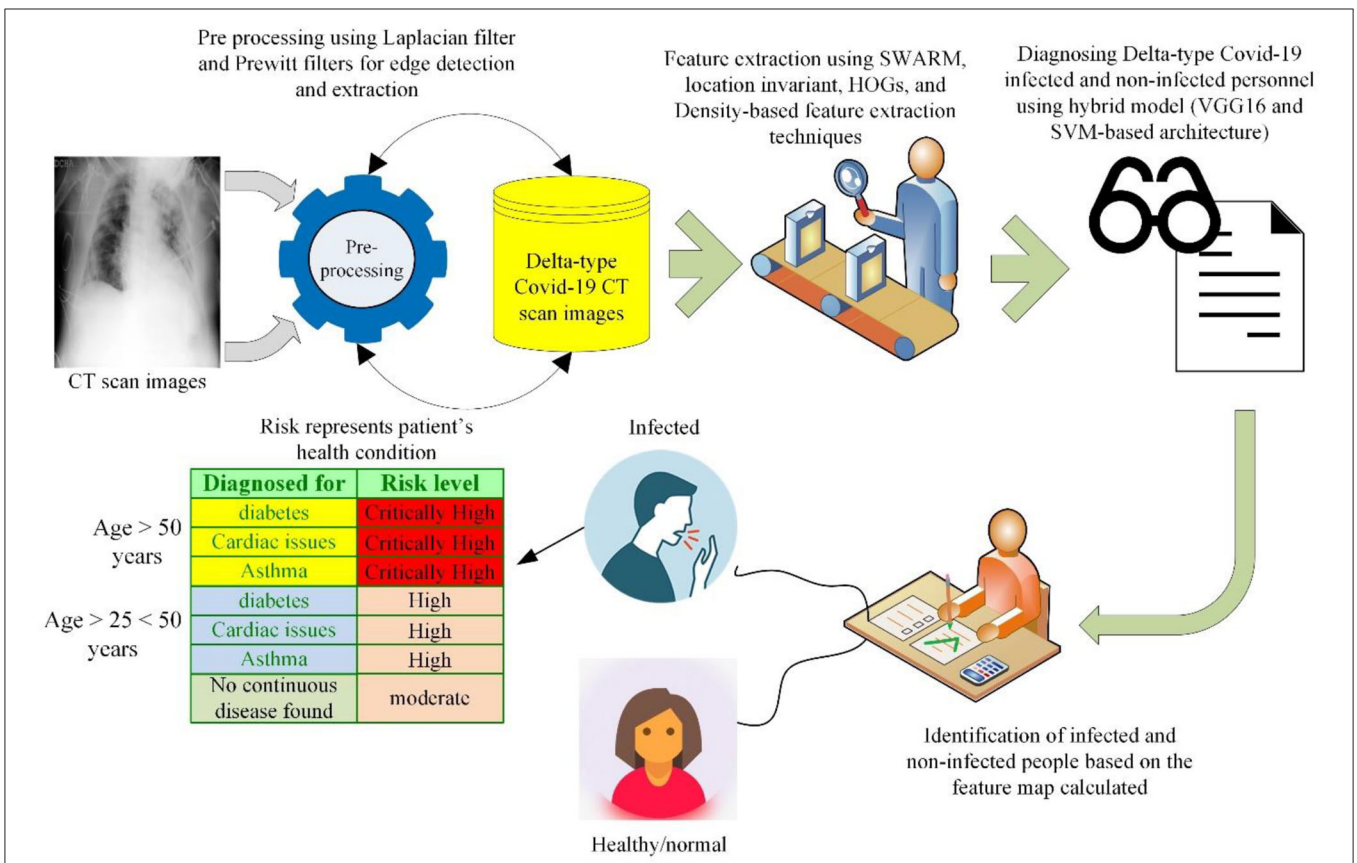

FIGURE 1 | Experimental setup of the proposed study.

- **Optimum diagnosing model**—the development of an optimum recognition model for accurate identification and diagnosing of Delta-type COVID-19-infected personnel. This hybrid model consists of a visual geometry group 16 (VGG16) and a support vector machine (SVM). The VGG16 model achieves the classification of the infected chest images, while the SVM classifier commits the statistical operations to calculate the severity of an individual patient. This statistical analysis will help assign a bed (for treatment purposes) to a patient on a priority basis that has a higher probability of being recovered.
- **Performance analysis**—the validity of the proposed model with other state of the art techniques to evaluate the applicability and integrity of the formulated hybrid model in the selected research domain. Also, different performance metrics such as F-score, accuracy, misclassification rate, specificity, the area under the curve (AUC), and confusion matrix are used for performance analysis purposes.
- **Variant-based validation**—after analyzing the extant, some models show poor performance for small datasets, while some models show poor capabilities for symptoms-based variations (different virus types). Keeping in view these challenges, the proposed hybrid model concluded with an outstanding performance for the COVID-19 variant (Delta type). Based on these performance capabilities, it can be applied to other variants of the severe acute respiratory syndrome coronavirus 2 (SARS-CoV-2) infections. Furthermore, this is non-data-driven architecture and even outperformed a small number of X-ray samples.
- **Patient's health status evaluation**—to the best of the research team's knowledge, much study is reported on the X-ray-based COVID-19 detection and diagnosing purposes (9–11), but

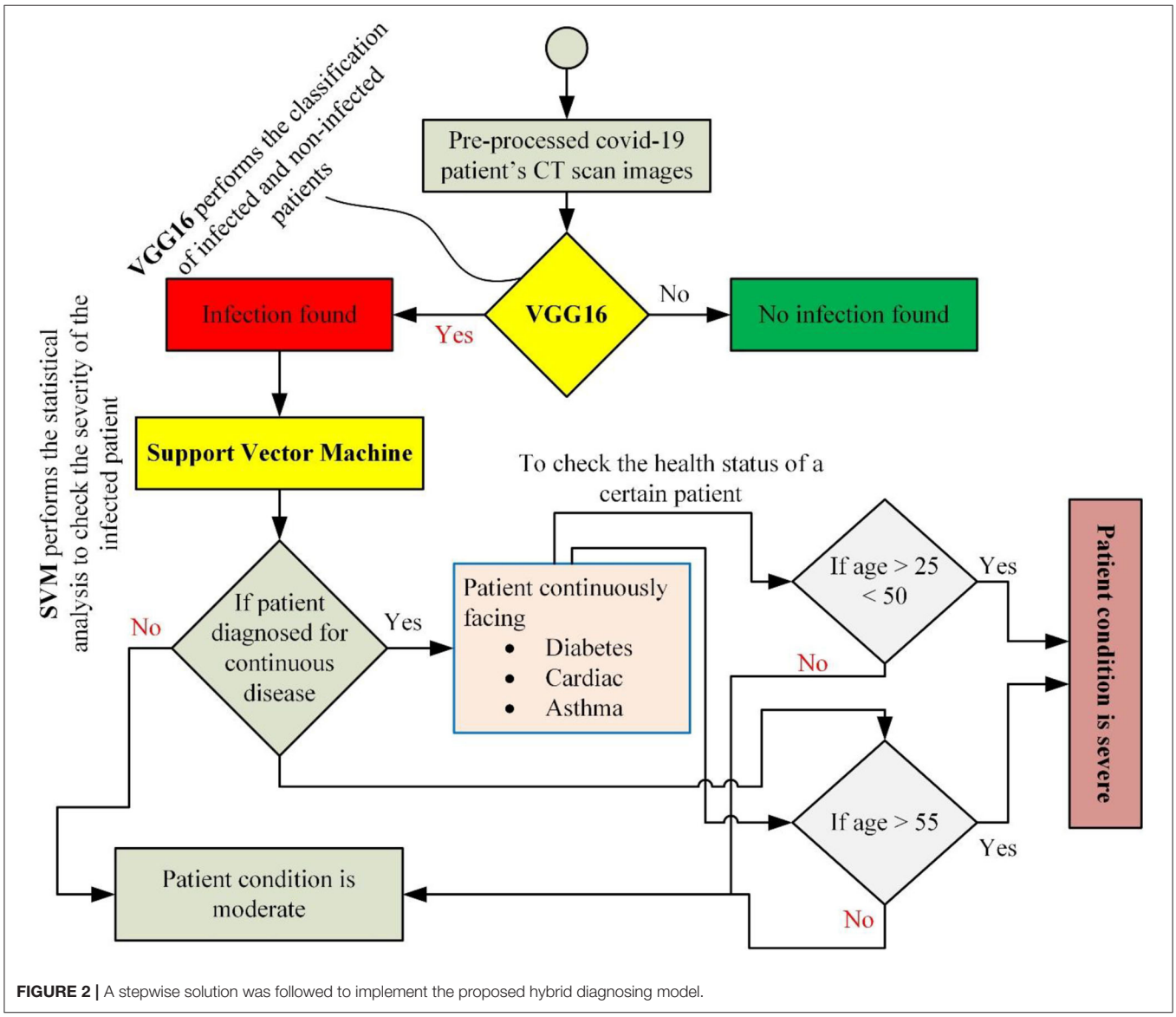

FIGURE 2 | A stepwise solution was followed to implement the proposed hybrid diagnosing model.

there is no study reported to check the severity of a particular patient using statistical and analytical techniques. This severity evaluation of a particular patient will ultimately help the state agencies and practitioners with different aspects:

- To calculate the strengths of this outbreak in a specific region based on patients' historical- and severity-based information.
- Also, this will help the doctors in performing priority-based treatment of specific patients. As we know, when an outbreak hits, mainly the senior personnel or the ones already facing some diseases (heart issues, diabetics, cough, or other lung problems) are more susceptible to being infected and may face severe conditions. With low hardware resource requirements, a timely decision model is required that helps the practitioners and doctors to identify the severe cases automatically.
- This premature analysis and modeling will help the state agencies to carry out their routine activities without interrupting their economy, hospital structure, and other daily activities.

The rest of the article is coordinated as follows. Section Literature Review outlined the background and research study reported in the extant. It also outlined the gaps in the extant and explained how the proposed model will address all these challenges in the extant. Section Methodology outlined the proposed experimental setup followed for diagnosing the COVID-19-infected personnel. In Section Results and Discussion of the article, the results and discussion section are briefly explained that outlined the performance analysis of the suggested model. Also, this section briefly explained the applicability of the proposed research study by comparing its results with other avant diagnosing models presented in the extant. Section Conclusion of the article outlined the conclusion of this research study pursued by the recommendation and future research study in Section Implications.

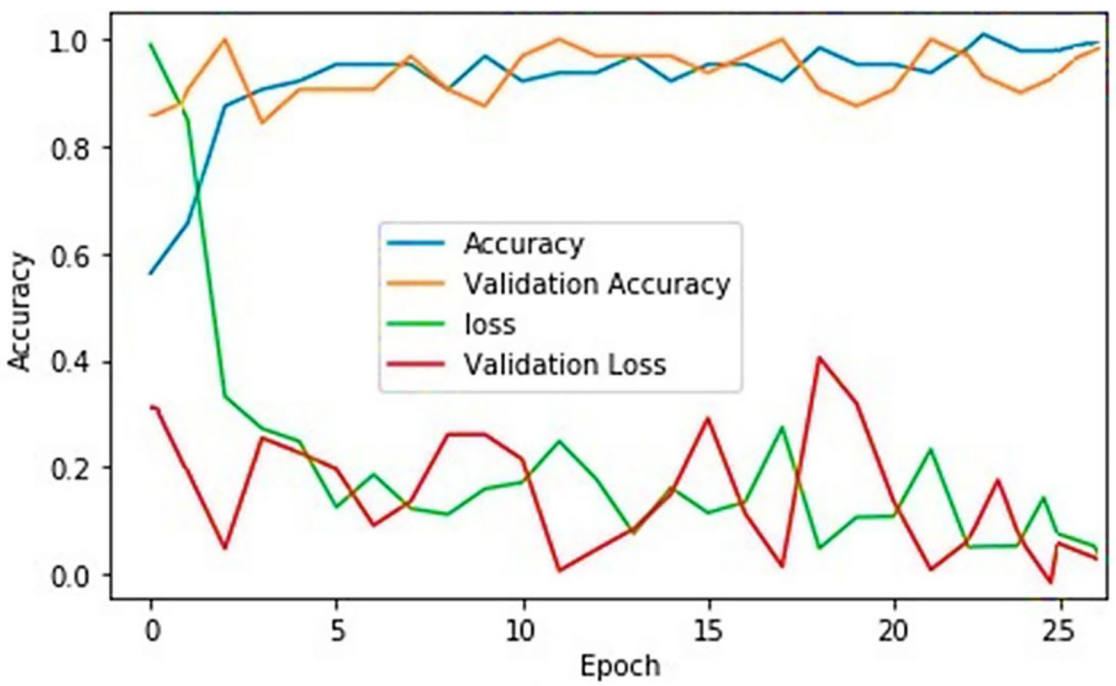

FIGURE 3 | Performance results of the suggested hybrid deep learning technique.

TABLE 1 | Details about the images database used for the experimental study.

Age-wise distribution	Infection-based distribution			Gender-wise distribution		Total number of samples selected from	
	Cardiac	Diabetes	Asthma	Male	Female	GitHub library	Accumulated samples
Age ≥ 50	1,020	924	1,644	59.8%	40.2%	2,600	988
Age>25<50	411	433	1,374	52.1%	47.%	1,700	518
Age>1≤25	5	0	33	63.7%	36.3%	35	3

LITERATURE REVIEW

At the end of 2019, the first case of a novel infection, latterly codenamed as COVID-19, was reported in Wuhan city in China. This virus expanded worldwide and affected millions of people in a short span of time (12–14). The aftershock of this outbreak results in the emergence of new variants (Delta type, Omicron, etc.) in different regions. The Delta-type variation of COVID-19 recently emerged in India and was disseminated quickly around India and even its symptoms were sensed in the neighboring countries, including Sri Lanka, Maldives, and southern regions of Pakistan. This variant concluded with high mortalities even in short span of time. The researchers and practitioners were busy synthesizing the symptoms and their underlined catastrophic effects on human lives that a new variant of COVID-19 emerged in South Africa's Gauteng province, where the achingly mutated breed of the virus was first figured out and was researched that it is more potent than other variants in escaping anterior immunity. This variant is codenamed as Omicron (15). Maria Van Kerkhove, the WHOs technical team lead on COVID-19, stated in a video posted on Twitter "*This variant has a large number of mutations and some of these mutations have some worrying characteristics.*"

These symptoms-based variations and consequently high mortalities puzzle the research community and practitioners to counter this outbreak. A smart machine learning model is required capable of not only countering Delta-type COVID-19, but can combat the afterward variants with optimum capabilities. Inspired by the applicability of AI and machine learning techniques in diverse domains such as traffic flow predictions (16) and smart object detection in smart homes for ensuring high security (17), many researchers proposed deep learning for classifying and recognizing the COVID-19 infection. Multiple convolutional neural network (CNN) classification models such as ResNet50V2, DenseNet201, and Inceptionv3 are suggested for identifying patients with COVID-19 using chest X-ray images (3, 18, 19). Experimental results for their models were calculated using only 468 images. It shows poor performance for larger datasets and its simulation time becomes very high for comparatively larger databases. Qiao et al. (20) proposed the focal loss-based neural network ensemble mechanism for COVID-19 identification purposes in this research study. They performed the simulations on X-ray images. They presented a novel-based approach, but their model shows small performance metrics values (low precision values of 0.783360.07, recall values of 0.860960.03, and F1-score values of 0.81686 0.03).

Salman et al. (21) suggested an artificial intelligence-based deep learning model for diagnosing the COVID-19 virus by applying chest images. They performed their analysis on

TABLE 2 | Set of parameters defined for the proposed hybrid model.

S. No	Parameter	Value
1.	Number of inputs	$100 \times 100 \times 1,200$
2.	Filter	64
3.	Total number of layers	5
4.	Number of hidden layers	3
5.	Kernel function size	(3×3)
6.	Batch size	32
7.	Epoch size	50
8.	Optimizer	Adam
9.	Activation function	Rectified Linear Unit and Tanh

TABLE 3 | Severity-based analysis.

Age (years)	Type of continuous disease diagnosed			Health status (risk level)	Output and comments
	Cardiac issues	Diabetes	Asthma		
Age ≥ 50	✓	✓	✓	Critically high	Patient requires proper medication and isolation. Also, he/she needs a significant attention of the caretakers.
Age ≥50	×	✓	✓	Critically high	
Age ≥ 50	✓	×	✓	Critically high	
Age ≥ 50	✓	✓	×	Critically high	
Age ≥ 50	✓	×	×	Critically high	
Age ≥ 50	×	✓	×	Critically high	
Age ≥ 50	×	×	✓	Critically high	
Age>25<50	✓	✓	✓	High	Patient requires proper medication and isolation. Also, he/she needs a significant attention of the caretakers.
Age>25<50	×	✓	✓	High	
Age>25<50	✓	×	✓	High	
Age>25<50	✓	✓	×	High	
Age>25<50	✓	×	×	High	
Age>25<50	×	✓	×	High	
Age>25<50	×	×	✓	High	
Age>1≤25	×	×	✓	High	Patient requires medication and attention of the caretaker.
Age>1≤25	×	×	×	Moderate	Patient needs only proper medication.

Colors are used to differentiate in-between different age categories.

130 different images. Their model performed an outstanding performance for this small amount of data, but fails in classifying comparatively larger datasets. The research article presented by Loey et al. (22) shows a generative adversarial network (GAN) with deep transfer learning for COVID-19 recognition using chest X-ray images. They performed their experimental study using 307 images for four different types of classes. Their model achieved 80.6% in much smaller testing accuracy, especially in healthcare applications. Additionally, the number of images used for experimental purposes is much smaller than a standard testing and validation model. Similarly, Chang et al. (5) have proposed VGG16 for diagnosing COVID-19 infection using chest X-ray images. An overall accuracy rate of 78% is achieved for this model, which is comparatively much smaller and ultimately it reflects a high misclassification rate. Anwar and Zakir proposed RT-PCR for identifying COVID-19 infection using deep learning models (8). For evaluating the performance of their model, they used three different strategies with varying learning rates. This model helps in reducing the dependency on PCR testing kits and colossal demands. An overall accuracy rate of 89.7% is recorded for their model, which ponders the incapability of this model in the proposed research domain. Dhiman and Kaur suggested a high optimization model for industrial engineering problems after inspiration by bioinspired-based techniques. Inspired by the collaborative behavior of spotted hyenas, Dhiman and Kumar suggested a novel metaheuristic algorithm named as Spotted Hyena Optimizer (SHO). The applicability of the SHO-based model is validated using different 29 state of the art benchmark functions (23, 24). Based on their performance analysis, they concluded that their models outperform the available models in the extant. Kaur et al. (25) presented the concept of metaheuristic paradigm for global optimization using a novel Tunicate Swarm and NOVA tests.

After studying the literature and assessing their capabilities and limitations, it was concluded that most of the techniques developed in the literature are either tested on small datasets or affected by low accuracy rates, while some of these models are

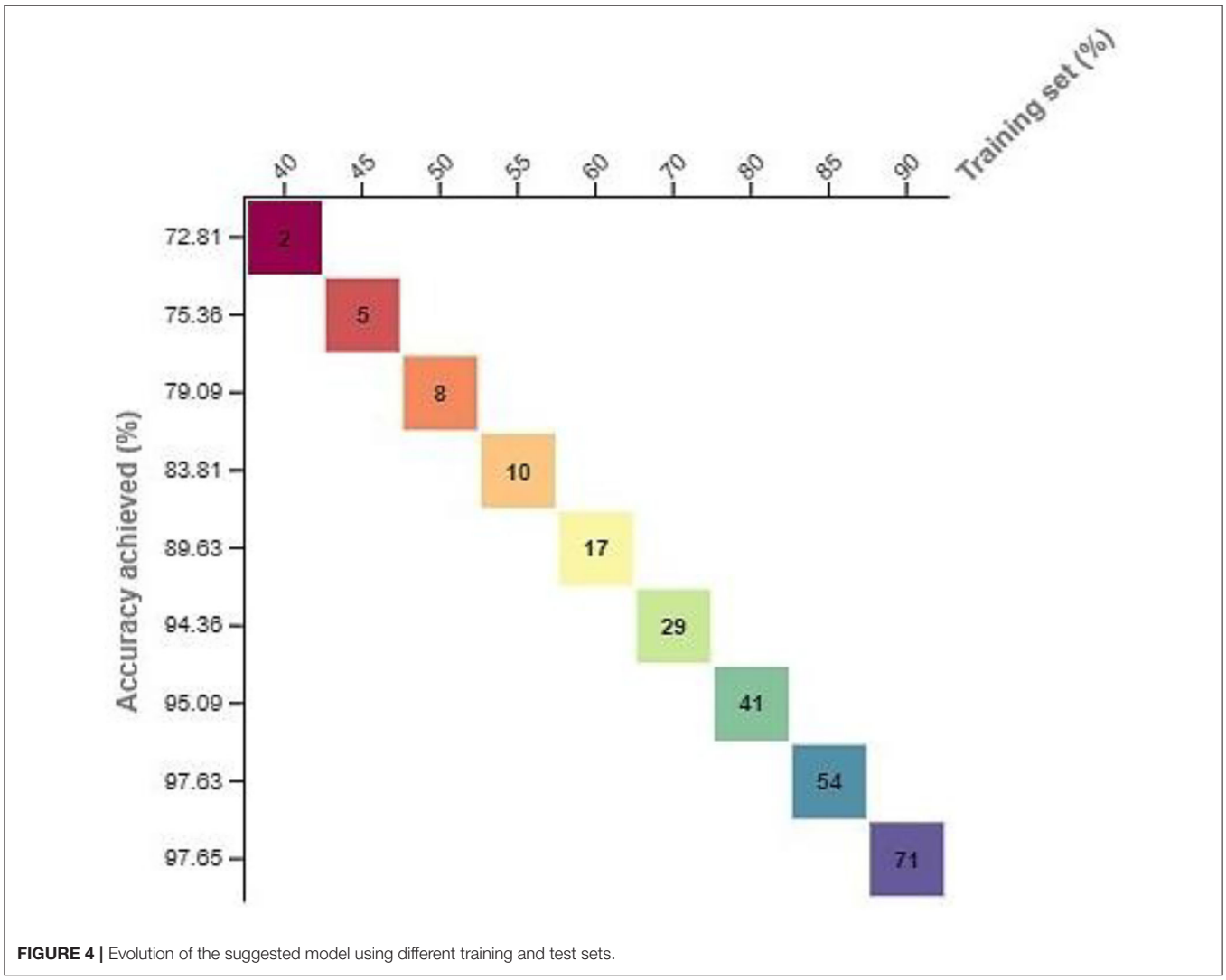

FIGURE 4 | Evolution of the suggested model using different training and test sets.

good for COVID-19, but fail in diagnosing the variants of the SARS-CoV-2-like COVID-19 (Delta type, Omicron, etc.). These difficulties in variant-based diagnosing are because of diverging symptoms and their underlined effects on human bodies. A smart machine learning model is required to combat all these challenges and perform optimum diagnosing for different variant-base infections. Keeping in view these questions in mind, a hybrid model is formulated in this study and was concluded with an outstanding performance for the COVID-19 variant (Delta type). Based on the performance capabilities, it can be concluded that this model can be applied to other variants of the SARS-CoV-2 infections. Furthermore, this is low data-hunger architecture and even outperformed a small number of X-ray samples.

METHODOLOGY

Figure 1 represents the experimental setup followed for the proposed research study. In this research study, a hybrid deep learning model is suggested for identifying Delta-type COVID-19-infected patients. This hybrid model comprises VGG16 and SVM classifiers, where the VGG16 architectures perform the classification tasks, while the SVM performs the statistical analysis to calculate the severity (health status) of patients. In this research model, different preprocessing and feature extraction techniques are used for ensuring high identification rates. To clarify the X-ray images and laterally assure high recognition rates, this research study has proposed Prewitt and Laplacian filters to extract the edge information of the infected region. Then, feature extraction techniques such as the Swarm-based feature extraction technique (26), histogram of oriented gradients (HoG), and location invariant features are proposed to calculate the feature map. In the X-ray images, most of the time, the resultant images are blurred, scaled, rotated, and many others and most of the feature extraction techniques fail in accumulating optimum astute value in such cases, but invariant feature extraction techniques are prominent in these cases because their feature accumulation capabilities are never affected by rotation and scaling (27).

After applying these feature extraction techniques, a fused feature map (features calculated by HoG, location invariant technique, and Swarm-based feature extraction technique) is developed that is provided to the hybrid model formulated in this research study. The diagnosing and classification task is performed using this feature map.

After executing the classification task on the feature map, if a person is diagnosed with the infection, then his/her severity is measured using statistical analysis based on different parameters such as age, suffering from a continuous disease (diabetes, cardiac problems, asthma, etc.), and health status. Being binary in nature (28), the SVM outperforms the identification of critically severe and severe conditions. The overall statistical operations followed for identifying the health status (severity) of a certain patient are given in a flowchart diagram in **Figure 2**. This stepwise solution is followed for identifying the severity of each patient based on the classification results generated by the VGG16 classifier.

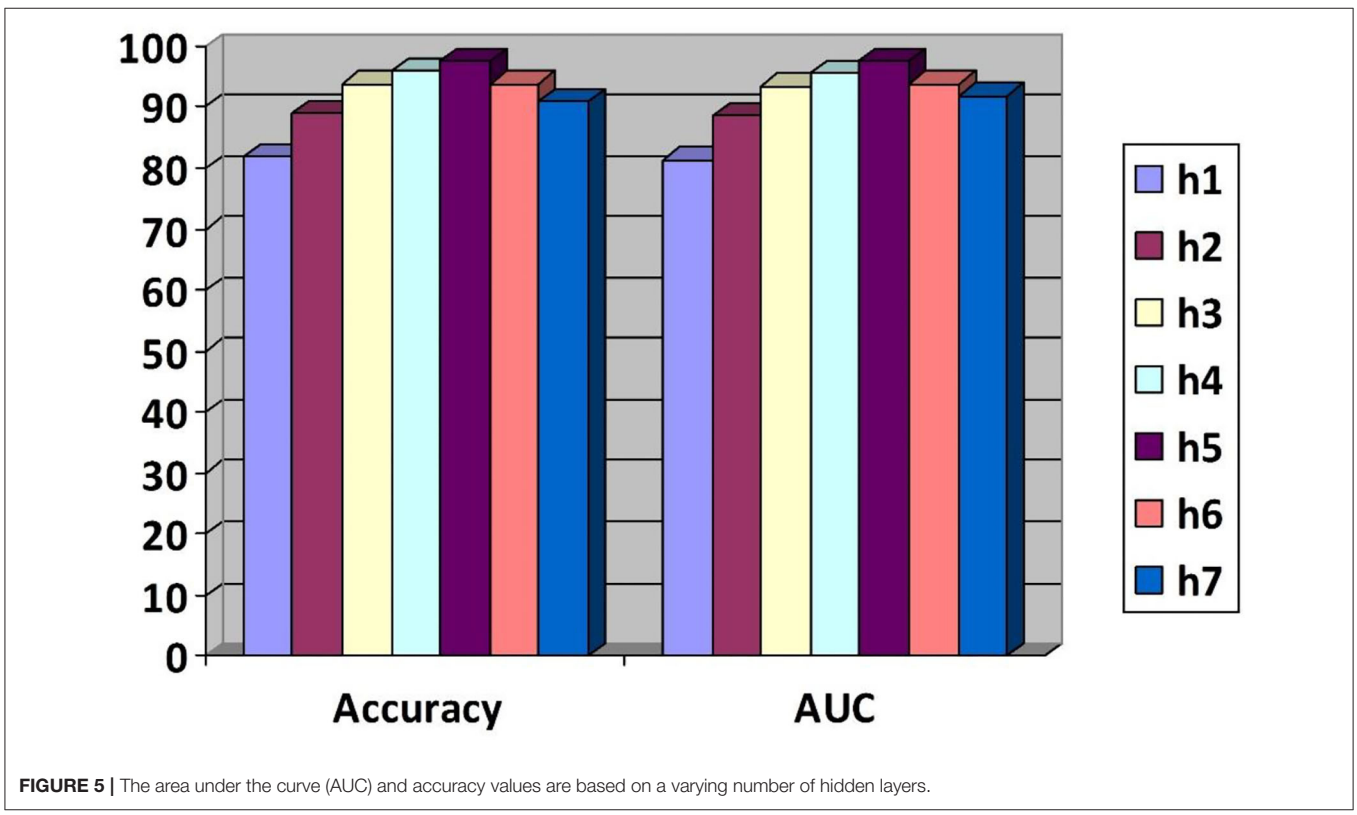

FIGURE 5 | The area under the curve (AUC) and accuracy values are based on a varying number of hidden layers.

RESULTS AND DISCUSSION

This part of the article shows the experimental results generated by the proposed hybrid model after applying the manipulated feature map. This study outperformed by simulating an overall accuracy rate of 97.37%, as shown in **Figure 3**. For this research study, a dataset[1] is selected from the GitHub library freely available for research and simulation purposes and some other Delta-type infection images are collected in the group from multiple patients in the hospital (Lady Reading Hospital, Peshawar, Pakistan) and the WHO reports (15). The details about the number of samples used for the experimental study are given in **Table 1**. A total of 5,844 samples were used for this experimental study. The details regarding the number of samples, gender, age, and infection details are given in **Table 1**. The accumulated samples in **Table 1** represent the number of samples collected from the hospital. This eminent recognition rate reflects the applicability of the proposed model for the identification of Delta-type COVID-19. Even based on these high-performance values, it can be concluded that this hybrid model can be employed for the identification of other COVID-19 variants.

From **Table 1**, it can be easily observed that this disease has a comparatively low infection in youngers (age $> 1 \leq$ 25 years). Different parameters are selected for the validation and applicability analysis of the proposed research study. The information regarding these parameters is shown in **Table 2**.

The statistical assessment was performed using the formulated research model (SVM) for describing the severity of any particular patient, as shown in **Table 1** (since the statistical analysis is performed only, if a patient is diagnosed with infection). There is no low level (risk level) defined for the patient because someone's life and health status are more important than anything. This severity-based analysis and underlined risk level are calculated after consulting a professional caretaker. The caretaker provided detailed information on the infection attack on aged and continuously diseased patients. **Table 3** outlines these metrics with a full description.

The formulated research model is also validated using different training and test sets and the different number of hidden layers (h). The simulated results are shown in **Figures 4**, **5**. The

[1]https://github.com/owid/covid-19-data/tree/master/public/data/

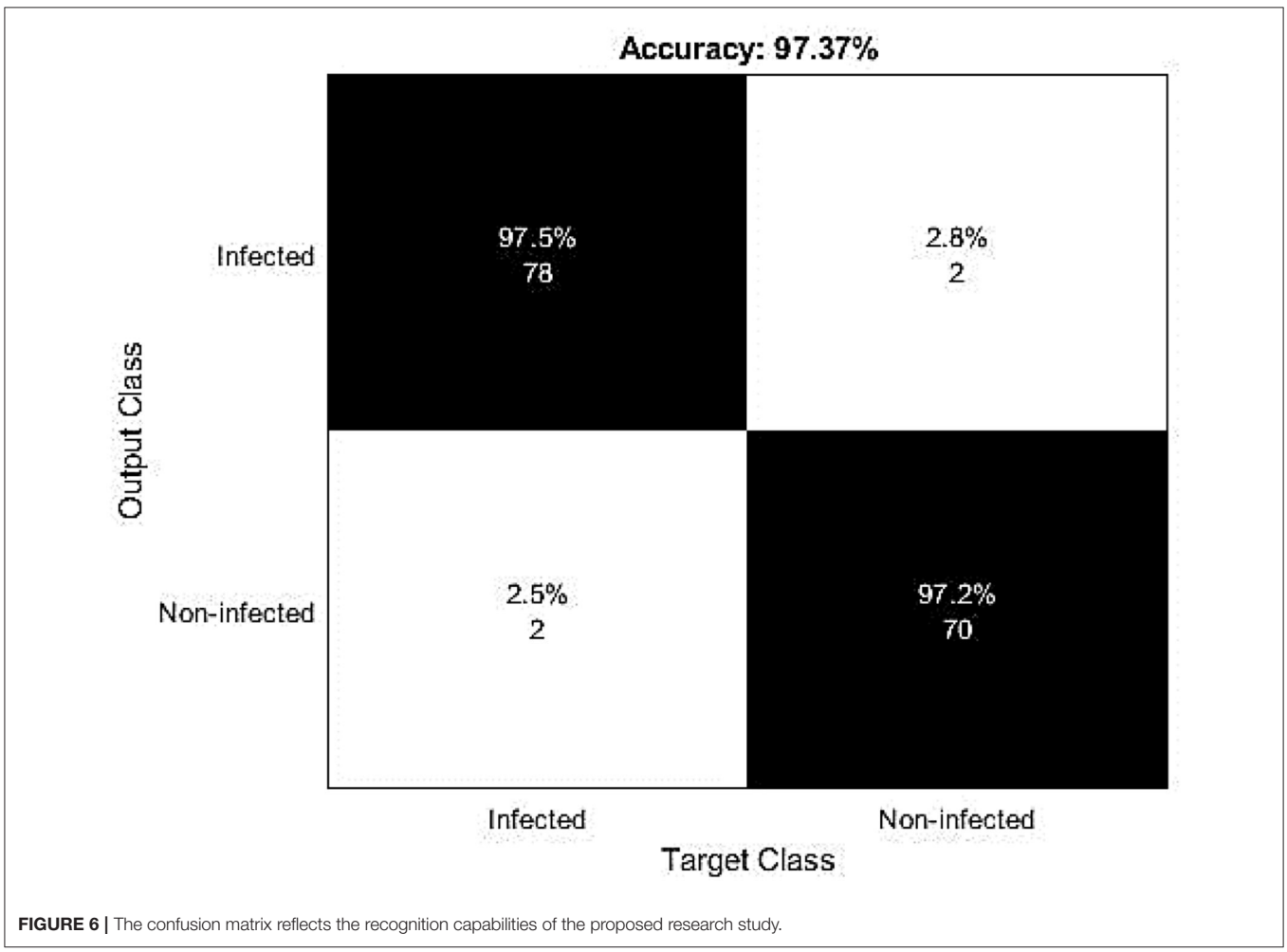

FIGURE 6 | The confusion matrix reflects the recognition capabilities of the proposed research study.

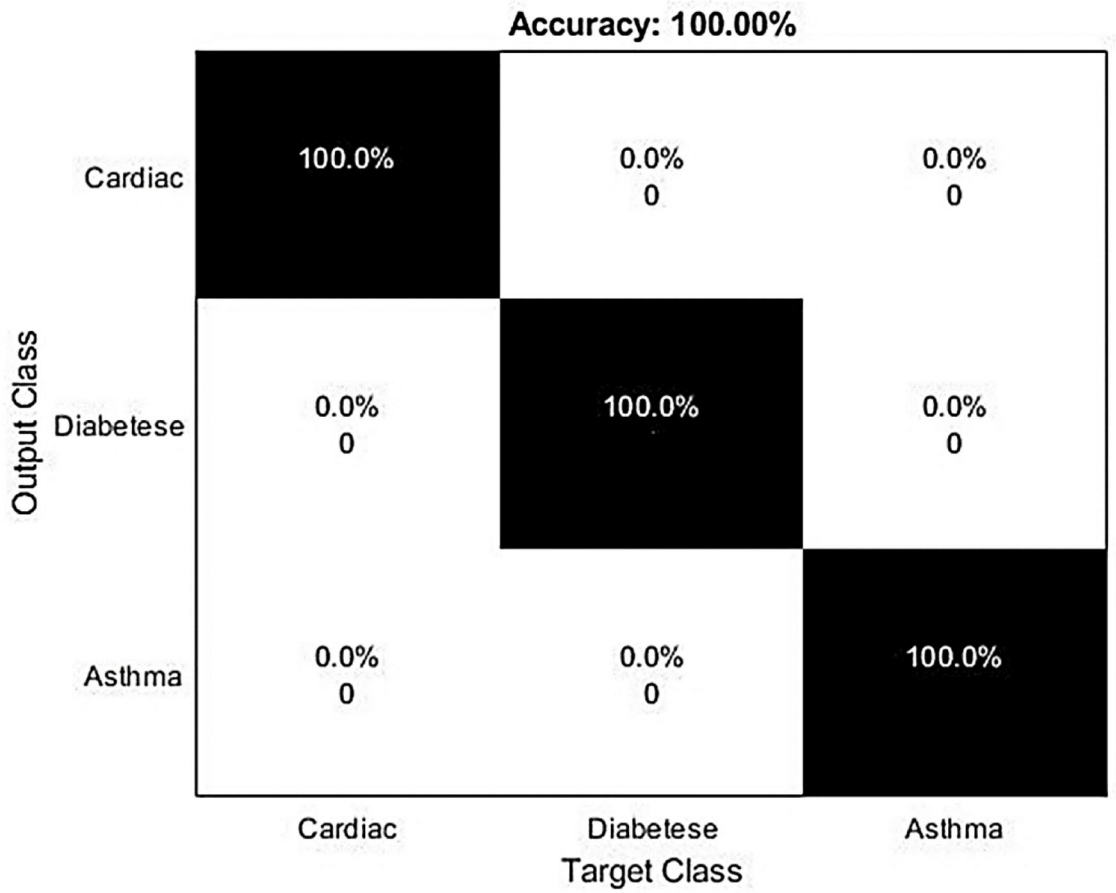

FIGURE 7 | Confusion matrix for severity-based analysis of the infected patients.

squares represent the accuracy values based on the training set, while the numbers in the square boxes represent the simulation time in minute(s). The simulation results are simulated with HP Core i3 3rd generation laptop with Intel processor [that is why the simulation time is recorded more comparative to the graphics processing unit (GPU)-based processors].

To perform these experiments, a training set of a varying number of samples is used. These samples started by dividing the overall data into 40% training data and the remaining test data and then 45% training data and the remaining test data and so on. At the same time, the accuracy of the corresponding technique is noted to validate the applicability of the proposed model. The corresponding results are shown in **Figure 4**. Using this varying number of samples, the performance of the proposed model is also evaluated using the different numbers of hidden layers based on the AUC values and accuracy as a performance indicator. Based on the simulated results, it was concluded that this model outperformed by generating the high AUC and accuracy values.

From **Figures 4**, **5**, it is observed that by increasing the number of hidden layers or the training set, the corresponding time consumption and accuracy of the model increase. But, after hidden layer 5, the accuracy of the model starts decreasing, which reflects the complexity of the circuit and high simulation cost.

The confusion matrix of this research study is given in **Figure 6**. The small number of false positive and false negative represents the materiality of the proposed hybrid deep learning model for the identification of Delta-type COVID-19 infection. **Figure 7** contains the diagnosing details of Delta-type COVID-19 infection using VGG16.

A total of 5,844 images were used (1,948 images for every three different classes with both the infected and non-infected states). The corresponding results based on infection and non-infection are given in **Figure 6**. These results were evaluated based on the clinical historical information and the results were found correct, as shown in **Figure 6**.

For this experimental and simulation study, we used an HP Core i3 machine. So, to avoid high-time consumption, a small number of samples are used for training and testing purposes. Some CT scan images are highly blurred and it is more difficult for the proposed model to accurately recognize that ultimately causing misclassification. While plotting a confusion matrix to evaluate the capabilities of this model for the severity-based analysis, a 100% accuracy is recorded for the

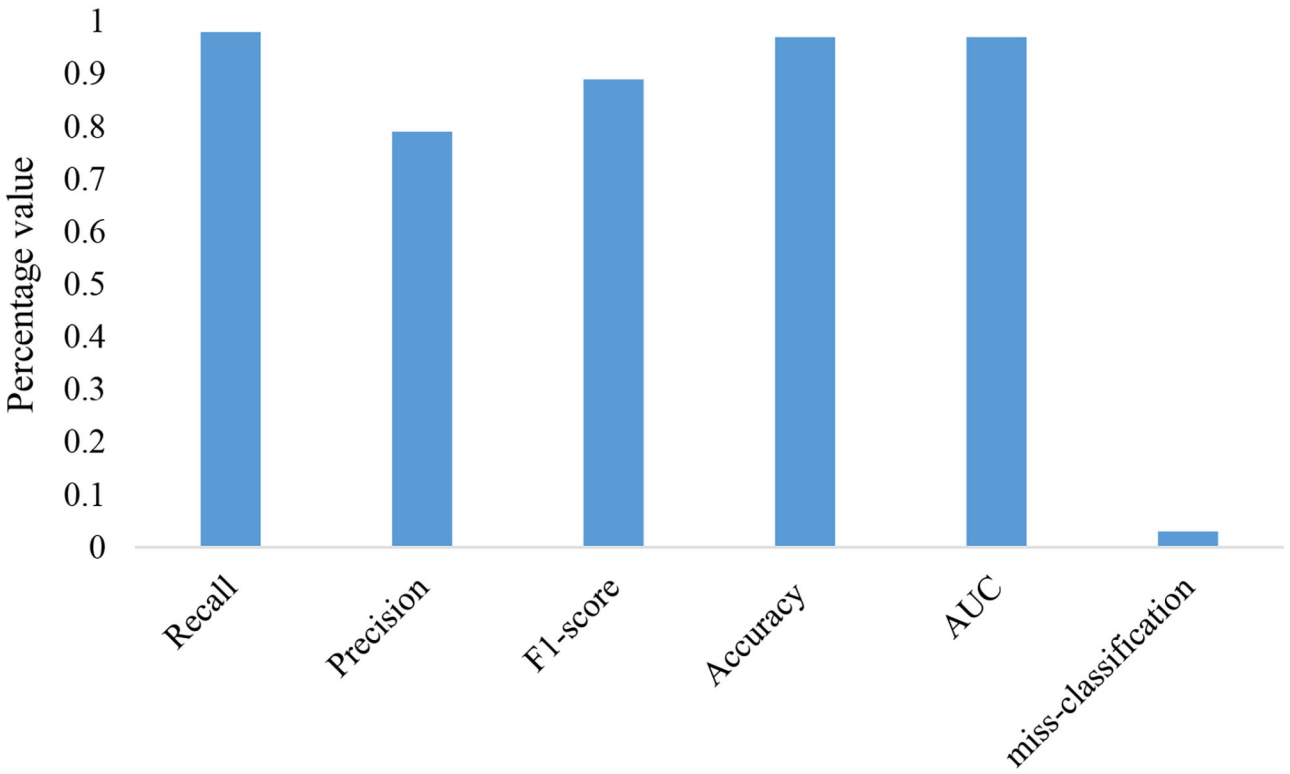

FIGURE 8 | Evolution of the proposed research model.

SVM-based severity analysis. This high accuracy rate reflects the applicability of the formulated research model in this research domain and it ultimately shows that if a patient has cardiac issues, asthma, or diabetes, then the patient has a high risk of mortality and needs proper treatment and high attention of the caretaker.

Other performance metrics such as F-score, misclassification rate, precision, recall, and other are used for evaluation purposes and the corresponding results are given in **Figure 8**. The small misclassification rate reflects the applicability of our model.

For performance validation purposes, different state of the art models are suggested for testing the applicability of the formulated research study in the targeted research domain. A list of these models is given below:

- **ResNet**—residual network or in short ResNet is the modified version of the CNN architecture extensively used for image classification and recognition purposes in diverse domains, including hyperspectral image classification (29) and digital image-based steganalysis (30). Keeping in view these applications of the ResNet, the recognition capabilities of the targeted research study are tested with the ResNet classifier.
- **CNN 1D Net**—this classification tool is extensively used in the extant for calculating the temporal dependencies and has proven its capabilities in the image classification and recognition domains. The CNN 1D Net is also suggested for validating the performance of the targeted model.
- **DenseNet**—Densely Connected Convolutional Network or Dense Convolutional Network or simply DenseNet is the modified version of the CNN architecture. Recently, it was observed that CNN architectures can be primarily deeper, higher accuracy, and more efficient to train if they comprise shorter connections between the layers closer to the input and the output layers (31). Keeping in view these recognition capabilities, the researchers proposed DenseNet in diverse domains such as computer vision and machine learning applications.

The applicability of the proposed model is compared with these state of the art models using the area under the curve (AUC) values as a performance metric. The higher AUC value for the proposed model shows the usability of the proposed model in the COVID-19 variants diagnosing and identification. The corresponding results are given in **Figure 9**.

Performance capabilities of the formulated research model are also validated using other evaluation and assessment metrics such as F-score, misclassification rate, and accuracy. The corresponding results are given in **Table 4**. From **Table 3**, it is concluded that after evaluating all the models on different performance metrics, our model outperformed by generating the high AUC, accuracy, and other performance values that muse the integrity of the selected research study in the targeted research topic.

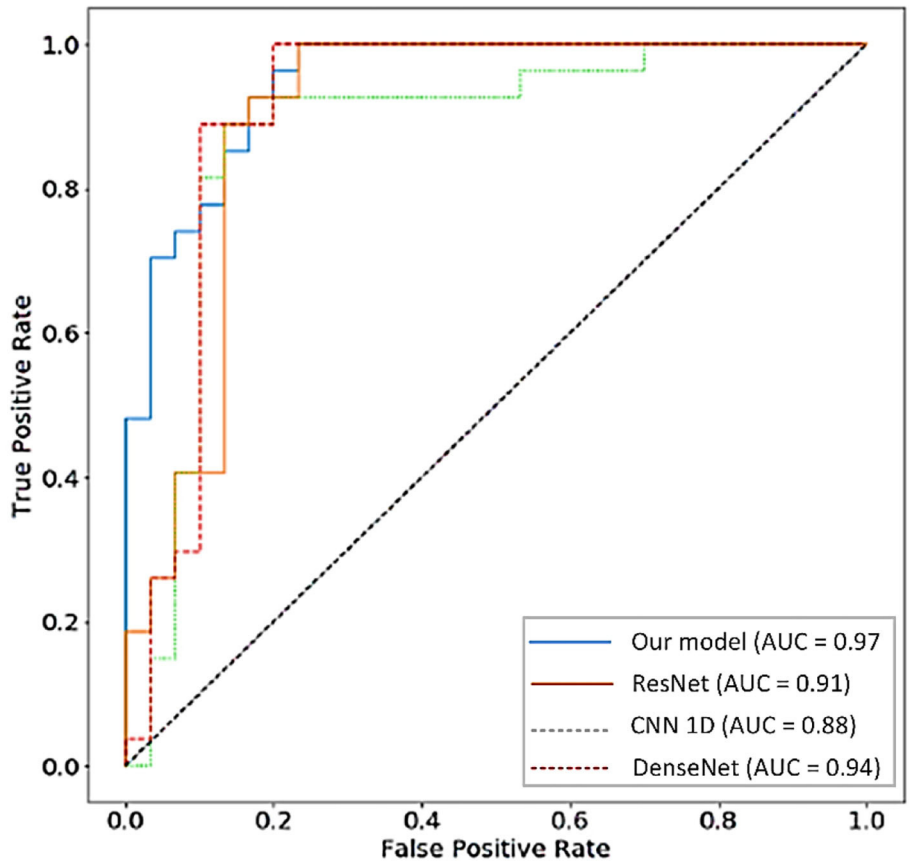

FIGURE 9 | The AUC values-based performance analysis of this research model with convolutional neural network one-dimensional (CNN 1D Net), residual network (ResNet), and Dense Convolutional Network (DenseNet) models.

TABLE 4 | Performance comparison with the targeted classification models.

Techniques	Recall	Precision	F1-score	Accuracy (%)	AUC
ResNet	0.93	0.86	0.90	0.92	0.91
DenseNet	0.93	0.86	0.87	0.95	0.94
CNN 1D Net	0.76	0.82	0.85	0.86	0.88
Proposed model	0.98	0.97	0.94	0.97	0.97

CONCLUSION

At the end of 2019, the emergence of SARS-CoV-2 and its aftermath of different variants such as Delta-type COVID-19 and Omicron puzzled the research community with its distinct symptoms and high mortality capabilities. Researchers around the world affiliated with both the government and nongovernment organizations contributed by developing different diagnosing and identification models for the inspection of COVID-19 and its variants, but most of these models have limitations in the form of time consumption, high implementations costs, capabilities to a specific type of infections, data hunger (performs well if a huge amount of data is available otherwise fails), and many others. In order to tackle this issue, a hybrid deep learning model is produced in this research for the automatic inspection of Delta-type COVID-19. A recognition rate of 97.37% is generated for the automatic identification of Delta-type infection based on the X-ray images. In this hybrid deep learning model, VGG16 and SVM are used for identification and classification purposes. The VGG16 is used for the classification and identification of the infected patients based on the X-ray images, while the SVM is used for the severity-based analysis of the infected patient based on the statistical analysis. These statistical analyses include age, suffering from continuous diseases (diabetes, cardiac issues, and asthma), and physical status.

The applicability of the presented model is tested with other state of architectures suggested by researchers in the proposed domain. These models include CNN 1D Net, DenseNet, and ResNet. The proposed model outperformed using the F-score, the AUC values, accuracy, precision, and misclassification rate as evaluation metrics. The high accuracy, the AUC, F-score, precision, and small misclassification rates compared to the selected state of the art models muse the pertinence of the formulated model in the targeted research

problem. To check the applicability of this model for other variations, two different datasets of COVID-19 (CC-19 and COVID-CT) were selected to test its applicability other than Delta-type infection. The proposed hybrid model proved its applicability by generating high identification rates and it ultimately reflects the adaptability of this model to various types of infection.

IMPLICATIONS

This research study has unlimited applications, especially in evaluating the severity of a certain infected patient. This severity-based analysis will help the caretakers and practitioners to provide healthcare facilities to the severe patient on an emergency basis to restrict high mortalities. The proposed model can be easily implemented and installed in hospitals, medical stores, and other healthcare centers to perform automatic diagnosing based on X-ray images.

DATA AVAILABILITY STATEMENT

The original contributions presented in the study are included in the article/supplementary material, further inquiries can be directed to the corresponding author.

AUTHOR CONTRIBUTIONS

HK: concept, data collection, and project supervision. SK: methodology and writing. SN: discussion and analysis. All authors contributed to the article and approved the submitted version.

FUNDING

This research work is supported by Qatar National Library and Qatar University Internal Grant No. IRCC-2021-010. The results obtained herein are solely the obligation of the writers.

REFERENCES

1. WHO. *WHO Coronavirus (COVID-19) Dashboard*. Available online at: https://covid19whoint/ (accessed July 18, 2021)
2. Togaçar M, Ergen B, Cömert Z. COVID-19 detection using deep learning models to exploit social mimic optimization and structured chest X-ray images using fuzzy color and stacking approaches. *Comput Biol Med.* (2020) 121:103805. doi: 10.1016/j.compbiomed.2020.103805
3. Alazab M, Awajan A, Mesleh A, Abraham A, Jatana V, Alhyari S. COVID-19 prediction and detection using deep learning. *Int J Comput Inform Syst Ind Manag Rev Appl.* (2020) 12:168–81.
4. Ismael AM, Sengür A. Deep learning approaches for COVID-19 detection based on chest X-ray images. *Expert Syst Appl.* (2021) 164:114054. doi: 10.1016/j.eswa.2020.114054
5. Chang YC, Liu AS, Chu WC. Using Deep learning algorithms in chest X-ray image COVID-19 diagnosis. In: *2021 IEEE 3rd Eurasia Conference on Biomedical Engineering, Healthcare and Sustainability (ECBIOS)* (Tainan, Taiwan), (2021). p. 74–6.
6. Karhan Z, Akal F. Covid-19 classification using deep learning in chest X-ray images. In; *2020 Medical Technologies Congress (TIPTEKNO)* (Antalya, Turkey), (2020).
7. Khan AA, Shafiq S, Kumar R, Kumar J, Haq AU. H3DNN: 3D deep learning based detection of COVID-19 virus using lungs computed tomography. In; *2020 17th International Computer Conference on Wavelet Active Media Technology and Information Processing (ICCWAMTIP)* (Chengdu, China), (2020). p. 83–186.
8. Anwar T, Zakir S. "Deep learning based diagnosis of COVID-19 using chest CT-scan images," in *2020 IEEE 23rd International Multitopic Conference (INMIC)*. (2020):1-5. doi: 10.1109/INMIC50486.2020.9318212
9. Jain R, Gupta M, Taneja S, Hemanth DJ. Deep learning based detection and analysis of COVID-19 on chest X-ray images. *Appl Intell.* (2021) 51:1690–700. doi: 10.1007/s10489-020-01902-1
10. Rehman A, Saba T, Tariq U, Ayesha N. Deep learning-based COVID-19 detection using CT and X-ray images: current analytics and comparisons. *IT Professional*. (2021) 23:63–8. doi: 10.1109/MITP.2020.3036820
11. Chandra TB, Verma K, Singh BK, Jain D, Netam SS. Coronavirus disease (COVID-19) detection in Chest X-Ray images using majority voting based classifier ensemble. *Expert Syst Appl.* (2021) 165:113909. doi: 10.1016/j.eswa.2020.113909
12. Holshue ML, DeBolt C, Lindquist S, Lofy KH, Wiesman J, Bruce H, et al. First case of 2019 novel coronavirus in the United States. *N Engl J Med.* (2020) 382:929–36. doi: 10.1056/NEJMoa2001191
13. Hui DS, Azhar E, Madani TA, Ntoumi F, Kock R, Dar O, et al. The continuing 2019-nCoV epidemic threat of novel coronaviruses to global health - the latest 2019 novel coronavirus outbreak in Wuhan, China. *Int J Infect Dis.* (2020) 91:264–6. doi: 10.1016/j.ijid.2020.01.009
14. Rothe C, Schunk M, Sothmann P, Bretzel G, Froeschl G, Wallrauch C, et al. Transmission of 2019-nCoV infection from an asymptomatic contact in Germany. *N Engl J Med*. (2020) 382:970–71. doi: 10.1056/NEJMc2001468
15. *World Health Organization (WHO).* Available online at: https://www.cnbc.com/2021/11/26/who-labels-newly-identified-covid-strain-as-omicron-says-its-a-variant-of-concern.html (accessed November 30, 2021).
16. Khan S, Nazir S, García-Magariño I, Hussain A. Deep learning-based urban big data fusion in smart cities: towards traffic monitoring and flow-preserving fusion. *Comput Electr Eng.* (2021) 89:106906. doi: 10.1016/j.compeleceng.2020.106906
17. Khan S, Nazir S, Khan HU. Smart object detection and home appliances control system in smart cities. *Comput Mater Continua*. (2021) 67:895–915. doi: 10.32604/cmc.2021.013878
18. Das AK, Ghosh S, Thunder S, Dutta R, Agarwal S, Chakrabarti A. Automatic COVID-19 detection from X-ray images using ensemble learning with convolutional neural network. *Pattern Anal Appl.* (2021) 24:1111–24. doi: 10.1007/s10044-021-00970-4
19. Wang L, Lin ZQ, Wong A. Covid-net: A tailored deep convolutional neural network design for detection of covid-19 cases from chest x-ray images. *Sci Rep.* (2020) 10:1–12. doi: 10.1038/s41598-020-76550-z
20. Qiao Z, Bae A, Glass LM, Xiao C, Sun J, FLANNEL. (focal loss based neural network ensemble) for COVID-19 detection. *J Am Med Inform Assoc.* (2021) 28:444–52. doi: 10.1093/jamia/ocaa280
21. Salman FM, Abu-Naser SS, Alajrami E, Abu-Nasser BS, Alashqar BA. Covid-19 detection using artificial intelligence. *Int. J. Eng. Res.* (2020) 4:18–25.
22. Loey M, Smarandache F, Khalifa NEM. Within the Lack of Chest COVID-19 X-ray dataset: a novel detection model based on gan and deep transfer learning. *Symmetry*. (2020) 12:651. doi: 10.3390/sym12040651
23. Dhiman G, Kaur A, STOA. A bio-inspired based optimization algorithm for industrial engineering problems. *Eng Appl Artif Intell.* (2019) 82:148–74. doi: 10.1016/j.engappai.2019.03.021
24. Dhiman G, Kumar V. Spotted hyena optimizer: a novel bio-inspired based metaheuristic technique for engineering applications. *Adv Eng Softw*. (2017) 114:48–70. doi: 10.1016/j.advengsoft.2017.05.014
25. Kaur S, Awasthi LK, Sangal AL, Dhiman G. Tunicate swarm algorithm: a new bio-inspired based metaheuristic paradigm for global optimization. *Eng Appl Artif Intell.* (2020) 90:103541. doi: 10.1016/j.engappai.2020.103541
26. Sahlol AT, Yousri D, Ewees AA, Al-qaness MAA, Damasevicius R, Elaziz MA. COVID-19 image classification using deep features and fractional-order marine predators algorithm. *Sci Rep*. (2020) 10:15364. doi: 10.1038/s41598-020-71294-2

27. Jehangir S, Khan S, Khan S, Nazir S, Hussain A. Zernike moments based handwritten pashto character recognition using linear discriminant analysis. *Mehran University Res J Eng Technol.* (2021) 40:152–9. doi: 10.22581/muet1982.2101.14
28. Khan S, Hafeez A, Ali H, Nazir S, Hussain A. Pioneer dataset and recognition of handwritten pashto characters using convolution neural networks. *Meas Control.* (2020) 53:2041–54. doi: 10.1177/00202940209 64826
29. Zhong Z, Li J, Luo Z, Chapman M. Spectral–spatial residual network for hyperspectral image classification: a 3-D deep learning framework. In; *IEEE Transactions on Geoscience and Remote Sensing*. (2017). p. 847–58.
30. Boroumand M, Chen M, Fridrich J. Deep residual network for steganalysis of digital images. In; *IEEE Transactions on Information Forensics and Security*. (2018). p. 1181–93.
31. Huang G, Liu Z, Van Der Maaten L, Weinberger KQ. Densely connected convolutional networks. In; *Proceedings of the IEEE Conference on Computer Vision and Pattern Recognition*. (2017). p. 4700–8.

Conflict of Interest: The authors declare that the research was conducted in the absence of any commercial or financial relationships that could be construed as a potential conflict of interest.

frontiers | Frontiers in Energy Research

ORIGINAL RESEARCH
published: 25 July 2022
doi: 10.3389/fenrg.2022.917419

Efficiency Enhancement of Thermophotovoltaic Cells With Different Design Configurations Using Existing Photon Recycling Technologies

Muhammad Usman[1], Ali H. Kazim[1]*, Aqsa Shabbir[2]*, Muhammad Salman Abbasi[1] and Jawad Sarwar[1]*

[1]Department of Mechanical Engineering, University of Engineering and Technology Lahore, Lahore, Pakistan, [2]Department of Electrical Engineering, Lahore College for Women University, Lahore, Pakistan

OPEN ACCESS

Edited by:
Yanwei Hu,
Harbin Institute of Technology, China

Reviewed by:
Meijie Chen,
Central South University, China
Haoran Li,
Northeast Electric Power University, China

***Correspondence:**
Muhammad Usman
usmanme132@gmail.com
Ali H. Kazim
ali.h.kazim@uet.edu.pk
Aqsa Shabbir
Aqsa_shabbir@outlook.com

Specialty section:
This article was submitted to Solar Energy, a section of the journal Frontiers in Energy Research

Received: 11 April 2022
Accepted: 23 May 2022
Published: 25 July 2022

Citation:
Usman M, Kazim AH, Shabbir A, Abbasi MS and Sarwar J (2022) Efficiency Enhancement of Thermophotovoltaic Cells With Different Design Configurations Using Existing Photon Recycling Technologies. Front. Energy Res. 10:917419. doi: 10.3389/fenrg.2022.917419

This work deals with different design configurations using existing photon recycling technologies such as front spectral filters and back surface reflectors (BSRs) to improve the efficiency of the thermophotovoltaic (TPV) cells. On the TPV cell surface, some photons absorb, but some quantity of them is lost due to the interference on the surface. On the other hand, BSR mounted on the backside of the cell reflects all photons which were not absorbed by TPV back to the front side of the cell and the emitter, which leads to the elevated temperature of the cell and more interference on the cell surface. This work aimed to design a configuration of the TPV system model using hybrid photon recycling technologies and to investigate the efficiencies of different TPV cells with numerous factors such as emitter temperature and reflectivity of the spectral filter. The design parameters and configuration of front filters with BSRs are studied under 2500 K temperature of the emitter. It is found that an InGaAs cell with reasonable bandgap energy of 0.72 eV, is the most favorable cell material as its bandgap wavelength (1.68 μm) is closely matched to the peak wavelength (1.65 μm) of the emissions spectra. The results show that the incorporation of magnesium oxide (MgO) spectral filter along with the BSR (R = 1) and the emitter temperature of 2200 K efficiency as high as 35% can be attained. This makes MgO a viable choice in TPV cell system under concentrated solar power plant.

Keywords: thermopholovtaics, photon recycling, thermophotovoltaic, design configuration, spectral filter, back surface reflectors

1 INTRODUCTION

The global energy crisis has increased due to the depletion of natural resources to meet the energy demands of the planet (Coyle and Simmons, 2014). Many countries use fossil fuels such as coal and natural gas, while some others use water and nuclear resources to generate electricity (Cherp et al., 2017; Onifade et al., 2021). Over the centuries, fossil fuels have been used for energy as they are an economical resource to rely on, for energy production. But they come up with the global warming problem which further leads to the problem of sea-level rise, fires, storms, and massive floods. Due to this, there is an increased interest in deploying renewable energy resources to meet the energy

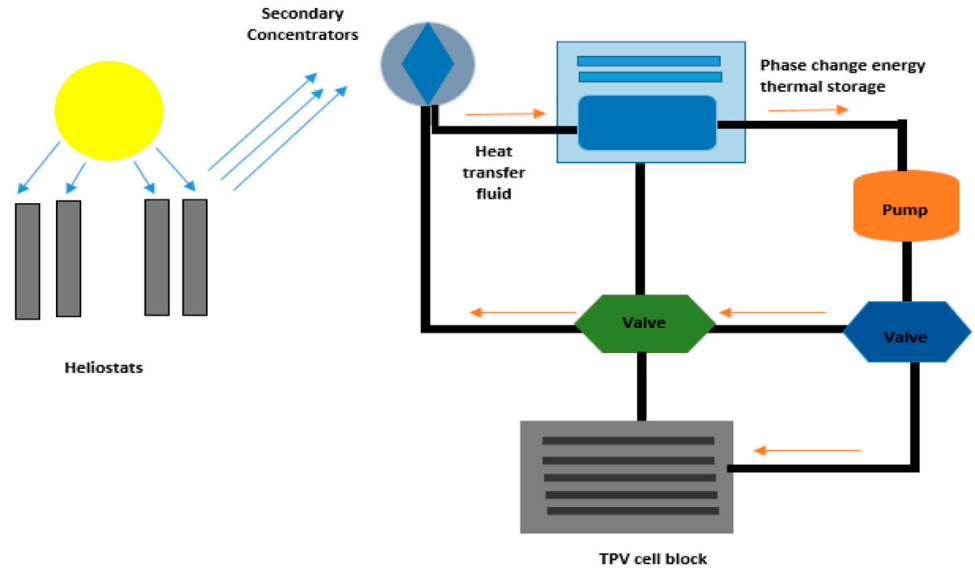

FIGURE 1 | Design of CSP-TPV combined power cycle. Secondary concentrators receive the sun rays through heliostats, which melt the HTF (molten tin, and Sn) and transfer it to the TES where it melts the PCM (silicon, Si). The TPV cell block contains graphite which explains the sun rays incident on the heliostats of the concentrated solar power plant which direct rays toward the secondary concentrators which focus them on the heating tower. In the heating tower, the heat transfer fluid (HTF) changes its phase and then melt the metal to be stored in the thermal energy storage for further use.

demand of the planet instead of relying solely on limited natural resources such as fossils (Romero et al., 2012; Li et al., 2014; Güney, 2019; Hansen et al., 2019). The extreme consumption of these resources is responsible for environmental degradation (Hank et al., 2020). The solution to these problems lies in the fact that renewable energy resources should be used instead of non-renewables for power generation (Hansen et al., 2019). As reported, by 2050, two out of three global energy demands will be met by renewable resources (Goorha and Denemark, 2010).

Wind and solar renewable energy resources are examples of renewable energy resources, but they are not dependable as they depend on weather conditions (Barber, 2018; Jung et al., 2018; Warren et al., 2018; Cendula et al., 2019). However, increased research in the field of renewable energy resources can help overcome this problem (Kazim et al., 2020). Concentrated solar power (CSP) uses focused Sun rays to generate electrical power and is widely used nowadays. Concentrated solar power also faces a lot of the irradiation at their surface due to which efficiency is decreased as irradiation is increased (Chen et al., 2016a). We cannot extract photons from the CSP as they cannot be stored for a longer period (Kazim et al., 2020). Thermophotovoltaics (TPVs) can be used in addition to the CSP, as it converts solar radiation to an intermediate form of energy (Boriskina et al., 2015). TPV is composed of a system that converts the electromagnetic radiation source from a heated body to the electrical power through photovoltaics (Datas and Vaillon, 2021). Renewable energy resources like thermophotovoltaics (TPVs) have emerged over the last decade to replace fossil fuels. Although there are many modern fossil plants that use combined cycle power plants to decrease the heat waste. Current CSP combined cycles have an efficiency of about 35–40% (Henry et al., 2014). TPV conversion of this heat waste into electricity is a promising technology. A TPV technology takes the heat from the heat source of the CSP, and this heat energy is further converted into electrical energy. TPV paired with CSP also utilizes lesser area for equipment (Seyf et al., 2016). TPV has extremely high reliability, low noise, high gravimetric, and long operation time advantages. TPV cells use a variety of heat sources such as chemical, nuclear, solar, and waste heat, which heats up radiators commonly known as emitters whose temperatures go up to 1,300–2,000 K (Nelson, 2003).

A CSP-TPV combined power cycle is shown in **Figure 1** which explains the Sun ray incident on the heliostats of the concentrated solar power plant which direct rays toward the secondary concentrators which focus them on the heating tower. In the heating tower, the heat transfer fluid (HTF) changes its phase and then melts the metal to be stored in the thermal energy storage for further use. The electrical power output, efficiency, and incident radiations of a TPV module are calculated using MATLAB. Secondary sources receive the reflected Sun rays from heliostats. The heat transfer fluid (HTF) heats up via the secondary collectors and goes to the thermal energy storage (TES) where it cools down and gets pumped back to repeat the cycle (Kazim et al., 2020). The schematic diagram in **Figure 2** shows the energy and temperature conversion of the system in which overall flow chart of Sun rays to electrical output is shown. T and Tmelt represent the temperature of the graphite emitter pipes and the temperature of the phase change material (PCM). The TES stores the thermal energy by melting the PCM via the heat of the HTF and maintains the temperature of the HTF that must enter the TPV cycle. Under high partial shading conditions (PSC), the HTF does not attain a temperature high enough to melt the PCM, now when HTF passes from the TES the PCM releases energy and heats up the HTF. Valves are fitted in the

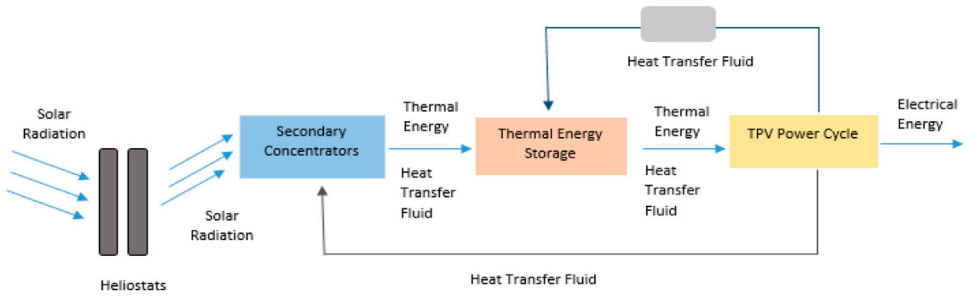

FIGURE 2 | Schematic diagram of a combined CSP-TPV power cycle shows the energy and temperature conversion of the system in which overall flow chart of sun rays to electrical output is shown." The block diagram shows the principle of energy transformation in the discussed configuration of a CSP plant with a TPV power cycle.

system to maintain the unidirectional flow of the HTF as they prevent the HTF from flowing back to the TES and collectors from the TPV power cycle (Kazim et al., 2020). Many other solar thermal conversion and thermal energy storage of phase change composites materials are used such as CuO/paraffin (Chen et al., 2019). The TPV power cycle consists of a hexagonal cell cavity that is surrounded by water and a filter, TPV cells, and a BSR enclosed in a graphite pipe. Graphite has a high emissivity value (>0.90) (Midilli et al., 2006) which makes them a good choice for use in these pipes. Most of the research that has been conducted utilizes the flat vertical plate TPV cell used in between emitter pipes. The hexagonal cavity used as its view factor is the same as that of the circular pipes (Yuksel et al., 2015). The performance of the TPV cells varies with the effect of temperature and radiations wavelengths that fall onto its surface, which is why most of the TPV cell arrays are equipped with spectral controls such as back surface reflectors (BSRs) and spectral filters as most of the emissions from the back body are below the bandgap (Rahmlow et al., 2007). The cell also receives the emission spectrum from the emitter which leads to the feverish temperature of the cell. Filters are used to improve the efficiency by removing any below-bandgap photons from the emission spectra of the emitter. The spectral filters are placed between the emitter and the TPV cell as they filter the photons that are below the bandgap of the TPV cell back to the emitter and let pass the higher bandgap photons as is (Rahmlow et al., 2004; Rahmlow et al., 2007; Chirumamilla et al., 2019). The photons with energy lower than the bandgap of the TPV cell cannot play part in transitions so they are filtered beforehand to reduce any interference at the surface of the cell and to keep the cell temperature lower (Rahmlow et al., 2007). On a TPV cell's surface, photons are absorbed, but some quantity of them is lost due to the interference on the surface. BSR is placed behind the TPV cells (Kazim et al., 2020). BSR mounted on the backside of the cell reflects the unabsorbed photons that are passed unabsorbed from the cell back to the active area of the TPV cell for the reabsorption which helps in increased efficiencies (Datas and Vaillon, 2021). BSR also reflects the below-bandgap photons back to the emitter and the emitter temperature is increased which improves the efficiency of the system (Wang et al., 2003). The specifications of the single-junction InGaAs (McClelland and Mankin, 2018) cells that are used in a TPV array are such that the top contact layer of InGaAs is 0.025 μm thick, which is followed by an emitter layer that is 0.1 μm thick. The other three layers are as follows, the InGaAs base layer, InP buffer layer, and the InP substrate layer which are 2.5, 0.3, and 625 μm thick, respectively (Kazim et al., 2020).

The thermophotovoltaic systems are not much efficient without any spectral control, and they have only a fraction of energy converted to electricity which is 16–18% approximately (Ferrari et al., 2014). There is a potential in improving the conversion efficiencies of TPV systems by optimizing the TPV device's design, design of the cavity, and other fabrication configurations which include the use of multilayer TPV cells, BSRs, and spectral filters (Phan et al., 2009). Wavelength-selective emitters achieve better TPV performance than Ti and Ni filters. The nanoparticle material–based emitters show suitable results with low bandgap PV cells (Chen et al., 2021). It has also been observed with high refractive index materials such as antimony selenide, antimony sulfide, and gallium telluride as a spectral filter in TPV which possibly achieve 20% efficiency at a temperature of 363.15 K for a 0.6 eV band of cell (Rahmlow et al., 2007). The TPV cell of the GaSb cell using the waste heat recovery with the spectral technology of the front filter at the operating temperature of 1,300–3,100 K was found to be 21.57% energy conversion efficiency (Utlu, 2020). Wernsman et al. (2004) calculated the efficiency with the use of the back surface reflector which is 23.6%. Another configuration is used in the back surface reflector which is known as the hybrid back surface reflector GaInAsSb TPV device. In this configuration, the GaInAsSb-based TPV cell is constructed and a surface reflector is mounted on the backside which has the potential of recirculating the infrared photons which further helps to improve the efficiency (Huang et al., 2004). For InGaAs cell of 0.74 eV, the recent study attained more than 15% TPV efficiency which becomes more than 30% with reflectivity of 100% which made TPV favorable for concentrated solar power plants at a temperature of emitter more than 2,000 K (Kazim et al., 2020). The aforementioned techniques are commonly used in TPV to increase efficiency, but up to an extent. There must be further improvements needed to work on TPV as it has significant room for improvements, unlike other solid-state heat

engines which are currently operating at their thermodynamic limits as compared to other heat engines.

This study is based on efficiency enhancement with the combination of spectral controls, that is, the use of spectral filters along with existing photon recycling technologies such as BSR to improve the efficiency of the TPV system beyond 30%. Before this only front filters or back surface reflectors were used to recycle the photons, but in this study, the front filter is used to stop the low bandgap photons which create the interference on the surface of the TPV cell. This technique reduces the interference on the TPV cell which also decreases the temperature reducing the waste heat which is lost in cooling the cell. Furthermore, the use of spectral filters will maintain the temperature of the cell, lesser energy will be utilized for cooling the cells and they also suppress the amount of interference on the surface of the cell by removing lower bandgap photons from the emission spectra and hence achieve better efficiencies than only BSRs (Isobe et al., 2020; Sergeev and Waits, 2020). It also includes the investigation of factors such as EQE, emitter temperature, back surface reflectors, and spectral filters on the efficiency of the TPV cell. **Section 2** includes the materials that can be used for TPV cells, losses in a TPV system, and the use of different spectral control techniques. **Section 3** presents the methodology followed throughout the study, which is followed by **Section 4** which outlines the results and accompanying discussion. **Section 5** concludes the study.

2 THERMOPHOTOVOLTAIC SYSTEMS

2.1 TPV Cell

The photovoltaic cells that are used in a TPV system use single-junction cells, but a multijunction cell can also be used (Datas and Cells, 2015). Many cells are compared in this study, which includes silicon (Si), germanium (Ge), silicon–germanium (SiGe), gallium antimonide (GaSb), indium gallium arsenide (InGaAs), indium gallium arsenide antimonide (InGaAsSb), gallium arsenide (GaAs), cadmium telluride (CdTe) (Midilli et al., 2006). Silicon-based TPV models have been used for many years, as Si has a bandgap of 1.12 eV at 300 K. Si has a single-crystal structure and belongs to the IV group. Ge has the lower bandgap energy of 0.66 eV and their conversion efficiency is 6.7%, these cells show poor performances and are used in multijunction solar converters. BSRs are usually feasible for the Ge cells as their major challenge is the high voltage factor (Kazim et al., 2020). SiGe cells can have an altered bandgap in between the range of 0.66 and 1.12 eV, and this bandgap can be tuned with the change in the composition of the cell (Pethuraja et al., 2012). InGaAs ($In_xGa_{1-x}As$) cells can have a bandgap ranging from 0 to 1 by changing the stoichiometry (i.e., the value of x) of the cells (Cabrera et al., 2018). GaSb cells have a conversion efficiency of 3% which can be improved to 18%. These cells have a bandgap of 0.72 eV and are the best choice for TPV generators. InGaAsSb has the tunable bandgaps and the lattice constants (Midilli et al., 2006) GaAs and CdTe have high absorptivity which allows us to use a layer of only a few microns (Kazim et al., 2020).

2.2 Optical Losses in the TPV System

The efficiency of TPV systems is reduced due to many practical losses, which can be enhanced by improving the components of the system (Seyf et al., 2016). These losses include the thermalization losses (Heidarzadeh et al., 2020) which are caused when the energy in the emission spectra is much higher than the energy of the bandgap and this also results in the heating of the cell. Non-absorption losses occur when the opposite happens, and the bandgap energy is higher than the energy in the emission spectra (Boulkhrachef, 2019). In other words, the emission spectra from the emitter consist of low bandgap photons that cannot take part in transitions and hence generate electrical power (Rahmlow et al., 2007).

These lower bandgap photons also create interference when they collide with the high bandgap photons at the surface of the cell. Due to this interference, much of the useful photon flux passes through the cell and goes without absorption, and energy is lost (Rahmlow et al., 2007). On the other hand, if the cell absorbs these lower bandgap photons they also result in additional heating of the cell and more energy is lost in the cooling of the TPV cell (Rahmlow et al., 2007). The reflective losses occur because photons get reflected from the top layer and due to the large emitter–cell distance they are not reabsorbed, and the transmission losses occur because of the cell's layer thickness (Nicholas and Tuley, 2012; Bernardi et al., 2015). Other losses also include radiative and non-radiative recombination losses which result in the recombination of the generated electron-hole pair and a photon, and a phonon are released, respectively, based on the properties of the cell's material (Yu and Zunger, 2012).

2.3 Photon Recycling

A TPV cell should be paired with photon recycling technologies to minimize the mentioned losses. Photon recycling refers to the methods in which only the photons that can be converted to the useful electrical power are allowed to reach the TPV cell and the non-convertible photons are suppressed and not able to reach the cell's surface (Rahmlow et al., 2007). This is also referred to as spectral control and there are different approaches to control the spectra. The cell should be placed close to the emitter to have the least edge effect and the view factor of nearly 1. The bandgap of a TPV cell should be closely matched to the blackbody radiation of the emitter and the peak wavelength of the spectrum so that a major part of the incoming photon flux is converted to electrical power (Rahmlow et al., 2007). The selective emitters emit the spectrum in a specific wavelength region when they are heated (Sakakibara et al., 2019). The selection of emitter material that allows such suppressive emissions is difficult and should be the cost-effective option. These emitters are composed of photonic crystals and rare earth metals (Sakr et al., 2014; Wang et al., 2014; Zhou et al., 2016a; Kim et al., 2018). Another method for spectral control is to add the filters between the heat source and the cell. The longer wavelength (lower bandgap) photons included in the emission spectra of the emitter, create interference at the cell's surface when they collide with the shorter wavelength (high bandgap) photons, and much of the useful photon flux passes unabsorbed from the cell (Rahmlow et al., 2007) and the temperature of the cell is also increased. Spectral filters do not

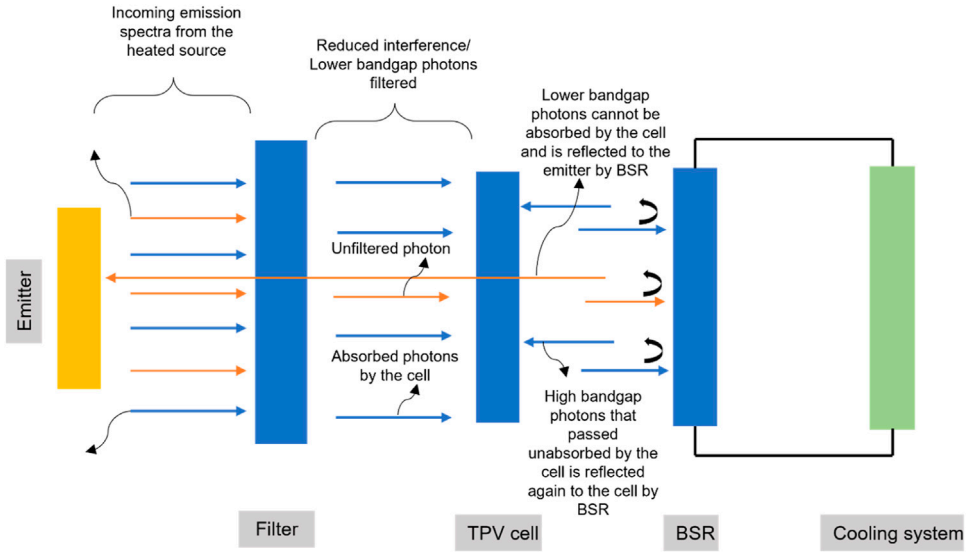

FIGURE 3 | TPV system with hybrid photon recycling technologies includes spectral filter and BSR in which concept of filtering and reflecting photons back to the front side of the TPV cell is explained.

transmit the below-bandgap (long wavelength) photons, from the incoming spectrum, and reflect them back to the heated body (Erdoğar et al., 2010; Chirumamilla et al., 2019). This way the lower energy photons are filtered before reaching the surface of the TPV cell and only high bandgap photons that can play part in transitions reach the cell. There is reduced optical loss due to interference at the surface of the cell and the temperature of the cell is not increased. Hence, less energy is lost in cooling the cell (Rahmlow et al., 2004; Rahmlow et al., 2007; Chirumamilla et al., 2019). The BSR, placed behind the TPV cell, reflects back low and high bandgap photons, that went unfiltered and unabsorbed from the cell, back to the emitter and the front face of the TPV cell, respectively (Kazim et al., 2020; Datas and Vaillon, 2021), which further improves the efficiency of the TPV systems. **Figure 3** shows the schematic of the mentioned procedure and how the incorporation of both the spectral filters and BSRs in a TPV system enhances the number of useful spectra from the emitter. In **Figure 3**, emitters which are graphite rod are shown which emit the radiations and the front spectral filter of MgO which stops the low bandgap photons reaching on the TPV cell front side. The TPV cell is placed in between the front filter and back surface reflector, after the TPV cell back surface reflector is placed which reflects all the unabsorbed radiations back to the TPV front side. The back surface reflector is attached to the backside of the TPV cell which is also mounted with a cooling system which maintains the TPV cell temperature to 300 K.

3 METHODOLOGY

The TPV system including the photon recycling technologies is modeled using MATLAB. The configuration of the TPV system has been made with the basic spectral control technologies, that is , front filters and BSRs. The simulation was run by changing the different cell types such as silicon, germanium, and other cells, varying emitter temperature, and reflectivity of the filters. Then, the efficiency of the TPV cells is calculated and the parameters that influence the improvement of the TPV device's efficiency are concluded. **Figure 4** represents the mentioned procedure in the form of a flow chart which explains the TPV system is modeled using MATLAB which encounters the variables that stop the low bandgap photons from reaching the front surface of the TPV cell, and then BSR variables reflect the unabsorbed photons back to the front side of the TPV cell. In this manner, the efficiency of different cells by varying the emitter temperature and reflectivity of BSR is calculated.

3.1 Cell Selection

The emissions from the graphite emitter are given by the Plank distribution function for the black bodies (Pfiester and Vandervelde, 2017) and the factor ε includes all the defects in the emissions. So, the emissive power E in W/m^2 within a certain wavelength λ band is given by **Eq. 1** (Yuan et al., 2015).

$$E(\lambda, T) = \int_{\lambda_1}^{\lambda_2} \frac{\varepsilon \times C_1}{\lambda^5 \left[e^{\left(\frac{C_2}{\lambda T}\right)} - 1 \right]} d\lambda \tag{1}$$

where $C_1 = 3.742 \times 10^8\ W/m^2\mu m^{-4}$, $C_2 = 1.4388 \times 10^4\ K\mu m$, and T is the temperature of the emitter in kelvin.

Wein's displacement law given by **Eq. 2** gives the value of the wavelength at which the emissive spectra is at its peak.

$$\lambda_P \times T = 2898 \mu m.K \tag{2}$$

The aforementioned equation shows that there is an inverse relationship between the peak wavelength and the emitter temperature. The bandgap wavelength λ_g should be larger than the peak wavelength λ_P. Excessive thermalization losses

FIGURE 4 | Flow chart representing the followed m*ethodology* which represents the mentioned procedure in the form of a flow chart which explains the TPV system is modeled using MATLAB which encounter the variables that stops the low bandgap photons reaching the front surface of TPV cell then BSR variables reflects the unabsorbed photons back to the front side of the TPV cell.

occur if λ_g is very large than λ_P. However, bandgap wavelength λ_g can be found by the bandgap energy of the cell in eV given by **Eq. 3** in the following equation (Anjani, 2021).

$$\lambda_g = \frac{hc}{E_g q} \tag{3}$$

where h is the Planck's constant, c is the speed of light, and q is the charge of an electron in Coulombs. The photons above the bandgap region, which have a wavelength shorter than λ_g, are included in the useful spectrum of the TPV cell. The percentage of energy above the bandgap $\eta_{E>Eg}$ (Bouzid and Dehimi, 2012) is given by the proportion of these photons above the bandgap and is estimated as follows:

$$\eta_{E>Eg} = \frac{E_{(\lambda_{min}\to\lambda_g)}}{E_{b(0\to\infty)}} \times 100\% \tag{4}$$

The total emitted power of the spectrum is calculated as follows, where σ is the Stefan–Boltzmann constant.

$$E_{b(0\to\infty)} = \int_0^\infty \frac{\varepsilon \times C_1}{\lambda^5\left[e^{\left(\frac{C_2}{\lambda T}\right)} - 1\right]} d\lambda = \varepsilon\sigma T^4 \tag{5}$$

3.2 Filter Selection

As stated, it is essential to place an optical filter between the emitter and the TPV cell to enhance the efficiency conversion of the overall system. The filter must have low absorptance and be highly transmissive, and it should be able to transmit the photons that have energy greater than the bandgap energy of the cell ($E_P > E_g$) and hence lies in the useful range.

Similarly, it should have large reflectance for the photons that have energy lower than the bandgap energy of the cell ($E_P < E_g$), as these photons cannot play part in transitions. The filter must have a wide spectral range and high melting points to sustain the incoming heat from the emitter. There are numerous filter technologies involving frequency selective surface (FSS), transparent conducting oxide (TCO), and all-dielectric filters (Bouzid and Dehimi, 2012). FSS are periodic arrays made of conducting oxides deposited on a dielectric substrate. These are band-pass filters and they do not allow the photons above the bandgap energy of the cell (Hristov, 2016). TCOs are also commonly known as plasma filters and these are the doped semiconductors with large bandgaps (Köstlin, 1982; Coutts, 1999). All-dielectric filters, also known as interference filters, are composed of thin layers of materials having different refractive indices (Coutts, 1999). Some filtering technologies also include the use of crystalline or polycrystalline materials for spectral control as listed in **Table 1** (Machrafi, 2012).

Currently, no nanoparticles have the photostability, suitable wavelength transparency, and near-infrared emission specifically for the TPV cell of InGaAs (Khalid et al., 2019). Apart from these properties, the MgO spectral filter is stable under the temperature conditions of up to 2800 K. MgO contributes by filtering the photons up to 0.4 μm. Contrary to this, Y_2O_3 is another suitable choice due to its light composition and wide spectra in wavelength and high temperature resistivity (Zhou et al., 2016b; Lee, 2018).

3.3 BSR Selection

BSRs are placed in the TPV systems behind the cell. They act as spectral control as they reflect back the low bandgap photons back to the emitter and they also help in improving the efficiency of the cell as they increase the intensity of the high bandgap photons at the active layer of the cell for the second pass absorption, that lie in the range of the cell (Wang et al., 2003; Kazim et al., 2020; Datas and Vaillon, 2021). BSRs must have high thermal stability and strong adhesion (Charache et al., 1996). Highly reflective materials with less absorbance, including metals like gold (Au) and silver (Ag) can be used as BSR (Machrafi, 2012; Datas and Cells, 2015; Chen et al., 2016b; Seyf et al., 2016; Karalis and Joannopoulos, 2017).

3.4 Characterization of the TPV System

3.4.1 External Quantum Efficiency

External quantum efficiency (EQE) tells the probability of photons that have been incident on the TPV cell absorbed by the cell and used in generating charge carriers (Ferrari et al., 2014) within the cell. The EQE of the photons with energy below the bandgap energy is zero. EQE is exclusively characteristic of the TPV cell device irrespective of the characteristics of the emitter (Kazim et al., 2020). Ideally, the EQE must be constant and equal to 1 but due to many losses that occur within the cell, radiative and non-radiative recombination losses are among those (Shockley and Queisser, 1961), the EQE shows an irregular behavior (Kazim et al., 2020).

The EQE data of the TPV cell can be determined experimentally or are also provided by the manufacturer of the cell. It is unique for all cells. Such an EQE plot for a 0.25 cm^2 n-p InGaAs cell has been drawn in **Figure 5**, using the experimental data given by Tuley et al. (2012) and the equation mentioned.

TABLE 1 | Crystalline materials used as spectral filters along with their melting points.

Material	Chemical symbol	Melting point (°C)	Temperature for a vapor pressure of 1.33 E-2 Pa (°C)	Transparency range (<pm)
Boron phosphide	BP	1,125 decomp	N/A	0.5–N/A
Barium titanate	$BaTiO_3$	1,625	N/A	N/A
Yttrium aluminum oxide	$Y_3A1_50_{12}$	1,930	N/A	0.2–5
Strontium titanate	SrTiO3	2,080	N/A	0.5–5
Spinel	$MgAl_2O_4$	2,135	N/A	0.2–5
Aluminum oxynitride	$Al_{23}O_{27}N_5$	2,170	N/A	0.2–5
Diamond	C	~3,500	N/A	0.2–3
Zinc selenide	ZnSe	1520	660	0.5–19
Zinc sulphide (wurtzite)	ZnS	1,700	800	0.4–12.5
Silicon nitride	Si_3N_4	1,900	800	N/A
Gallium phosphide	GaP	1,457	920	05–N/A
Lanthanum fluoride	LaE_3	1,493	900	0.1–10
Silicon carbide	SiC	2,830	1000	0.5–4
Magnesium oxide	MgO	2,825	1300	0.4–7
Titanium oxide	TiO_2	1,560–1,843	1,300	0.4–4
Silicon	Si	1,414	1337	1.1–6.5
Sapphire	Al_2O_3	2,054	1,550	0.2–5
Boron nitride	BN	2,967	1,600	0.2–N/A
Aluminum nitride	AIN	3,000	1,750	N/A
Yttria	Y_2O_3	2,439	2,000	0.3–7

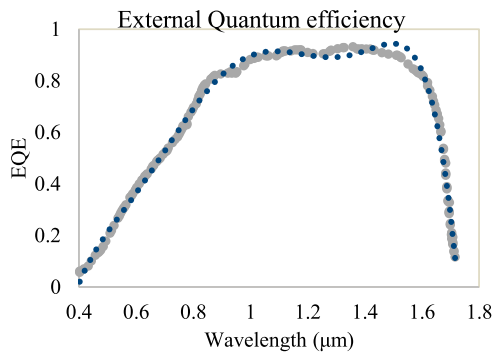

FIGURE 5 | Experimentally measured data and curve of best fit for the 0.25 cm^2 n-p InGaAs cell (Tuley et al., 2012).

$$EQE(\lambda) = -55\lambda^8 + 441.46\lambda^7 - 0.0015\lambda^6 + 0.0029\lambda^5 - 0.0034\lambda^4 + 0.0025\lambda^3 - 0.0011\lambda^2 + 260.91\lambda - 26.89 \quad (6)$$

The average external quantum efficiency $\underline{EQE}$ for the wavelength equal to or smaller than the bandgap wavelength is given as follows:

$$\underline{EQE} = \frac{1}{\lambda_g - \lambda_{min}} \left(\int_{\lambda_{min}}^{\lambda_g} EQE(\lambda).d\lambda \right) \quad (7)$$

where λ_{min} is the shortest wavelength for which the EQE has been recorded. The calculated $\underline{EQE}$ for a 0.25 cm^2 n-p InGaAs cell is 0.7097.

3.4.2 Double Diode Model

The double diode model is equivalent to the TPV system design used here, and it represents the voltage–current behavior of the

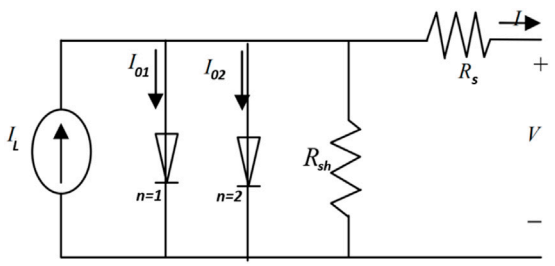

FIGURE 6 | Double diode model equivalent to the TPV system (Jena et al., 2015).

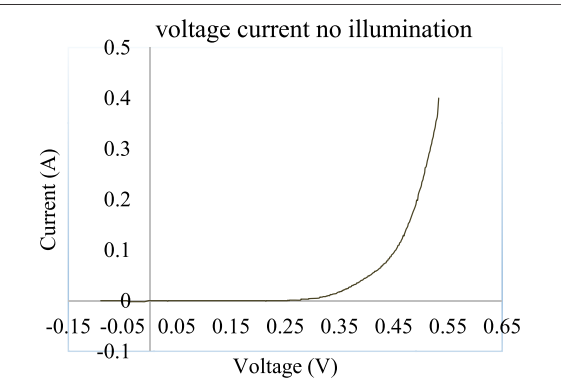

FIGURE 7 | IV characteristics of a 0.25 cm^2 n-p InGaAs cell were recorded in dark Tuley, 2012.

TABLE 2 | Different PV cell materials are compared.

Materials	E_g (eV)	λ_g (μm)	λ_g–λ_p (μm)
InGaAsSb	0.55	2.25	0.60
Ge	0.66	1.88	0.22
GaSb	0.72	1.72	0.07
InGaAs	0.74	1.68	0.02
CIS	1.00	1.24	−0.42
Si	1.12	1.11	−0.55
CdTe	1.50	0.83	−0.83
CGS	1.70	0.73	−0.93

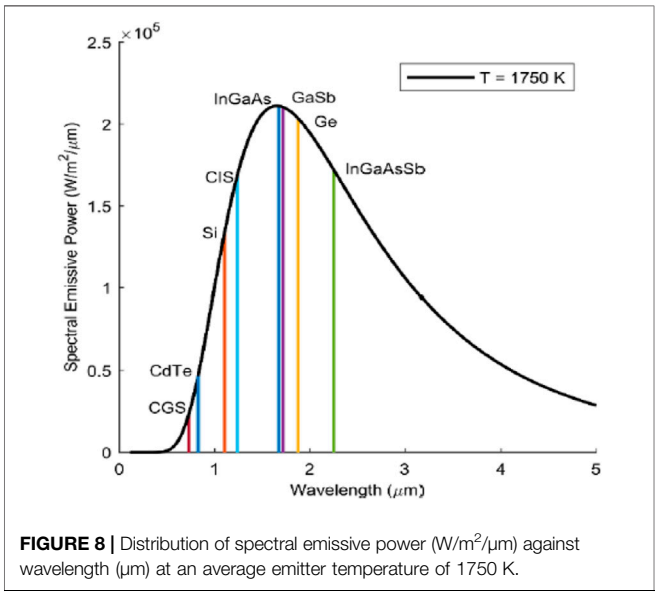

FIGURE 8 | Distribution of spectral emissive power (W/m^2/μm) against wavelength (μm) at an average emitter temperature of 1750 K.

system. The second diode incorporates the recombination losses in the depletion region (Jena et al., 2015). The equation gives the current–voltage characteristics (Hejri et al., 2014) of the model and **Figure 6** represents the circuit diagram for the double diode model.

$$I = I_L - I_{01}\left(e^{\frac{q(V+IR_s)}{n_1 kT_c}} - 1\right) - I_{02}\left(e^{\frac{q(V+IR_s)}{n_2 kT_c}} - 1\right) - \frac{V + IR_s}{R_{sh}} \quad (8)$$

I_L is the photocurrent in ampere, I_{01} and I_{02} are the anti-parallel saturation current of diodes one and two, respectively, n_1 and n_2 are the ideality factors of the diodes one and two taken as 1 (Rißland and Breitenstein, 2013) and 2 (Breitenstein et al., 2013), respectively. T_c is the temperature of the cell in kelvin, k is the Boltzmann constant while, R_s and R_{sh} are the series and shunt resistances, respectively. The shunt resistance must be very much greater than the series resistance in the circuit. Some assumptions are made to simplify **Eq. 8**, which include neglecting -1 from 2nd and third terms, also that R_{sh} is very large due to very high quality of cell fabrication and a large amount of photon injection. So, the simplified equation becomes as follows:

$$I = I_L - I_{01}\left(e^{\frac{q(V+IR_s)}{kT_c}}\right) - I_{02}\left(e^{\frac{q(V+IR_s)}{2kT_c}}\right) \quad (9)$$

3.4.3 The IV Characteristics

The photon flux $\varphi\left(m^{-2}s^{-1}\right)$ (Norton et al., 2015) is the number of photons having energy greater than or equal to the bandgap energy emitted by the emitter per unit time and is given as follows:

$$\varphi\left(m^{-2}s^{-1}\right) = \frac{E_{(\lambda_{min}\to\lambda_g)}}{\left(\frac{1}{(\lambda_{min}+\lambda_g)(10^{-6})}\right)\left(\int_{\lambda_{min}\times 10^{-6}}^{\lambda_g\times 10^{-6}} \frac{hc}{\lambda} d\lambda\right)} \quad (10)$$

The denominator in **Eq. 10** denotes the average energy of photons from the emitter, and wavelengths ranging from λ_{min} to λ_g. I_L is the photocurrent (Midilli et al., 2006) when the TPV device is illuminated and is calculated as follows:

$$I_L = Area\,of\,module \times q \times \varphi \times \underline{EQE} \quad (11)$$

The dark saturation current I_{01} and I_{02} can be found by putting $I_L = 0$, so **Eq. 9** becomes

$$I = I_{01}\left(e^{\frac{q(V+IR_s)}{kT_c}}\right) + I_{02}\left(e^{\frac{q(V+IR_s)}{2kT_c}}\right) \quad (12)$$

The dark saturation currents are calculated by simultaneously solving **Eq. 12** using two sets of measured currents at the voltage values of $0.35\,V$ and $0.41\,V$, under dark conditions.

Figure 7 shows the IV characteristics of a $0.25\,cm^2$ n-p InGaAs cell. I_{01} and I_{02} are found experimentally by putting $R_s = 0.25\,m\Omega cm^2$ and a set of other experimental data recorded in the dark (Tuley et al., 2012). The potential difference across the external circuit when the net current through the external circuit is zero is called as the open-circuit voltage V_{OC}. It can be found by modifying **Eq. 9** as follows (Meyer, 2017):

$$I_L = I_{01}\left(e^{\frac{q(V_{OC})}{kT_c}}\right) - I_{02}\left(e^{\frac{q(V_{OC})}{2kT_c}}\right) \quad (13)$$

Fill factor η_{FF} is the ratio of the product of the V_m and I_m to the product of V_{OC} and I_L. Here to find V_m we compare the theoretical limit η_{FF} formulated by Green et al. (2003) and Shockley and Queisser (1961) given by **Eqs 14**, **15**.

$$\eta_{FF,Green} = \frac{\frac{V_{OC}}{V_c} - ln\,ln\left(\frac{V_{OC}}{V_c} + 0.72\right)}{\frac{V_{OC}}{V_c} + 1} \quad (14)$$

$$\eta_{FF,Shockley} = \frac{\left(\frac{V_m}{V_c}\right)^2}{\left(1 + \frac{V_m}{V_c} - e^{-\frac{V_m}{V_c}}\right) \times \frac{V_{OC}}{V_c}} \quad (15)$$

where V_c is the thermal voltage given as follows:

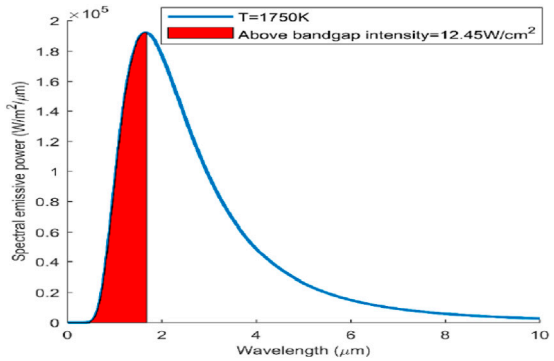

FIGURE 9 | Curve shows the spectral emissive power distribution for a graphite emitter at a temperature of 1750 K, and ε = 0.91. The red shaded region is the emissive intensity, having energy above the bandgap energy (0.74 eV) for an InGaAs TPV cell.

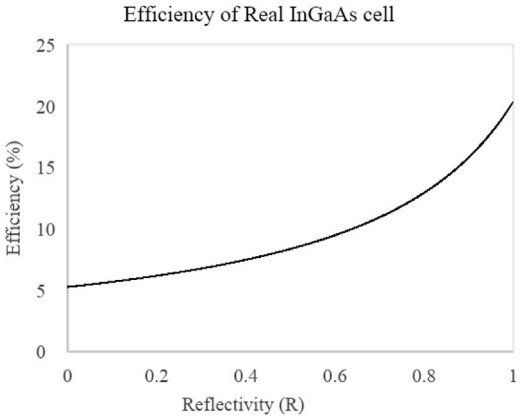

FIGURE 10 | η of a real 0.25 cm^2 InGaAs module (avg EQE = 0.7097) with respect to BSR reflectivity R for an emitter temperature of 1750 K. The efficiency of the module increases with the increasing R.

$$V_c = \frac{kT_{cell}}{q} \tag{16}$$

To find V_m, **Eqs 14**, **15** and solve for unknown V_m

3.4.4 Efficiency of the TPV System

The efficiency of the TPV system which includes back surface reflector and spectral filters with reflectivity R is given as follows (Scranton et al., 2016):

$$\eta = \frac{I_L \times V_m}{\int_0^{\infty} \frac{\varepsilon \times C_1}{\lambda^5\left[exp\,exp\left(\frac{C_2}{\lambda T}\right)-1\right]} d\lambda - \int_0^{\lambda_{Filter}} \frac{\varepsilon \times C_1}{\lambda^5\left[exp\,exp\left(\frac{C_2}{\lambda T}\right)-1\right]} d\lambda - R\int_{\lambda_g}^{\infty} \frac{\varepsilon \times C_1}{\lambda^5\left[exp\,exp\left(\frac{C_2}{\lambda T}\right)-1\right]} d\lambda} \tag{17}$$

The aforementioned relation **Eq. 17** shows how the efficiency of the system varies with the incorporation of photon recycling technologies. The output power of the cell remains the same but the effective energy at the input of the cell is decreased by the factor of the reflectivity of each spectral control technique incorporated. If only BSR is included in the system then the efficiency is enhanced to a certain extent, on the other hand, when filtering technology is incorporated along with the BSR (second term in the denominator), low energy photons are filtered, which further reduces the energy at the input by the factor of reflectivity R of the filter and hence the overall efficiency of the TPV system is enhanced. The efficiency of such hybrid TPV systems will always be greater than the systems which use single technology, that is, either spectral filter or BSR for photon recycling.

4 RESULTS AND DISCUSSION

4.1 Cell Selection Based on Spectral Emissive Power

Table 2 shows different PV cell materials along with their bandgap energy E_g and bandgap wavelength λ_g through **Eq. 3**. Through Wein's displacement law in **Eq. 2** the peak wavelength, λ_p has been calculated as 1.656 μm at the emitter temperature of 1750 K. Lenert et al. (2014) has concluded that for the optimum TPV cell, the bandgap and the peak wavelengths should be well-matched to minimize the thermalization losses and achieve better performances. **Figure 8** compares the useful region of the emissive power above the bandgap for all the materials listed in **Table 2** to the plank's distribution curve for a TPV cell at a constant temperature. The analysis was performed for a single cell and not for the array that is why no mismatch losses are considered and the irradiance is taken as 100% (Kazim et al., 2020).

It can be noted from **Figure 8** that the CGS and CdTe cells have the lowest bandgap wavelengths and hence the lowest spectral emissive power region above the bandgap ($\eta_{E>Eg}$ is 0.377% and 1.01%). Si is the most widely used material in the world of photovoltaics (Saga, 2010) but as can be seen from **Figure 8**, its bandgap wavelength is very much smaller than the peak wavelength and the area of spectral power is not large enough as well ($\eta_{E>Eg}$ = 5.83%). CIS behaves as the Si does. In the case of InGaAsSb (E_g = 0.55 eV)), the bandgap energy is the least, which shows that an exceedingly small amount of energy is needed to generate the electron-hole pair. However, the bandgap wavelength is much higher than the peak wavelength (λ_g-λ_p = 0.6 μm) and this higher bandgap wavelength results in overheating of the cell and thermalization losses (Kazim et al., 2020). Ge, GaSb, and InGaAs have less difference between the bandgap wavelength and Wein's peak wavelength of the emitter, that is, 0.2, 0.07, and 0.02 μm, respectively, and the percentage area above the bandgap are also within the acceptable range (34.44%, 28.17%, and 26.31% respectively). Furthermore, these materials which ($E_g > 0.6\,eV$) need lesser control for Auger recombination and lower series resistances improve the TPV cell performance (Tuley and Nicholas, 2010). GaSb and InGaAs cells have the advantage over Ge (single element) cells in that their bandgaps can be tuned by changing the stoichiometry of these cells. For ternary and quaternary PV cells, as the number of materials increases, the spectral power and efficiency also increase with even lower emitter temperatures (Tong et al., 2015). InP substrates are the lower frequency substrates, they also help in overcoming the lower efficiency of TPV cells. Therefore, the

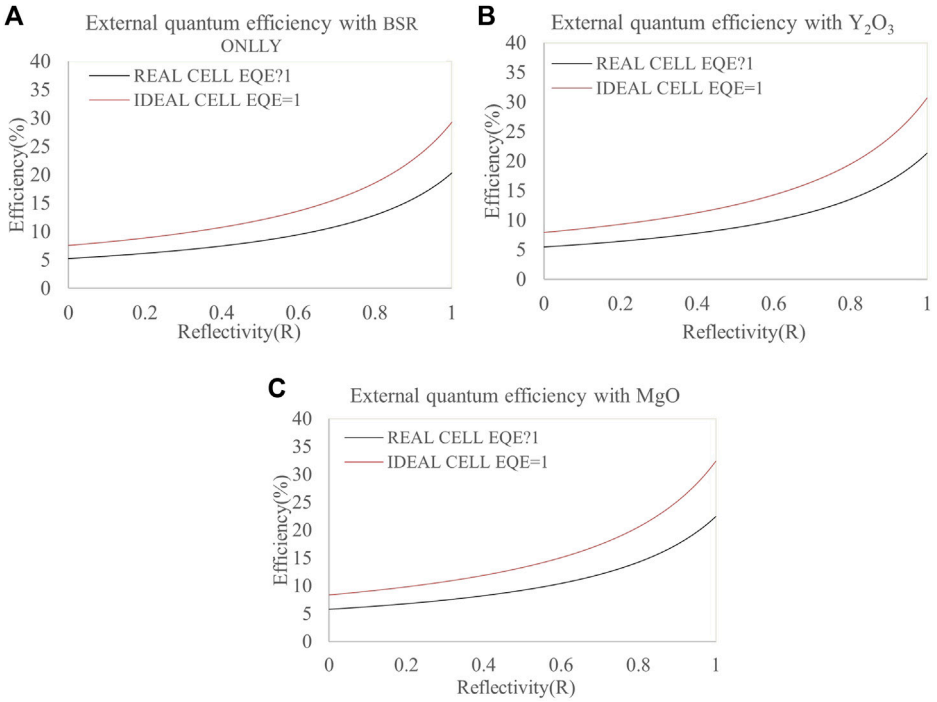

FIGURE 11 | Efficiency of the real TPV module (EQE = 0.709) compared to the ideal TPV module (EQE = 1) for different photon recycling technologies **(A)** EQE with BSR only, **(B)** EQE with Y_2O_3 recorded at an emitter temperature of 1750 K, and **(C)** EQE with MgO.

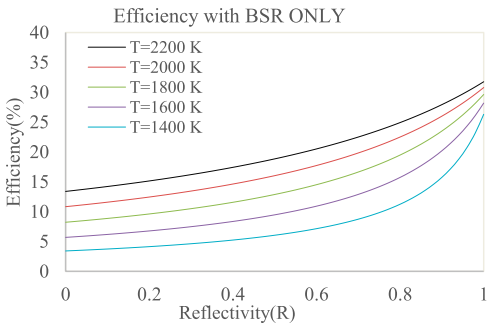

FIGURE 12 | Effect of increasing emitter temperature on the efficiency (η) of a real 0.25 cm^2 InGaAs TPV cell (avg EQE = 0.7097) with respect to the reflectivity R of the BSR. The efficiency of the cell increases with the increasing T.

$In_{0.53}Ga_{0.47}As$ grown on the InP substrate, due to its widely available data reported in the literature and uses in TPV technology, are selected for further analysis (Seyf et al., 2016; Wang et al., 2020).

4.2 Selection of the Filter

The selected filter must have a wide transparency range and high melting point because of the high emitter temperatures. FSS and TCO filters are not used as they are very costly and have high absorption near the plasma frequency, respectively. All-dielectric filters on the other hand show interference among different filter layers and have small wavelength ranges (Machrafi, 2012). Crystalline materials Y_2O_3 and MgO are used for filtering the low bandgap photons from the emission spectra of the emitter since these have a wide transmission range $(0.3 - 7\mu m)$ and $(0.4 - 7\mu m)$, respectively. The photons with longer wavelengths are filtered and the interference at the cell surface is reduced which helps to maintain the temperature of the cell at 300 K as well. The selected materials also have high melting points which help them in sustaining the high amount of heat energy coming from the radiator source. As the efficiency of the cell is the function of temperature and since these filters also act as heat shields and do not allow the conduction of heat from the radiator body to the cell, the cell temperature does not increase (Machrafi, 2012).

4.3 Efficiency of the Real Cell

The $In_{0.53}Ga_{0.47}As$ grown on the InP substrate, the region of the spectral emissive power that is above the bandgap of InGaAs $(E_g = 0.74\,eV)$ is the useful portion for the generation of electron-hole pairs and hence electrical power. For the emitter temperature of 1750 K, the useful emissive power region is as shown in **Figure 9**. For the real module (EQE ≠ 1) the average external quantum efficiency is calculated using **Eq. 7** and found to be 0.7097 (Kazim et al., 2020). The photocurrent I_L for a 0.25 cm^2 module is calculated using **Eq. 11** and is 1.44 A which takes the total number of photons falling on the TPV cell into account. Photocurrent density I_{ph} is 5.79 A/cm^2. **Eq. 12** gives values of the

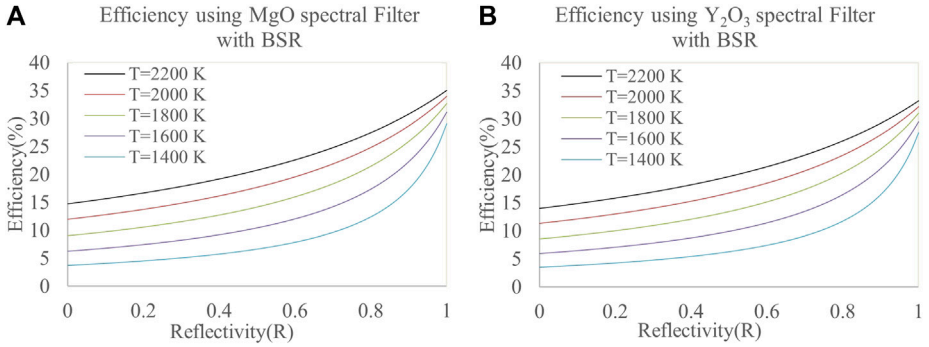

FIGURE 13 | (A) BSR used along with the MgO spectral filter. The efficiency of the module increases with the increasing T. **(B)** Effect of increasing emitter temperature on the efficiency (η) of a real 0.25 cm^2 InGaAs TPV cell (EQE = 0.7097) with respect to the reflectivity R of the BSR used along with the Y_2O_3 spectral filter.

dark saturation currents $I_{01} = 3.22 \times 10^{-9}\ A$ and $I_{02} = 1.83 \times 10^{-5}\ A$ that are found by putting $R_s = 0.25\ m\Omega cm^2$ for an InGaAs cell (Tuley et al., 2012). These values of saturation currents are calculated using the data sets from **Figure 5**. Relations (13–16) are used to determine the values of V_{oc} and V_m, which are 0.51 and 0.43, V respectively. The effect of reflectivity (R) on the efficiency (η) of the TPV cell is shown in **Figure 10**.

As can be seen from the graph in **Figure 10**, the efficiency of the TPV cell with absolutely no reflectivity (R = 0) is exceptionally low, that is, 5.5%. But as the reflectivity is increased to almost 1, the efficiency of the cell at the emitter temperature of 1750 K also increases and reaches almost 20.3% for a real TPV cell.

4.4 Comparison of Efficiency Enhancement Achieved Through This Work Compared to the Previous Studies

4.4.1 The Efficiency of the Real Cell Vs. the Ideal Cell

It has been recorded that the external quantum efficiency can be improved using a cell material that has a high coefficient of absorption (Wang et al., 2020), high reflective coatings at the back of the cell (BSR), and using textured front surface (Ray et al., 2015), using cells with lower bandgap energy that are composed of quantum nanostructures (Datas et al., 2017) and the use of multijunction or tandem cells can also improve the EQE (Moss et al., 2018). In this section, the efficiency of the real TPV cell (EQE ≠ 1) is compared with the ideal one (EQE = 1) with different photon recycling technologies. For the EQE = 1, it is supposed that all the photons that fall on the surface of the TPV cell, are utilized by the cell, and produce electrical power through the external circuit by generating an equal number of electron-hole pairs (Kazim et al., 2020).

For an ideal TPV cell, the saturation currents I_{01} and I_{02} are the same as calculated for the real case scenario. The photocurrent and the photocurrent density are calculated as $I_L = 2.04\ A$ and $I_{ph} = 8.15\ A/cm^2$, respectively. V_{oc} and V_m are 0.52 and 0.44 V, respectively. The efficiencies of the real and ideal TPV module with BSR, with Y_2O_3 as a spectral filter and MgO as filter are compared in **Figure 11**, all recorded at the emitter temperature of 1750 K. **Figures 11A–C** show the existing room for improvement in a real TPV module. An ideal 0.25 cm^2 InGaAs TPV cell (EQE = 1) can attain efficiencies for BSR, Y_2O_3, and MgO as high as 29.2,%, 30.6%, and 32.3%, in contrast to 20.3%, 21.2%, and 22.4% efficiencies of the real TPV cell (EQE = 0.709), at the maximum reflectivity of 1 and an average temperature of 1750K, respectively. It can be seen that the real (EQE = 0.709) and the ideal (EQE = 1) TPV cell which uses MgO filters between the emitter and the cell, attain better efficiencies of 22.4% and 32.3%, respectively. Although compared to the earlier studies which used BSR behind the cell surface reported the efficiencies of 20.3% and 29.2% for the real (EQE = 0.709) and the ideal (EQE = 1) TPV cell, respectively, at 1750 K emitter temperature (Kazim et al., 2020).

4.4.2 Effect of Emitter Temperature on Efficiency

As the temperature of the blackbody emitter is increased, the spectral emissive power and hence the photon flux above the bandgap is also improved which increases the photogenerated current (Machrafi, 2012). Hence, the increasing emitter temperature improves the efficiency of the TPV cell. **Figure 12** shows the performance of the TPV cell with the use of BSR only as the emitter temperature is increased. The efficiency of the cell goes from 26.2% to 31.7% as the temperature is raised from 1400 to 2200 K. **Figures 13A,B** illustrate how the performance of the TPV cell is improved at elevated emitter temperatures as the spectral filters are incorporated along with the BSR with the increasing emitter's temperature. The efficiency of the TPV cell that uses Y_2O_3 spectral filter with BSR at maximum reflectivity, R = 1 (**Figure 13B**) improves efficiency from 27 to 33.2% as the temperature goes from 1400 to 2200 K. Similarly, with MgO as the spectral filter used along with BSR (**Figure 13A**), the efficiency of the cell is further improved from 29 to 35% as the temperature is increased. This increase in the efficiencies is since the low energy bandgap photons and hence the interference at the surface of the cell is reduced with the incorporation of the filter and cell temperature is also maintained at 303 K. Hence, the efficiency of the TPV system is enhanced as the temperature of the emitter is elevated. The previous studies have shown that this increase in efficiency reaches 31.7% at 2200 K emitter

TABLE 3 | Spectral technology–wise efficiency improvement; (η at the emitter temperatures of 1400, 1600, 1800, 2000, and 2200 K).

Temperature (K)	η with only BSR (%)	η with Y_2O_3 (%)	η with MgO (%)
1400	26.3	27.5	29
1600	28.2	29.5	31.1
1800	29.6	31	32.6
2000	30.8	32.2	34
2200	31.7	33.2	35

temperature if only BSR is incorporated in the system (Kazim et al., 2020). However, if hybrid spectral optimization technologies are used, that is, BSR paired with front spectral filters, the efficiencies can be improved even further.

4.4.3 Effect of Different Filtering Technologies on Efficiency

Spectral control technologies have proven to enhance the efficiencies of the current TPV systems. **Figures 14A–E** demonstrate how different photon recycling technologies including BSR, MgO, and Y_2O_3 spectral filters, improve the overall efficiency of the cell at various emitter temperatures. The efficiency values at maximum reflectivity (R = 1), from **Figures 14A–E** are extracted and listed in tabular form in **Table 3**. The crystalline spectral filters are better than the

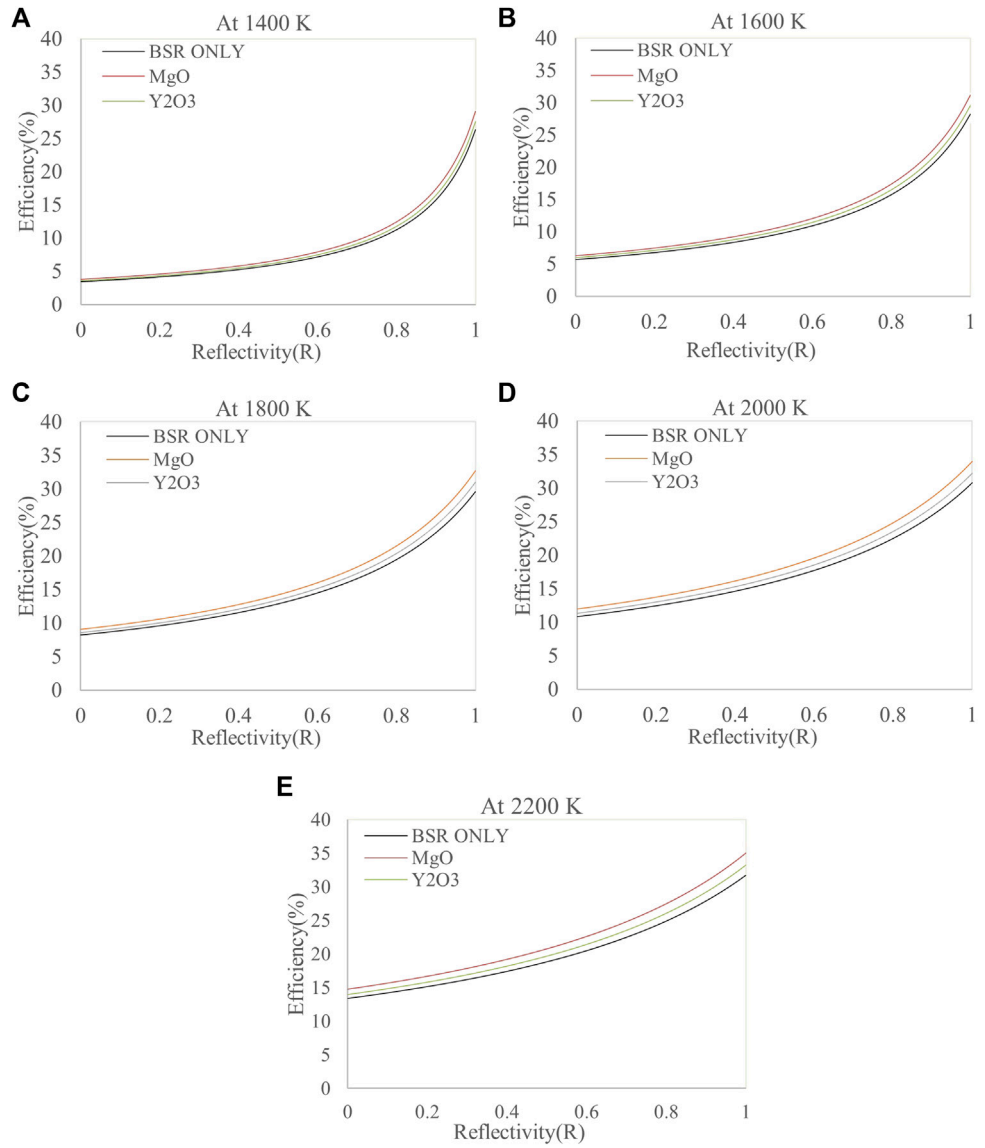

FIGURE 14 | (A–E) Effect on efficiency improvement with BSR Only, Y_2O_3, and MgO spectral filters at the temperatures of 1400, 1600, 1800, 2000, and 2200 K.

BSRs and they can increase the efficiency of the cell much more than BSRs. The MgO spectral filter maximizes the efficiency improvement rather than Y_2O_3. The overall efficiency with MgO is 35% which is more than with the use of BSRs only, that is, 31.7% (Kazim et al., 2020). With MgO as the front filter at 2200 K there is an almost 3.3% efficiency increase while with Y_2O_3 as a filter, this increase is 1.4% more than the previous technique of BSR. This shows that there is quite a room for improvement in the efficiencies of the TPV systems with the incorporation of hybrid spectral controls.

5 CONCLUSION

In this work, the design parameters and configuration of front filters with BSRs are studied under 2500 K temperature of the emitter. It is found that cells with moderate bandgap energy like Ge (0.66 eV), GaSb (0.72 eV), and InGaAs (0.74 eV) are most favorable as their bandgap wavelength is well-matched with the peak wavelength calculated through Wein's law, in addition, they provide lower recombination rates and high photon flux above the bandgap region. It can be concluded that MgO is better than the Y_2O_3 spectral filter because with the use of the MgO front filter at 2200 K there is about a 3.3% efficiency increase while with the Y_2O_3 spectral filter used along with BSR, this increase is 1.4% than the previous technique of using BSR only. The overall efficiency attained with the proposed hybrid technique, that is, the use of MgO as a filter along with BSR, is 35% and this hybrid technique also helps in reducing the interference at the cell surface and maintaining the cell temperature at almost 303 K while acting as a heat shield between the emitter and the cell. Thus, with such improvements in research, TPV has the capability to replace the CSP plant turbine.

DATA AVAILABILITY STATEMENT

The raw data supporting the conclusion of this article will be made available by the authors, without undue reservation.

AUTHOR CONTRIBUTIONS

MU, AK, and AS were involved in experimentation and the other authors helped in data analysis and write up.

SUPPLEMENTARY MATERIAL

The Supplementary Material for this article can be found online at: https://www.frontiersin.org/articles/10.3389/fenrg.2022.917419/full#supplementary-material

REFERENCES

Anjani, N. R. (2021). *The Form of Jakarta-Berlin Paradiplomacy in Sister City Cooperation in the Field of Culture under International Relations*.

Barber, J. (2018). Hydrogen Derived from Water as a Sustainable Solar Fuel: Learning from Biology. *Sustain. Energy Fuels* 2 (5), 927–935. doi:10.1039/c8se00002f

Bernardi, M. P., Dupré, O., Blandre, E., Chapuis, P. O., Vaillon, R., and Francoeur, M. (2015). Impacts of Propagating, Frustrated and Surface Modes on Radiative, Electrical and Thermal Losses in Nanoscale-Gap Thermophotovoltaic Power Generators. *Sci. Rep.* 5 (1), 11626. doi:10.1038/srep11626

Boriskina, S. V., Tong, J. K., Ferry, V., Michel, J., and Kildishev, A. (2015). Breaking the Limits of Optical Energy Conversion. *Opt. Photonics News* 26 (7), 48–51. doi:10.1364/opn.26.7.000048

Boulkhrachef, S. (2019). Higher-Order Sliding Mode Control of a Wind Energy Conversion System. *Nonlinear Dyn. Syst. Theory* 19 (4), 486–496.

Bouzid, F., and Dehimi, L. (2012). Performance Evaluation of a GaSb Thermophotovoltaic Converter. *Rev. Des. Energies Renouvelables* 15 (3), 383–397.

Breitenstein, O., Rißland, S., and cells, s. (2013). A Two-Diode Model Regarding the Distributed Series Resistance. *Sol. Energy Mater. Sol. Cells* 110, 77–86. doi:10.1016/j.solmat.2012.11.021

Cabrera, A., Ramos, A., Artacho, I., Gomez, M., Gavin, K., Martí, A., et al. (2018). "Thermophotovoltaic Efficiency Measurement: Design and Analysis of a Novel Experimental Method," in 2018 Spanish Conference on Electron Devices (CDE) (Salamanca, Spain: IEEE). doi:10.1109/cde.2018.8596820

Cendula, P., Mayer, M. T., Luo, J., and Grätzel, M. (2019). Elucidation of Photovoltage Origin and Charge Transport in Cu2O Heterojunctions for Solar Energy Conversion. *Sustain. Energy Fuels* 3 (10), 2633–2641. doi:10.1039/c9se00385a

Charache, G., DePoy, D. M., Baldasaro, P. F., and Campbell, B. C. (1996). Thermophotovoltaic Devices Utilizing a Back Surface Reflector for Spectral Control. *AIP Conf. Proc.* 358, 339. doi:10.1063/1.49697

Chen, M., Chen, X., Yan, H., and Zhou, P. (2021). Theoretical Design of Nanoparticle-Based Spectrally Emitter for Thermophotovoltaic Applications. *Phys. E Low-Dimensional Syst. Nanostructures* 126, 114471. doi:10.1016/j.physe.2020.114471

Chen, M., He, Y., Huang, J., and Zhu, J. (2016). Synthesis and Solar Photo-Thermal Conversion of Au, Ag, and Au-Ag Blended Plasmonic Nanoparticles. *Energy Convers. Manag.* 127, 293–300. doi:10.1016/j.enconman.2016.09.015

Chen, M., He, Y., Ye, Q., Zhang, Z., and Hu, Y. (2019). Solar Thermal Conversion and Thermal Energy Storage of CuO/Paraffin Phase Change Composites. *Int. J. Heat Mass Transf.* 130, 1133–1140. doi:10.1016/j.ijheatmasstransfer.2018.11.026

Chen, M., He, Y., Zhu, J., and Wen, D. (2016). Investigating the Collector Efficiency of Silver Nanofluids Based Direct Absorption Solar Collectors. *Appl. Energy* 181, 65–74. doi:10.1016/j.apenergy.2016.08.054

Cherp, A., Vinichenko, V., Jewell, J., Suzuki, M., and Antal, M. (2017). Comparing Electricity Transitions: A Historical Analysis of Nuclear, Wind and Solar Power in Germany and Japan. *Energy Policy* 101, 612–628. doi:10.1016/j.enpol.2016.10.044

Chirumamilla, M., Krishnamurthy, G. V., Knopp, K., Krekeler, T., Graf, M., Jalas, D., et al. (2019). Metamaterial Emitter for Thermophotovoltaics Stable up to 1400 °C. *Sci. Rep.* 9 (1), 7241. doi:10.1038/s41598-019-43640-6

Coutts, T. (1999). *Renewable Sustainable Energy Rev*.

Coyle, E. D., and Simmons, R. A. (2014). *Understanding the Global Energy Crisis*. West Lafayette, Indiana, USA: Purdue University Press.

Datas, A., and Cells, S. (2015). Optimum Semiconductor Bandgaps in Single Junction and Multijunction Thermophotovoltaic Converters. *Sol. Energy Mater. Sol. Cells* 134, 275–290. doi:10.1016/j.solmat.2014.11.049

Datas, A., Martí, A., and Cells, S. (2017). Thermophotovoltaic Energy in Space Applications: Review and Future Potential. *Sol. Energy Mater. Sol. Cells* 161, 285–296. doi:10.1016/j.solmat.2016.12.007

Datas, A., and Vaillon, R. (2021). "Thermophotovoltaic Energy Conversion," in *Ultra-High Temperature Thermal Energy Storage, Transfer and Conversion* (Amsterdam, Netherlands: Elsevier), 285–308. doi:10.1016/b978-0-12-819955-8.00011-9

Erdoğar, N., Mungan, A., and Bilensoy, E. (2010). Preparation and Characterization of Cationic Nanoparticles Loaded with Mitomycin C by

Double Emulsion and Ionotropic Gelation Techniques. *J. Control Release* 148 (148), e78–9. doi:10.1016/j.jconrel.2010.07.015

Ferrari, C., Melino, F., Pinelli, M., Spina, P. R., and Venturini, M. (2014). Overview and Status of Thermophotovoltaic Systems. *Energy Procedia* 45, 160–169. doi:10.1016/j.egypro.2014.01.018

Goorha, P. (2010). "Modernization Theory," in *The International Studies Encyclopedia*. Editor R. A. Denemark (Malden, Ma: Wiley-Blackwell).

Green, M. A., Emery, K., King, D. L., Igari, S., and Warta, W. (2003). Solar Cell Efficiency Tables (Version 22). *Prog. Photovolt. Res. Appl.* 11, 347–352. doi:10.1002/pip.499

Güney, T. (2019). Renewable Energy, Non-Renewable Energy and Sustainable Development. *Int. J. Sustain. Dev. World Ecol.* 26 (5), 389–397. doi:10.1080/13504509.2019.1595214

Hank, C., Sternberg, A., Köppel, N., Holst, M., Smolinka, T., Schaadt, A., et al. (2020). Energy Efficiency and Economic Assessment of Imported Energy Carriers Based on Renewable Electricity. *Sustain. Energy Fuels* 4 (5), 2256–2273. doi:10.1039/d0se00067a

Hansen, K., Breyer, C., and Lund, H. (2019). Status and Perspectives on 100% Renewable Energy Systems. *Energy* 175, 471–480. doi:10.1016/j.energy.2019.03.092

Heidarzadeh, H., Rostami, A., and Dolatyari, M. (2020). Management of Losses (Thermalization-Transmission) in the Si-QDs Inside 3C-SiC to Design an Ultra-High-Efficiency Solar Cell. *Mater. Sci. Semicond. Process.* 109, 104936. doi:10.1016/j.mssp.2020.104936

Hejri, M., Mokhtari, H., Azizian, M. R., Ghandhari, M., and Soder, L. (2014). On the Parameter Extraction of a Five-Parameter Double-Diode Model of Photovoltaic Cells and Modules. *IEEE J. Photovoltaics* 4 (3), 915–923. doi:10.1109/jphotov.2014.2307161

Henry, A., Prasher, R., and Science, E. (2014). The Prospect of High Temperature Solid State Energy Conversion to Reduce the Cost of Concentrated Solar Power. *Energy Environ. Sci.* 7 (6), 1819–1828. doi:10.1039/c4ee00288a

Hristov, H. D. (2016). "Fresnel Zone Plate Antenna," in *Handbook of Antenna Technologies* (Berlin, Germany: Springer), 1187–1248. doi:10.1007/978-981-4560-44-3_42

Huang, R. K., Wang, C. A., Connors, M. K., Turner, G. W., and Dashiell, M. (2004). Hybrid Back Surface Reflector GaInAsSb Thermophotovoltaic Devices. *AIP Conf. Proc.* 738, 329. doi:10.2172/836454

Isobe, K., Okino, R., and Hanamura, K. (2020). Spectral Absorptance of a Metal-Semiconductor-Metal Thin-Multilayer Structured Thermophotovoltaic Cell. *Opt. Express* 28 (26), 40099–40111. doi:10.1364/oe.410828

Jena, D., Ramana, V. V., and Reviews, S. E. (2015). Modeling of Photovoltaic System for Uniform and Non-Uniform Irradiance: A Critical Review. *Renew. Sustain. Energy Rev.* 52, 400–417. doi:10.1016/j.rser.2015.07.079

Jung, K. W., Sohn, M. R., Lee, H. M., Yang, I. S., Sung, S. D., Kim, J., et al. (2018). Silver Bismuth Iodides in Various Compositions as Potential Pb-Free Light Absorbers for Hybrid Solar Cells. *Sustain. Energy Fuels* 2 (1), 294–302. doi:10.1039/c7se00477j

Karalis, A., and Joannopoulos, J. D. (2017). Transparent and 'opaque' Conducting Electrodes for Ultra-Thin Highly-Efficient Near-Field Thermophotovoltaic Cells. *Sci. Rep.* 7 (1), 14046. doi:10.1038/s41598-017-13540-8

Kazim, A. H., Asif, M., Nadeem, K., Shoukat, Z., Nazir, R., Malik, M. S., et al. (2020). Efficiency Enhancement of a Thermophotovoltaic System Integrated with a Back Surface Reflector. *IEEE Access* 8, 153226–153239. doi:10.1109/access.2020.3017504

Khalid, A., Norello, R., N. Abraham, A., Tetienne, J.-P., J. Karle, T., W. C. Lui, E., et al. (2019). Biocompatible and Biodegradable Magnesium Oxide Nanoparticles with *In Vitro* Photostable Near-Infrared Emission: Short-Term Fluorescent Markers. *Nanomaterials* 9 (10), 1360. doi:10.3390/nano9101360

Kim, J. M., Park, K. H., Kim, D. S., Hwang, B. Y., Kim, S. K., Chae, H. M., et al. (2018). Design and Fabrication of Spectrally Selective Emitter for Thermophotovoltaic System by Using Nano-Imprint Lithography. *Appl. Surf. Sci.* 429, 138–143. doi:10.1016/j.apsusc.2017.07.300

Köstlin, H. (1982). Application of Thin Semiconductor and Metal Films in Energy Technology. *Adv. Solid State Phys.* 22, 229–254.

Lee, E. (2018). *Synthesis and Luminescence Properties of Bi3+, Yb3+ Co-Doped Y2O3 Phosphor Powder and Thin Film for Application in Solar Cells*. Bloemfontein, SA: University of the Free State.

Lenert, A., Bierman, D. M., Nam, Y., Chan, W. R., Celanović, I., Soljačić, M., et al. (2014). A Nanophotonic Solar Thermophotovoltaic Device. *Nat. Nanotech.* 9 (2), 126–130. doi:10.1038/nnano.2013.286

Li, H., Yu, Y., Niu, F., Shafik, M., and Chen, B. (2014). Performance of a Coupled Cooling System with Earth-To-Air Heat Exchanger and Solar Chimney. *Renew. Energy* 62, 468–477. doi:10.1016/j.renene.2013.08.008

Machrafi, H. (2012). Philosophy for Controlling Auto-Ignition in an HCCI Engine. *Green Energy Technol.* 2012, 323–366. doi:10.2174/978160805285111201010323

McClelland, A., and Mankin, M. (2018). *Optical Measurements for Scientists and Engineers: A Practical Guide*. Cambridge: Cambridge University Press.

Meyer, E. L. (2017). Extraction of Saturation Current and Ideality Factor from Measuring Voc and Isc of Photovoltaic Modules. *Int. J. Photoenergy* 2017, 8479487. doi:10.1155/2017/8479487

Midilli, A., Dincer, I., and Ay, M. (2006). Green Energy Strategies for Sustainable Development. *Energy Policy* 34 (18), 3623–3633. doi:10.1016/j.enpol.2005.08.003

Moss, R. W., Henshall, P., Arya, F., Shire, G. S. F., Eames, P. C., and Hyde, T. (2018). Simulator Testing of Evacuated Flat Plate Solar Collectors for Industrial Heat and Building Integration. *Sol. Energy* 164, 109–118. doi:10.1016/j.solener.2018.02.004

Nelson, R. E. (2003). TPV Systems and State-of-Art Development. *AIP Conf. Proc.* 653, 3. doi:10.1063/1.1539359

Nicholas, R. J., and Tuley, R. S. (2012). Thermophotovoltaic (TPV) Devices: Introduction and Modelling. *Funct. Mater. Sustain. Energy Appl.* 2012, 67–90. doi:10.1533/9780857096371.1.67

Norton, M., Amillo, A. M. G., and Galleano, R. (2015). Comparison of Solar Spectral Irradiance Measurements Using the Average Photon Energy Parameter. *Sol. Energy* 120, 337–344. doi:10.1016/j.solener.2015.06.023

Onifade, S. T., Alola, A. A., Erdoğan, S., and Acet, H. (2021). Environmental Aspect of Energy Transition and Urbanization in the OPEC Member States. *Environ. Sci. Pollut. Res.* 28 (14), 17158–17169. doi:10.1007/s11356-020-12181-1

Pethuraja, G. G., Welser, R. E., Sood, A. K., Lee, C., Alexander, N. J., Efstathiadis, H., et al. (2012). Effect of Ge Incorporation on Bandgap and Photosensitivity of Amorphous SiGe Thin Films. *Mater. Sci. Appl.* 3, 67. doi:10.4236/msa.2012.32010

Pfiester, N. A., and Vandervelde, T. E. (2017). Selective Emitters for Thermophotovoltaic Applications. *Phys. Status Solidi A* 214 (1), 1600410. doi:10.1002/pssa.201600410

Phan, H. T., Caney, N., Marty, P., Colasson, S., and Gavillet, J. (2009). Surface Wettability Control by Nanocoating: The Effects on Pool Boiling Heat Transfer and Nucleation Mechanism. *Int. J. Heat Mass Transf.* 52 (23-24), 5459–5471. doi:10.1016/j.ijheatmasstransfer.2009.06.032

Rahmlow, T. D., Jr, DePoy, D. M., Fourspring, P. M., Ehsani, H., Lazo-Wasem, J. E., and Gratrix, E. J. (2007). Development of Front Surface, Spectral Control Filters with Greater Temperature Stability for Thermophotovoltaic Energy Conversion. *AIP Conf. Proc.* 890, 59. doi:10.1063/1.2711720

Rahmlow, T. D., Jr, Lazo-Wasem, J. E., and Gratrix, E. J. (2004). "New Performance Levels for TPV Front Surface Filters," in , 738, 180. *AIP Conf. Proc.* doi:10.1063/1.1841893

Ray, M. K., Sasmal, S., and Maity, S. (2015). Improvement of Quantum Efficiency and Reflectance of GaAs Solar Cell. *Int. J. Eng. Res. General Sci.* 3 (2), 642.

Rißland, S., and Breitenstein, O. (2013). Considering the Distributed Series Resistance in a Two-Diode Model. *Energy Procedia* 38, 167–175. doi:10.1016/j.egypro.2013.07.264

Romero, M., Steinfeld, A., and Science, E. (2012). Concentrating Solar Thermal Power and Thermochemical Fuels. *Energy Environ. Sci.* 5 (11), 9234–9245. doi:10.1039/c2ee21275g

Saga, T. (2010). Advances in Crystalline Silicon Solar Cell Technology for Industrial Mass Production. *NPG Asia Mater* 2, 96–102. doi:10.1038/asiamat.2010.82

Sakakibara, R., Stelmakh, V., Chan, W. R., Ghebrebrhan, M., Joannopoulos, J. D., Soljacic, M., et al. (2019). Practical Emitters for Thermophotovoltaics: A Review. *J. Photonics Energy* 9 (3), 032713. doi:10.1117/1.jpe.9.032713

Sakr, E. S., Zhou, Z., and Bermel, P. (2014). High Efficiency Rare-Earth Emitter for Thermophotovoltaic Applications. *Appl. Phys. Lett.* 105 (11), 111107. doi:10.1063/1.4895932

Scranton, G., Patrick Xiao, T., Ganapati, V., Holzrichter, J., Peterson, P. F., and Yablonovitch, E. (2016). "Highly Efficient Thermophotovoltaics Enabled by Photon Re-Use," in 2016 IEEE 43rd Photovoltaic Specialists Conference (PVSC) (Portland, OR, USA: IEEE). doi:10.1109/pvsc.2016.7749766

Sergeev, A., and Waits, C. M. (2020). Effects of Photon Recycling, Trapping, and Reuse on Thermophotovoltaic Conversion Efficiency and Output Power. *J. Photonics Energy* 10 (3), 035501. doi:10.1117/1.jpe.10.035501

Seyf, H. R., Henry, A., and Science, E. (2016). Thermophotovoltaics: A Potential Pathway to High Efficiency Concentrated Solar Power. *Energy Environ. Sci.* 9 (8), 2654–2665. doi:10.1039/c6ee01372d

Shockley, W., and Queisser, H. J. (1961). Detailed Balance Limit of Efficiency of P-n Junction Solar Cells. *J. Appl. Phys.* 32 (3), 510–519. doi:10.1063/1.1736034

Tong, J. K., Hsu, W. C., Huang, Y., Boriskina, S. V., and Chen, G. (2015). Thin-Film 'Thermal Well' Emitters and Absorbers for High-Efficiency Thermophotovoltaics. *Sci. Rep.* 5 (1), 10661. doi:10.1038/srep10661

Tuley, R. S., and Nicholas, R. J. (2010). Band Gap Dependent Thermophotovoltaic Device Performance Using the InGaAs and InGaAsP Material System. *J. Appl. Phys.* 108 (8), 084516. doi:10.1063/1.3488903

Tuley, R. S., Orr, J. M. S., Nicholas, R. J., Rogers, D. C., Cannard, P. J., and Dosanjh, S. (2012). Lattice-Matched InGaAs on InP Thermophovoltaic Cells. *Semicond. Sci. Technol.* 28 (1), 015013. doi:10.1088/0268-1242/28/1/015013

Utlu, Z. (2020). Thermophotovoltaic Applications in Waste Heat Recovery Systems: Example of GaSb Cell. *Int. J. Low-Carbon Technol.* 15 (2), 277–286. doi:10.1093/ijlct/ctz049

Wang, C., Murphy, P. G., O'Brien, P. W., Shiau, D. A., Anderson, A. C., Liau, Z. L., et al. (2003). Wafer-Bonded Internal Back-Surface Reflectors for Enhanced TPV Performance. *AIP Conf. Proc.* 653, 473. doi:10.1063/1.1539402

Wang, H., Ye, H., and Zhang, Y. (2014). Preparation and Performance Evaluation of Er2O3 Coating-Type Selective Emitter. *Sci. China Technol. Sci.* 57 (2), 332–338. doi:10.1007/s11431-014-5456-x

Wang, J., Zhang, J., Zhou, Y., Liu, H., Xue, Q., Li, X., et al. (2020). Highly Efficient All-Inorganic Perovskite Solar Cells with Suppressed Non-Radiative Recombination by a Lewis Base. *Nat. Commun.* 11 (1), 177–179. doi:10.1038/s41467-019-13909-5

Warren, E. L., Deceglie, M. G., Rienäcker, M., Peibst, R., Tamboli, A. C., and Stradins, P. (2018). Maximizing Tandem Solar Cell Power Extraction Using a Three-Terminal Design. *Sustain. Energy Fuels* 2 (6), 1141–1147. doi:10.1039/c8se00133b

Wernsman, B., Siergiej, R. R., Link, S. D., Mahorter, R. G., Palmisiano, M. N., Wehrer, R. J., et al. (2004). Greater Than 20% Radiant Heat Conversion Efficiency of a Thermophotovoltaic Radiator/Module System Using Reflective Spectral Control. *IEEE Trans. Electron Devices* 51 (3), 512–515. doi:10.1109/TED.2003.823247

Tuley, R., Orr, J., Nicholas, R., Rogers, D., Cannard, P., and Dosanjh, S. (2012). "Lattice-Matched InGaAs on InP Thermophovoltaic Cells," Semiconductor Science and Technology, 28(1), p. 015013.

Yu, L., and Zunger, A. (2012). Identification of Potential Photovoltaic Absorbers Based on First-Principles Spectroscopic Screening of Materials. *Phys. Rev. Lett.* 108 (6), 068701. doi:10.1103/PhysRevLett.108.068701

Yuan, X., Tavakkoli, F., and Vafai, K. (2015). Analysis of Natural Convection in Horizontal Concentric Annuli of Varying Inner Shape. *Numer. Heat. Transf. Part A Appl.* 68 (11), 1155–1174. doi:10.1080/10407782.2015.1032016

Yuksel, A., Heltzel, A., and Howell, J. R. (2015). Design and Optimization of Thermal Selective Emitters for High-Efficiency Thermophotovoltaic (TPV) Power Generation. *Energy Sustain.* doi:10.1115/es2015-49581

Zhou, Z., Sakr, E., Sun, Y., and Bermel, P. (2016). Solar Thermophotovoltaics: Reshaping the Solar Spectrum. *J. Nanophot.* 5 (1), 1–21. doi:10.1515/nanoph-2016-0011

Zhou, Z., Yehia, O., and Bermel, P. (2016). Integrated Photonic Crystal Selective Emitter for Thermophotovoltaics. *J. Nanophot.* 10 (1), 016014. doi:10.1117/1.jnp.10.016014

Conflict of Interest: The authors declare that the research was conducted in the absence of any commercial or financial relationships that could be construed as a potential conflict of interest.

Publisher's Note: All claims expressed in this article are solely those of the authors and do not necessarily represent those of their affiliated organizations, or those of the publisher, the editors, and the reviewers. Any product that may be evaluated in this article, or claim that may be made by its manufacturer, is not guaranteed or endorsed by the publisher.

NOMENCLATURE

Symbols

C Speed of light [ms^{-1}]

C_1 3.742 × 108 [$W/m\mu m^{-4}$]

C_2 1.4388 × 104 [Kμm]

E Spectral emissive power [W/m^2]

e Exponential constant [2.71828]

E_b (0→∞) Blackbody spectral emissive power [W/m^2]

Eg Bandgap energy [eV]

H Planck's constant [m^2/kgs]

I_{01} Ideal dark saturation current [A]

I_{02} Non-ideal dark saturation current [A]

I_L Photocurrent [A]

I_{ph} Photocurrent density [A/cm^2]

n_1 First diode ideality factor

n_2 Second diode ideality factor

Q Electron charge [1.6 × 10–19C]

R BSR reflectivity

R_s Series resistance [ohm]

R_{sh} Shunt resistance [ohm]

T Temperature of the emitter [K]

T_c Temperature of the TPV cell [K]

V_c Thermal voltage

V_m Maximum voltage [A]

V_{oc} Open-circuit voltage [V]

Greek Symbols

σ Stefan–Boltzmann constant [W/m^2K^4]

ε Emissivity constant

λ Wavelength [μm]

φ Photon flux [W/m^2]

$\eta_E > E_g$ Percentage of photons with energy above bandgap energy of the TPV cell [%]

H TPV conversion efficiency [%]

Subscript and Superscript

C Cell

S Series

S_h Shunt

G Bandgap

O_c Open circuit

S_c Short circuit

Ph Photogenerated

M Maximum

Abbreviations

BSR Back surface reflector

CdTe Cadmium telluride

CSP Concentrated solar power

EQE External quantum efficiency

FF Fill factor

GaAs Gallium arsenide

GaSb Gallium antimonide

Ge Germanium

InGaAs Indium gallium arsenide

InGaAsSb Indium gallium arsenide antimonide

InP Indium phosphide

PV Photovoltaic

Si Silicon

SiGe Silicon–germanium

TES Thermal energy storage

TPV Thermophotovoltaic

frontiers | Frontiers in Energy Research

TYPE Original Research
PUBLISHED 07 September 2022
DOI 10.3389/fenrg.2022.951233

OPEN ACCESS

EDITED BY
Enio Pedone Bandarra Filho,
Federal University of Uberlandia, Brazil

REVIEWED BY
Carolina Beicker,
Federal University of Uberlandia, Brazil
Waqar Ahmed,
University of Technology Malaysia, Malaysia
Ravinder Kumar,
Lovely Professional University, India

*CORRESPONDENCE
M. A. Mujtaba,
m.mujtaba@uet.edu.pk

SPECIALTY SECTION
This article was submitted to Solar Energy,
a section of the journal
Frontiers in Energy Research

RECEIVED 23 May 2022
ACCEPTED 08 August 2022
PUBLISHED 07 September 2022

CITATION
Farhan M, Shahid MI, Jamil F, Usman M, Mujtaba MA, Saleem MW, Nasir Shah S, Saghir S, Yusuf AA, Mousa M and El-Shafay AS (2022), Performance evaluation of compound parabolic solar collector using different nanofluids: An experimental study.
Front. Energy Res. 10:951233.
doi: 10.3389/fenrg.2022.951233

Performance evaluation of compound parabolic solar collector using different nanofluids: An experimental study

Muhammad Farhan[1], Muhammad Ihsan Shahid[1], Furqan Jamil[2], Muhammad Usman[3], M. A. Mujtaba[3]*, Muhammad Wajid Saleem[4], Syed Nasir Shah[5], Shahid Saghir[1], Abdulfatah Abdu Yusuf[6], Mohamed Mousa[7] and A.S. El-Shafay[8,9]

[1]Mechanical Engineering Department, University of Management and Technology, Sialkot Campus, Lahore, Pakistan, [2]Mechanical Engineering Department, University of Wah, Wah Cantonment, Pakistan, [3]Department of Mechanical Engineering, University of Engineering and Technology Lahore, Lahore, Pakistan, [4]Department of Mechanical and Mechatronics Engineering, College of Engineering, Dhofar University Salalah, Salalah, Oman, [5]Energy Engineering Department, University of Engineering and Technology, Taxila, Pakistan, [6]Department of Mechanical Engineering, Kampala International University, Ishaka, Uganda, [7]Electrical Engineering Department, Faculty of Engineering and Technology, Future University in Egypt, New Cairo, Egypt, [8]Department of Mechanical Engineering, College of Engineering, Prince Sattam Bin Abdulaziz University, Alkharj, Saudi Arabia, [9]Mechanical Power Engineering Department, Faculty of Engineering, Mansoura University, Mansoura, Egypt

The article reports an experimental study on a non-tracking compound parabolic collector (CPC) with nanofluid and hybrid nanofluids (NFs). An experimental setup was fabricated having a concentration ratio of 4.17, 0.828 m^2 collector area, 24° of half acceptance angle, and an evacuated tube receiver having 1.85 m length. Fluids like water and NFs have been investigated in CPC performance improvement, but current research deals with NFs and hybrid NFs in a CPC as rare studies are found on a CPC using NFs. The 0.010 and 0.015 wt% concentration were used of nanofluids (NFs) which were silica/water + ethylene glycol (SiO_2)/(H_2O + EG), and hybrid nanofluids of magnesium oxide + carbon black/water (MgO + CB/H_2O) and carbon black + graphene nanoplatelets/water (CB + GNPs/H_2O) at flow rates of 0.020, 0.015, and 0.010 kg/s. The experimentation was performed under real climate conditions of Taxila, Pakistan, and solar irradiance and ambient temperature were measured to determine the performance of the CPC in comparison to a simple base fluid which was water. The experimental results revealed that a maximum temperature difference of 8.5°C with an around thermal efficiency of 38.51% was achieved for hybrid pair of MgO + CB at a flow rate of 0.010 kg/s and volumetric concentration of 0.015 wt%. The efficiency variation using NFs (SiO_2/EG + H_2O) varies from 12.8% to 59.1% from lowest 0.010 kg/s to highest 0.020 kg/s flow rates, and volumetric concentrations (0.010 and 0.015 wt%) of nanoparticles. For similar experimental conditions, efficiency variation for (CB + GNPs) pair varies from 14.2% to 65.6% for aforementioned conditions. Efficiency variation from 15.3% to 66.3% was attained using MgO + CB in the base fluid of water for said flow rates and

volumetric concentrations of nanoparticles. In addition, an efficiency enhancement of 24.3%, 30.8%, and 31.5% was observed for SiO_2/EG + H_2O, CB + GNPs/H_2O, and MgO + CB/H_2O, respectively, at maximum flow rates and volumetric concentration of nanoparticles as compared to water. Therefore, the usage of hybrid-based NF in the CPC is beneficial in terms of efficiency enhancement, and it will bring young research workers to get deep into this field to bring revolution in the area of solar energy.

KEYWORDS

compound parabolic solar collector, hybrid NFs, thermal analysis, efficiency enhancement, solar energy

Introduction

The escalating rate of fossil fuel depletion, global warming, and growing energy demands can be proficiently faced by utilizing solar energy (Tiwari and Tiwari, 2017; Xu and Wang, 2017; Dimri et al., 2018). Solar energy is an abundantly available energy source which can be converted either to electricity (with PV) or to useful heat (with thermal collectors) (Korres and Tzivanidis, 2018; Subramani et al., 2018). A potential design to enhance the efficiency of solar collectors is incorporating the concept of concentration. Compound parabolic collectors (CPCs) are efficient concentrating solar collectors due to their ability for producing hot temperature-based water, and thus, they are mostly suited for domestic hot water applications. Furthermore, even when sun rays do not strike the collector at an optimized angle, they can still maintain water at a high temperature without a tracking system. This reason makes the CPC a potential candidate as a more efficient solar collector for low-temperature applications (Gilani and Hoseinzadeh, 2021). Verma et al. (2018) identified that one of the paramount sources of sustainable energy is solar energy, which is abundantly available in almost all areas in South Asia having a potential of about 2.9 million MW without disturbing the environmental conditions. Ghafoor et al. (2016) analyzed in the country of Pakistan that about 30% of the energy is utilized by the construction sector yearly. Thus, the literature demonstrates the increase in energy utilization to overcome energy demand.

Kim et al. (2013) investigated several residential and industrial practices working in the intermediate temperature (100°C–300°C) range accompanied by various solar thermal collectors. Various daily use applications such as solar stills, extraction of oil, generation of electricity at a small level, textile, and food industry technology mandate energy fonts in the abovementioned low to medium range temperatures. Hachicha et al. (2013) as well as Li et al. (2017) investigated flat plate collectors in a low temperature range, while concentrating ones were considered for the medium temperature range. Bellos and Tzivanidis (2019) analyzed that the CPC is suitable for medium temperature ranges in diverse applications. Snail et al. (1984) and Ayompe et al. (2011) examined a non-tracking CPC with an evacuated tube and found 50% thermal effectiveness and 65% optical performance. Jiang et al. (2020) analyzed the tubular absorber CPC and found that it is efficient, systematic, and diverse especially appropriate for industrial and other medium-temperature applications. Gilani and Hoseinzadeh (2021) investigated CPC advantages over flat plate solar collectors in terms of power production, cost-effectiveness, and CO_2 reduction. Ayompe et al. (2011) and Snail et al. (1984) studied a tracking system with a solar thermal collector and concluded that improvement in the overall efficiency of the system was carried out. Detailed investigation revealed the 15% better results achieved by accompanying the tracking system with solar collectors. Oloketuyi et al. (2020) investigated the hybrid compound parabolic collector (HCPC) both experimentally and mathematically for refrigeration purposes. Numerical results showed that for attaining 70°C–85°C desorption temperature, 350–450 W/m^2 solar radiation intensity was required. Acosta-Herazo et al. (2020) investigated the CPC photoreactor's absorption performance for solar radiation by changing several variables and found the boundary wall of the receiver has a considerable effect on the performance of CPCs. Leong et al. (2018) experimentally investigated copper and titania NFs by varying particle concentrations, surfactants, sonication time, and pH value. PVP surfactants and neutral base fluids exhibited higher values of thermal conductivity at higher volumetric concentrations of nanoparticles in base fluids. Vijayakumar et al. (2021) investigated that by using NFs in CPCs, thermal performance and efficiency of the system enhance significantly. Bhalla and Khullar analyzed to improve the performance and efficiency of solar collectors without a tracking system; non-imaging concentrators along with advanced working fluids can be employed. In the current work, a nanofluid-based receiver is employed in a non-imaging concentrator CPC to enhance the thermal performance of the collector (Bhalla and Khullar, 2021). Harrabi et al. (2021) investigated NFs in different solar collectors and found thermal performance enhancement by the use of NFs. The payback period was reduced by 0.62 years as compared to mineral thermal oil by using 0.3% MWCNT/oil in CPCs.

Hybrid NFs exhibited an increased heat transfer rate owing to enhanced thermal conductivity as compared to simple NFs.

The hybrid NFs have high density, viscosity, and thermal conductivity as compared to the base fluid, but have lower specific heat capacity. Higher thermal conductivity is one of the core advantages of hybrid NFs, but greater viscosity is one of the limitations of hybrid NFs. The product of specific heat capacity and density represents the quantity of heat that fluid can transport. The product is generally high for the hybrid NFs as compared to the base fluid; hence, the NFs are the ideal heat transfer fluid. Takabi and Salehi (2014) investigated hybrid NFs by dispersing nanosized particles of various metals and non-metals in different base fluids. Different thermal properties were obtained by using different volumetric concentrations. Sundar et al. (2014) measured and found that the stability of hybrid NFs in most cases is not exceeding more than 15 days by employing direct and indirect enhancement methods. Toghraie et al. (2016) investigated that by increasing temperature and volumetric concentrations, the thermal conductivity of hybrid NFs increases. Zeng and Xuan (2018) experimentally investigated Ag/SiO_2 and MWCNT's and found that a hybrid of these yielded 5.4% and 1.3% enhanced results than unitary ones of Ag, SiO_2, and MWCNT's correspondingly. Chen et al. (2017) experimentally analyzed ATO-CuO hybrid NFs and found a hybrid of these (99.6% absorption fraction of solar irradiations) and mono of each have 89.8% and 89.5% correspondingly. Solar thermal efficiency of hybrid NFs was 92.5%, whereas NFs have 80.7% and 81.3% correspondingly. Campos et al. (2019) carried out a simulation study and found that a silver and graphene oxide combined unit has 20% greater system efficiency than an individual of each. Amjad et al. (2018) investigated the use of nanofluids in water desalination.

Farajzadeh et al. (2018) investigated a flat plate solar collector (FPSC) experimentally and numerically using Al_2O_3 and TiO_2 NFs, and found efficiency enhancement of 19% and 21% correspondingly. Under similar experimental conditions, a hybrid of Al_2O_3 and TiO_2 yielded a 26% efficiency enhancement. Amjad et al. (2017a) investigated steam production by using gold-based nanofluids. Bellos and Tzivanidis (2018) experimentally investigated a parabolic trough collector (PTC) by using mono (Al_2O_3/Oil and TiO_2/Oil) and hybrid NFs (Al_2O_3 + TiO_2/Oil). Hybrid NFs enhanced 0.74% efficiency, and mono of each enhanced 0.34% and 0.341% correspondingly under similar experimental conditions. Chen et al. (2016) investigated the photothermal conversion efficiency of mono (Au, Ag in water) and hybrid (Au + Ag)/H_2O NFs and found that hybrid NFs have nearly 30.97% efficiency than mono ones (11.90% + 19.01%) correspondingly. Menbari et al. (2017) experimentally analyzed Al_2O_3 + CuO/water in a direct absorption solar collector (DASC) and found that enhancement in efficiency by hybrid nanofluid is higher than that in NFs under similar experimental conditions. Qamar et al. (2021) investigated the dispersion stability of ZnO-based nanofluids. The performance of solar collectors has been thoroughly investigated by varying solar collector materials under similar climatic conditions by Belkhode et al. (2021). Ahmadi et al. (2021) performed energy and exergy analysis on Agro-product drying technologies powered by solar energy. Discussion on applications of tracked and non-tracked solar thermal collectors and their limitations were also discussed by Ahmadi et al. (2020). Amjad et al. (2017b) studied the effect of hybrid nanofluids in direct absorption. Khalil et al. (2020) investigated the performance of hybrid nanofluids in parabolic trough collectors. The summary of various hybrid NFs in different applications is summarized in Table 1.

Several studies have been (Chen et al., 2016; Menbari et al., 2016; Toghraie et al., 2016; Amjad et al., 2017a; Amjad et al., 2017b; Chen et al., 2017; Menbari et al., 2017; Amjad et al., 2018; Bellos and Tzivanidis, 2018; Farajzadeh et al., 2018; Wang et al., 2018; Zeng and Xuan, 2018; Campos et al., 2019; Ahmadi et al., 2020; Khalil et al., 2020; Ahmadi et al., 2021; Belkhode et al., 2021; Qamar et al., 2021) carried out in the literature on the use of hybrid NFs in various solar collectors for efficiency improvements. Critical analysis of the literature reveals that numbers of studies are available for parabolic collectors using different NFs in various solar collectors, but the rare study was found on CPCs using hybrid-based NFs. Therefore, in the present work, the solar CPC system is experimentally investigated with SiO_2/H_2O + EG nanofluids and hybrid NFs of MgO + CB/H_2O and CB + GNPs/H_2O. Nanofluids and hybrid NFs at two different volumetric concentrations and three different mass flow rates are experimentally analyzed in the current work, and a comparison is done with base fluid water in order to measure the enhancement of CPC efficiency. Thus, this research will attract young research workers who are working on the thermal management of CPC. An experimental investigation will be carried out by keeping in view objectives like the selection and preparation of nanoparticles and their potential evaluation in CPC setups under real climatic conditions.

Preparation of nanofluids and hybrid nanofluids

In the preparation of NFs and hybrid NFs, stabilization of nanoparticles in the respective base fluid is always a difficult task owing to the presence of cohesive and van der Waals forces. In several studies, a two-step method was used for NF preparation in which particle preparation and dispersion in base fluid were carried out separately. To avoid the sedimentation of nanoparticles, several additional techniques like ultrasonication, surfactant addition, and high-pressure homogenization may be adopted (Babar and Ali, 2019). Suresh et al. (2011) used a two-step method to prepare Al_2O_3–Cu/water with various particle concentrations. A specific amount of sodium lauryl sulfate and Al_2O_3–Cu nanoparticles were suspended in the base fluid along with

TABLE 1 Summary of various investigators on various hybrid NFs in different applications.

Hybrid nanoparticles	Base fluid	Concentration of particles	Solar system	Findings	References
Al_2O_3–TiO2	Water	0.1 wt%	FPSC	Hybrid NFs depicted more efficiency enhancement than unitary ones.	Farajzadeh et al. (2018)
Gold–silver	Water	1.75 ppm Au—0.15 ppm Ag	DASC	Photothermal conversion efficiency of hybrid particles is found to be more efficient than that of unitary ones for the same experimental conditions.	Chen et al. (2016)
CuO–γ Al_2O_3	Water, EG	Not fixed	DASC	Hybrid NFs were more efficient than the unitary of any of these in DASC.	Menbari et al. (2016)
Ag–ZnO	Silicone Oil	1.0 mg/ml	DASC	240% photothermal efficiency enhancement was observed in comparison to base fluid for hybrid NFs.	Wang et al. (2018)
Sn–SiO_2–Ag	Water	0.01–0.05 vol%	DASC	By utilizing hybrid NFs, considerable efficiency enhancement was observed as compared to unitary and base fluids.	Zeng et al. (2016)
Co-C/therminol	Therminol	—	DASC	Considerable efficiency enhancement was observed by employing hybrid NFs	Ahmadi et al. (2021)
SiC-PCM	Water	SiC: 0.1% mass fraction	Photovoltaic/ thermal (PV/T)	Thermal efficiency enhancement was observed by employing hybrid NF in PV/T.	Al-Waeli et al. (2017)
Al_2O_3–ZnO	Water	0.5%	PV/T	Exergy and energy efficiency enhancement was observed by utilizing hybrid NFs as compared to NFs.	Younis et al. (2018)
Cu–TiO_2	Water	0.2 wt%	PV/T	5.84% thermal efficiency enhancement was noted as compared to base fluids for the same experimental conditions.	Sathieshkumar, (2018)
Ag–SiO_2–CNT	Water	0.006 wt% (Ag-SiO2) 0.067 wt% CNT	PV/T	Considerable increase in thermal and electrical efficiency observed by incorporating hybrid NFs in PV/T setup.	Hjerrild et al. (2016)
Ag–SiO_2	Water	0.0205 wt%	PV/T	12% increase in energy scattering ability was noted by using hybrid NFs as compared to base fluids.	Crisostomo et al. (2017)
CuO/Sylterm 800	Sylterm 800	5% by volume	CPC	Nanofluid utilization in the system increases the flow heat transfer coefficient by 17.41% and 15.53% for high and low operating temperatures, respectively.	Korres et al. (2019)

TABLE 2 Recent work on various hybrid NFs.

Hybrid nanofluid	Sonication time (h)	Magnetic stirring (h)	Stability (days)	Investigator
Al_2O_3–Ag/water	0.5	—	2	Allahyar et al. (2016)
Cu–TiO_2/water and EG	6	3	7	Esfe et al. (2015)
TiO_2–SiO_2/water and EG	2	1	14	Hamid et al. (2018)
MWCNTs–ZnO/water and EG	3	2	10	Esfe et al. (2017)

ultrasonication to avoid cluster formation. Parsian and Akbari (2018) prepared a hybrid nanofluid of Al_2O_3–Cu/EG using a two-step method. Nanoparticles in a specific amount dispersed in base fluid and the solution was sonicated for 7 h to stabilize the solution, and the solution remained stable for 3 days. The summary of various hybrid NFs studies by various authors is summarized in Table 2.

In this study, various nanosized particles are used in a solar collector system for thermal enhancement. Extremely pure nanosized particles were used which were carbon black, graphene nanoplatelets, and magnesium oxide (shown in Figure 1) that were purchased from Nanostructured and Amorphous Materials, Inc., Houston, United States and Advanced Chemical Supplier Material LLC, Pasadena, CA. The TEM images of the particles are given in Figure 2.

Nanosized particles were mixed with different base fluids in different ways. The method used to prepare NFs and hybrid NFs was a two-step method. At the start, a specific concentration of granular nanoparticles was dispersed in base fluids. Homogenizer was used for stirring purposes at 6,000–8,500 rpm; stirring at a higher frequency led to rupturing of grains of nanoparticles to thoroughly blend them into the base fluid. After that, an ultrasonic vibrator was used to break covalent bonds among particles. The sonication of

FIGURE 1
(A) Carbon black NPs, **(B)** graphene nanoplatelets, and **(C)** MgO nanoparticles.

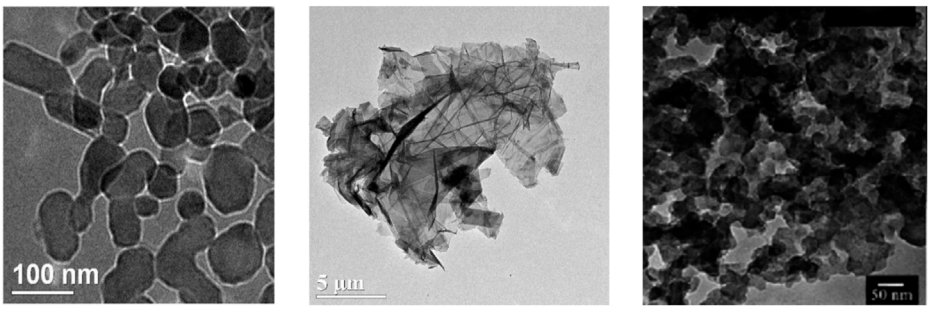

FIGURE 2
TEM image of MgO (left), graphene nanoplatelets (middle), and carbon black (right) (Courtesy: Nanostructured and Amorphous Materials, Inc., Houston, United States; Advanced Chemical Supplier Material LLC, Pasadena, CA, United States).

nanofluid and hybrid NFs reduces the mixture space and thoroughly homogenized it. Sonication of NFs was done for 3–4 (SiO_2/H_2O + EG) hours and 5–6 h for MGO + CB and CB + GNPs for hybrid NFs in the base fluid of water so that the mixture may stabilize.

A simple flow diagram for the preparation of nanofluid and hybrid NFs is illustrated in Figure 3. The prepared NFs and hybrid NFs are shown in Figure 4.

The stability of nanofluid and hybrid nanofluid was thoroughly observed, and no sedimentation of particles was found in 9 days after their preparations. The stable NFs and hybrid nanofluids are shown in Figure 5.

Experimental setup

The experimental setup was installed at the Energy Engineering Department of University of Engineering and Technology, Taxila, Pakistan. For the present experimental setup, the direction of the compound parabolic solar collector was demarcated by the solar pathfinder. The pathfinder identified all directions in a circle dome for the selection of solar collector orientation. It identifies the tree and building shadows, the intensity of radiations, and the direction of the collector along the axes.

The system schematic diagram is shown in Figure 6. It explains the flow of fluids and observation of flow rate by a flow meter and measurement of temperature at the inlet and outlet of CPSC.

Experimental methodology

An experimental study was carried out by using water nanofluids and hybrid NFs, that is, SiO_2 in the hybrid base fluid of water and ethylene glycol, MgO + CB and CB + GNPs in distilled water as base fluid. The experimentation was carried out to check the thermal performance of the compound parabolic collector for real climatic conditions of Taxila, Pakistan. The geographical location of Taxila has a latitude of 33.74°N and a longitude as 72.78°E. NFs and hybrid NFs were prepared by the two-step method *via* using a homogenizer and

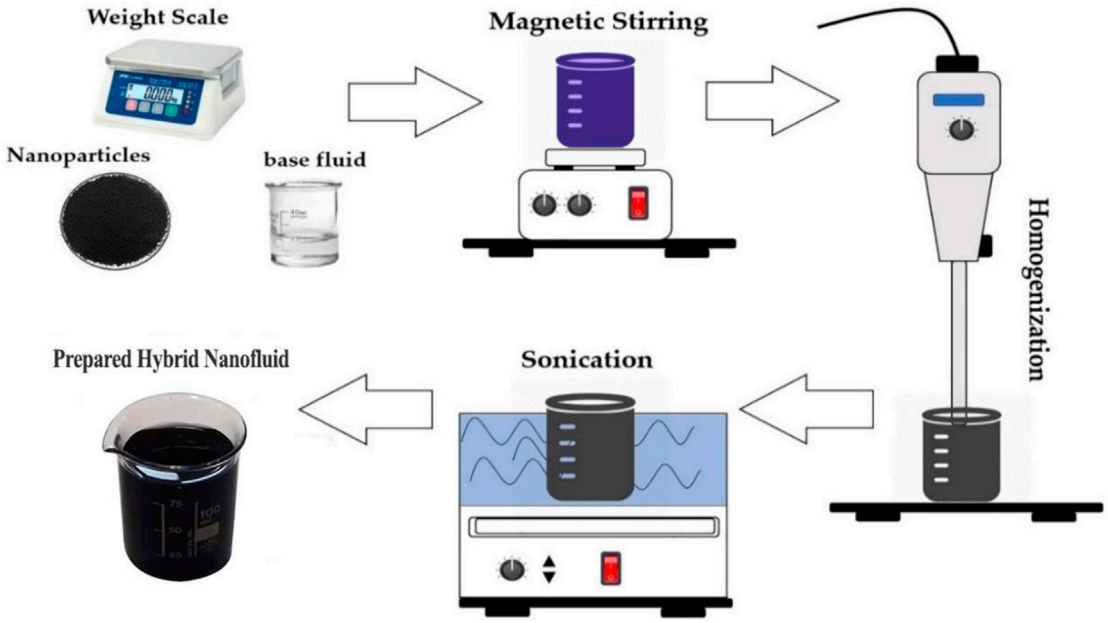

FIGURE 3
Schematic diagram of NFs and hybrid NFs.

FIGURE 4
Prepared NFs and hybrid NFs: **(A)** MgO + CB/water, **(B)** MgO + CB/water, **(C)** SiO_2/water + EG, **(D)** SiO_2/water + EG, **(E)** CB + GNPs, and **(F)** CB + GNPs.

ultrasonic vibrator. The variation in results for both configurations at different flow rates (0.01, 0.015, and 0.020 kg/s) and volumetric concentrations (0.010 and 0.015 wt%) of NFs and hybrid NFs were examined. The experimentation was done in October–November 2020. The time for experimentation was 10:00 a.m. to 3:00 p.m. on a daily

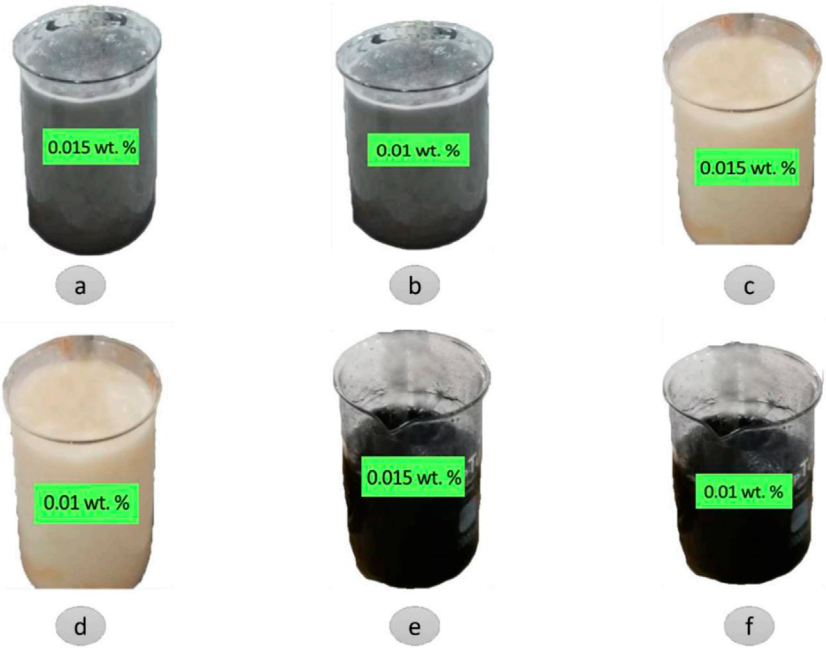

FIGURE 5
Stable NFs and hybrid NFs after 9 days: **(A)** CB + MgO, **(B)** CB + MgO, **(C)** SiO_2/water + EG, **(D)** SiO_2/water + EG, **(E)** CB + GNPs, and **(F)** CB + GNPs.

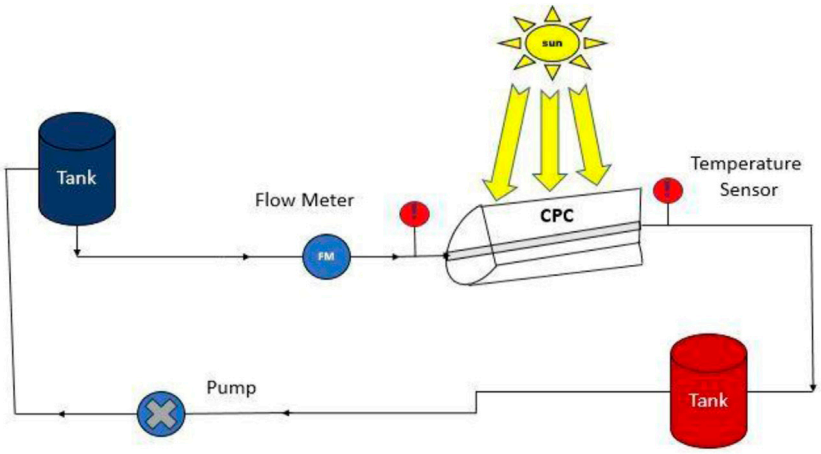

FIGURE 6
System schematic diagram.

basis for moderate weather of Taxila. The experimental setup made of the close loop to examine the thermal efficiency of CPSC setup at some specific properties and operating conditions for water, nanofluids, and hybrid NFs. First, the leakage at every point is tested and the proper flow rate was set. Cold water/NFs/hybrid NFs enter from the pump to the compound parabolic solar collector which heats up water/NFs/hybrid NFs. For steady output, high-temperature water from the collector enters the storage tank. The normal water from the outside of the tank goes toward the source side. In this way, the loop continues. To check the temperatures at the inlet and outlet valves, sensors were installed with great care. The

K-type thermocouples (5 TC-TT-KI-24-2M, Omega United States) having an uncertainty of ±0.1°C were used to measure the temperature. The flow rate for H_2O, NFs, and hybrid NFs is measured by a flow meter installed at the inlet port. A flow rate measuring sensor (OKY3430-0) having a measuring range from 1 to 30 L/min was used to measure the flow rate. Wind velocity was recorded by anemometer with an uncertainty range of 200–3,000 ns. A pyranometer is used to measure hourly solar radiations. A fiber optic temperature sensor is used to measure ambient temperature. After every 15 min, experimental readings are measured, but the hourly values show the average readings. To assure accuracy, values are repeated at the same flow rate and concentrations of fluids for 2 days. As the solar rays reach the compound parabolic collector, it reflects these radiations to a focus line made by the receiver. The angle of incidence for coming radiations is important to reflect maximum solar radiations. The water passes from the inlet valve to the solar collector and removes by the outlet temperature valve. The collector temperature at these two valves is measured by thermometers. The outlet water goes to a hot thermal storage tank for steady flow. Water, NFs, and hybrid NFs are continued in the loop of water heating by the solar system. To avoid consolidation and ensure stability, NFs and hybrid NFs re-blended and homogenized every morning. Energy potential (Q_s), heat gain (Q_u), and thermal efficiency (η_{th}) of CPSC can be calculated by using Eqs 1–3 (Bellos et al., 2016):

$$Q_s = A_a.G_e, \tag{1}$$

where A_a is the area of the absorber tube and G_e is the incident solar irradiance on the collector.

$$Q_u = m.C_p.(T_{out} - T_{in}), \tag{2}$$

where m is the mass flow rate of fluid and C_p is the specific heat capacity of working fluid.

Thermal efficiency (η_{th}) of CPSC can be calculated by using

$$\eta_{th} = \frac{Q_u}{Q_s}, \tag{3}$$

Results and discussion

In this section, the experimentation is carried out for Taxila climate under real conditions. The ambient temperature varies from 22.5°C to 26.8°C. The solar radiations are captured by a pyranometer whose maximum ranges go to 1220 W/m^2, while the collector inlet and outlet temperatures are measured with a fiber optic heat transfer temperature sensor. The experimentation is carried out with four fluids, that is, water, NFs, and two concentrations of hybrid NFs. The timing for experimentation was set as 10: 00 a.m. to 3:00 p.m.

Validation of experimental setup

The accuracy of the experimental setup was validated by comparing the heat gain of CPCs with the published work of Akhtar et al. (2020). Figure 7 represents the comparison b/w current work and published work. Experimentation of the published work was performed in March to May, while current experimentation is conducted in September to November under the real climatic condition of Taxila. The overall pattern of heat gain is similar at a similar flow rate; however, variations in starting, optimum, and ending points are due to seasonal variations.

Climate conditions

The present work basically shows a comparison of the thermal enhancement of nanofluids and hybrid nanofluids as compared to water. As this system is used for low–medium range temperature applications, the average outlet temperature achieved from the collector is 45°C–53°C. From the experimentation, it is concluded that the minimum radiations gained by the ambient condition of Taxila are 4.5 kWh/m^2/day. The average peak hours of weather gave solar radiation as 6.1 kWh/m^2. From the average look of annually solar irradiance, the existing radiation are higher than the minimum requirements for solar potential applications. Figure 8 predicts the environmental conditions of Taxila, Pakistan. The annual trend of the model shows the ambient temperature and wind velocity. The overall impact of temperature changes from 22.5°C to 26.8°C.

The average solar radiation measured through scenarios for 6 h are shown in Figure 9. The intensity of radiation depends upon different factors which reduce its irradiance. The clouds, dust, humidity, and wind velocity are those factors that influence the intensity of radiation. The increase in ambient temperature is roughly proportional to the removal of humidity and high radiations. These climatic parameters affect the solar collector output and system efficiency.

Effect of efficiency with time, flow rate, and concentration of nanoparticles using water nanofluids and hybrid nanofluids

The experimental outcomes conclude that the thermal analysis is mainly dependent on the thermal efficiency attained by the solar thermal collector. Average values taken for figures at similar test conditions are considered. The thermal efficiency indicates the overall performance of the solar thermal collector which directly changes with the intensity of solar radiations. At constant flow rate and weather

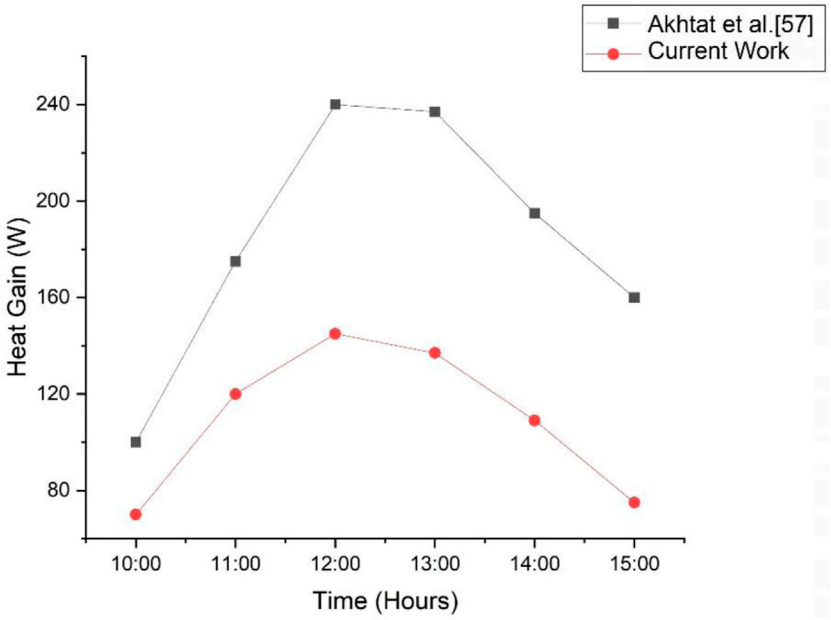

FIGURE 7
Validation of experimental setup.

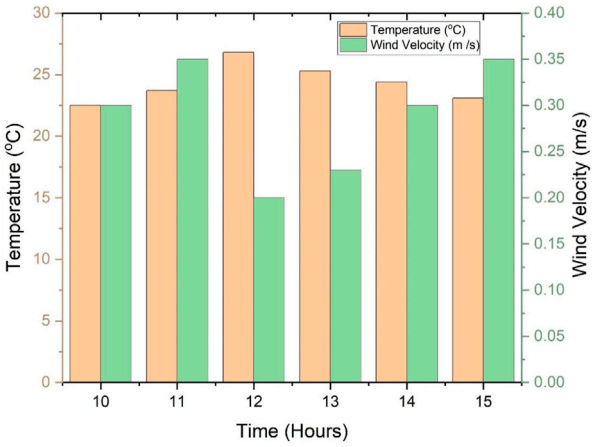

FIGURE 8
Average Taxila climate conditions.

conditions, the thermal performance of CPC increases due to the enhanced surface area and thermal properties of nanoparticles and hybrid nanoparticles.

From Figures 10A–D, it is obvious that due to the variation in particle concentration, the trend of thermal efficiency and other parameters also varies accordingly. The efficiency of water improved from 12.5% to 34.8%. The variation increases with an increase in the flow rate; no doubt the temperature difference decreases with the increase of flow, and efficiency increases with flow rate. This direct and inverse relation is the main drive for variation of graphs. The efficiency achieved using NFs of (SiO_2/EG + H_2O) varies from 20.8% to 59.13% for Taxila climate. For same climatic conditions, efficiency for hybrid NFs (CB + GNPs) varies from 14.2% to 65.68%. Efficiency varies from 15.3% to 66.36% by using hybrid NFs of MgO + CB in the base fluid of water at higher concentration and flow rate.

Effect of solar heat gain with time, flow rate, and concentration of nanoparticles using water, nanofluids, and hybrid nanofluids

The solar heat gain varies with the specific heat capacity of fluids and temperature difference at different concentration ratios and flow rates. Average values taken for figures at similar test conditions are considered. The variation of water NFs and two concentrations of hybrid NFs are shown in Figure 11. The hybrid NFs gave 31.5% improved results than simple base fluid water.

From Figures 11A–D, it is obvious that due to the variation in particle concentration, the trend of solar heat gain and other parameters also varies accordingly. The solar heat gain changes from 77.85 to 470 W at a lower flow of

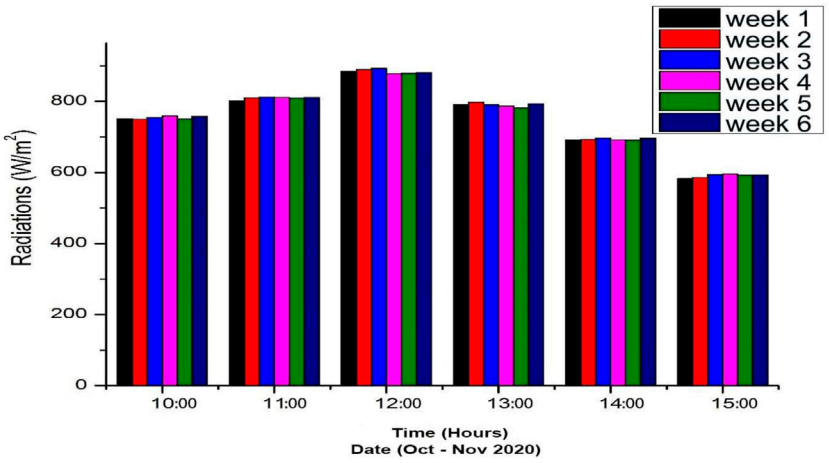

FIGURE 9
Average solar radiation data.

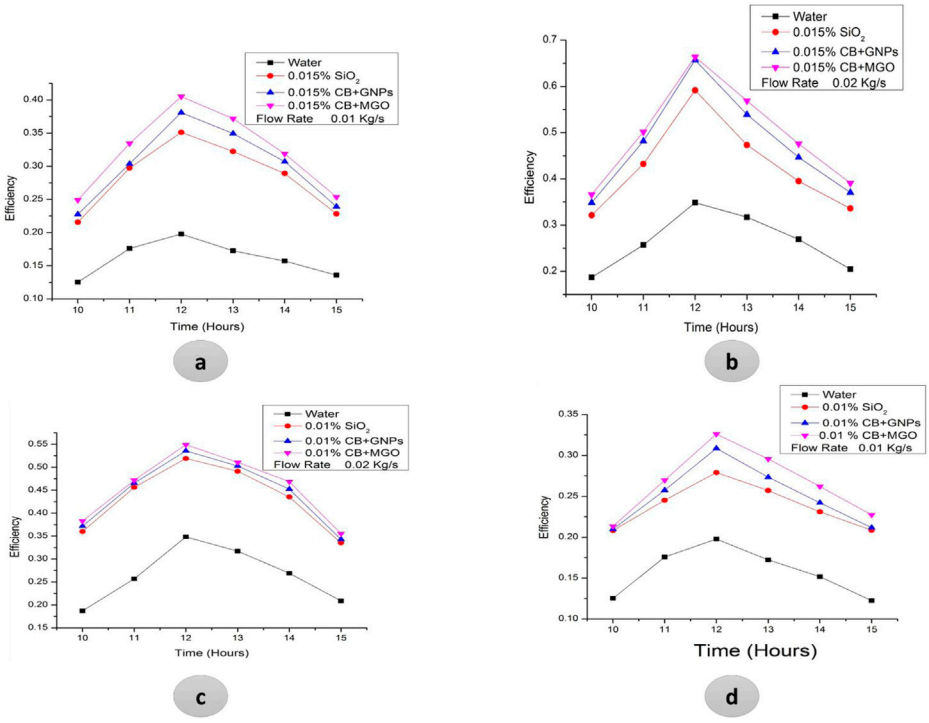

FIGURE 10
Efficiency at different flow rates with different concentrations of NFs and hybrid NFs. **(A)** 0.01 kg/s, with 0.015 wt% concentration of NFs and hybrid NFs. **(B)** 0.020 kg/s, with 0.015 wt% concentration of NFs and hybrid NFs. **(C)** for 0.020 kg/s and 0.010 wt% concentration of NFs and hybrid NFs. **(D)** 0.010 kg/sand 0.010 wt% concentration of NFs and hybrid NFs.

0.01 kg/s to the highest flow of 0.020 kg/s for water and hybrid NFs (MgO + CB/water), respectively. At such a high flow rate, the solar gain and efficiency were high, but the temperature difference will be minimum as compared to the remaining flow rates. The maximum solar gain is achieved at high concentration and the flow rate was 470 W.

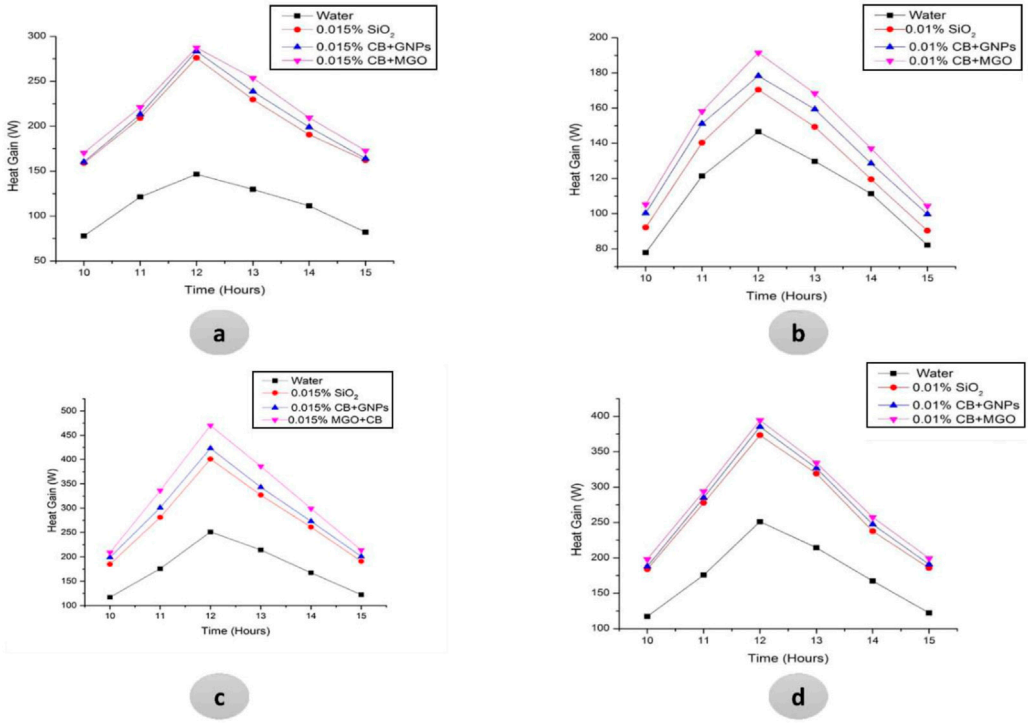

FIGURE 11
Solar heat gain received by CPCs at different flow rates for different concentrations of NFs and hybrid NFs for Taxila climate. **(A)** 0.010 kg/sand 0.015 wt% flow rate and concentration of NFs and hybrid NFs, respectively. **(B)** 0.01 kg/s flow rate and 0.010 wt% concentration of NFs and hybrid NFs. **(C)** 0.020 kg/s flow rate and 0.015 wt% concentration of NFs and hybrid NFs. **(D)** 0.020 kg/s flow rate and 0.010 wt% concentration of NFs and hybrid NFs.

Temperature difference with time, flow rate, and concentration of nanoparticles using water, nanofluids, and hybrid nanofluids

The line graph in Figure 12 indicates the variation of temperature difference at three different flow rates. Average values taken for figures at similar test conditions are considered.

From Figures 12A–D, it is obvious that due to the variation in particle concentration, the trend of the temperature difference and other parameters also varies accordingly. For water, variation in temperature is 1.4°C–3.4°C for higher to lowest flow rates. While at the same climate conditions, the NFs (hybrid base fluid EG + water and nanoparticles of SiO_2) gave improved results at 2°C–7.8°C, respectively. This range varies from 2.1°C to 7.7°C for CB + GNPs in the base fluid of water. For hybrid NFs of CB + MgO, this range varies from 2.4°C to 8.5°C for higher to lowest flow rates, respectively.

Compound parabolic collector comparison at different flow rates for nanofluids and hybrid nanofluids

In Figure 13, the comparison is carried out for two concentrations of NFs and hybrid NFs at three flow rates. The sedimentation of particles is proportional to the concentration ratio of NFs and hybrid NFs. The lower concentration at high flow rate bounces minimum sedimentation than the high concentration at high flow rates. Also, to avoid amalgamation and ensure stability, NFs and hybrid NFs were re-blended and homogenized every morning.

Uncertainty analysis

Uncertainty analysis is necessary to obtain refined data by eliminating outliers. Thermal efficiency uncertainty in the system is calculated by the root sum square method (Akhtar et al., 2020).

$$\alpha = f\ (b_1, b_2, b_3.....), \quad (4)$$

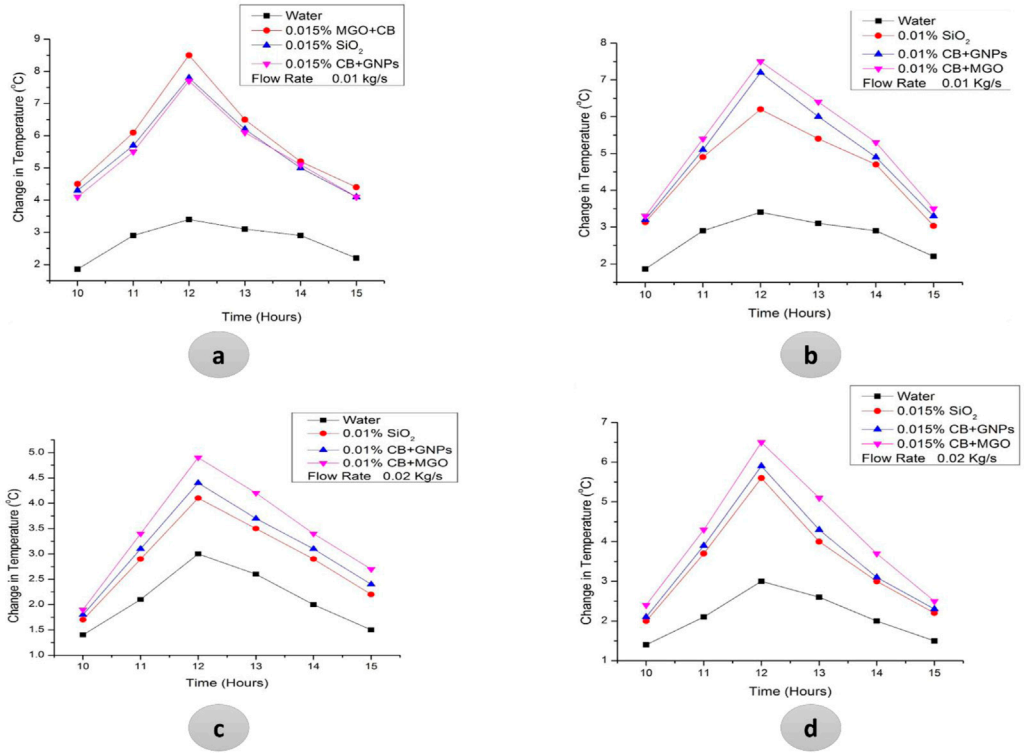

FIGURE 12
Change in temperature delta T for different concentrations. **(A)** 0.015 wt% concentrations at 0.01 kg/s flow rate. **(B)** 0.010 wt% concentrations at 0.01 kg/s flow rate. **(C)** 0.010 wt% concentrations at 0.020 kg/s flow rate. **(D)** 0.015 wt% concentrations at 0.020 kg/s flow rate.

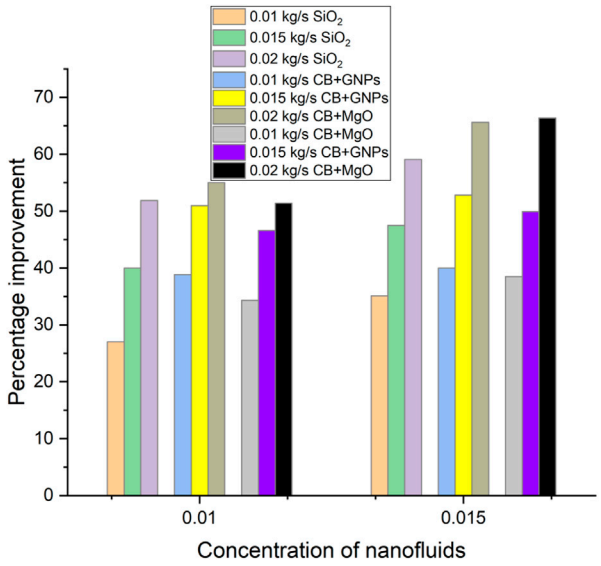

FIGURE 13
Comparison of CPC for NFs and hybrid NFs.

$$\mathfrak{C}_{\alpha} = \sqrt{\left(\frac{\delta\alpha}{\delta b_1}.\mathfrak{C}b_1\right)^2 + \left(\frac{\delta\alpha}{\delta b_2}.\mathfrak{C}b_2\right)^2 + \left(\frac{\delta\alpha}{\delta b_3}.\mathfrak{C}b_3\right)^2 \ldots .} \quad (5)$$

Uncertainty for the thermal efficiency is calculated as around 3.5%.

Conclusion

In the present work, the thermal enhancement of CPCs using NFs and hybrid NFs as heat transfer fluids was investigated. The results of temperature difference of receiver were increased with high particle concentrations and reduced with high flow rates. In all scenarios, efficiencies of CPCs using NFs and hybrid NFs were higher than those of CPCs using base fluid (water). The highest thermal efficiency achieved by experimentation is 66.3% for MgO + CB pair at the highest flow rate and the highest concentration of nanoparticles (0.020 kg/s and 0.015 wt%). Maximum efficiency gain by water at the highest flow rate (0.020 kg/s) is 34.8% under similar experimental conditions. In short, it is concluded as follows:

•Efficiency is calculated by using four types of fluids (water, SiO_2/H_2O + EG (50:50), CB + GNPs/H_2O, and MgO + CB/H_2O) at different flow rates and volumetric concentrations of nanoparticles.
•By using water as working fluid variations in temperature difference, heat gain and thermal efficiency are observed from 3.4°C to 1.4°C, 77.8 to 252 W, and 12.5% to 34.8% from the lowest to the highest flow rate.
•By using hybrid base fluid (water and ethylene glycol) and nanoparticles of SiO_2, maximum temperature difference was attained at the lowest flow rate and the highest concentration is 7.8°C, and variations in temperature difference, heat gain, and thermal efficiency are observed from 7.8°C to 2°C, 140.2 to 446.3 W, and 12.8% to 59.13% from the lowest to the highest flow rate and volumetric concentrations.
•By using a hybrid of two non-metallic CB + GNPs in the base fluid of water, maximum temperature difference was attained at the lowest flow rate and the highest concentration is 7.7°C, and variations in temperature difference, heat gain, and thermal efficiency are observed from 7.7°C to 2.1°C, 94.6 to 488.4 W, and 14.2% to 65.68% from the lowest to the highest flow rate and volumetric concentration of the non-metallic pair.
•Thermal enhancement of CPSC is improved by using NFs and optimum results are achieved by using hybrid NFs.
•The increasing behavior of temperature difference and solar heat gain is different at the same flow rates.
•By using various combinations of hybrid NFs, one optimized hybrid NF can be used to obtain optimum results.
•The optimum temperature difference attained by MgO + CB is 8.5°C for the lowest flow rate and the highest concentration of nanoparticles and variations in temperature difference, heat gain, and thermal efficiency are observed from 8.5°C to 2.4°C, 101.5 to 495 W, and 15.3% to 66.3%. The hybrid NFs gave 31.5% improved results than water. The hybrid NFs are more suitable to improve the thermal output of solar collectors. The presented results of experimentations are beneficial for low–medium range industrial applications of CPCs using hybrid NFs.

In the present research work, experimentation is presented by using NFs and different hybrid NFs of metallic and non-metallic hybrid, non-metallic hybrid, and hybrid base fluid using metallic hybrid pair and non-metallic hybrid pair.

•Earlier work was done using CuO and Al_2O_3 NFs with a compound parabolic collector. In the present work, all thermal analyses were performed by using NFs and hybrid NFs. In the future, other types of hybrid NFs may be used to improve the thermal performance of CPC for low–medium range temperature applications.
•CPC thermal performance can also be increased by utilizing metallic hybrid in hybrid base fluids.
•The use of different pairs of hybrid base fluids for metal and non-metal hybrid nanoparticles can lead to a novel work.

Data availability statement

The original contributions presented in the study are included in the article/Supplementary Material; further inquiries can be directed to the corresponding author.

Author contributions

MF: contributed as investigation, writing orignal draft. MIS: Writing draft, and investigation. FJ: writing—review and editing. MU: formal analysis. MM: writing—review and editing, software, and resources. MWS: writing—review and editing. SN: validation. SS: data curation. AY: writing—review and editing. MM: writing—review and editing, and funding acquisition. AE-S: writing—review and editing.

Conflict of interest

The authors declare that the research was conducted in the absence of any commercial or financial relationships that could be construed as a potential conflict of interest.

Publisher's note

All claims expressed in this article are solely those of the authors and do not necessarily represent those of their affiliated organizations, or those of the publisher, the editors, and the reviewers. Any product that may be evaluated in this article, or claim that may be made by its manufacturer, is not guaranteed or endorsed by the publisher.

References

Acosta-Herazo, R., Valadés-Pelayo, P. J., Mueses, M. A., Pinzón-Cárdenas, M. H., Arancibia-Bulnes, C., and Machuca-Martínez, F. (2020). An optical and energy absorption analysis of the solar compound parabolic collector photoreactor (CPCP): The impact of the radiation distribution on its optimization. *Chem. Eng. J.* 395, 125065. doi:10.1016/j.cej.2020.125065

Ahmadi, A., Das, B., Ehyaei, M. A., Esmaeilion, F., El Haj Assad, M., Jamali, D. H., et al. (2021). Energy, exergy, and techno-economic performance analyses of solar dryers for agro products: A comprehensive review. *Sol. Energy* 228, 349–373. doi:10.1016/j.solener.2021.09.060

Ahmadi, M. H., Baghban, A., Sadeghzadeh, M., Zamen, M., Mosavi, A., Shamshirband, S., et al. (2020). Evaluation of electrical efficiency of photovoltaic thermal solar collector. *Eng. Appl. Comput. Fluid Mech.* 14, 545–565. doi:10.1080/19942060.2020.1734094

Akhtar, F., Ali, M., Sheikh, N. A., and Shehryar, M. (2020). Experimental investigation of solar compound parabolic collector using Al2O3/H2O nanofluid in a subtropical climate. *Therm. Sci.* 25, 201. doi:10.2298/TSCI191207201A

Al-Waeli, A. H. A., Sopian, K., Chaichan, M. T., Kazem, H. A., Ibrahim, A., Mat, S., et al. (2017). Evaluation of the nanofluid and nano-PCM based photovoltaic thermal (PVT) system: An experimental study. *Energy Convers. Manag.* 151, 693–708. doi:10.1016/j.enconman.2017.09.032

Allahyar, H. R., Hormozi, F., and ZareNezhad, B. (2016). Experimental investigation on the thermal performance of a coiled heat exchanger using a new hybrid nanofluid. *Exp. Therm. Fluid Sci.* 76, 324–329. doi:10.1016/j.expthermflusci.2016.03.027

Amjad, M., Gardy, J., Hassanpour, A., and Wen, D. (2018). Novel draw solution for forward osmosis based solar desalination. *Appl. Energy* 230, 220–231. doi:10.1016/j.apenergy.2018.08.021

Amjad, M., Raza, G., Xin, Y., Pervaiz, S., Xu, J., Du, X., et al. (2017). Volumetric solar heating and steam generation via gold nanofluids. *Appl. Energy* 206, 393–400. doi:10.1016/j.apenergy.2017.08.144

Amjad, M., Yang, Y., Raza, G., Gao, H., Zhang, J., Zhou, L., et al. (2017). Deposition pattern and tracer particle motion of evaporating multi-component sessile droplets. *J. Colloid Interface Sci.* 506, 83–92. doi:10.1016/j.jcis.2017.07.025

Ayompe, L. M., Duffy, A., McCormack, S. J., and Conlon, M. (2011). Validated TRNSYS model for forced circulation solar water heating systems with flat plate and heat pipe evacuated tube collectors. *Appl. Therm. Eng.* 31, 1536–1542. doi:10.1016/j.applthermaleng.2011.01.046

Babar, H., and Ali, H. M. (2019). Towards hybrid nanofluids: Preparation, thermophysical properties, applications, and challenges. *J. Mol. Liq.* 281, 598–633. doi:10.1016/j.molliq.2019.02.102

Belkhode, P. N., Shelare, S. D., Sakhale, C. N., Kumar, R., Shanmugan, S., Soudagar, M. E. M., et al. (2021). Performance analysis of roof collector used in the solar updraft tower. *Sustain. Energy Technol. Assessments* 48, 101619. doi:10.1016/j.seta.2021.101619

Bellos, E., Korres, D., Tzivanidis, C., and Antonopoulos, K. A. (2016). Design, simulation and optimization of a compound parabolic collector. *Sustain. Energy Technol. Assessments* 16, 53–63. doi:10.1016/j.seta.2016.04.005

Bellos, E., and Tzivanidis, C. (2019). A review of concentrating solar thermal collectors with and without nanofluids. *J. Therm. Anal. Calorim.* 135, 763–786. doi:10.1007/s10973-018-7183-1

Bellos, E., and Tzivanidis, C. (2018). Thermal analysis of parabolic trough collector operating with mono and hybrid nanofluids. *Sustain. Energy Technol. Assessments* 26, 105–115. doi:10.1016/j.seta.2017.10.005

Bhalla, V., and Khullar, V. (2021). *Design and thermal analysis of nanofluid-based compound parabolic concentrator*.

Campos, C., Vasco, D., Angulo, C., Burdiles, P. A., Cardemil, J., and Palza, H. (2019). About the relevance of particle shape and graphene oxide on the behavior of direct absorption solar collectors using metal based nanofluids under different radiation intensities. *Energy Convers. Manag.* 181, 247–257. doi:10.1016/j.enconman.2018.12.007

Chen, M., He, Y., Huang, J., and Zhu, J. (2016). Synthesis and solar photo-thermal conversion of Au, Ag, and Au-Ag blended plasmonic nanoparticles. *Energy Convers. Manag.* 127, 293–300. doi:10.1016/j.enconman.2016.09.015

Chen, N., Ma, H., Li, Y., Cheng, J., Zhang, C., Wu, D., et al. (2017). Complementary optical absorption and enhanced solar thermal conversion of CuO-ATO nanofluids. *Sol. Energy Mater. Sol. Cells* 162, 83–92. doi:10.1016/j.solmat.2016.12.049

Crisostomo, F., Hjerrild, N., Mesgari, S., Li, Q., and Taylor, R. A. (2017). A hybrid PV/T collector using spectrally selective absorbing nanofluids. *Appl. Energy* 193, 1–14. doi:10.1016/j.apenergy.2017.02.028

Dimri, N., Tiwari, A., and Tiwari, G. N. (2018). Effect of thermoelectric cooler (TEC) integrated at the base of opaque photovoltaic (PV) module to enhance an overall electrical efficiency. *Sol. Energy* 166, 159–170. doi:10.1016/j.solener.2018.03.030

Esfe, M. H., Esfandeh, S., Saedodin, S., and Rostamian, H. (2017). Experimental evaluation, sensitivity analyzation and ANN modeling of thermal conductivity of ZnO-MWCNT/EG-water hybrid nanofluid for engineering applications. *Appl. Therm. Eng.* 125, 673–685.

Esfe, M. H., Wongwises, S., Naderi, A., Asadi, A., Safaei, M. R., Rostamian, H., et al. (2015). Thermal conductivity of Cu/TiO2–water/EG hybrid nanofluid: Experimental data and modeling using artificial neural network and correlation. *Int. Commun. Heat. Mass Transf.* 66, 100–104.

Farajzadeh, E., Movahed, S., and Hosseini, R. (2018). Experimental and numerical investigations on the effect of Al2O3/TiO2H2O nanofluids on thermal efficiency of the flat plate solar collector. *Renew. Energy* 118, 122–130. doi:10.1016/j.renene.2017.10.102

Ghafoor, D. A., Rehman, T., Munir, A., Ahmad, M., and Iqbal, M. (2016). Current status and overview of renewable energy potential in Pakistan for continuous energy sustainability. *Renew. Sustain. Energy Rev.* 60, 1332–1342. doi:10.1016/j.rser.2016.03.020

Gilani, H. A., and Hoseinzadeh, S. (2021). Techno-economic study of compound parabolic collector in solar water heating system in the northern hemisphere. *Appl. Therm. Eng.* 190, 116756.

Hachicha, A. A., Rodríguez, I., Capdevila, R., and Oliva, A. (2013). Heat transfer analysis and numerical simulation of a parabolic trough solar collector. *Appl. Energy* 111, 581–592. doi:10.1016/j.apenergy.2013.04.067

Hamid, K. A., Azmi, W. H., Nabil, M. F., and Mamat, R. (2018). Experimental investigation of nanoparticle mixture ratios on TiO2-SiO2 nanofluids heat transfer performance under turbulent flow. *Int. J. Heat Mass Transf.* 118, 617–627. doi:10.1016/j.ijheatmasstransfer.2017.11.036

Harrabi, I., Hamdi, M., and Hazami, M. (2021). Long-term performances and technoeconomic and environmental assessment of Al2O3/water and MWCNT/oil nanofluids in three solar collector technologies. *J. Nanomater.* 2021. doi:10.1155/2021/6461895

Hjerrild, N. E., Mesgari, S., Crisostomo, F., Scott, J. A., Amal, R., and Taylor, R. A. (2016). Hybrid PV/T enhancement using selectively absorbing Ag-SiO 2/carbon nanofluids. *Sol. Energy Mater. Sol. Cells* 147, 281–287. doi:10.1016/j.solmat.2015.12.010

Jiang, C., Yu, L., Yang, S., Li, K., Wang, J., Lund, P. D., et al. (2020). A review of the compound parabolic concentrator (CPC) with a tubular absorber. *Energies* 13, 695. doi:10.3390/en13030695

Khalil, A., Amjad, M., Noor, F., Hussain, A., Nawaz, S., Filho, E. P. B., et al. (2020). Performance analysis of direct absorption-based parabolic trough solar collector using hybrid nanofluids. *J. Braz. Soc. Mech. Sci. Eng.* 42, 573. doi:10.1007/s40430-020-02654-2

Kim, Y. S., Balkoski, K., Jiang, L., and Winston, R. (2013). Efficient stationary solar thermal collector systems operating at a medium-temperature range. *Appl. Energy* 111, 1071–1079. doi:10.1016/j.apenergy.2013.06.051

Korres, D., Bellos, E., and Tzivanidis, C. (2019). Investigation of a nanofluid-based compound parabolic trough solar collector under laminar flow conditions. *Appl. Therm. Eng.* 149, 366–376. doi:10.1016/j.applthermaleng.2018.12.077

Korres, D., and Tzivanidis, C. (2018). A new mini-CPC with a U-type evacuated tube under thermal and optical investigation. *Renew. Energy* 128, 529–540. doi:10.1016/j.renene.2017.06.054

Leong, K. Y., Razali, I., Ku Ahmad, K. Z. K., Ong, H. C., Ghazali, M. J., and Abdul Rahman, M. R. A. (2018). Thermal conductivity of an ethylene glycol/water-based nanofluid with copper-titanium dioxide nanoparticles: An experimental approach. *Int. Commun. Heat Mass Transf.* 90, 23–28. doi:10.1016/j.icheatmasstransfer.2017.10.005

Li, Q., Zheng, C., Shirazi, A., Bany Mousa, O. B., Moscia, F., Scott, J. A., et al. (2017). Design and analysis of a medium-temperature, concentrated solar thermal collector for air-conditioning applications. *Appl. Energy* 190, 1159–1173. doi:10.1016/j.apenergy.2017.01.040

Menbari, A., Alemrajabi, A. A., and Ghayeb, Y. (2016). Experimental investigation of stability and extinction coefficient of Al 2 O 3 -CuO binary nanoparticles dispersed in ethylene glycol-water mixture for low-temperature direct absorption solar collectors. *Energy Convers. Manag.* 108, 501–510. doi:10.1016/j.enconman.2015.11.034

Menbari, A., Alemrajabi, A. A., and Rezaei, A. (2017). Experimental investigation of thermal performance for direct absorption solar parabolic trough collector (DASPTC) based on binary nanofluids. *Exp. Therm. Fluid Sci.* 80, 218–227. doi:10.1016/j.expthermflusci.2016.08.023

Oloketuyi, I. S., Ajide, O. O., Odesola, F. I., Oyewola, O. M., and Adaramola, M. S. (2020). Examination of heat transfer performance of a nonimaging hybrid compound parabolic collector in low latitude and cloudy region. *Environ. Prog. Sustain. Energy.* 39, e13339. doi:10.1002/ep.13339

Parsian, A., and Akbari, M. (2018). New experimental correlation for the thermal conductivity of ethylene glycol containing Al2O3-Cu hybrid nanoparticles. *J. Therm. Anal. Calorim.* 131, 1605–1613. doi:10.1007/s10973-017-6694-5

Qamar, A., Arshad, A., Anwar, Z., Shaukat, R., Amjad, M., Imran, S., et al. (2021). Dispersion stability and rheological characteristics of water and ethylene glycol based ZnO nanofluids. *Therm. Sci.* 25.

Sathieshkumar, N. (2018). Performance analysis of hybrid solar photovoltaic thermal collector with nanoparticles. *Int. J. Curr. Res. Eng. Technol.* 1, 6–11.

Snail, K. A., O'Gallagher, J. J., and Winston, R. (1984). A stationary evacuated collector with integrated concentrator. *Sol. Energy* 33, 441–449. doi:10.1016/0038-092X(84)90196-8

Subramani, J., Nagarajan, P. K., Mahian, O., and Sathyamurthy, R. (2018). Efficiency and heat transfer improvements in a parabolic trough solar collector using TiO2 nanofluids under turbulent flow regime. *Renew. Energy* 119, 19–31. doi:10.1016/j.renene.2017.11.079

Sundar, L. S., Singh, M. K., and Sousa, A. C. M. (2014). Enhanced heat transfer and friction factor of MWCNT-Fe3O4/water hybrid nanofluids. *Int. Commun. Heat Mass Transf.* 52, 73–83. doi:10.1016/j.icheatmasstransfer.2014.01.012

Suresh, S., Venkitaraj, K. P., Selvakumar, P., and Chandrasekar, M. (2011). Synthesis of Al2O3-Cu/water hybrid nanofluids using two step method and its thermo physical properties. *Colloids Surfaces A Physicochem. Eng. Aspects* 388, 41–48. doi:10.1016/j.colsurfa.2011.08.005

Takabi, B., and Salehi, S. (2014). Augmentation of the heat transfer performance of a sinusoidal corrugated enclosure by employing hybrid nanofluid. *Adv. Mech. Eng.* 6, 147059. doi:10.1155/2014/147059

Tiwari, S., and Tiwari, G. N. (2017). Thermal analysis of photovoltaic thermal integrated greenhouse system (PVTIGS) for heating of slurry in potable biogas plant: An experimental study. *Sol. Energy* 155, 203–211. doi:10.1016/j.solener.2017.06.021

Toghraie, D., Chaharsoghi, V. A., and Afrand, M. (2016). Measurement of thermal conductivity of ZnO-TiO2/EG hybrid nanofluid. *J. Therm. Anal. Calorim.* 125, 527–535. doi:10.1007/s10973-016-5436-4

Verma, S. K., Tiwari, A. K., Tiwari, S., and Chauhan, D. S. (2018). Performance analysis of hybrid nanofluids in flat plate solar collector as an advanced working fluid. *Sol. Energy* 167, 231–241. doi:10.1016/j.solener.2018.04.017

Vijayakumar, P., Kumaresan, G., Gokul Kumar, S. G., and Eswaran, M. (2021). A review on applications of nanofluid in evacuated tube heat pipe integrated with compound parabolic concentrator. *Mater. Today Proc.* 45, 1227–1232. doi:10.1016/j.matpr.2020.04.250

Wang, X., He, Y., Chen, M., and Hu, Y. (2018). ZnO-Au composite hierarchical particles dispersed oil-based nanofluids for direct absorption solar collectors. *Sol. Energy Mater. Sol. Cells* 179, 185–193. doi:10.1016/j.solmat.2017.11.012

Xu, Z. Y., and Wang, R. Z. (2017). Comparison of CPC driven solar absorption cooling systems with single, double and variable effect absorption chillers. *Sol. Energy* 158, 511–519. doi:10.1016/j.solener.2017.10.014

Younis, A., Elsarrag, E., Alhorr, Y., and Onsa, M. (2018). The influence of Al2O3-ZnO-H2O nanofluid on the thermodynamic performance of photovoltaic-thermal hybrid solar collector system. *Innov. Ener Res.* 7, 1463–2576. doi:10.4172/2576-1463.1000187

Zeng, J., Xuan, Y., and Duan, H. (2016). Tin-silica-silver composite nanoparticles for medium-to-high temperature volumetric absorption solar collectors. *Sol. Energy Mater. Sol. Cells* 157, 930–936. doi:10.1016/j.solmat.2016.08.012

Zeng, J., and Xuan, Y. (2018). Enhanced solar thermal conversion and thermal conduction of MWCNT-SiO2/Ag binary nanofluids. *Appl. Energy* 212, 809–819. doi:10.1016/j.apenergy.2017.12.083

Nomenclature

Symbols

^{A}r Receiver area (m^2)

^{A}a Aperture area (m^2)

A Aperture width (m)

Au Gold

Ag Silver

Al_2O_3 Alumina

Cp Specific heat capacity (J/kg.K)

CPSC Compound parabolic solar collector

CB Carbon black

CuO Copper oxide

DASC Direct absorption solar collector

EG Ethylene glycol

FPSC Flat plate solar collector

HCPC Hybrid compound parabolic collector

HVAC Heating, ventilation, and air conditioning

H_2O Water

GNPs Graphene nanoplatelets

G_e Solar irradiance (W/m^2)

m' Mass flow rate (kg/s)

MgO Magnesium oxide

MWCNTs Multiwall carbon nanotubes

PV/T Photovoltaic/thermal

PTC Parabolic trough collector

^{Q}u Solar heat gain (W)

Q_s Energy potential (W)

ΔT Temperature difference (°C)

^{T}a Ambient temperature (°C)

^{Tc} Collector temperature (°C)

^{Ti} Inlet temperature (°C)

TiO_2 Titania

SiO_2 Silica

Greek letters

η_{th} Thermal efficiency

frontiers | Frontiers in Energy Research

TYPE Original Research
PUBLISHED 29 September 2022
DOI 10.3389/fenrg.2022.979942

OPEN ACCESS

EDITED BY
K. Sudhakar,
Universiti Malaysia Pahang, Malaysia

REVIEWED BY
Muhammad Wakil Shahzad,
Northumbria University,
United Kingdom
Shanmuga Priya S.,
Manipal Institute of Technology, India

*CORRESPONDENCE
M. A. Mujtaba,
m.mujtaba@uet.edu.pk

SPECIALTY SECTION
This article was submitted to Solar Energy,
a section of the journal
Frontiers in Energy Research

RECEIVED 28 June 2022
ACCEPTED 22 August 2022
PUBLISHED 29 September 2022

CITATION
Ditta A, Tabish AN, Mujtaba MA, Amjad M, Yusuf AA, Chaudhary GQ, Razzaq L, Abdelrahman A and Kalam MA (2022), Experimental investigation of a hybrid configuration of solar thermal collectors and desiccant indirect evaporative cooling system.
Front. Energy Res. 10:979942.
doi: 10.3389/fenrg.2022.979942

Experimental investigation of a hybrid configuration of solar thermal collectors and desiccant indirect evaporative cooling system

Allah Ditta[1], Asif Nadeem Tabish[2], M. A. Mujtaba[3]*, Muhammad Amjad[3], Abdulfatah Abdu Yusuf[4], Ghulam Qadar Chaudhary[5], Luqman Razzaq[6], Anas Abdelrahman[7] and M. A Kalam.[8]

[1]Centre of Energy Research and Development, University of Engineering and Technology Lahore, Lahore, Pakistan, [2]Department of Chemical Engineering, University of Engineering and Technology Lahore, Lahore, Pakistan, [3]Department of Mechanical, Mechatronics and Manufacturing Engineering, University of Engineering and Technology Lahore, Lahore, Pakistan, [4]Department of Mechanical Engineering, Kampala International University, Ishaka, Uganda, [5]Department of Mechanical Engineering, Mirpur University of Science and Technology, Mirpur, AJK, Pakistan, [6]Department of Mechanical Engineering Technology, University of Gujrat, Gujrat, Pakistan, [7]Mechanical Engineering, Faculty of Engineering and Technology, Future University in Egypt, New Cairo, Egypt, [8]Faculty of Engineering and IT, University of Technology Sydney, Ultimo, NSW, Australia

This paper presents the integrated performance of a solar-assisted desiccant dehumidifier along with Maisotsenko cycle (M-cycle) counter flow heat and mass exchanger. This system handles latent load and sensible load separately. The hybrid configuration of solar thermal collectors was analyzed for efficiency of solar collectors and solar fraction. High consumption of fossil fuels, which are already present in a limited amount, is also associated with environmental problems and climate change issues, as these increase the chances of global warming. These issues demand of us to shift towards renewable energy resources. Increase in world energy use results in a number of environmental problems, such as climate change, in addition to global warming and ozone depletion. In building services, HVAC systems are major concerns. To overcome the requirement, conventional air conditioning and vapor compression systems are mainly used for air conditioning, although these also have some environmental problems. Solar thermal applications in combination with other renewable-energy-dependent cooling practices have generated a huge interest towards sustainable solutions, keeping in view several techno-economical, environmental, and climatic advantages. The experimental investigation reveals that the maximum outlet temperature and efficiency of solar thermal collectors was 87°C and 56% respectively. The maximum cooling capacity of the system is evaluated at 4.6 kW.

KEYWORDS

HVAC, solar thermal collector, desiccant dehumidifier, evaporative cooling, solar energy research highlights

Highlights

1- The solar thermal collector mainly evacuated tube collector and flat plate collector, which were used for the regeneration of solid desiccant wheel
2- The parametric analysis of operating conditions is carried out with the configuration of counter flow HMX on Process air stream
3- The minimum outlet temperatutre from the M-Cycle is 14.7°C with a low inlet temperature of 27°C
4- The Maximum cooling capacity of the system is evaluated at 4.6 kW

1 Introduction

The amount of energy consumed to perform a special action, produce or manufacture something, or simply inhabit a building is termed as energy consumption (Sikder et al., 2016). Growing populations and improved living standards around the world have had a large impact on energy consumption (Wu J. et al., 2020; Khan et al., 2020). These factors affect the economic growth of a country. Economic growth has a strong correlation with energy consumption (Wang and Wang, 2020; Knight and Schor, 2014). In China and other Asian countries during the period of 2000–2008, economic growth accelerated the demand for electricity based on coal, and resulted in emissions of carbon dioxide CO_2 (Wu H et al., 2020; Farooq et al., 2019). Unfortunately, two-thirds of CO_2 emissions have already been consumed, and the remaining portion will be spent by 2050, making the energy-water-environment nexus crucial to achieving the COP21 target of keeping environmental temperature increase below 2°C. Though recent technical advancements in the electricity and desalination industries have increased their efficiency, they are still only running at 35% and 10% of their thermodynamic limitations, respectively, which has a significant impact on energy consumption and carbon emissions. Desalination process research is vital to meeting the energy needs of a growing global population while also lowering per capita energy consumption and safeguarding the planet's natural resources (Shahzad et al., 2017). It means that increase in the economic growth results in an increase in energy consumption. Energy consumption in higher education buildings make up 40% of total energy consumption in the United Kingdom (United Kingdom) (Amber et al., 2020). So, emissions can be minimized by cutting of energy consumption. In developing countries, economic development is necessary to achieve this aim.

In developed countries, the energy consumption in building sectors contributes 20%–40% to total energy usage (Bahadori-Jahromi et al., 2017), (Kashif et al., 2020). With the increasing demand of thermal comfort in buildings like offices and other industrial buildings, HVAC systems account for about 10%–20% of total energy consumption (Lu et al., 2019; González and Fiorito, 2015). It is clear that energy consumption is increasing day by day, especially in building services (Pérez-Lombard et al., 2008; Petri et al., 2017). In the modern era, fossil fuels like coal and oil used for energy production are depleting rapidly (Brandt, 2011; Murphy et al., 2011). So, there is a need to move towards an alternative source of energy generation (Halim, 2013; Berbel and Posadillo, 2018).

The Sun is the major source of life on earth; when using this source to power a system, it serves as a "free" source of energy for many processes at the same time. In comparison with other sources of energy, solar energy has great advantages of being remarkably clean and environmentally friendly (Mahmud et al., 2018; Choudhary and Srivastava, 2019). Solar energy is a major source of renewable energy and, based on methods of its capture and conversion, solar power can be classified as either active solar or passive solar energies (Abdelkareem et al., 2018). Rapid increases in energy consumption day by day and considerably high prices of fossil fuels demand the replacement of traditional refrigeration systems that require high amounts of energy (Moriarty and Honnery, 2019). For large systems, a number of solar-based cooling technologies exist that can be used in combination with solar thermal collectors (Baral et al., 2015; Ma et al., 2017). Solar-assisted desiccant air conditioning is a renewable technology which saves a lot of energy (Angrisani et al., 2016). Because this system does not have a compressor in it, energy consumption is very low as compared to other refrigeration systems. The energy consumption equipment's includes axial fans and water pumps, which consumes a small amount of energy.

The emerging cooling technology hybrid indirect evaporative cooling-mechanical vapor compression (IEC-MVC) combines the benefits of IEC and MVC, allowing for precise temperature and humidity regulation, excellent energy efficiency, and little water usage (Chen et al., 2022). When compared to conventional mechanical vapor compression (MVC) chillers, the indirect evaporative cooler (IEC) is seen as a more efficient and environmentally friendly option for cooling purposes. However, IEC is a passive cooler and has no real control over the ambient temperature or humidity of the supplied air. When the relative humidity of the air is high, IEC performance suffers. We explore a hybrid approach that integrates IEC and MVC in order to get around these restrictions. In the IEC, pre-cooling occurs when energy is reclaimed from the exhausted air of a room and applied to the outside air before further processing with MV (Chen et al., 2021).

As an alternative to traditional air conditioning systems, indirect evaporative cooling technology has evolved as an energy-efficient, low-cost, and sustainable method of cooling indoor spaces. This is because it may reduce cooling costs by as much as half compared to conventional cooling methods like forced air and vapor compression, as well as desiccant cooling. Jamil et al. (2021) investigated an innovative humidifier-aided

regenerative indirect evaporative cooler that reduces fouling tendency and water management difficulties by doing away with hydrophilic surfaces used in the system. The proposed setup has an optimal cooling efficiency of 83.82 percent and a performance coefficient of 44 percent. Scaling trends of the coefficient of performance are as follows: Primary air inlet temperature > primary air outlet temperature > primary air velocity. The effectiveness of the cooler scales is as follows: Secondary air outlet temperature > primary air inlet temperature > primary air humidity > primary air outlet.

In terms of coefficient of performance (COP), M-CYCLE-based desiccant air conditioning systems are 60%–65% more efficient than conventional air conditioning systems providing the same inlet conditions (Kashif Shahzad et al., 2018). The main advantage of this solution is that it can provide the required comfort level with comparatively less effective dehumidification (Cui et al., 2019). When discussing these air conditioning systems the factors air inlet temperature, regeneration air temperature, and humidity are important. An important component of the desiccant dehumidifier is the special desiccant wheel that is solely used to adsorb the moisture content from air during dehumidification (Hu et al., 2016). A lot of materials are used for thermal storage in desiccant cooling systems like silica gel, paraffin wax, stearic acid, and $CaCl_2$.6H2O (Leng et al., 2006; Alghamdi, 2017). Choosing which material depends on the energy consumed by them. An experimental analysis shows that if a system exists without solar energy and storage material the energy consumption by it is 23.57 kW. On the other hand, the average energy saving percentage of paraffin wax, stearic acid, and $CaCl_2.6H_2O$ is 75.86%, 78%, and 64.6% respectively, by using them as storage materials (Kabeel et al., 2018). This study was carried out by using Silica gel as a storage material in solar-assisted desiccant air conditioning system.

The COP of this desiccant-based cooling system is strongly contingent on the operating parameters and can be increased by unbalancing the flow of air through the dehumidifier (Wu et al., 2019). When performing the second law analysis, the reversible COP of this system is found to be 2.64 while operating in ventilation mode and around 3.03 on recirculation mode. In ventilation mode, COP can be improved 10%–15% by unbalancing the air flow. Moreover, in recirculation COP increases by 50% (Anisimov et al., 2015). A numerical technique is used to execute the thermal calculations of an indirect evaporative cooler (IEC) based on a model of combined parallel heat and mass exchanger with counter flow regenerative arrangement. The results calculated from mathematical simulation show the high effectiveness of the presented model (Kilkovský, 2020).

In Hong Kong, a hybrid configuration of solar-assisted liquid desiccant dehumidifier (LDD) along with indirect evaporative cooler was carried out in an elevated temperature region with a high humidity ratio. The results show that, by increasing the solar collector's area, the cooling capacity as well as moisture removal rate were increased. Moreover, the air conditioning system based on LDD indirect evaporative cooler saves about 47% energy consumption when compared with a mechanical vapor compression refrigeration system (Chen et al., 2017).

From the above mentioned studies, it is clear that the working ability of the IEC is significantly affected by the humidity level of air. Furthermore, it is clear that the cooling capacity and moisture removal rate can be increased by increasing the regeneration temperature. To achieve such configuration, solar thermal collectors as a renewable energy source are used in association with SDD-IEC. Dew point evaporative cooling is a perfect option for removing the sensible heat that is produced by electronics, data centers, and electric cars since it uses so little power (Lin et al., 2021).

Due to higher building demand for HVAC applications, there is a need to use renewable energy resources for these applications to mitigate an intensive use of energy. Solar desiccant evaporative cooling is an emerging technique that can be more helpful in severe climate conditions with minimum energy requirement for its operation. In the majority of studies carried out on SDD-IEC, a cross flow heat exchanger was usually used. In this study, however, a counter flow heat exchanger was used as an indirect evaporative cooler and an integrated system of thermal collectors (evacuated tube collectors and Flat Plate Collectors) were utilized for regeneration process through hot water. The current work is carried out in UET Taxila (Latitude: 33.7660 Longitude: 72.8250), where temperature in the summer is high and the climate is humid. It is worth mentioning that the present study experimentally evaluates the effect of operational parameters such as humidity, temperature, and rotational speed of desiccant wheel on the performance of the system. The current study is novel in terms of parametric analysis of SDD-IEC by using EES, experimental evaluation of solar water heating system in term of collector's efficiency, temperature profile and sensible heat factor, and validation of key aspects of the cooling system.

2 Materials and methods

2.1 Experimental setup

The experimental setup has a hybrid configuration of solar water heating system and solid desiccant indirect evaporative cooler.

2.1.1 Solar array for water heating

Solar thermal collectors were used as a renewable source of energy to heat water to regenerate the desiccant wheel. Solar thermal collectors consist of a hybrid configuration of flat plate collectors (FPCs) and evacuated tube collectors along with a storage tank. The FPCs are the cheapest source among collectors and it does not require the tracking of the Sun. FPCs are designed for moderate temperatures. To achieve the required regenerative temperature, FPCs are linked with evacuated tube collectors (ETCs). The space between glass and absorber is evacuated to reduce the convection losses in ETC.

FIGURE 1
Experimental setup of solar thermal collectors.

The cover area of flat plate and ETC is 4.7 and 6.8 m^2 respectively. An auxiliary source consisting of electric heaters is also used for backup source. The collector's arrays are mounted on the roof of energy engineering department UET Taxila. To minimize the environmental impacts on the efficiency of collectors, the rubber foam of thickness 5 mm is used to insulate the loop circuit. To record the temperature values at different points of the solar water heating system, K type thermocouples are used. However, to control the water flow rate through the collector's ball, valves are installed at various points. Similarly, a pressure relief valve is used in the tank to release steam. The solar water heating system works continuously throughout the day. The set value for the temperature of hot water is 75 C. The experimental setup of solar collectors is shown in Figure 1. The intensity of solar light is measured using a pyranometer.

2.1.2 Cooling system

The cooling system comprises of a solid desiccant dehumidifier, enthalpy wheel, indirect evaporative cooler (counter flow heat and mass exchanger), direct evaporative cooler, and heating coils. The system handles the latent as well as sensible load separately. A solid desiccant dehumidifier is used to handle the latent load of the system whereas the indirect evaporative cooler handles the sensible load. The whole system is separated into two portions: the process side and the regeneration side. This experimental setup can be viewed in Figure 2.

2.2 Experimental procedure

Before performance evaluation of the system, the sensors are calibrated and tested initially with different operating conditions. The cooling system was tested by varying the mass flow rate, humidity level of inlet air, rpm of desiccant wheel, and regeneration temperature. After measuring the system's initial performance, the experimental data was collected by running the system. The solar loop was stared at 8 a.m. so that it can achieve the required regenerative temperature. The desiccant cooling system works from 9 a.m. to 4 p.m. The schematic diagram of the integrated solar-assisted solid desiccant dehumidifier in the direct evaporative cooler has been represented in Figure 3. The ambient air is forced to enter in the system at 1 through a fan, goes through the desiccant wheel in the process side, and leaves at 2 as shown in Figure 3. In this process, the humidity level of air is decreased but the temperature rises up (latent heating of ambient air). Further, from processes 2–3 the dehumidified air passes through the heat recovery wheel for temperature reduction. Then air is passed through the indirect evaporative cooler for sensible cooling and leaves the system at 4. Afterwards, on the regeneration side, the room air is sensibly cooled in the direct evaporative cooler and leaves at 6. Then the heat exchange phenomena take place between the process air and regeneration air from 6 to 7. Later, the regeneration air achieves the required regenerative temperature of desiccant wheel (70°C) by passing through the heating coils. At last, from 7 to 8 this heated air moves over the desiccant wheel to absorb the moisture content in it and leave the system at 9.

2.3 Thermal resistance model

The thermal resistance model given in Figure 4 illustrates the modes of heat transfer in an evacuated tube collector. Heat is transferred between fluid and receiver through convection.

FIGURE 2
Experimental setup of the solid desiccant indirect evaporative cooler.

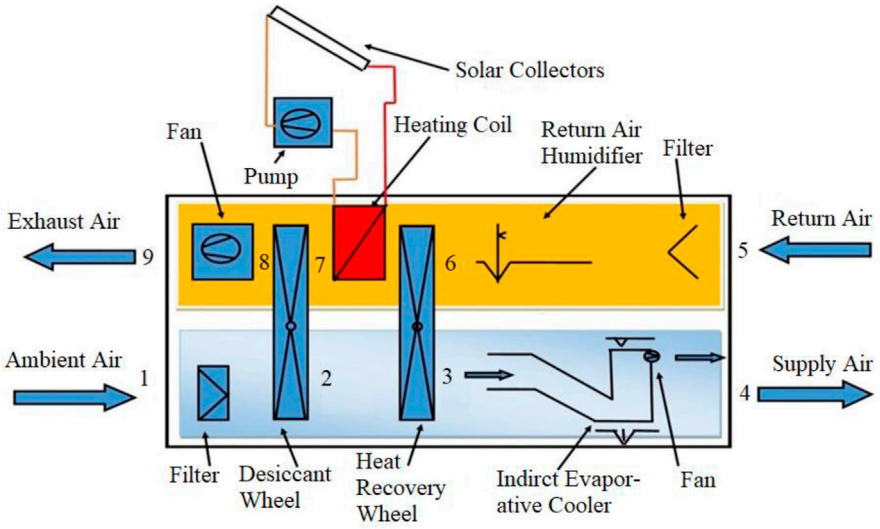

FIGURE 3
Schematic of solar-assisted desiccant indirect evaporative cooler.

3 Measuring instruments

At various points in the solar-assisted desiccant air conditioning system (SDAC) the parameters of air were measured to analyze the system performance. The parameters that were measured were humidity, temperature, and air flow rate. The pressure difference measured from manometers gives the air flow rate of process air and the regeneration air. DHT-22 Sensors were used to measure the temperature and humidity level of the air along with a data logger based on the Arduino program. The intensity of solar light was measured by using LI-19 data logger.

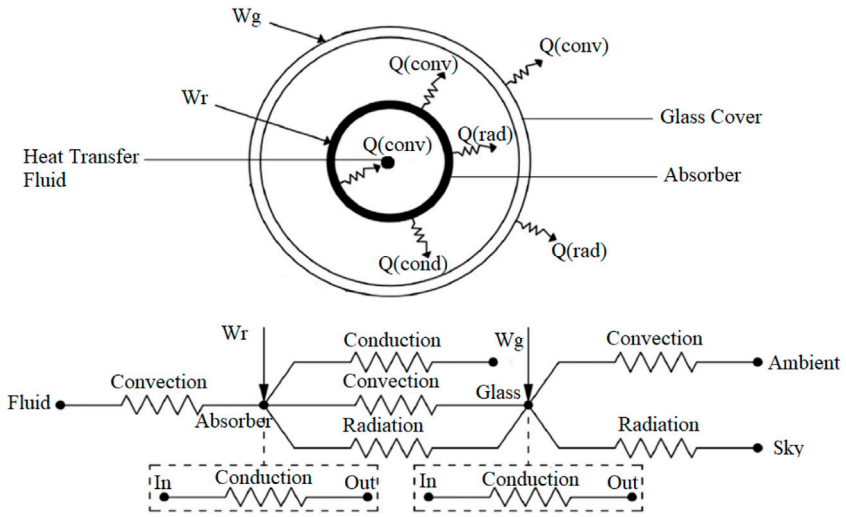

FIGURE 4
Thermal resistance model of evacuated tube collector.

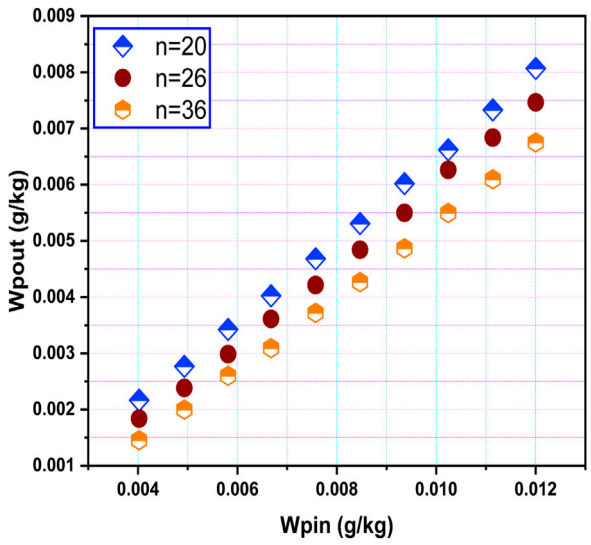

FIGURE 5
Effect of W_{pin} on W_{pout} for Silica gel desiccant.

4 Results and discussion

4.1 Parametric analysis of desiccant wheel

In this section, parametric analysis of desiccant wheel for desiccant material silica gel SiO2 has been done by EES software.

4.1.1 Effect of process inlet humidity ratio

The Process inlet parameters like W_{pin} and T_{pin} influence the other parameters of desiccant wheel. The effect of W_{pin} on W_{pout} for Silica gel desiccant wheel (DW) is shown in Figure 5. The analysis is carried out on rotation speeds of the desiccant wheel i.e., 20, 26, and 36 rph. The W_{pin}, has direct influence on the W_{pout}. At higher W_{pin} more moisture is removed in the air. Thus, the outlet humidity increases with inlet humidity, which causes higher moisture removal. Additionally, it can be viewed that the dehumidification of air is more favorable at lower rotation speeds. When considering the different speeds of the desiccant wheel, the graph shows that at the lowest speed the W_{pout} is greater as compared to the highest speed of rotation at each W_{pin}. This shows the moisture removal by desiccant increases with the increase of speed.

4.1.2 Effect of regeneration temperature

Regeneration air always has a dominant role on specifying process outlet conditions. The effect of T_{reg} on W_{pout} and DW is as shown in Figure 6. Dehumidification by desiccant wheel is mostly exaggerated by regeneration temp. Raising the Treg improves the moisture removal capability of the desiccant material which results in lowering the process outlet humidity ratio because desiccant wheel is regenerated in a better way. However, the rotation speed also has an important effect on W_{pout}. At lower speeds dehumidification is minimum as compared to high speed, which results in higher humidity ratio on the process outlet.

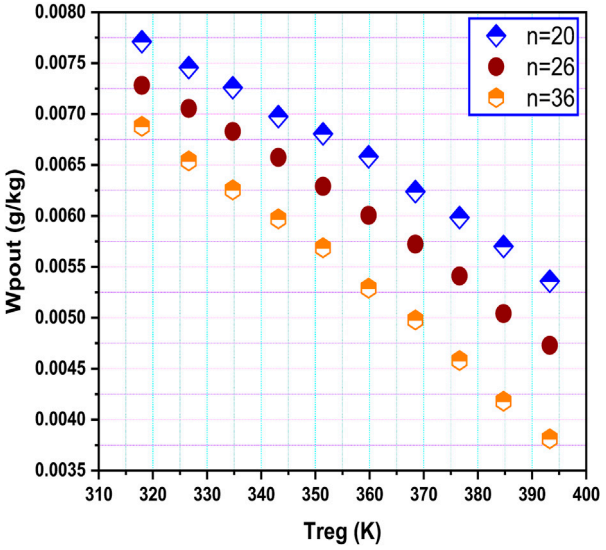

FIGURE 6
Effect of regeneration temperature on process outlet humidity ratio.

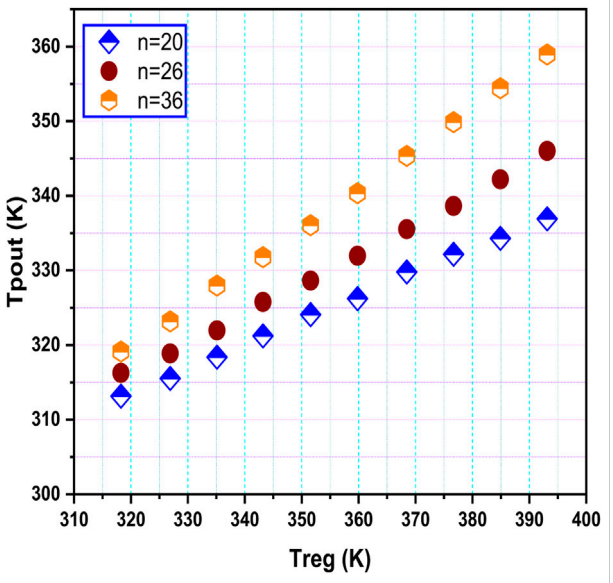

FIGURE 7
Effect of regeneration temperature on process outlet Temperature.

4.1.3 Effect of regeneration temperature on process outlet temperature

Additionally, T_{reg} affects T_{pout} and DT of process air outlet and is as shown in Figure 7. Increases in T_{reg} increase the outlet temperature of process air T_{pout}. High T_{reg} gives high T_{pout}. This is due to the increase in heat of adsorption with additional latent heat to sensible heat conversion. On the other hand, at low T_{reg} the outlet temp T_{pout} is close to each other at each rotation of the wheel but shows a significant effect at high Treg on the rotation speeds. At high Treg and N, DT of the air dominates as compared to less T_{reg} and N.

4.1.4 Effect of rotation speed of desiccant wheel

The speed "n" of desiccant wheel influences the W_{pout} of the process outlet air with different W_{pin}, $T_{sin,}$ and T_{reg}. The effect of speed N on W_{pout} and W at different W_{pin} is as shown in Figure 8. The rotational speed has an important role in the accomplishment of the dehumidification process at a low rotation speed.

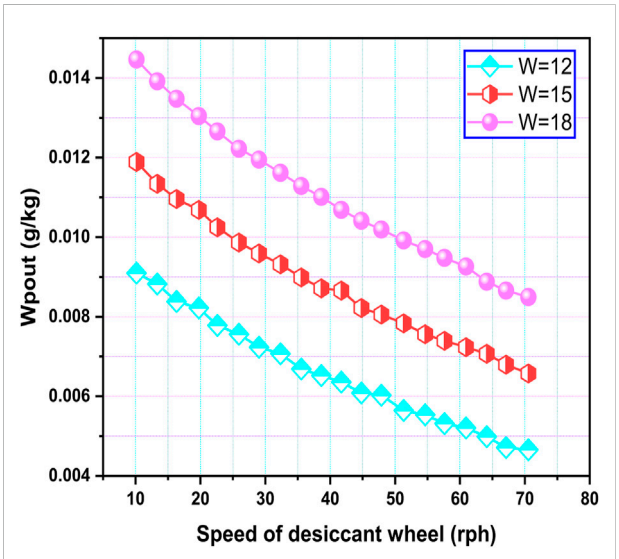

FIGURE 8
Effect of rotational speed of the wheel on process outlet humidity ratio.

4.1.5 Variation of temperature and cooling capacity of solar desiccant coolings

The process inlet T_{pin} and the process outlet temperature of M-Cycle $T_{po\ (mc)}$ along with cooling capacity Q_c is shown in Figure 9: Variation of cooling capacity and temperatures of SDC. Increases in inlet temperature results in a decrease in inlet humidity ratio, so the cooling capacity increases. The process outlet temperature increases with increases in inlet temperature. The maximum cooling capacity achieved is 4.6 kW.

4.2 Analysis of thermal collectors

4.2.1 Thermal energy shares

The solar thermal energy flows vary as the function of time exists in Figure 10: Variation of thermal Energy flows with respect to time. $Q_{(fall)}$ is the solar thermal energy on earth and $Q_{(sol)}$ is the thermal energy provided by the solar thermal collectors. Due to

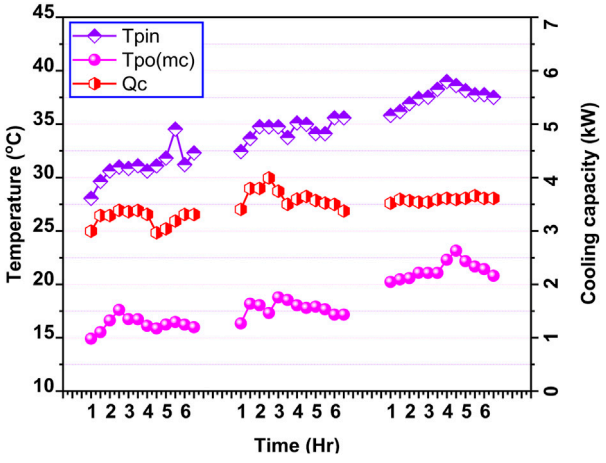

FIGURE 9
Variation of cooling capacity and temperatures of SDC.

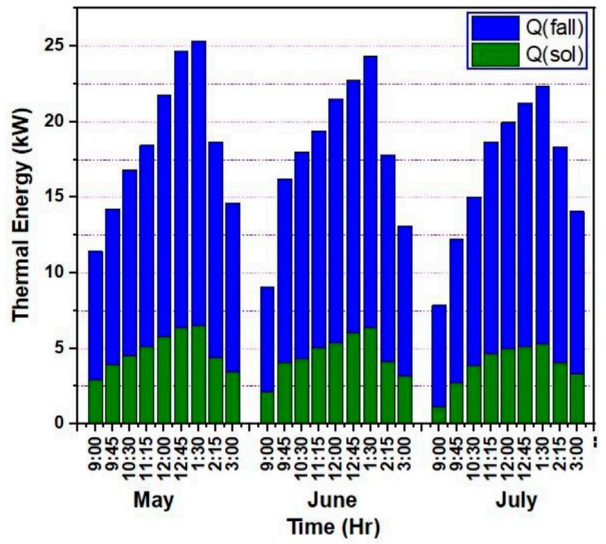

FIGURE 10
Variation of thermal Energy flows with respect to time in the year (2017)

higher intensities of solar light in the month of May, the $Q_{(fall)}$ is high. Moreover, the energy obtained from the collectors is also high in this month as compared to others. The maximum and minimum energy gain is 6.58 and 1.22 kW respectively. The average energy gain for three selected days of different months is 4.3 kW. While the average energy fall on the earth's surface is 9.42 kW.

4.2.2 Temperature profile of solar water heating system

Another aspect of utilizing solar energy is for the regeneration purposes of desiccant wheel through solar

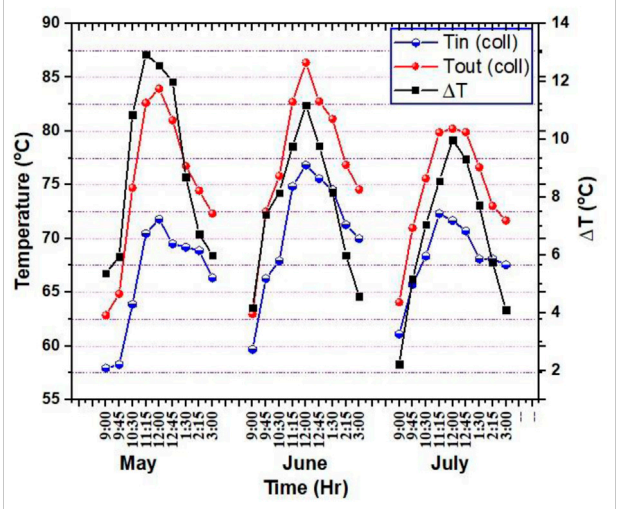

FIGURE 11
Variation of temperature of collectors with respect to time in three different months.

thermal collectors. The variation of temperatures of a solar water heating system and the time is shown in Figure 11: Variation of temperature of collectors with respect to time of three different months. The intensity of solar radiation strongly affects the output of collectors. As seen from the figure, the temperature gradient is low in the morning because of low solar intensity in the morning. The maximum temperature outlet achieved through the collector is 87.49°C. However, the maximum temperature gain is 12.33°C, with solar intensity of 868 W/m^2. While the minimum temperature gain is 2.33°C, corresponding to solar intensity of 351 W/m^2. For 3 days the average outlet temperature is 76.33°C, with an average solar intensity of 671 W/m^2.

4.2.3 Effect of solar intensity on collector's efficiency

Solar irradiance influences the efficiency of collectors. Increases in solar irradiance results in high efficiency of collectors. Variation of collector efficiency along with solar irradiance is shown in Figure 12: Variation of collector efficiency with respect to solar irradiance. When the solar intensity is low the efficiency decreases. The observation shows that maximum collector efficiency is 56% with solar irradiance of 868 W/m^2. In the month of July, minimum efficiency was observed at 9 a.m. at 22%, corresponding to solar intensity of 351 W/m^2. The average resulting efficiency for 3 days is 45%.

The observation shows that the moisture removal rate in desiccant wheel decreases as the rotational speed of the wheel increases for both process and regeneration streamline. When the inlet temperature of the process stream line increases, inlet

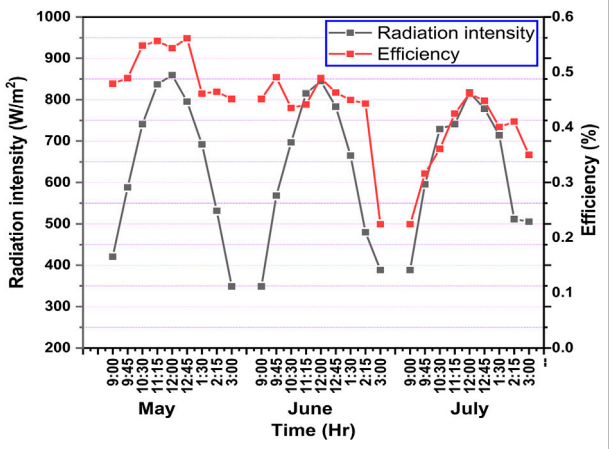

FIGURE 12
Variation of collector efficiency with respect to solar irradiance.

humidity ratio decreases, which corresponds to enhancing the cooling capacity of the system. Moreover, the collector's efficiency is dependent on the intensity of solar irradience.

5 Conclusion

The performance of an integrated solar desiccant cooling (SDC) system was experimentally monitored for three selected days in summer months under the hot and humid climate of Taxila, Pakistan.

- The experimental results show that, for thermal comfort conditions, the SDC system gives better output. The other systems that were based on only indirect evaporative cooler do not have the capability to produce such thermal comfort in the severe weather conditions of summer.
- The maximum outlet temperature of collectors is 87°C. However, the maximum reputed efficiency is 56%. The minimum outlet temperature from the M-Cycle is 14.7°C with a low inlet temperature of 27°C.
- An increase in the process inlet temperature results in a decrease in inlet humidity ratio, hence the cooling capacity enhances.
- The Maximum monitored cooling capacity of the system is 4.6 kW. The parametric analysis shows that the moisture removal rate is high with a low speed of rotation of desiccant wheel or vise versa.
- At 20 rph of desiccant wheel, the moisture removal rate is tremendous.
- The current study concludes that the energy consumption by the system was minimized when utilizing solar energy to regenerate the desiccant material through thermal collectors.

Data availability statement

The raw data supporting the conclusion of this article will be made available by the authors, without undue reservation.

Author contributions

AD (Writing—Original Draft; Data Curation), AT (Writing—Review and Editing; Ideas; formulation or evolution of overarching research goals and aims), MM (Formal Analysis, Writing—Review and Editing), MA (Writing—Review and Editing), AY (Writing—Review and Editing), GC (Writing—Review and Editing), LR (Writing—Review and Editing; Software), AA (Writing—Review and Editing; Funding acquisition), MK (Writing—Review and Editing).

Acknowledgments

The current work acknowledges the research Renewable Energy Research and Development Center (RERD) UET Taxila Pakistan.

Conflict of interest

The authors declare that the research was conducted in the absence of any commercial or financial relationships that could be construed as a potential conflict of interest.

Publisher's note

References

Abdelkareem, M. A., Assad, M. E. H., Sayed, E. T., and Soudan, B. (2018). Recent progress in the use of renewable energy sources to power water desalination plants. *Desalination* 435, 97–113. doi:10.1016/j.desal.2017.11.018

Alghamdi, J. (2017). *Thermal energy storage technologies for zero carbon housing in the UK*. Wales: Cardiff University.

Amber, K. P., Ahmad, R., Chaudhery, G. Q., Khan, M. S., Akbar, B., and Bashir, M. A. (2020). Energy and environmental performance of a higher education sector – a case study in the United Kingdom. *Int. J. Sustain. Energy* 6451, 497–514. doi:10.1080/14786451.2020.1720681

Angrisani, G., Roselli, C., Sasso, M., Tariello, F., and Vanoli, G. P. (2016). Performance assessment of a solar-assisted desiccant-based air handling unit considering different scenarios. *Energies* 9 (9), 724. doi:10.3390/en9090724

Anisimov, S., Pandelidis, D., and Jedlikowski, A. (2015). Performance study of the indirect evaporative air cooler and heat recovery exchanger in air conditioning system during the summer and winter operation. *Energy* 89, 205–225. doi:10.1016/j.energy.2015.07.070

Bahadori-Jahromi, A., Rotimi, A., Mylona, A., Godfrey, P., and Cook, D. (2017). Impact of window films on the overall energy consumption of existing UK hotel buildings. *Sustainability* 9 (5), 731. doi:10.3390/su9050731

Baral, S., Kim, D., Yun, E., and Kim, K. C. (2015). Experimental and thermoeconomic analysis of small-scale solar organic Rankine cycle (SORC) system. *Entropy* 17 (4), 2039–2061. doi:10.3390/e17042039

Berbel, J., and Posadillo, A. (2018). Review and analysis of alternatives for the valorisation of agro-industrial olive oil by-products. *Sustainability* 10 (1), 237. doi:10.3390/su10010237

Brandt, A. R. (2011). Oil depletion and the energy efficiency of oil production: the case of California. *Sustainability* 3 (10), 1833–1854. doi:10.3390/su3101833

Chen, Y., Yu, W., Wu, P., Yang, H., and Luo, Y. (2017). Energy performance of solar assisted desiccant enhanced evaporative cooling air conditioning system. *Procedia Eng.* 205, 4195–4202. doi:10.1016/j.proeng.2017.10.181

Chen, Q., Kum Ja, M., Burhan, M., Akhtar, F. H., Shahzad, M. W., Ybyraiymkul, D., et al. (2021). A hybrid indirect evaporative cooling-mechanical vapor compression process for energy-efficient air conditioning. *Energy Convers. Manag.* 248, 114798. doi:10.1016/j.enconman.2021.114798

Chen, Q., Ja, M. K., Burhan, M., Shahzad, M. W., Ybyraiymkul, D., Zheng, H., et al. (2022). Experimental study of a sustainable cooling process hybridizing indirect evaporative cooling and mechanical vapor compression. *Energy Rep.* 8, 7945–7956. doi:10.1016/j.egyr.2022.06.019

Choudhary, P., and Srivastava, R. K. (2019). Sustainability perspectives-a review for solar photovoltaic trends and growth opportunities. *J. Clean. Prod.* 227, 589–612. doi:10.1016/j.jclepro.2019.04.107

Cui, X., Sun, L., Zhang, S., and Jin, L. (2019). On the study of a hybrid indirect evaporative pre-cooling system for various climates. *Energies* 12 (23), 4419. doi:10.3390/en12234419

Farooq, M., Saeed, M. A., Imran, M., Uddin, G. M., Asim, M., Bilal, H., et al. (2019). CO2 capture through electro-conductive adsorbent using physical adsorption system for sustainable development. *Environ. Geochem. Health* 42, 1507–1515. doi:10.1007/s10653-019-00318-2

González, J., and Fiorito, F. (2015). Daylight design of office buildings: Optimisation of external solar shadings by using combined simulation methods. *Buildings* 5 (2), 560–580. doi:10.3390/buildings5020560

Halim, M. A. (2013). Harnessing sun's energy with quantum dots based next generation solar cell. *Nanomaterials* 3 (1), 22–47. doi:10.3390/nano3010022

Hu, S.-C., Shiue, A., Chiu, Y.-S., Wang, A., and Chen, J. (2016). Simplified heat and mass transfer model for cross-flow and countercurrent flow packed bed tower dehumidifiers with a liquid desiccant system. *Sustainability* 8 (12), 1264. doi:10.3390/su8121264

Jamil, M. A., Bin Xu, B., Dala, L., Sultan, M., Jie, L., and Shahzad, M. W. (2021). Experimental and normalized sensitivity based numerical analyses of a novel humidifier-assisted highly efficient indirect evaporative cooler. *Int. Commun. Heat Mass Transf.* 125, 105327. doi:10.1016/j.icheatmasstransfer.2021.105327

Kabeel, A. E., Abdelgaied, M., and Al Ali, M. (2018). Energy saving potential of a solar assisted desiccant air conditioning system for different types of storage. *Environ. Prog. Sustain. Energy* 37 (4), 1448–1454. doi:10.1002/ep.12795

Kashif, M., Niaz, H., Feng, Y., Niaz, Y., Ali, I., Sultan, M., et al. (2020). Study on desiccant and evaporative cooling systems for livestock thermal comfort: theory and experiments. *Energies* 13, 2675. doi:10.3390/en13112675

Kashif Shahzad, M., Ali, M., Ahmed Sheikh, N., Qadar Chaudhary, G., Shahid Khalil, M., and Rashid, T. U. (2018). Experimental evaluation of a solid desiccant system integrated with cross flow Maisotsenko cycle evaporative cooler. *Appl. Therm. Eng.* 128, 1476–1487. doi:10.1016/j.applthermaleng.2017.09.105

Khan, Z., Ali, M., Jinyu, L., Shahbaz, M., and Siqun, Y. (2020). Consumption-based carbon emissions and trade nexus : Evidence from nine oil exporting countries. *Energy Econ.* 89, 104806. doi:10.1016/j.eneco.2020.104806

Kilkovský, B. (2020). Review of design and modeling of regenerative heat exchangers. *Energies* 13 (3), 759. doi:10.3390/en13030759

Knight, K. W., and Schor, J. B. (2014). Economic growth and climate change: a cross-national analysis of territorial and consumption-based carbon emissions in high-income countries. *Sustainability* 6 (6), 3722–3731. doi:10.3390/su6063722

Leng, G., Navarro, H., Yu, Q., Wellio, G., Qiao, G., Li, C., et al. (2006). Design of composite materials/devices for thermal storage–A critical review. *Veruscript Funct. Nanomater.* 2, 1–28. doi:10.22261/ghv5w9

Lin, J., Shahzad, M. W., Li, J., Long, J., Li, C., and Chua, K. J. (2021). A robust physics-based model framework of the dew point evaporative cooler: From fundamentals to applications. *Energy Convers. Manag.* 233, 113925. doi:10.1016/j.enconman.2021.113925

Lu, S., Wang, W., Wang, S., and Cochran Hameen, E. (2019). Thermal comfort-based personalized models with non-intrusive sensing technique in office buildings. *Appl. Sci. (Basel).* 9 (9), 1768. doi:10.3390/app9091768

Ma, Y., Saha, S. C., Miller, W., and Guan, L. (2017). Comparison of different solar-assisted air conditioning systems for Australian office buildings. *Energies* 10 (10), 1463. doi:10.3390/en10101463

Mahmud, M. A., Huda, N., Farjana, S. H., and Lang, C. (2018). Environmental impacts of solar-photovoltaic and solar-thermal systems with life-cycle assessment. *Energies* 11 (9), 2346. doi:10.3390/en11092346

Moriarty, P., and Honnery, D. (2019). Energy efficiency or conservation for mitigating climate change? *Energies* 12 (18), 3543. doi:10.3390/en12183543

Murphy, D. J., Hall, C. A. S., Dale, M., and Cleveland, C. (2011). Order from chaos: a preliminary protocol for determining the EROI of fuels. *Sustainability* 3 (10), 1888–1907. doi:10.3390/su3101888

Pérez-Lombard, L., Ortiz, J., and Pout, C. (2008). A review on buildings energy consumption information. *Energy Build.* 40 (3), 394–398. doi:10.1016/j.enbuild.2007.03.007

Petri, I., Kubicki, S., Rezgui, Y., Guerriero, A., and Li, H. (2017). Optimizing energy efficiency in operating built environment assets through building information modeling: a case study. *Energies* 10 (8), 1167. doi:10.3390/en10081167

Shahzad, M. W., Burhan, M., Ang, L., and Ng, K. C. (2017). Energy-water-environment nexus underpinning future desalination sustainability. *Desalination* 413, 52–64. doi:10.1016/j.desal.2017.03.009

Sikder, S. K., Eanes, F., Asmelash, H. B., Kar, S., and Koetter, T. (2016). The contribution of energy-optimized urban planning to efficient resource use–A case study on residential settlement development in dhaka city, Bangladesh. *Sustainability* 8 (2), 119. doi:10.3390/su8020119

Wang, Q., and Wang, L. (2020). Renewable energy consumption and economic growth in OECD countries : a nonlinear panel data analysis. *Energy* 207, 118200. doi:10.1016/j.energy.2020.118200

Wu, H., Salles, F., and Zajac, J. (2019). A critical review of solid materials for low-temperature thermochemical storage of solar energy based on solid-vapour adsorption in view of space heating uses. *Molecules* 24 (5), 945. doi:10.3390/molecules24050945

Wu, H., Xu, L., Ren, S., Hao, Y., and Yan, G. (2020). How do energy consumption and environmental regulation affect carbon emissions in China ? New evidence from a dynamic threshold panel model. *Resour. Policy* 67, 101678. doi:10.1016/j.resourpol.2020.101678

Wu, J., Abban, O. J., Boadi, A. D., Haris, M., Ocran, P., and Addo, A. A. (2020). Exploring the relationships among CO 2 emissions , urbanization , economic growth , economic structure , energy consumption , and trade along the BRI based on income classification. *Energy, Ecol. Environ.* 6, 213–231. doi:10.1007/s40974-020-00176-0

10.3389/fenrg.2022.979942

Nomenclature

T Temperature (°C)

W Humidity Ratio (g/kg)

Qc Cooling capacity (kW)

N Speed of rotation of desiccant wheel (rpm)

$\mathbf{Q_{(sol)}}$ Thermal energy from Collectors (kW)

$\mathbf{Q_{(fall)}}$ Thermal energy fall on earth (kW)

Eta Efficiency of Collectors

$\Delta\mathbf{T}$ Temperature gain (°C)

Subscripts

$\mathbf{P_{in}}$ Process inlet conditions

$\mathbf{P_{out}}$ Process outlet conditions

reg Regeneration conditions

$\mathbf{in_{(coll)}}$ Collector Inlet Conditions

$\mathbf{o_{(coll)}}$ Collector outlet conditions

frontiers | Frontiers in Energy Research

TYPE Original Research
PUBLISHED 10 October 2022
DOI 10.3389/fenrg.2022.1017293

OPEN ACCESS

EDITED BY
Muhammad Amjad,
University of Engineering and Technology, Lahore, Pakistan

REVIEWED BY
Amjad Hussain,
University of Engineering and Technology, Lahore, Pakistan
Muhammad Farhan,
University of Engineering and Technology, Lahore, Pakistan
Yanwei Hu,
Harbin Institute of Technology, China

*CORRESPONDENCE
Gwi Hyun Lee,
ghlee@kangwon.ac.kr

SPECIALTY SECTION
This article was submitted to Solar Energy, a section of the journal Frontiers in Energy Research

RECEIVED 11 August 2022
ACCEPTED 23 September 2022
PUBLISHED 10 October 2022

CITATION
Tamoor M, Hussain MI, Bhatti AR, Miran S, Arif W, Kiren T and Lee GH (2022), Investigation of dust pollutants and the impact of suspended particulate matter on the performance of photovoltaic systems.
Front. Energy Res. 10:1017293.
doi: 10.3389/fenrg.2022.1017293

Investigation of dust pollutants and the impact of suspended particulate matter on the performance of photovoltaic systems

Muhammad Tamoor[1], Muhammad Imtiaz Hussain[2], Abdul Rauf Bhatti[1], Sajjad Miran[3], Waseem Arif[3], Tayybah Kiren[4] and Gwi Hyun Lee[5]*

[1]Department of Electrical Engineering and Technology, Government College University Faisalabad, Faisalabad, Pakistan, [2]Agriculture and Life Sciences Research Institute, Kangwon National University, Chuncheon, Korea, [3]Department of Mechanical Engineering, University of Gujrat, Gujrat, Pakistan, [4]Department of Computer Science (RCET), University of Engineering and Technology, Lahore, Pakistan, [5]Interdisciplinary Program in Smart Agriculture, Kangwon National University, Chuncheon, Korea

The purpose of this study is to investigate the potential of airborne particulate matter (PM10 and PM2.5) and its impact on the performance of the photovoltaic (PV) system installed in the Sargodha region, being affected by the crushing activities in the hills. More than 100 stone crushers are operating in this region. Four stations within this region are selected for taking samples during the summer and winter seasons. Glass–fiber papers are used as a collection medium for particulate matter (PM) in a high-volume sampler. The concentration of PM is found above the permissible limit at all selected sites. The chemical composition, concentration, and the formation of particulate matter (PM10 and PM2.5) layers on the surface of the photovoltaic module varies significantly depending on the site's location and time. The accumulation of PM layers on the PV module surface is one of the operating environmental factors that cause significant reduction in PV system performance. Consequently, it leads to power loss, reduction of service life, and increase in module temperature. For the PV system's performance analysis, two PV systems are installed at the site, having higher PM concentration. One system is cleaned regularly, while the other remains dusty. The data of both PV systems are measured and compared for 4 months (2 months for the summer season and 2 months for the winter season). It is found that when the level of suspended particulate matter (PM10 and PM2.5) increases, the energy

Abbreviations: PV, photovoltaic; W, watt; kW, kilowatt; kWh, kilowatt hour; MWh, megawatt hour; A, ampere; V, volt; SLD, single-line diagram; PR, performance ratio; AC, alternating current; DC, direct current; MPPT, maximum power point tracking; NOCT, nominal operating cell temperature; GHI, global horizontal irradiance; POA, plane of the array; DHI, diffuse horizontal irradiance; DNI, direct normal irradiance; Ta, ambient temperature; Tm, PV module temperature; Ws, wind speed at proposed site; E, solar irradiation on photovoltaic module; PM, particulate matter; NAAQS, National Ambient Air Quality Standard; EPA, Environmental Protection Agency; CI, cleanness index; and ASHRAE, American Society of Heating, Refrigerating, and Air-Conditioning Engineers.

generation of the dusty PV system (compared to the cleaned one) is reduced by 7.48% in May, 7.342% in June, 10.68% in December, and 8.03% in January. Based on the obtained results, it is recommended that the negative impact of PM on the performance of the PV system should be considered carefully during the decision-making process of setting solar energy generation targets in the regions with a high level of particulate matter.

KEYWORDS

particulate matter, photovoltaic system (PV system), solar irradiation, ambient air quality, PM10−2.5

1 Introduction

Solar energy is the most important and primary renewable energy source due to its free availability and environmental friendliness (Thapar, 2019). In the next few years, the benefits and advantages of solar energy, either directly or indirectly, will be observed by everyone globally (Bono, 2018). Solar energy technologies and applications that have been widely used include photovoltaic systems (Chaichan and Kazem, 2018), concentrated solar power stations (Xingping et al., 2019), solar water heating system (Maraj et al., 2019), solar water desalination (Chaichan and Kazem, 2015), Trombe walls (Martín-Consuegra et al., 2021), solar air heating, and space conditioning (Ojike and Okonkwo, 2019). Due to the declining cost and higher electrical efficiency of photovoltaic modules, there has been growing interest maximize the production of solar energy (Schleifer et al., 2022; Tamoor et al., 2022). Hachich et al. (2019) showed that the electrical efficiency of commercial and modern solar cells increases to 20%. Additionally, the photovoltaic modules can also be installed in a number of locations, including the building's envelope (Middelhauve et al., 2021), plain areas, mountains, oceans, and deserts. They can also operate as standalone or hybrid with other systems (such as wind, diesel generators, and batteries) (Kazem et al., 2017; Jain and Sawle, 2021; Chen and Zhu, 2022; Nkuriyingoma et al., 2022). Among the various practical applications of renewable energy sources, the photovoltaic (PV) system has attracted attention and is widely used in the field of energy generation due to its low operation, maintenance costs, and relatively high energy conversion efficiency (Gil et al., 2020; Soomar et al., 2022). In many countries, photovoltaic conversion of solar energy has begun to make a significant contribution to energy generation, and more than 91% of the global photovoltaic market relies on crystalline silicon-based solar cells. Crystalline silicon solar cells have a current efficiency record of 26.7%, against an intrinsic limit of 29% (Andreani et al., 2019). Many developing and developed countries are planning to shift to renewable energy resources to meet the energy demands of growing populations and improve the operation of national utility grids (Tamoor et al., 2020; Tamoor et al., 2021; Miran et al., 2022; Tamoor et al., 2022; Tamoor et al., 2022; Tamoor et al., 2022). However, the performance of all types of photovoltaic modules is affected by a large number of environmental factors (air temperature, wind speed, the angle of incident irradiation, solar radiation intensity, solar radiation spectrum, air pollution, snow, aging, dirt, and shadows) (Hassan et al., 2016; Kazem et al., 2017; Chaichan and Kazem, 2018). Fouad et al. (2017) proposed that the performance of photovoltaic modules can be affected by more than 30 factors, which are mainly related to the environment, including solar irradiation, dust accumulation, PV module temperature, and shading. One of the most important factors that affect the energy conversion of photovoltaic modules in many regions is dust accumulation (Chaichan et al., 2015). Because dust particles lower and disperse the intensity of the solar irradiation impacting on the photovoltaic modules, as a result, the conversion efficiency is reduced by accumulated dust. It was observed that the rate of dust accumulation on photovoltaic modules depends on a number of factors, like local weather conditions, airborne particle concentration, type and size of particle distribution, composition, shape, and density (Javed e t al., 2017; Cui et al., 2021). Dust accumulation on the surface of any photovoltaic module will depend on the dust type, weather, surrounding environment, PV module characteristics, and installation design (Konyu et al., 2020). The efficiency and output energy of a PV module would decline as the rate of dust deposition on the module surface increases. In desert regions, dust accumulation reduces the total output energy of photovoltaic modules by an average of almost 40% within a year (Ahmed and Massier, 2019). The solar energy incident on the surface of Earth in 1 hour is nearly equal to the total consumption of Earth in 1 year (Tomin et al., 2022). When solar irradiation passes through the atmosphere, it is absorbed by solid particles and droplets in the atmosphere and reflected by water vapor and air molecules, resulting in significant loss of energy. However, solar radiation is absorbed by dust and other pollutants and scattered backward, resulting in a decrease in direct solar radiation and an increase in diffuse solar radiation. Hence, compared to clean air in non-industrial rural areas, cities and polluted areas generally receive less total solar irradiation (Darwish et al., 2018). Another important aspect that greatly affects the rate of dust deposition on the PV module is how close it is to an area where dust is most likely to be airborne (Cheema et al., 2021). The particle size distribution of dust deposited on the surface of photovoltaic modules and its chemical and physical

properties have a major impact on the degradation in the performance of the photovoltaic module (Kaldellis and Kapsali, 2011). The size of deposited solid particles has a significant impact on the absorption and scattering of incident radiation on the photovoltaic module, resulting in a decrease in the efficiency of photovoltaic modules. Larger particles are more likely to resuspend with the airflow, promoting the deposition of smaller particles. Compared with large particles with the same quality and volume of the deposited dust, fine/small particles have a larger specific surface area and have a greater impact in degradation of the photovoltaic cell performance (Weber et al., 2014). The size of dust particles gathered on the surface is divided into three different ranges: small-sized particles (up to 5.0 μm in diameter) that come from large-spaced areas, medium particles (20.0 μm–40.0 μm in diameter) that contain dust deposits from regional sources, and large-sized particles (50.0 μm–70 μm) that come from automobiles, humans, and livestock. Gravity or other forces related to heat transfer and fluid flow causes solid particles or droplets to accumulate on a PV module surface (Jiang and Lu, 2015). The performance of photovoltaic modules is reduced by solid particles. This causes power losses, which reduces the system efficiency and increases temperature, which further reduces system performance and service life. The chemical composition of deposited dust, its concentration, and the creation of a dust layer on the photovoltaic surface vary greatly depending on location and time (Styszko et al., 2019). In addition, after the East Asian monsoon, PM concentrations vary seasonally due to major fluctuations in rainfall and regional circulation (Lou et al., 2019). The impact of dust deposition on the performance of PV modules is observable, but the dust composition might be different depending on the location, so the degree of reduction in the photovoltaic module efficiency may vary from location to location (Andrea et al., 2019). However, the solar panel manufacturer typically guarantees 80% of the nominal module power for up to 25 years, and the output power is highly dependent on local environmental conditions and ambient intensity. Dust deposition has no effect on the open circuit voltage of a photovoltaic module, but it has a significant impact on the short circuit current, resulting in a drop in output current and, as a result, power generation is decreased. The dust deposition represents a massive loss in energy production and an economic loss for a photovoltaic power plant (Mustafa et al., 2020). Several research studies have examined the detrimental effects of dust accumulation on the surface of photovoltaic modules. Salimi et al. (2019) investigated the impact of relative humidity and wind speed on a performance ratio called the cleanness index (CI) that compares the performance of clean photovoltaic modules to that of dirty photovoltaic modules as a result of dust precipitation. According to the study, the cleanness index was positive when measuring the effects of wind speed, and the cleanness index was negative when measuring the effects of dust concentration and relative humidity. Dust deposits on photovoltaic modules cause their performance to decrease by 8%–12% per month. Kazem and Chaichan (2016) investigated that the physical properties and characteristics of dust are crucial in stimulating the final outcome of photovoltaic modules, while Alnasser et al. (2020) highlighted that dust composition and its physical and chemical properties are the factors that determine its detrimental effect on photovoltaic module performance. Jiang, Lu, and Sun (2011) pointed out that fine dust particles caused a more significant decrease in photovoltaic performance than coarse dust particles. Small dust particles are blown far away by the wind, and their accumulation on the surface of photovoltaic modules prevents the passage of radiation and increases the scattering of light because it adheres more clearly to the surface of photovoltaic modules than larger particles (Tanesab et al., 2015). Lu and Zhao (2019) investigated that ground-mounted photovoltaic systems had higher dust accumulation rates than roof-mounted systems, especially when the station was close to traffic. Furthermore, photovoltaic modules installed at a fixed tilt angle have more dust accumulations on the surface than photovoltaic modules installed with Sun-tracking systems (whether single or dual axis). Table 1 presents a comparative analysis of this proposed research study and previous research studies on the effects of dust on photovoltaic systems. Manju et al (2018) investigated various methods of dust removal from photovoltaic modules, including dry cleaning with clothes, cleaning with water, and the use of compressed air, mechanical brushes, vibration, electrostatic electricity, and ultrasound. Zorrilla-Casanova et al. (2011) showed that utilizing water to clean photovoltaic modules is more efficient than using dry cleaning, but using this technique in water-scarce deserts is an expensive process. Chaichan et al. (2019) explained that the techniques that must be followed for cleaning photovoltaic modules depend on the primary dust constituents and their chemical properties. The location of the photovoltaic modules and the type of dust accumulation due to the topography of the area directly affect the selection of appropriate cleaning techniques. In the agricultural area, dust particles consist of organic pollen, leaves, bird droppings, and soil. In the coastal area, salt can accumulate on photovoltaic modules. In the urban area, dust particles are primarily composed of carbon that comes from automotive exhaust. Dust particles in desert regions are primarily made of minerals (sand, quartz, silica, *etc.*) (Middleton, 2017; Chen et al., 2020; Fan et al., 2021). The stone crushing sector supplying construction materials is crucial for both employment and the economy in developing countries. These sectors are generally labor-intensive and small-scale. Stone crushing has a significant impact on the socio-economic environment of the local population. The different processes related to the breaking, size reduction, and transferring of stones can release dust (Ganguly and Das, 2020). Stone crushers also produce dust as a by-product due to mechanical reduction and screening operations (Von Schneidemesser et al., 2020). Due to the crushing activity in the crushing zone, both the natural

TABLE 1 Comparative analysis of the proposed research study and previous research studies on the effects of dust on photovoltaic systems.

Reference	Year	Period of study	PV device	Efficiency losses	Condition and comments	Location
Guan et al.	2017	8 days	Photovoltaic module installed at 30° tilt angle	24.32% losses in output energy	It was observed that dust reduced the temperature of the PV module, which also negatively affected the PV module efficiency	China
Abderrezek and Fathi	2017	Laboratory tests are performed using a variety of testing instruments	Photovoltaic module	10% to 16% losses in output energy	Amount of sun light traveling varies with dust types	Algeria
Gholami et al.	2018	70 days	Photovoltaic module	21.5% losses in output energy	In desert condition	Iran
Hachicha et al.	2019	Laboratory tests are performed using a variety of testing instruments	Photovoltaic module	1.7% reduction in energy per g/m^2 of dust accumulation	There is a linear relationship between energy production and dust density	United Arab Emirates
Shah et al.	2020	3.5 months	Photovoltaic module	Output energy of a dusty PV module was compared to that of a cleaned PV module, reductions were 3% for 10 days, 5% for 20 days, 7% for 1 month, and 13% for 3 months	Most suitable cleaning period was found to be 15 days because it maintained a realistic balance between cleaning costs and energy loss	United Arab Emirates
Al-Badra et al.	2020	6 weeks	Photovoltaic module	Efficiency of the dusty PV module decreased by 3.7% and that of coated PV module decreased by 2.74%, and the combined efficiency of the coated and vibrating PV module decreased by 1.45%	Coating and vibrating PV module have the least efficiency loss, so it is the best	Egypt
Dhaouadi et al.	2021	15 weeks	Photovoltaic module	Results show a 30% decrease in sun light traveling when PV modules leave dust after 15 weeks	Dust particles were found to be rich in carbon, oxygen, silicon, and calcium, thus proving the presence of calcite and silica	United Arab Emirates
Yazdani and Yaghoubi	2022	6 months	Photovoltaic module	Output energy reduction value was not linear; the average daily loss is roughly 9%	Outdoor experiments under semi-arid weather conditions; measurement of short-circuit current	Iran

environment of the hills and air quality of the surrounding area are endangered. This pollutant air (airborne pollutants) also affects photovoltaic energy system performance. Taking into consideration the dust produced as a by-product in the stone crushing sector, the efficiency and output energy of a photovoltaic energy generation installed in the area near to the crushing zone would decline as the rate of dust accumulation on the PV module surface increases. In order to optimize the output energy of the PV system in stone crushing zones, a comprehensive analysis of the impact of dust accumulation is crucial. To the best of the author's knowledge, no such research study has been conducted; hence, a comprehensive methodology is definitely needed, especially in severe environments like stone crushing zones. A research study is presented to analyze the effects of dust accumulation on the PV energy generation system in crushing zones. With the guidance of this study, commercial and residential PV system installers could more precisely plan their systems in stone crushing zones, which should ultimately result in higher output energy from PV systems. The aim of the study is to evaluate and assess air pollution (particulate matter) produced by stone crushers in the crushing zone and the impact of airborne pollutants on the performance of photovoltaic energy systems.

2 Methodology and experimental setup

2.1 Air quality monitoring

An outdoor station, consisting of a wind vane, beaker, and thermo hygrometer, was installed outside on the roof of the tall building near the crushing zone. Wind speed and direction were continuously monitored every hour to determine the wind speed and wind direction for the air quality monitoring. It has been

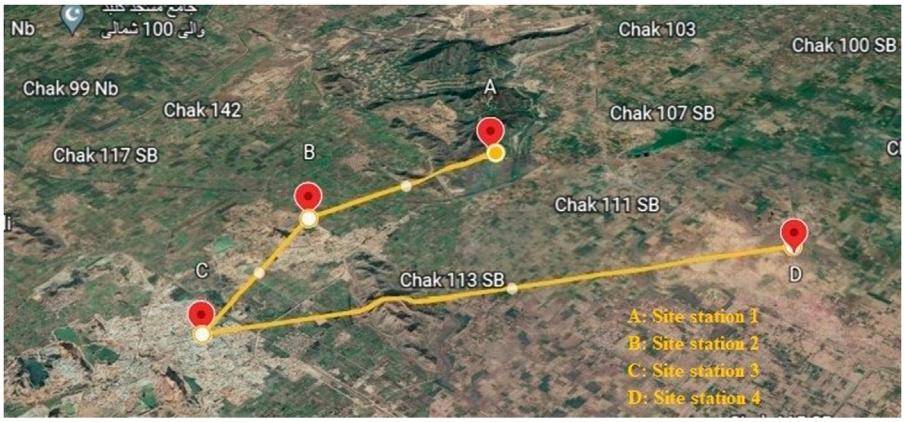

FIGURE 1
Test station in the Sargodha crushing zone.

observed and recorded that the wind was blowing from the west to the east in the Sargodha region. During the experiment, the wind direction is very important to achieve a suitable result. A higher precipitation pattern was also observed. Four sampling sites were selected for the study of PM concentration in this region. Stone crushing activities were carried out at these four sampling sites located on both sides of the Grand Trunk (GT) road as shown in Figure 1.

Experiments were conducted in two seasons: winter and summer. December and January were selected for the winter season and May and June for the summer season because the weather conditions of the crushing area change throughout the year. A three-day experiment was performed at four sampling sites, and then the average of these values was calculated to estimate the exact PM concentration. In this way, experimental values for 12 days were calculated for each season. Sampling of ambient air was performed for 24 h. For experiments, a large volume air sampler was used for air sampling. The recovery medium used in these experiments was Whatman glass microfiber filter paper. The dust concentration was calculated from the weight difference of the filter paper before and after sampling. After compiling the experimental results, all parameters were analyzed according to the National Ambient Air Quality Standard (NAAQS) methods prescribed by the Environmental Protection Agency (EPA), Pakistan.

2.2 Photovoltaic system

First, PM concentration was analyzed on all four selected sites. After PM concentration analyses, the HelioScope simulation model of the photovoltaic power generation was developed by taking different parameters under consideration, like the architectural design of the building, photovoltaic power system specifications, and the shading conditions. HelioScope is one of the finest simulation software for modeling and analyzing the PV system (Goel and Sharma, 2021). To enable energy system designers to use a single software program to create a whole PV system design, HelioScope simulation software combines all the features of PVSyst with AutoCAD design features. HelioScope makes it possible to create 3D model designs and estimate energy production (kWh) using a same simulation tool. From small to large size, and for every kind of surface, including flat or uneven surfaces, it is capable of designing photovoltaic systems. It has the benefit of being able to provide a very accurate estimate for the PV system size that would be installed at the proposed area, monthly and annual energy production (kWh), system performance ratio (PR), expected energy production (kWh/kWp), photovoltaic system losses, photovoltaic plant layout, number of PV modules and inverters, single line diagram (SLD), shading analysis, electrical wiring selection, total collector irradiation, annual global horizontal irradiation, SketchUp, and CAD integration (Tamoor et al., 2022). The comparison of HelioScope with other PV system simulation software is shown in Table 2.

Later, two 10.20-kW grid systems are designed and installed at the site, which have higher PM concentration to analyze the effect of PM concentration on the performance of the photovoltaic energy generation system. For the photovoltaic system performance analysis, one system is cleaned on a regular basis while the other is not cleaned at all and remains dusty.

2.2.1 Photovoltaic modules

In both systems, the Jinko Solar mono crystalline (JKM510M-7TL4-V) type photovoltaic module was used. For the photovoltaic array size, the PV array design factor of 1.35 is used. A 10.20 kW the grid system consisting of 20 W × 510 W

TABLE 2 Comparison of HelioScope with other PV system simulation software (Tamoor et al., 2022).

Value	HelioScope	SAM	PVSyst	PV*SOL
Modeling time-step	Hourly	Hourly	Hourly	Hourly
Decomposition of global horizontal irradiance (GHI)	Erbs model	N/A	Erbs model	Reindl
PV module model	Shockley's single diode model	CEC single diode model	Shockley's single diode model	Enhances single diode
Transposition model	Perez model	Perez model	Perez model	Hay–Davies
Radiation components	GHI and DHI	DNI and DHI	User selection	GHI
Temperature model	Sandia model	NOCT	Thermal balance equation	Thermal balance equation
Albedo	0.2	0.2	0.2	0.2
Module cover/IAM loss	ASHRAE	Model dependent	ASHRAE	ASHRAE
DC–AC ratio	User selection	1.2	User selection	User selection
DC wiring losses	Calculated	2%	1.5%	Calculated
Mismatch losses	Calculated	2%	1%	2%
Total DC derate	Calculated	0.96	0.95	0.975
AC wiring/cabling losses	0.50%	1%	0%	N/A

TABLE 3 Solar photovoltaic module specification.

PV module model	Jinko Solar (JKM510M-7TL4-V)
Rated peak power (Pmax)	510.0 W
Rated current (Imax)	12.320 A
Short-circuit current (Isc)	13.050 A
Rated maximum voltage (Vmax)	41.400 V
Open circuit voltage (Voc)	48.940 V
Efficiency of the PV module (%)	20.17%
Temperature coefficient of the PV module	−0.35 percentage per °C
Operating temperature	−40.0°C to 85.0°C

Jinko Solar PV modules has a maximum power voltage of 41.400 V and open circuit voltage of 48.940 V. The specification of 510 W mono crystalline Jinko Solar is given in Table 3. Both photovoltaic systems are installed at 18° tilt angle and at an azimuth angle of 180°. A manually movable structure with a 2 up x 5 wide frame size is used for installation and orientation of the PV modules.

2.2.2 Photovoltaic inverter

A Solis three phase inverter, model number Solis-3P10K-4G, is used in the installation of the test system. Table 4 shows the detailed specifications of the Solis three-phase inverter. They convert the DC power produced by photovoltaic modules into three-phase AC power at the frequency of 50.0 Hz and synchronize the output power with the utility distribution system. The Solis-3P10K-4G inverter only operates when connected to the utility AC grid and cannot be operated as a standalone mode.

2.3 Experimental process

In order to more accurately study the impact of dust accumulation on photovoltaic modules, an experimental setup is installed. The schematic diagram of the experimental process is shown in Figure 2. The experimental design process and data measurement are divided into two parts, Part-1: air quality monitoring and assessment and Part-2: PV system analysis. Air quality monitoring and assessment includes selection of sampling sites in the stone crushing zone, and air quality monitoring at all selected sites uses different apparatuses like wind vane, thermo hygrometer, high-volume air sampler, glass–fiber filter papers, and analytical balance in the summer

TABLE 4 Solis three-phase inverter detail specification.

Photovoltaic inverter model	Solis-3P10K-4G
Maximum DC input power(kW)	12.0 kW
Maximum DC input voltage(V)	1000.0 V
Start-up voltage(V)	180.0 V
MPPT number	2.0
Maximum input current	11.0 A
Rated output power(kW)	10.0
Rated grid frequency(Hz)	50/60 Hz
Rated grid voltage(V)	400.0 V
Maximum output current(A)	15.9 A
Maximum efficiency	98.7%

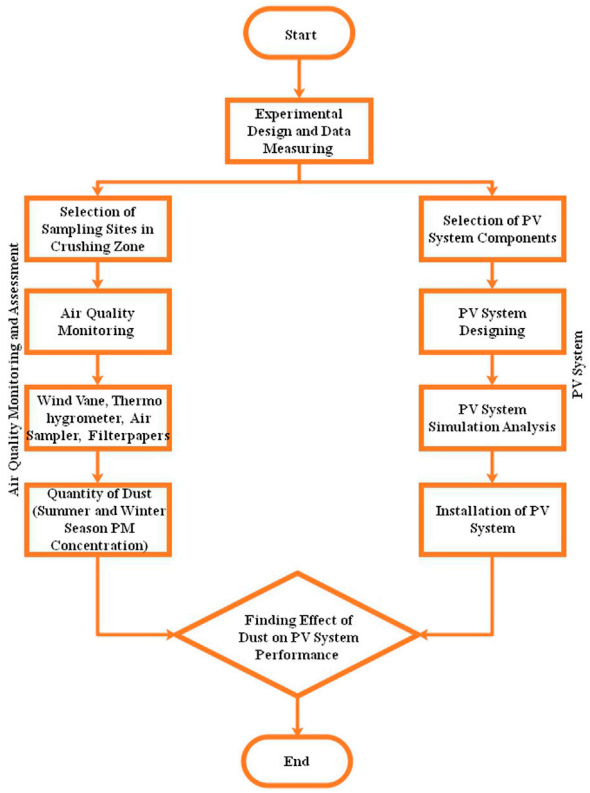

FIGURE 2
Schematic diagram of the experimental process.

and winter seasons. The dust concentration was calculated from the weight difference of the filter paper before and after sampling. PV system analysis includes the selection of PV system components like PV modules, inverts, and electrical wiring. After selection, the PV system is designed. HelioScope simulation software is used to perform the simulation study of the designed PV system. Finally, the effect of dust on the performance of the photovoltaic system is found.

3 Results

3.1 Air quality assessment

3.1.1 Winter season particulate matter concentration

The calculated PM concentrations on all four stations as compared to National Ambient Air Quality Standard in the winter season are shown in Figure 3. The calculated concentration at site station 1 is 520.236 μg/m^3, at site station 2 is 525.76 μg/m^3, at site station 3 is 316.087 μg/m^3, and at site station 4 is 182.34 μg/m^3. From the experimental study, it is found that the concentration of PM at site station 1, site station 2, site station 3, and site station 4, which is the residential area, is above the NAAQS values. A very high difference is observed between the experimental value and NAAQS, which leads to an adverse impact on photovoltaic power generation.

3.1.2 Summer season particulate matter concentration

The calculated PM concentrations on all four stations as compared to national ambient air quality standard in the summer season are shown in Figure 4. The calculated concentration at site station 1 is 416.049 μg/m^3, at site station 2 is 439.177 μg/m^3, at site station 3 is 228.98 μg/m^3, and at site station 4 is 155.45 μg/m^3. From the experimental study, it is found that the concentration of PM at site station 1, site station 2, site station 3 and site station 4, which is residential area, is above the NAAQS values. A very high difference is observed between the experimental value and NAAQS, which leads to an adverse impact on photovoltaic power generation.

3.2 Particulate matter concentration impact on the photovoltaic system

3.2.1 Simulation of the photovoltaic energy generation system

The simulation model of the photovoltaic power generation is developed by taking different parameters under consideration like the architectural design of the building, photovoltaic power system specifications, and the shading conditions. The physical characteristics of the photovoltaic power system (like the size of the system, azimuth and tilt angle of the system, orientation, height, and type of PV modules and inverters) are modeled in HelioScope simulation software. Photovoltaic modules and building blocks are simplified using a parameterized model that takes into account the real size and shape of the components. In the parameter setting column, detailed photovoltaic module parameters (such as PV cell pattern, tilt and azimuth angle, and distance between PV modules and rows) are imported. The weather data are based on the current weather conditions at the chosen location. Shading modeling is simulated automatically.

In the simulation, the overall energy performance is evaluated on a monthly basis by using a photovoltaic monitoring system that receives real-time data directly from the meter. The complete monthly power generation data from January 2020 to December 2020 have been extracted. The simulation results of a designed photovoltaic system showed that the annual energy generation is 15.79 MWh, the performance ratio (PR) is 88.1%, and the power generation (kWh/kWp) is 1548.2. Figure 5 shows the photovoltaic system's monthly power production.

Figure 5 shows that the maximum produced power is 1,708.2 kWh in May, and minimum produced power is

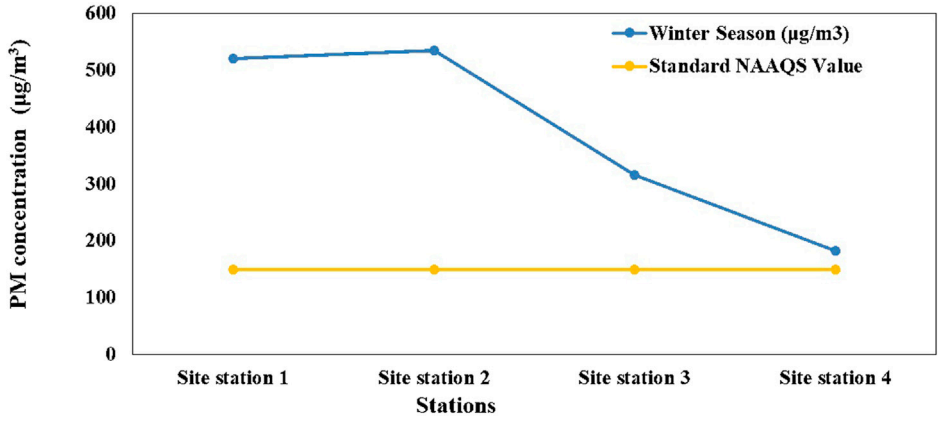

FIGURE 3
PM concentration in the winter season.

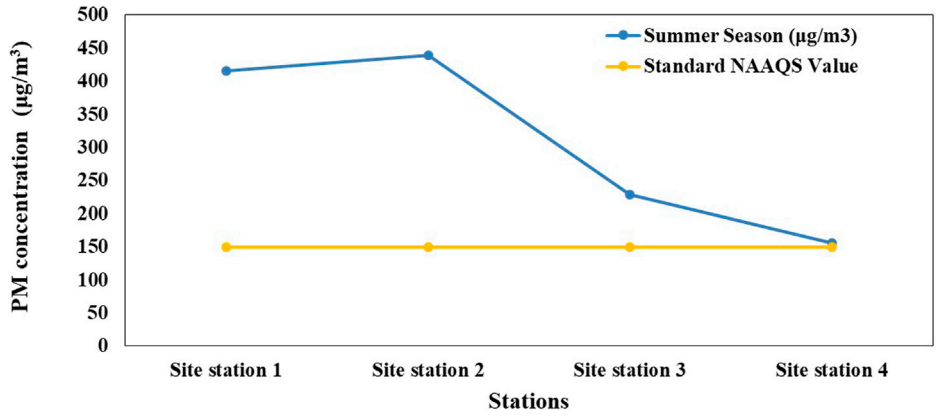

FIGURE 4
PM concentration in the summer season.

841.1 kWh in December. For solar energy applications, accurate and precise measurements of global horizontal irradiance (GHI) are crucial. It is necessary to use GHI to forecast the output of solar thermal collectors or photovoltaic system. Thus, understanding GHI is crucial for activities like resource assessment during photovoltaic installation planning and optimizing photovoltaic plant operation (Nouri et al., 2020; Toledo et al., 2020). The global horizontal irradiance of the site is 204.4 kWh/m^2 in May and 79.7 kWh/m^2 in December. The annual global horizontal irradiance is shown in Figure 6.

Determining the irradiance incident on the plane of the array (POA) as a function of time is a crucial step in calculating photovoltaic system performance. Several factors influence the plane of the array irradiance like orientation of the PV modules, shading, Sun position, latitude, longitude, and weather conditions (Nour et al., 2019; Meyers, 2021; Blum et al., 2022). The plane of array irradiance of the site is 206.3 kWh/m^2 in May and 99.7 kWh/m^2 in the February. The plane of the array irradiance is shown in Figure 7.

3.2.1.1 Photovoltaic system losses

Figure 8 represents major photovoltaic system losses, like temperature losses, irradiance losses, mismatch losses, soiling losses, electrical wiring losses, reflection losses, clipping losses, shading losses, inverters losses, and AC system losses. The temperature losses are 6.2%, irradiance losses are 0.4%, mismatch losses are 4.0%, soiling losses are 2.0%, electrical wiring losses are 0.3%, reflection losses are 3.2%, clipping losses are 0.0%, shading losses are 0.4%, inverter losses are 3.0% and AC system losses are 0.5%.

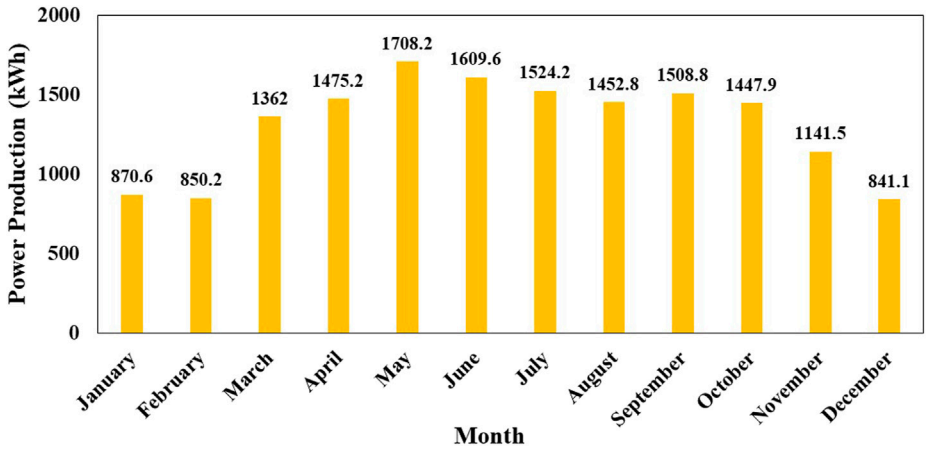

FIGURE 5
Photovoltaic system monthly power production.

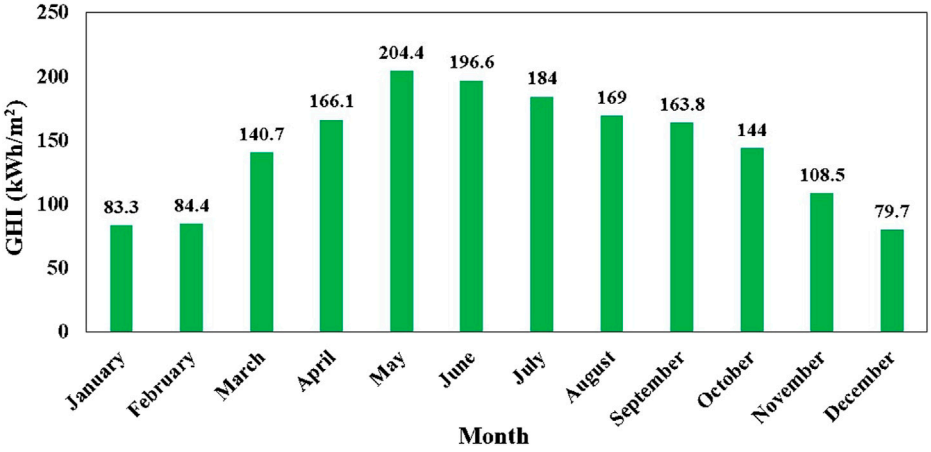

FIGURE 6
Annual global horizontal irradiance (GHI).

3.2.1.2 Soiling loss impact on the photovoltaic system

The concept "soiling losses" refers to a reduction in power or yield as a result of accumulation of dust, sand, snowfall, and other falling particles on the photosensitive surface of the photovoltaic module. By concentrating on dust soiling, a thin layer of paper-sized dust particles with a diameter of less than 10 microns covers the surface of the PV module. The continuously accumulating dust increasing the soiling impact will result in reducing the energy of the photovoltaic system from daily to annual rates. Generally, dust characteristics (e.g., chemical composition and size of particle), local environment condition (e.g., humidity, temperature, wind speed, and direction), and photovoltaic module installation (e.g., irradiation level, tilt angle, and azimuth angle) influence the accumulation impact of dust (particulate matter) on the performance of the photovoltaic system. The impact of soiling losses is shown in Table 5.

3.2.1.3 Temperature impact on photovoltaic system performance

The accumulation of a particulate matter layer on the photovoltaic module surface is one of the operating environmental factors that cause significant reduction in PV system performance, which further leads to power loss, reduces service life, reduces irradiance, and increases module temperature.

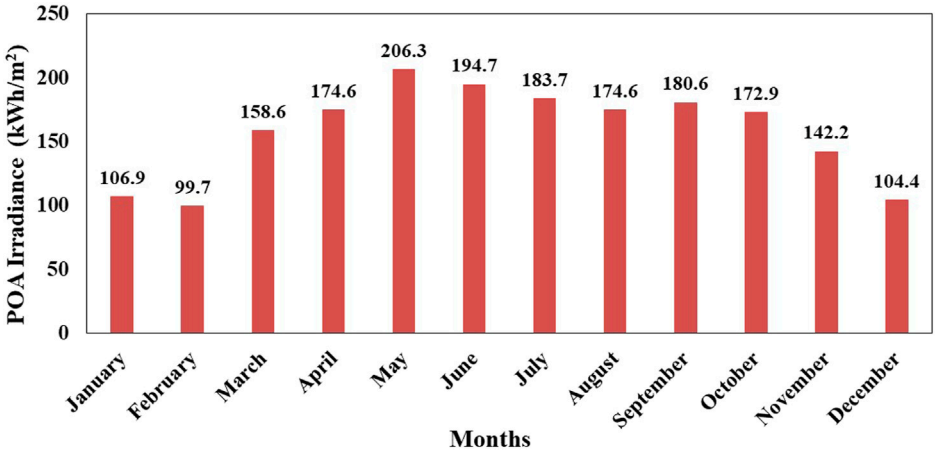

FIGURE 7
Plane of the array (POA) irradiance.

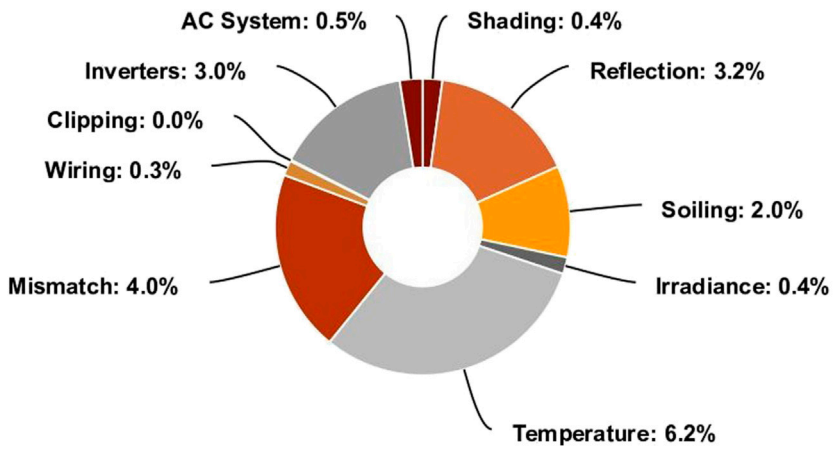

FIGURE 8
Major photovoltaic system losses.

The normal operating temperature for photovoltaic modules is 25°C. The performance of photovoltaic modules is most significantly impacted by temperature. However, because the selected site for the PV system is in a hot climate region, the ambient temperature (Ta) of the photovoltaic modules has increased excessively. The PV module temperature is calculated as follows (Kim et al., 2021):

$$T_m = E\left(e^{a+b(Ws)}\right) + T_a. \quad (1)$$

Here,

- T_m: PV module temperature (°C)
- E : solar irradiation on the photovoltaic module (W/m^2)
- Ws: wind speed at a proposed site
- T_a: ambient temperature (°C)
- a : coefficient for photovoltaic modules upper temperature (°C) limit
- b : coefficient that determines how much temperature (°C) of photovoltaic modules decreases when speed of wind increases

By using Equation no. 1 for PV module temperature, 6.2% losses are calculated. It is found that the efficiency of the photovoltaic module decreases as the temperature of the photovoltaic module increases. In a simulation study, power is analyzed at different irradiance levels with temperature variation as shown in Table 6.

TABLE 5 Soiling loss impact on the PV system.

Soiling losses (%)	Annual energy generation	Performance ratio (%)
2	15.79 MWh	88.1
3	15.15 MWh	83.5
4	15.01 MWh	78.6
5	14.85 MWh	75.8
6	14.71 MWh	75.0
7	14.57 MWh	74.3
10	14.14 MWh	72.1
15	13.42 MWh	68.5
20	12.68 MWh	64.7

TABLE 6 Power variation of the PV module at different temperature levels.

Irradiance level (W/m^2)	Variation in PV module output power					
	25°C	30°C	35°C	40°C	45°C	50°C
1,000	510.3	501.4	492.3	483.1	473.9	464.5
800	409.3	402.1	394.9	387.5	380.1	372.6
600	306.7	301.3	295.9	290.4	284.8	279.2
400	203.2	199.6	196.0	192.3	188.6	184.9
200	99.6	97.8	96.0	94.1	92.3	90.4
100	48.2	47.3	46.4	45.5	44.6	43.6

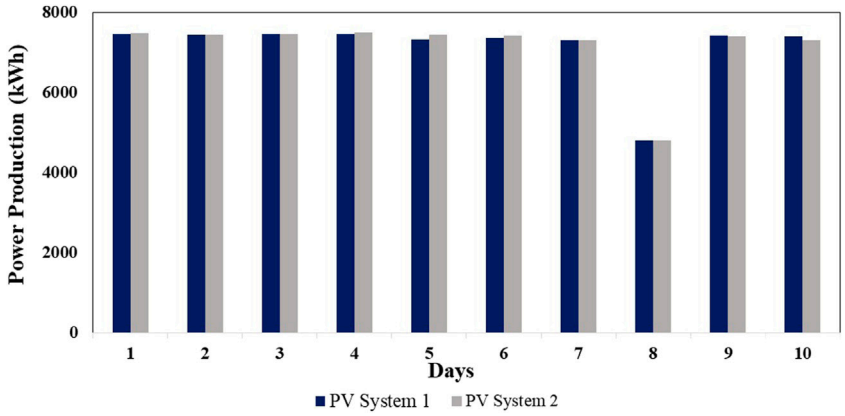

FIGURE 9
Comparison of cleaned PV systems.

FIGURE 10
Installed PV systems.

TABLE 7 Parameters of the photovoltaic systems for May.

Parameter	Cleaned PV system	Dusty PV system
Maximum power	7451.85 W	6893.8 W
Open circuit voltage (V_{oc})	821.14 V	812 V
Short-circuit current (I_{sc})	11.16 A	10.44 A
Maximum voltage (V_{mpp})	652.69 V	645.42 V
Maximum current (I_{mpp})	11.12 A	10.68 A

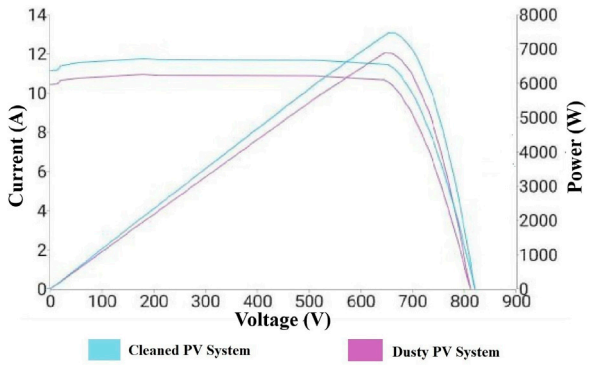

FIGURE 11
I–V curve of cleaned and dusty PV systems to compare system performance in May.

TABLE 8 Parameters of the photovoltaic systems for June.

Parameters	Cleaned PV system	Dusty PV system
Maximum power	7430.91 W	6885.3 W
Open circuit voltage (V_{oc})	820.2 V	811.0 V
Short-circuit current (I_{sc})	11.0 A	10.31 A
Maximum voltage (V_{mpp})	659.25 V	651.86 V
Maximum current (I_{mpp})	11.27 A	10.56 A

From Table 6, it is observed that at normal operating temperature 25°C and irradiance level 1000 W/m^2, the output power of the PV module is 510.3 W, and at 50°C operating temperature and irradiance level 100 W/m^2, the power output of the PV module is 43.6 W. From the simulation result, it is found that dust accumulation has a significant impact on the performance of the PV system because it increases module temperature and reduces the amount of irradiance that reaches the surface of the modules.

3.2.2 Power generation comparison of installed photovoltaic systems

3.2.2.1 Comparison of cleaned photovoltaic systems

To examine the power production and efficiency of both cleaned 10.20-kW PV systems installed near the stone crushing zone, readings of power production from both PV systems are taken for 10 days in April. The power production from both photovoltaic systems is shown in Figure 9.

Figure 9 shows that the maximum power produced by the installed photovoltaic system 1 and system 2 in 1 day is 7,463 and 7491 kWh, respectively. The power produced by both systems is almost the same because PV systems having same specification are installed near the crushing zone. The photovoltaic systems produced lower power due to bad weather condition, i.e., it rained at day 9.

3.2.2.2 Comparison of cleaned and dusty photovoltaic systems

For the photovoltaic system performance analysis, one system is cleaned on a regular basis, while the other is not cleaned at all and remains dusty. The experimental setup of the installed clean and dusty photovoltaic energy generation systems is shown in Figure 10.

The average data of both systems are calculated and compared for 4 months (2 months for the summer season and 2 month for the winter season). In the summer season, the comparison between both systems is performed in May and June, and in the winter season, the comparison between both systems is performed in January and December. Table 7 shows the parameters of both photovoltaic systems for May.

Table 7 shows that for May, the average power produced by the cleaned PV system is 7451.85 W and the average power produced by the dusty PV system is 6893.8 W. So, 7.48% power is reduced due to PM concentration on the surface of the photovoltaic modules. The I–V curve of cleaned and dusty PV systems to compare system performance in May is shown in Figure 11.

Table 8 shows that for June, the average power produced by the cleaned PV system is 7430.91 W and the average power produced by the dusty PV system is 6885.3 W. So, 7.342% power is reduced due to PM concentration on the surface of the photovoltaic modules. The I–V curve of cleaned and dusty PV systems to compare system performance in June is shown in Figure 12.

Table 9 shows that for December, the average power produced by the cleaned PV system is 6892.06 W and the average power produced by the dusty PV system is 6155.6 W. So, 10.68% power is reduced due to PM concentration on the surface of the photovoltaic modules. The I–V curve of cleaned and dusty PV systems to compare system performance in December is shown in Figure 13.

Table 10 shows that for January, the average power produced by the cleaned PV system is 6892.06 W and the average power produced by the dusty PV system is 6155.6 W. So, 8.03% power is reduced due to PM concentration on the surface of the photovoltaic modules. The I–V curve of cleaned and dusty PV systems to compare system performance in January is shown in Figure 14.

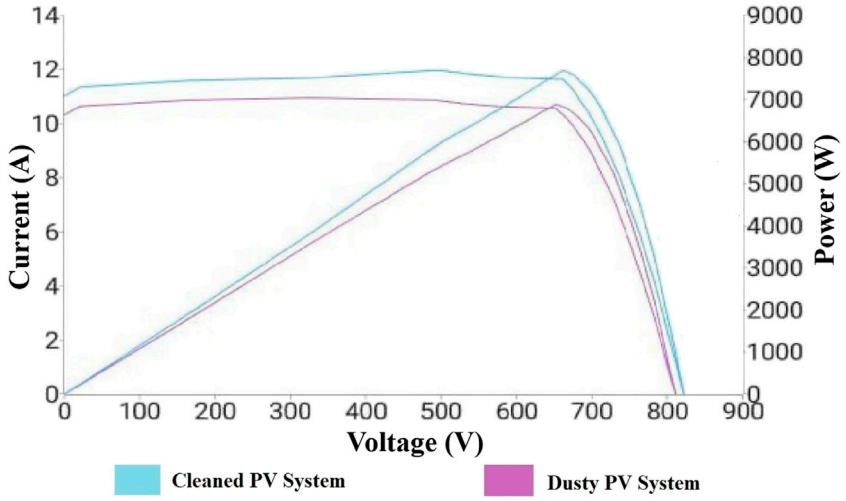

FIGURE 12
I–V curve of cleaned and dusty PV systems to compare system performance in June.

TABLE 9 Parameters of the photovoltaic systems for December.

Parameter	Cleaned PV system	Dusty PV system
Maximum power	6892.06 W	6155.6 W
Open circuit voltage (V_{oc})	768.34 V	757.0 V
Short-circuit current (I_{sc})	11.02 A	9.99 A
Maximum voltage (V_{mpp})	621.91 V	612.73 V
Maximum current (I_{mpp})	11.08 A	10.05 A

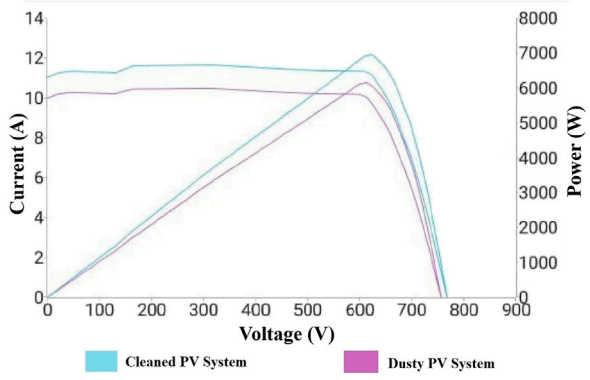

FIGURE 13
I–V curve of cleaned and dusty PV systems to compare system performance in December.

4 Discussion

This study investigates the effects of particulate matter (PM2.5 and PM10) on the photovoltaic energy generation system by analyzing actual energy data from two PV systems installed near the Sargodha stone crushing zone in the winter and summer seasons. The methodologies used in this research are the air quality assessment at four selected sites, designing and simulation study of the PV system, analyzing actual energy data and system losses of two PV systems installed near the stone crushing zone, and other meteorological parameters (like GHI and POA) that are different from those in previous assessments, which typically focus on PM influences on solar irradiance and simulated photovoltaic energy output (Peters et al., 2018; Son et al., 2020).

Air quality experiments were conducted in two seasons: winter and summer. December and January were selected for the winter season and May and June for the summer season because the weather conditions of the crushing area change throughout the year. A three-day experiment was performed at four sampling sites, and then the average of these values was calculated to estimate the exact PM concentration. In this way, experimental values for 12 days were calculated for each season. After compiling the experimental results, all parameters were analyzed according to the National Ambient Air Quality Standard (NAAQS) standard methods prescribed by the Environmental Protection Agency (EPA), Pakistan. In the winter season, the calculated PM concentration at site station

TABLE 10 Parameters of the photovoltaic systems for the January.

Parameter	Cleaned PV system	Dusty PV system
Maximum power	7362.0 W	6770.5 W
Open circuit voltage (V_{oc})	814.49 V	805.0 V
Short-circuit current (I_{sc})	11.04 A	10.27 A
Maximum voltage (V_{mpp})	654.2 V	646.8 V
Maximum current (I_{mpp})	11.25 A	10.47 A

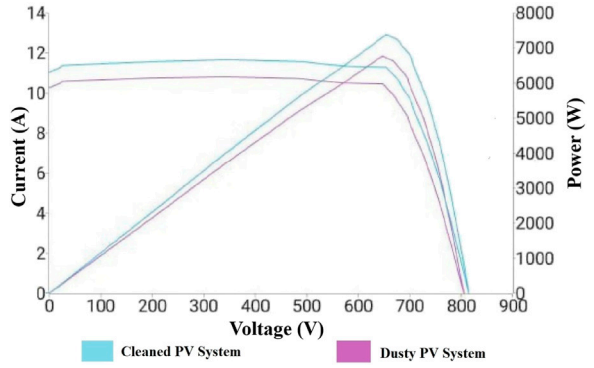

FIGURE 14
I–V curve of cleaned and dusty PV systems to compare system performance in January.

1 is 520.236 μg/m^3, at site station 2 is 525.76 μg/m^3, at site station 3 is 316.087 μg/m^3, and at site station 4 is 182.34 μg/m^3. In the summer season, the calculated PM concentration at site station 1 is 416.049 μg/m^3, at site station 2 is 439.177 μg/m^3, at site station 3 is 228.98 μg/m^3, and at site station 4 is 155.45 μg/m^3. From the experimental study, it is found that the concentration of PM at site station 1, site station 2, site station 3, and site station 4, which is residential area, is above the NAAQS values. A very high difference is observed between the experimental value and NAAQS, which leads to an adverse impact on photovoltaic power generation.

The simulation model of the photovoltaic power generation is developed by taking different parameters under consideration. The simulation results of a designed photovoltaic system showed that the annual energy generation is 15.79 MWh and the performance ratio (PR) is 88.1%, the performance ratio in this research is high as compared to the research study (Navothna and Thotakura, 2022), and the power generation (kWh/kWp) is 1548.2. The maximum monthly energy production is 1,708.2 kWh, the maximum global horizontal irradiance (GHI) is 204.4 kWh/m^2, and the maximum plane of array irradiance (POA) is 206.3 kWh/m^2 in May. Soiling losses due to the accumulation of dust influence the performance of the PV system. The simulation results show that when the soiling losses are 2%, the annual energy generation of the photovoltaic system is 15.79 MWh, and the performance ratio is 88.1%. The annual energy generation and performance ratio of the PV system declines as the percentage of soiling losses increases. The annual energy generation and performance ratio of the PV system declines as the percentage of soiling losses increases. The performance of photovoltaic modules is most significantly impacted by temperature. At normal operating temperature 25°C and 1000 W/m^2 irradiance level, the output power of the PV module is 510.3 W, and at 50°C operating temperature and 100 W/m^2 irradiance level, the power output of the PV module is 43.6 W.

For 4 months, Figure 15 displays the impact of PM10 and PM2.5 concentrations on the rate of reduction of photovoltaic energy generation. The findings reveal that the amount of photovoltaic energy generation decreases with the deterioration of air quality. The reduction rate of photovoltaic

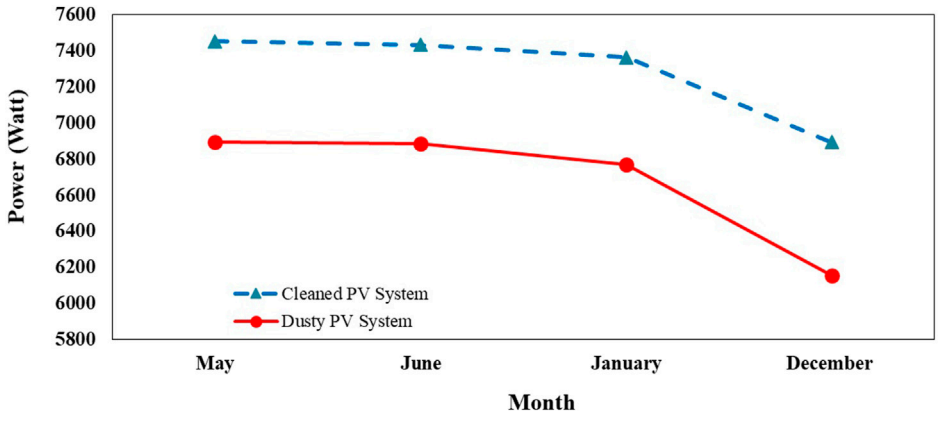

FIGURE 15
PM concentration impact on photovoltaic energy generation.

energy generation due to PM10 and PM2.5 is higher in the dusty photovoltaic energy generation system than in the cleaned photovoltaic energy generation system. In May, the average power produced by the cleaned PV system is 7451.85 W and the average power produced by the dusty PV system is 6893.8 W. In June, the average power produced by the cleaned PV system is 7430.91 W and the average power produced by the dusty PV system is 6885.3 W. In December, the average power produced by the cleaned PV system is 6892.06 W and the average power produced by the dusty PV system is 6155.6 W. In January, the average power produced by the cleaned PV system is 6892.06 W and the average power produced by the dusty PV system is 6155.6 W. It was found that when the level of suspended particulate matter (PM10 and PM2.5) increases, the energy generation of the dusty PV system is reduced by 7.48% in May, 7.342% in June, 10.68% in December, and 8.03% in January under bad air quality, 439.177 μg/m^3 and 535.76 μg/m^3 in the summer and winter seasons, respectively, as compared to the photovoltaic energy generation systems that are regularly cleaned.

Based on the aforementioned results, it can be predicated that a large amount of suspended particulate matter (PM10 and PM2.5) reduces the energy generation of the photovoltaic system. It is important to note that these high levels of particulate matter (PM10 and PM2.5) are damaging to photovoltaic generation because the higher the concentration of PM10 and PM2.5, the greater the adverse impact on photovoltaic power generation. The limitations of this study are that it investigated the impact of suspended particulate matter on the performance of the photovoltaic energy generation system. These suspended particulate matters (PM2.5 and PM10) are produced during the stone crushing process. Based on a comparative analysis of the proposed research study and previous research studies on the effects of dust on photovoltaic systems, Guan et al. (2017) performed a similar study for 8 days only, Hachicha et al. (2019) performed laboratory tests, and Al-Badra et al. (2020) performed a similar study for 6 weeks, proposed a research which provides good result because this research is performed in all seasons of the year, and investigated all environmental impacts produced due to the change in weather.

5 Conclusion

Many environmental factors influence photovoltaic energy system production, and particulate matter (PM10 and PM2.5) can be one of the main causes of the reduction of photovoltaic energy. Particulate matter (PM10 and PM2.5) is a mixture of different pollutants and varies significantly depending on site location and time. This study aims to investigate the process of particulate matter (PM10 and PM2.5) accumulation on the photovoltaic system installed near the stone crushing zone in the Sargodha region, one of the most polluted crushing zones in Pakistan. The four sampling stations were selected for sampling during the summer and winter seasons. December and January were selected for the winter season and May and June for the summer season because the weather conditions of the crushing area change throughout the year. Glass–fiber filter papers are used as a collection medium for particulate matter in a high-volume sampler. A three-day experiment was performed at four sampling sites, and then the average of these values was calculated to estimate the exact PM concentration. In this way, experimental values for 12 days were calculated for each season. After compiling the experimental results, all parameters were analyzed according to the National Ambient Air Quality Standard (NAAQS) methods prescribed by the Environmental Protection Agency (EPA), Pakistan. In the winter season, the calculated PM concentration at site station 1 is 520.236 μg/m^3, at site station 2 is 525.76 μg/m^3, at site station 3 is 316.087 μg/m^3, and at site station 4 is 182.34 μg/m^3. In the summer season, the calculated PM concentration at site station 1 is 416.049 μg/m^3, at site station 2 is 439.177 μg/m^3, at site station 3 is 228.98 μg/m^3, and at site station 4 is 155.45 μg/m^3.

For the photovoltaic system performance analysis, two PV systems installed at the site have higher PM concentrations, where one system is cleaned on a regular basis while the other is not cleaned at all and remains dusty. The HelioScope simulation model of the photovoltaic power generation is developed by taking different parameters under consideration like the architectural design of the building, photovoltaic power system specifications, and shading conditions. Simulation results show that the annual energy generation is 15.79 MWh and the performance ratio (PR) is 88.1%; the performance ratio in this research is high as compared to that of the research study (Navothna and Thotakura, 2022). The power generation (kWh/kWp) is 1548.2, the maximum produced power is 1,708.2 kWh in May, and the minimum produced power is 841.1 kWh in December. The global horizontal irradiance (GHI) of the site is 204.4 kWh/m^2 in May and 79.7 kWh/m^2 in December. The plane of array irradiance (POA) of the site is 206.3 kWh/m^2 in May and 99.7 kWh/m^2 in February. Major losses of PV systems are also calculated using simulation software. The temperature losses are 6.2%, irradiance losses are 0.4%, mismatch losses are 4.0%, soiling losses are 2.0%, electrical wiring losses are 0.3%, reflection losses are 3.2%, clipping losses are 0.0%, shading losses are 0.4%, inverter losses are 3.0%, and AC system losses are 0.5%. The losses in this research are lower than losses in the research study (Navothna and Thotakura, 2022). The annual energy generation and performance ratio of the PV system decline as the percentage of soiling losses and temperature of the site increases.

The data of both PV systems are measured and compared for 4 months (2 months for the summer season and 2 months for the winter season). The average power produced by the cleaned PV

system is 7451.85, 7430.91, 6892.06, and 6892.06 W, and the average power produced by the dusty PV system is 6893.8, 6885.3, 6155.6, and 6155.6 W May, June, December, and January, respectively. It was found that when the level of suspended particulate matter (PM10 and PM2.5) increases, the energy generation of the dusty PV system is reduced by 7.48% in May, 7.342% in June, 10.68% in December, and 8.03% in January under bad air quality, 439.177 μg/m^3 and 535.76 μg/m^3 in the summer and winter seasons, respectively, as compared to the photovoltaic energy generation system that is regularly cleaned. Based on the obtained results, it is recommended that the negative impact of PM on the performance of the PV system should be considered carefully during the decision-making process of setting solar energy generation targets in the regions with a high level of particulate matter.

Data availability statement

The original contributions presented in the study are included in the article/Supplementary Material; further inquiries can be directed to the corresponding author.

Author contributions

Conceptualization, MT, AB, and SM; methodology, MT, MH, AB, and SM; software, MT, SM, WA, TK, MH, and GL; validation, MT, AB, SM, and GL; formal analysis, MT, MH, GL, and TK; investigation, MT, AB, and SM; resources, MT, SM, and MH; writing—original draft preparation, MT, AB, SM, and TK; writing—review and editing, MT, AB, SS, MH, and GL; visualization, MT, AB, SM, TK, and WA; supervision, AB, SS, MH, and GL; project administration, MT, AB, SM, MH, and GL; funding acquisition, MH and GL. All authors have read and agreed to the published version of the manuscript.

Funding

This work was supported by the National Research Foundation of Korea (NRF) grant funded by the Korea government (MSIT) (No. 2022R1F1A1062793); Korea Institute of Planning and Evaluation for Technology in Food, Agriculture and Forestry (IPET) through Technology Commercialization Support Program, funded by Ministry of Agriculture, Food and Rural Affairs (MAFRA) (No. 821048-3).

Acknowledgments

The authors gladly acknowledge the continued support of the Department of Electrical Engineering and Technology, GC University Faisalabad.

Conflict of interest

The authors declare that the research was conducted in the absence of any commercial or financial relationships that could be construed as a potential conflict of interest.

The reviewer AH and reviewer MF declared a shared affiliation with the author TK at the time of the review.

The handling editor declared a shared affiliation with the author TK, MPS at the time of the review.

Publisher's note

References

Abderrezek, M., and Fathi, M. (2017). Experimental study of the dust effect on photovoltaic panels' energy yield. *Sol. Energy* 142, 308–320. doi:10.1016/j.solener.2016.12.040

Ahmed, A., and Massier, T. (2019). "Impact of climate change and high PV penetration on power factor profile," in *2019 IEEE industry applications society annual meeting* (IEEE), 1–6.

Al-Badra, M. Z., Abd-Elhady, M. S., and Kandil, H. A. (2020). A novel technique for cleaning PV panels using antistatic coating with a mechanical vibrator. *Energy Rep.* 6, 1633–1637. doi:10.1016/j.egyr.2020.06.020

Alnasser, T. M., Mahdy, A. M., Abass, K. I., Chaichan, M. T., and Kazem, H. A. (2020). Impact of dust ingredient on photovoltaic performance: An experimental study. *Sol. Energy* 195, 651–659. doi:10.1016/j.solener.2019.12.008

Andrea, Y., Pogrebnaya, T., and Kichonge, B. (2019). Effect of industrial dust deposition on photovoltaic module performance: Experimental measurements in the tropical region. *Int. J. Photoenergy*, 1–10. doi:10.1155/2019/1892148

Andreani, L. C., Bozzola, A., Kowalczewski, P., Liscidini, M., and Redorici, L. (2019). Silicon solar cells: Toward the efficiency limits. *Adv. Phys. X* 4 (1), 1548305. doi:10.1080/23746149.2018.1548305

Blum, N. B., Wilbert, S., Nouri, B., Lezaca, J., Huckebrink, D., Kazantzidis, A., et al. (2022). Measurement of diffuse and plane of array irradiance by a combination of a pyranometer and an all-sky imager. *Sol. Energy* 232, 232–247. doi:10.1016/j.solener.2021.11.064

Bono, M. D. (2018). *What is solar energy and how do solar panels work?* USA: SunPower Corporation.

Chaichan, M. T., Kazem, H. A., Al-Waeli, A. H., and Sopian, K. (2019). The effect of dust components and contaminants on the performance of photovoltaic for the four regions in Iraq: A practical study. *Renew. Energy Environ. Sustain.* 5, 3. doi:10.1051/rees/2019009

Chaichan, M. T., and Kazem, H. A. (2018). *Generating electricity using photovoltaic Solar plants in Iraq*. Springer. doi:10.1007/978-3-319-75031-6

Chaichan, M. T., and Kazem, H. A. (2015). Water solar distiller productivity enhancement using concentrating solar water heater and phase change material (PCM). *Case Stud. Therm. Eng.* 1 (5), 151–159. doi:10.1016/j.csite.2015.03.009

Chaichan, M. T., Mohammed, B. A., and Kazem, H. A. (2015). Effect of pollution and cleaning on photovoltaic performance based on experimental study. *Int. J. Sci. Eng. Res.* 6 (4), 594–601.

Cheema, A., Shaaban, M. F., and Ismail, M. H. (2021). A novel stochastic dynamic modeling for photovoltaic systems considering dust and cleaning. *Appl. Energy* 300, 117399. doi:10.1016/j.apenergy.2021.117399

Chen, G., and Zhu, Y. (2022). Advanced control for grid-connected system with coordinated photovoltaic and energy storage. *Front. Energy Res.* 10, 901354. doi:10.3389/fenrg.2022.901354

Chen, J., Pan, G., Ouyang, J., Ma, J., Fu, L., and Zhang, L. (2020). Study on impacts of dust accumulation and rainfall on PV power reduction in East China. *Energy* 194, 116915. doi:10.1016/j.energy.2020.116915

Cui, Y. Q., Xiao, J. H., Xiang, J. L., and Sun, J. H. (2021). Characterization of soiling bands on the bottom edges of PV modules. *Front. Energy Res.* 9, 665411. doi:10.3389/fenrg.2021.665411

Darwish, Z. A., Kazem, H. A., Sopian, K., Alghoul, M. A., and Alawadhi, H. (2018). Experimental investigation of dust pollutants and the impact of environmental parameters on PV performance: An experimental study. *Environ. Dev. Sustain.* 20 (1), 155–174. doi:10.1007/s10668-016-9875-7

Dhaouadi, R., Al-Othman, A., Aidan, A. A., Tawalbeh, M., and Zannerni, R. (2021). A characterization study for the properties of dust particles collected on photovoltaic (PV) panels in Sharjah, United Arab Emirates. *Renew. Energy* 171, 133–140. doi:10.1016/j.renene.2021.02.083

Fan, S., Wang, Y., Cao, S., Sun, T., and Liu, P. (2021). A novel method for analyzing the effect of dust accumulation on energy efficiency loss in photovoltaic (PV) system. *Energy* 234, 121112. doi:10.1016/j.energy.2021.121112

Fouad, M. M., Shihata, L. A., and Morgan, E. I. (2017). An integrated review of factors influencing the perfomance of photovoltaic panels. *Renew. Sustain. Energy Rev.* 80, 1499–1511. doi:10.1016/j.rser.2017.05.141

Ganguly, K. K., and Das, D. (2020). Analysing the barriers in Indian stone crushing industries: An ISM and fuzzy AHP approach. *Int. J. Appl. Manag. Sci.* 12 (3), 242–264. doi:10.1504/IJAMS.2020.108072

Gholami, A., Khazaee, I., Eslami, S., Zandi, M., and Akrami, E. (2018). Experimental investigation of dust deposition effects on photo-voltaic output performance. *Sol. Energy* 159, 346–352. doi:10.1016/j.solener.2017.11.010

Gil, G. M. V., Cunha, R. B. A., Di Santo, S. G., Monaro, R. M., Costa, F. F., and Sguarezi Filho, A. J. (2020). Photovoltaic energy in South America: Current state and grid regulation for large-scale and distributed photovoltaic systems. *Renew. Energy* 162, 1307–1320. doi:10.1016/j.renene.2020.08.022

Goel, S., and Sharma, R. (2021). Analysis of measured and simulated performance of a grid-connected PV system in eastern India. *Environ. Dev. Sustain.* 23 (1), 451–476. doi:10.1007/s10668-020-00591-7

Guan, Y., Zhang, H., Xiao, B., Zhou, Z., and Yan, X. (2017). *In-situ* investigation of the effect of dust deposition on the performance of polycrystalline silicon photovoltaic modules. *Renew. energy* 101, 1273–1284. doi:10.1016/j.renene.2016.10.009

Hachicha, A. A., Al-Sawafta, I., and Said, Z. (2019). Impact of dust on the performance of solar photovoltaic (PV) systems under United Arab Emirates weather conditions. *Renew. Energy* 141, 287–297. doi:10.1016/j.renene.2019.04.004

Hachicha, A. A., Al-Sawafta, I., and Said, Z. (2019). Impact of dust on the performance of solar photovoltaic (PV) systems under United Arab Emirates weather conditions. *Renew. Energy* 141, 287–297. doi:10.1016/j.renene.2019.04.004

Hassan, Q., Jaszczur, M., Przenzak, E., and Abdulateef, J. (2016). *The PV cell temperature effect on the energy production and module efficiency*. Contemporary Problems of Power Engineering and Environmental Protection (Gliwice, Poland), 33–40.

Jain, S., and Sawle, Y. (2021). Optimization and comparative economic analysis of standalone and grid-connected hybrid renewable energy system for remote location. *Front. Energy Res.* 9, 724162. doi:10.3389/fenrg.2021.724162

Javed, W., Wubulikasimu, Y., Figgis, B., and Guo, B. (2017). Characterization of dust accumulated on photovoltaic panels in Doha, Qatar. *Sol. Energy* 142, 123–135. doi:10.1016/j.solener.2016.11.053

Jiang, H., Lu, L., and Sun, K. (2011). Experimental investigation of the impact of airborne dust deposition on the performance of solar photovoltaic (PV) modules. *Atmos. Environ.* 45 (25), 4299–4304. doi:10.1016/j.atmosenv.2011.04.084

Jiang, Y., and Lu, L. (2015). A study of dust accumulating process on solar photovoltaic modules with different surface temperatures. *Energy Procedia* 75, 337–342. doi:10.1016/j.egypro.2015.07.378

Kaldellis, J. K., and Kapsali, M. (2011). Simulating the dust effect on the energy performance of photovoltaic generators based on experimental measurements. *Energy* 36 (8), 5154–5161. doi:10.1016/j.energy.2011.06.018

Kazem, H. A., Al-Badi, H. A., Al Busaidi, A. S., and Chaichan, M. T. (2017). Optimum design and evaluation of hybrid solar/wind/diesel power system for Masirah Island. *Environ. Dev. Sustain.* 19 (5), 1761–1778. doi:10.1007/s10668-016-9828-1

Kazem, H. A., and Chaichan, M. T. (2016). Experimental analysis of the effect of dust's physical properties on photovoltaic modules in Northern Oman. *Sol. Energy* 139, 68–80. doi:10.1016/j.solener.2016.09.019

Kazem, H. A., and Chaichan, M. T. (2016). Experimental analysis of the effect of dust's physical properties on photovoltaic modules in Northern Oman. *Sol. Energy* 139, 68–80. doi:10.1016/j.solener.2016.09.019

Kim, M., Kim, H., and Jung, J. H. (2021). A study of developing a prediction equation of electricity energy output via photovoltaic modules. *Energies* 14 (5), 1503. doi:10.3390/en14051503

Konyu, M., Ketjoy, N., and Sirisamphanwong, C. (2020). Effect of dust on the solar spectrum and electricity generation of a photovoltaic module. *IET Renew. Power Gener.* 14 (14), 2759–2764. doi:10.1049/iet-rpg.2020.0456

Lou, S., Yang, Y., Wang, H., Smith, S. J., Qian, Y., and Rasch, P. J. (2019). Black carbon amplifies haze over the North China Plain by weakening the East Asian winter monsoon. *Geophys. Res. Lett.* 46 (1), 452–460. doi:10.1029/2018GL080941

Lu, H., and Zhao, W. (2019). CFD prediction of dust pollution and impact on an isolated ground-mounted solar photovoltaic system. *Renew. Energy* 131, 829–840. doi:10.1016/j.renene.2018.07.112

Manju, B., Bari, A., and Pavan, C. M. (2018). Automatic solar panel cleaning system. *Int. J. Adv. Sci. Res. Eng.* 4 (7), 26–31. doi:10.31695/IJASRE.2018.32778

Maraj, A., Londo, A., Gebremedhin, A., and Firat, C. (2019). Energy performance analysis of a forced circulation solar water heating system equipped with a heat pipe evacuated tube collector under the Mediterranean climate conditions. *Renew. energy* 140, 874–883. doi:10.1016/j.renene.2019.03.109

Martín-Consuegra, F., Alonso, C., Pérez, G., Frutos, B., Guerrero, A., and Oteiza, I. (2021). Design, optimization and construction of a prototype for a thermochromic Trombe wall. *Adv. Build. Energy Res.* 15 (2), 161–178. doi:10.1080/17512549.2019.1684365

Meyers, B. E. (2021). "Identification of best plane-of-array irradiance sensor for PV system performance analytics," in *2021 IEEE 48th photovoltaic* specialists conference (PVSC) (IEEE), 1208–1212.

Middelhauve, L., Girardin, L., Baldi, F., and Maréchal, F. (2021). Potential of photovoltaic panels on building envelopes for decentralized district energy systems. *Front. Energy Res.* 9 (ARTICLE), 689781. doi:10.3389/fenrg.2021.689781

Middleton, N. J. (2017). Desert dust hazards: A global review. *Aeolian Res.* 24, 53–63. doi:10.1016/j.aeolia.2016.12.001

Miran, S., Tamoor, M., Kiren, T., Raza, F., Hussain, M. I., and Kim, J. T. (2022). Optimization of standalone photovoltaic drip irrigation system: A simulation study. *Sustainability* 14 (14), 8515. doi:10.3390/su14148515

Mustafa, R. J., Gomaa, M. R., Al-Dhaifallah, M., and Rezk, H. (2020). Environmental impacts on the performance of solar photovoltaic systems. *Sustainability* 12 (2), 608. doi:10.3390/su12020608

Navothna, B., and Thotakura, S. (2022). Analysis on large-scale solar PV plant energy performance–loss–degradation in coastal climates of India. *Front. Energy Res.* 10, 301. doi:10.3389/fenrg.2022.857948

Nkuriyingoma, O., Özdemir, E., and Sezen, S. (2022). Techno-economic analysis of a PV system with a battery energy storage system for small households: A case study in Rwanda. *Front. Energy Res.* 10, 957564. doi:10.3389/fenrg.2022.957564

Nour, C. A., Migan-Dubois, A., Badosa, J., Bourdin, V., Marchand, C., and Akiki, T. (2019). "Evaluation of the plane of array irradiance for a photovoltaic installation equipped with flat reflectors in different geographical locations," in *2019 IEEE 46th photovoltaic specialists conference (PVSC)* (IEEE), 1572–1577.

Nouri, B., Wilbert, S., Blum, N., Kuhn, P., Schmidt, T., Yasser, Z., et al. (2020). Evaluation of an all sky imager based nowcasting system for distinct conditions and five sites. In *AIP Conf. Proc.*, 2303. Daegu, South Korea: AIP Publishing LLC, 180006.

Ojike, O., and Okonkwo, W. I. (2019). Study of a passive solar air heater using palm oil and paraffin as storage media. *Case Stud. Therm. Eng.* 14, 100454. doi:10.1016/j.csite.2019.100454

Peters, I. M., Karthik, S., Liu, H., Buonassisi, T., and Nobre, A. (2018). Urban haze and photovoltaics. *Energy Environ. Sci.* 11 (10), 3043–3054. doi:10.1039/c8ee01100a

Salimi, H., Mirabdolah Lavasani, A., Ahmadi-Danesh-Ashtiani, H., and Fazaeli, R. (2019). Effect of dust concentration, wind speed, and relative humidity on the performance of photovoltaic panels in Tehran. *Energy Sources, Part A Recovery, Util. Environ. Eff.*, 1–11. doi:10.1080/15567036.2019.1677811

Schleifer, A. H., Murphy, C. A., Cole, W. J., and Denholm, P. (2022). Exploring the design space of PV-plus-battery system configurations under evolving grid conditions. *Appl. Energy* 308, 118339. doi:10.1016/j.apenergy.2021.118339

Shah, A. H., Hassan, A., Laghari, M. S., and Alraeesi, A. (2020). The influence of cleaning frequency of photovoltaic modules on power losses in the desert climate. *Sustainability* 12 (22), 9750. doi:10.3390/su12229750

Son, J., Jeong, S., Park, H., and Park, C. E. (2020). The effect of particulate matter on solar photovoltaic power generation over the Republic of Korea. *Environ. Res. Lett.* 15 (8), 084004. doi:10.1088/1748-9326/ab905b

Soomar, A. M., Hakeem, A., Messaoudi, M., Musznicki, P., Iqbal, A., and Czapp, S. (2022). Solar photovoltaic energy optimization and challenges. *Front. Energy Res.* 10. doi:10.3389/fenrg.2022.879985

Styszko, K., Jaszczur, M., Teneta, J., Hassan, Q., Burzyńska, P., Marcinek, E., et al. (2019). An analysis of the dust deposition on solar photovoltaic modules. *Environ. Sci. Pollut. Res.* 26 (9), 8393–8401. doi:10.1007/s11356-018-1847-z

Tamoor, M., Abu Bakar Tahir, M., Zaka, M. A., and Iqtidar, E. (2022). Photovoltaic distributed generation integrated electrical distribution system for development of sustainable energy using reliability assessment indices and levelized cost of electricity. *Environ. Prog. Sustain. Energy* 41 (4), e13815. doi:10.1002/ep.13815

Tamoor, M., Bhatti, A. R., Farhan, M., and Miran, S. (2022). Design of on-grid photovoltaic system considering optimized sizing of photovoltaic modules for enhancing output energy. *Eng. Proc.* 19 (1), 2.

Tamoor, M., Bhatti, A. R., Farhan, M., Miran, S., Raza, F., and Zaka, M. A. (2021). Designing of a hybrid photovoltaic structure for an energy-efficient street lightning system using PVsyst software. *Eng. Proc.* 12 (1), 45.

Tamoor, M., Habib, S., Bhatti, A. R., Butt, A. D., Awan, A. B., and Ahmed, E. M. (2022). Designing and energy estimation of photovoltaic energy generation system and prediction of plant performance with the variation of tilt angle and interrow spacing. *Sustainability* 14 (2), 627. doi:10.3390/su14020627

Tamoor, M., Tahir, M. S., Sagir, M., Tahir, M. B., Iqbal, S., and Nawaz, T. (2020). Design of 3 kW integrated power generation system from solar and biogas. *Int. J. Hydrogen Energy* 45 (23), 12711–12720. doi:10.1016/j.ijhydene.2020.02.207

Tanesab, J., Parlevliet, D., Whale, J., Urmee, T., and Pryor, T. (2015). The contribution of dust to performance degradation of PV modules in a temperate climate zone. *Sol. Energy* 120, 147–157. doi:10.1016/j.solener.2015.06.052

Thapar, V. (2019). A revisit to solar radiation estimations using sunshine duration: Analysis of impact of these estimations on energy yield of a PV generating system. *Energy Sources, Part A Recovery, Util. Environ. Eff.*, 1–25. 1–25. doi:10.1080/15567036.2019.1677819

Toledo, C., Gracia Amillo, A. M., Bardizza, G., Abad, J., and Urbina, A. (2020). Evaluation of solar radiation transposition models for passive energy management and building integrated photovoltaics. *Energies* 13 (3), 702. doi:10.3390/en13030702

Tomin, N., Shakirov, V., Kozlov, A., Sidorov, D., Kurbatsky, V., Rehtanz, C., et al. (2022). Design and optimal energy management of community microgrids with flexible renewable energy sources. *Renew. Energy* 183, 903–921. doi:10.1016/j.renene.2021.11.024

Von Schneidemesser, E., Driscoll, C., Rieder, H. E., and Schiferl, L. D. (2020). How will air quality effects on human health, crops and ecosystems change in the future? *Phil. Trans. R. Soc. A* 378 (2183), 20190330. doi:10.1098/rsta.2019.0330

Weber, B., Quiñones, A., Almanza, R., and Duran, M. D. (2014). Performance reduction of PV systems by dust deposition. *Energy Procedia* 57, 99–108. doi:10.1016/j.egypro.2014.10.013

Xingping, Z., Xiaoying, Z., Yuanbo, Y., Kun, W., Wei, C., and Xiaolan, W. (2019). "Operation mode and economic analysis of concentrating solar power station," in *2019 4th international conference* on intelligent green Building and smart grid (IGBSG) (IEEE), 751–755.

Yazdani, H., and Yaghoubi, M. (2022). Dust deposition effect on photovoltaic modules performance and optimization of cleaning period: A combined experimental–numerical study. *Sustain. Energy Technol. Assessments* 51, 101946. doi:10.1016/j.seta.2021.101946

Zorrilla-Casanova, J., Philiougine, M., Carretero, J., Bernaola, P., Carpena, P., Mora-López, L., et al. (2011). "Analysis of dust losses in photovoltaic modules," in *World renewable energy congress-Sweden; 8-13 may; 2011* (Linköping, Sweden: Linköping University Electronic Press), 2985–2992. No. 057. doi:10.3384/ecp110572985

frontiers | Frontiers in Energy Research

TYPE Original Research
PUBLISHED 09 January 2023
DOI 10.3389/fenrg.2022.1025045

OPEN ACCESS

EDITED BY
Muhammad Amjad,
University of Engineering and Technology, Pakistan

REVIEWED BY
Fahad Noor,
University of Engineering and Technology, Pakistan
Muhammad Aftab Akram,
Pak-Austria Fachhochschule Institute of Applied Sciences and Technology, Pakistan
Amjad Hussain,
University of Engineering and Technology, Pakistan
Binghong Chen,
University of Shanghai for Science and Technology, China

*CORRESPONDENCE
Jianfeng Huang,
huangjf@sust.edu.cn

SPECIALTY SECTION
This article was submitted to Solar Energy,
a section of the journal
Frontiers in Energy Research

RECEIVED 22 August 2022
ACCEPTED 23 September 2022
PUBLISHED 09 January 2023

CITATION
Syed N, Feng Y, Fahad R, Sahito IA and Huang J (2023), Carbon nanomaterials staked with nonwoven (EG/PAN/CQDs) composite as a counter electrode for enhanced photons and photocatalytic efficiency.
Front. Energy Res. 10:1025045.
doi: 10.3389/fenrg.2022.1025045

Carbon nanomaterials staked with nonwoven (EG/PAN/CQDs) composite as a counter electrode for enhanced photons and photocatalytic efficiency

Noureen Syed[1,2,3], Yongqiang Feng[1], Raja Fahad[2], Iftikhar Ali Sahito[3] and Jianfeng Huang[1]*

[1]School of Materials Science and Engineering, Shaanxi University of Science and Technology, Xi'an, China, [2]Department of Textile Engineering, Mehran University of Engineering and Technology, Jamshoro, Pakistan, [3]Center of Excellence in Nanotechnology and Materials, Mehran University of Engineering and Technology, Jamshoro, Pakistan

Prior studies on heavy metal heterojunction with carbon nanomaterials for dye-sensitized solar cells (D-SSCs) found that they were not only toxic but also had poor stability and led to a difficult synthesis. In this work, nanomaterials with flexible nonwoven sheets were employed to improve cell efficiency and were easily synthesized with high stability, durability, washability, and flexibility. By incorporating carbon quantum dots (CQDs) into the anode and counter electrodes, it is possible to boost photon efficiency by scattering the sunlight and turning a huge amount into current density. Here in this research, Textile carbon–based flexible dye-sensitized solar cells (TC-DSSC) with N-doped CQDs may significantly increase solar cell efficiency. Carbon-based nanoparticles stacked with textile apparel (nonwoven bamboo) sheets enabled the desired flexible end applications to be achieved. The prepared material significantly increased solar cell efficiency to 11.26% compared to 8.04% of the one without CQDs. Carbon-based nanomaterials are stacked with textile apparel (nonwoven bamboo) sheets to make them lightweight, highly flexible, wearable, and user-friendly. Furthermore, compared to pure expanded graphite on the nonwoven substrate, a single electrode incorporating CQDs offered low impedance and high current/voltage. On the other hand, when tested for photocatalytic activity using spectrophotometry, the proposed counter electrode made of expanded graphite, PAN, and CQDs loaded on nonwoven material completely degraded the methylene blue dye in a very short period of time. The N-CQDs may prove to be very stable with outstanding washing endurance anchored with expanded graphite layered on a nonwoven medium with an optimum thickness.

KEYWORDS

photovoltaic properties, CQDs (carbon quantum dots), DSSC (dye-sensitized solar cell), photocatalytic activity, expanded graphite, carbon nanomaterial

Introduction

For photovoltaic devices, many approaches have been put forth to date; however, a promising strategy to meet third-generation demand (especially for solar cells) that enables low-cost and improved long-term stability in DSSC with ease of manufacturing provides to expand research area. Polymer-based or apparel-based photon devices have recently received a lot of interest in producing flexible devices. Fabrics covered with carbon nanomaterials have demonstrated excellent flexibility and deformability for shaping into almost any shape and integrating with any portable electronic equipment as a sustainable power source, in contrast to traditional solar cells with a planar structure (Brown et al., 2014; Fu et al., 2018; Sadasivuni et al., 2019). The electrical conductivity of improved graphite staked with carbon quantum dots (CQDs) is a potential attraction to conventional solar cells of carbonaceous materials with flexible bases induced charge transfer process; it efficiently decomposes methylene blue dye.

The exceptionally low toxicity, chemical inertness, and excellent power conversion efficiency of CQDs make them a special class. Nanostructures, such as nanosheets, nanorods, mesoporous films, and nano-sized dots, are being incorporated into textile apparel to enhance the surface area, act as a barrier against redox reactions, and work as conductive junctions. Due to their simplicity to manufacture, low-cost, theoretically high power conversion efficiency (Sahito et al., 2015a), and minimum environmental impact, textile carbon–based dye-sensitized solar cells (DSSCs) have attracted a lot of attention (Saravanan et al., 2017; Heo et al., 2018; Lv et al., 2022) (Ahmed et al., 2020; Mousa et al., 2022). The key to increasing the efficiency of this research is tailoring the CQDs utilized as electrodes (Li et al., 2019; Sharif et al., 2022). One of the best solutions to replace costly platinum (Pt) electrodes in a dye-sensitized solar cell is as follows: counter electrode (CE) may be covered with CQDs prepared by expanded graphite by combining nonwoven sheets, producing a typical solar cell that comprises economic benefits over other solar cells. Therefore, to find cost-effective materials, carbon-based nanomaterials, polymers, and compounds are more effective. To create highly effective flexible wearable solar cells with nanomaterials that are user-friendly (Sahito et al., 2015b), skin-friendly, light-weight, and powerful solar cell output devices, it is crucial to customize the selection of electrode designs and materials (Guo et al., 2017; Singh and Shougaijam, 2022). It has been proven that carbon materials are an excellent solution to resolve the issues raised above. However, pure expanded graphite is very inexpensive and conductive with less electro-catalytic nature; therefore, fulfilling synchronized character by incorporation of CQDs has been achieved (Riaz et al., 2019). Additionally, in this work, nanostructured electronics were effectively incorporated into textile constructions to expand the application and replace costly FTO- and Pt-based electrodes. In addition, CQDs, with their unique luminous property, may be employed to enhance photovoltaic qualities (Sahito et al., 2016). The CQDs produce electrons that are widely used in circuits, catalysis, photovoltaics, storage devices, and other applications when exposed to light irradiation (Guo et al., 2017; Zhang et al., 2018; Li et al., 2019; Khan et al., 2020; Ramanujam et al., 2020; Lv et al., 2022; Sharif et al., 2022; Singh and Shougaijam, 2022). The photo-excitation performance and, consequently, electron concentration of the final CQDs are considerably increased by doping CQDs with N elements. For wearable DSSC to be highly effective, the clarity and flexibility of the front electrode must be improved (He et al., 2020). There has not been a lot of published research on improving the front electrode's transparency in stacked-type solar cells. Only a small percentage of photons were able to stimulate and adjust the semiconductor's electron-hole separation in the majority of the suggested system, which used a back illumination strategy. Here, we describe a stacked and expanded graphite carbon structure–based dye-sensitized solar panel (TC-DSSC). A highly transparent and conductive carbon front electrode (CFE) was made *via* CQDs functionalization, and solar system–produced TiO_2 that had been hydrothermally coated with CQDs that contained natural dye was examined for photovoltaic activity (Peerakiatkhajohn et al., 2016; Kandi et al., 2017; Kong et al., 2018).

Additionally, cathode composite has been suggested for photocatalytic activity and demonstrated 100% methylene blue dye degradation under UV light for 10 ppm solution in 25 min only. Testing on nonwoven clothing textiles has been performed to establish their physical enhancement, which includes flexibility, durability, and stability (Fu et al., 2018; Tao et al., 2019). The recommended TC-DSSC showed 4% higher efficiency compared to TG-DSSC, and CQDs containing solar cell efficiency demonstrated increased photovoltaic performance with a high Jsc of 19.60 mA cm^{-2}. Investigations on the impact of charge transport and all electrochemical characteristics on solar cells were extensive. The produced C-DSSC is incredibly adaptable and can be incorporated or sewn into clothing for wearable batteries, power gadgets, or self-powered medical devices. The proposed study provides an example of a straightforward flexible solar cell for future needs.

Experimental

Materials

Transparent fluorinated tin oxide glass (FTO) was used for the C-DSSC assembly, and a nonwoven bamboo sheet was utilized. Sodium nitrate ($NaNO_3$, close to 100%), concentrated sulfuric acid (H_2SO_4, 98%), hydrogen peroxide (H_2O_2, 35%), polyacrylonitrile (PAN), concentrated hydrochloric acid (36.5%),

and methylene blue dye were purchased from Sigma Aldrich. Graphite powder was bought from Bay Carbon, United States. For the electrolyte spacer, iodide electrolyte and 40 μm surlyn sheet were used for assembling the electrode.

Fabrication of photo anode electrode

To get more photon-containing electrodes, the CQDs-based front electrode (CFE) was meticulously constructed to obtain better efficiency and sheet conductivity requirements. Various CFE sheets with varying carbon quantum dots content weight percentages were prepared for this purpose. First, five FTO glass electrodes of 2 × 2 cm^2 size were washed with ethanol and water and mixed in a 1:1 ratio. The CF FTO was ultrasonically washed for 2 h and then dried for another 2 h. The washed CF FTO were clamped by tape for applying TiO^2 paste. Paste preparation was carried out by thoroughly mixing 10 mL of ethanol and TiO^2 powder till a smooth paste was realized. Furthermore, TiO^2 containing FTO electrodes was prepared, and to get scalpel printing thickness up to 6–8 μm thick, a coat was applied, and vacuum heat was applied at different temperatures i.e., low to high (70–450°C). The baked coated glass was cooled down to around 70°C. Afterward, CQDs containing dye solution were prepared. For dyeing, natural strawberries were meshed in an extractor, and strawberry juice was taken out, vacuum filtered, and kept at a temperature of 100°C. CQDs dye-containing solution was prepared by 1:1 stock solution and immersed into TiO_2 coated FTO glass for 24 h under the dark.

Fabrication of textile-CQDs dye-sensitized solar cell and precursors synthesis

Carbon-based textile solar cells are highly demanded due to their flexibility and higher electrical conductivity with long stability. For achieving all these characteristics and improved electrochemical efficiency, different composites were examined in this work. Nonwoven, as a base material compared with woven cloth material, is highly approachable because of having high thermal stability and excellent absorbency and providing a smooth structure. To get high conductivity and photo electron properties, initially, five 2 × 2 cm^2 of fabric were cut into pieces and washed with acetone and water, respectively. They were then dried and tape-casted using 40-, 60-, and 80-mm tape. The expanded graphite paste was evenly spread on the substrate using the doctor blade method, and the practice was continued till a homogenous coating was achieved. The graphite-coated fabric was then clamped with another tape, and PAN (polyacrylonitrile) nanofiber dip CQDs were coated on a graphite nonwoven sheet. The absorbed PAN by CQDs enables the graphite paste to be more stable, improves its deposition, and enhances its efficiency. However, for strong bonding, air drying was realized at 150°C for 2 hours in a dry oven.

Graphite oxide (GO) is a byproduct of graphite oxidation processes like Hummer's method, as given in our previous work (Sahito et al., 2016). The graphite crystal structure was synthesized to include oxygen-containing groups (epoxide and hydroxyl) by oxidizing it. Because these oxygen groups interact with water, the GO becomes hydrophilic. Water is introduced between the GO sheets due to their hydrophilicity, causing them to disperse easily. For synthesis, graphite (5 g) was put into a flask with 2.5 ml of sodium nitrate and 115 ml of sulfuric acid (high immaculateness grade). The suspension was mixed under a magnetic stirrer for 30 min at 0 °C (the suspension tone was dark). Then, the mixture was left for 3 days at room temperature. For making the mixture highly oxidized, this suspension was treated with water (the shade of the suspension changed to more dispersed, and the suspension turned out to be more porous). 10 ml of water was added to the flask, and the entire stock was left for 30 min at room temperature. Afterward, 21 ml of hydrogen peroxide (reagent grade) was added. The mixture become more expanded, and the shade of the acquired suspension changed to light grey. After the solution was conditioned for 24 h at room temperature, it was filtered over and again and washed with refined water. The filtered cake was thermalized using a microwave oven at a high temperature until it turned out highly conductive. This thermal heating of waves with high temperatures made the cake highly expanded.

Using the dip-and-dry coating process, a stock solution was created before creating the cathode electrode. 3 mg of GO particles were diluted in the stock solution and sonicated for 30 min to make the solution. The nonwoven cut sheet was dipped into the solution for 20 min, dried at 100°C for 15 min, and then repeated dip coating to achieve high loading. Additionally, GO/nonwoven requires stability, an improved electrical channel, and an active site with strong bonds without redox capability and CQDs with PAN coating were used as a second layer. PAN nanofibers were made using the electrospinning process followed by previously reported work (Yang et al., 2010). In brief, PAN was dissolved in DMF solvent with 12% polymer and was used to produce nanofibers through electrospinning. This solution was agitated for 24 h to ensure homogenous mixing. A 5 ml syringe with a tiny tip that measured 0.5 mm across the inward distance was used to inject the electrospinning fluid. A collector and a high voltage of 15 kV were employed in conjunction with the needle's drops to produce an electric field that was exceedingly concentrated. Aluminum foil 0.5 mm thick was used to cover a metal plate that served as the collector and was connected by terminals. The collector was configured with a 15 cm working distance. A syringe pump was used to regulate the polymer arrangement's flow rate. The 1 ml/h flow rate was the most effective (Li et al., 2016; Jiao et al., 2019; Mahala et al., 2020; Lv et al., 2021), and for CQDs, the synthesis process was followed

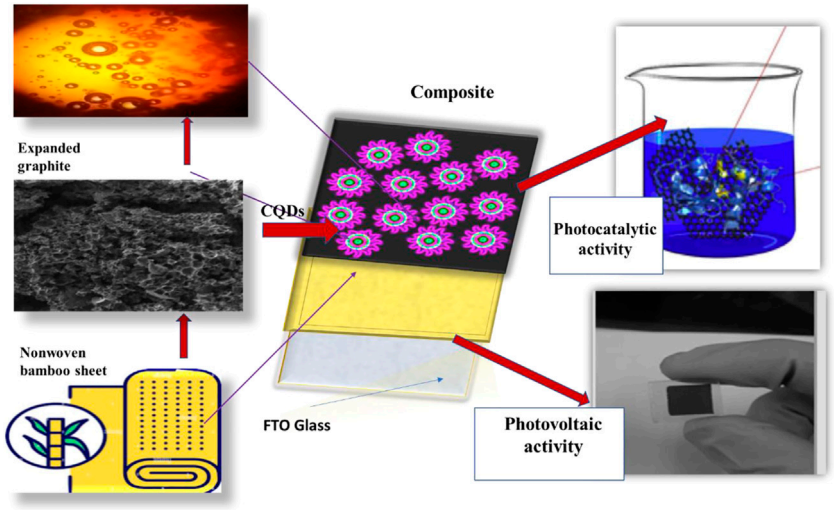

FIGURE 1
Schematic illustration of composite to experimental work.

by a previously reported work. The hydrothermal approach has been used to synthesize N-CQDs (Cao and Yu, 2016; Lu et al., 2018; Ren et al., 2019). In brief, 3 g citric acid and 3 g urea (0.11 wt%) was placed in a measuring beaker. Then, 30 ml of deionized water was added, the suspension was placed in a magnetic stirrer for 5 min at room temperature, and the homogeneous solution was moved into a 100 ml hardened steel reactor with a Teflon liner for the quick aqueous response at 140–240°C for 2–10 h, respectively. After cooling to ambient temperature, the final suspension was filtered through a 0.22 μm filter paper to remove big particles. Then, it was transferred to a 20 ml dialysis machine (1 kDa sub-atomic weight cutoff) and dialyzed in 1.5 L purified water several times for 48 h, yielding a pale-yellow N-CQD solution.

The second layer of CQDs loaded PAN nanofibers was applied by making stock solution, and the dip solution coating method was used again to coat this nanofiber layer on the graphite oxide layer. PAN nanofibers were repeatedly dip coated, followed by drying at 70°C to get high absorbency of CQDs on PAN nanofibers. For combining the nonwoven, loaded GO was first clamped, and PAN/CQDs were pasted on it accurately with the same size of 2 × 2 cm^2.

To avoid short circuits in textile CQDs dye-sensitized solar cells (TC-DSSC), the fibrous structure of the cathode should exceed interfacial contact, or it may cause short circuits and lead to low photovoltaic activity. To lower this risk, a gel type of electrolyte was prepared as a polymer electrolyte (Sahito et al., 2017). For the preparation of the polymeric electrolyte, PVA was dissolved in water with a 1:1 ratio. The synthesized electrolyte was added and continuously stirred until a homogenous polymer-containing electrolyte was obtained following the full dissolution of PVA and gel formation. Using a syringe, the electrolyte was injected into the closed assembly of (TC-DSSC). All procedures are explained by schematic illustration, as shown in Figure 1.

Characterizations

The microstructure and surface morphology of the precursors and PAN/CQDs/GO nonwoven were recorded by transmission electron microscopy (TEM) and scanning electron microscopy (SEM, JEOL model JSM 6010 LA) instrument operated at an accelerating voltage of 10 kV. EDX was attached to FESE, with EDX to analyze the presence of nanoparticles on the surface of PAN nanofibers. XRD was performed using a Rigaku RINT-2000 diffractometer with a source of filtered Cu Ka radiation. XRD pattern of graphene oxide (GO) was also examined. All precursors were analyzed by different characterizations. For CQDs, the particle size and size distribution were examined by using the Zeta sizer (Malvern Zeta Sizer Nano ZS series, United Kingdom) by dispersing nanoclusters at a temperature of 25 °C in aqueous media. The Origin Pro 8.5 and ImageJ software were used for data analysis, curve fitting, and fiber diameter distribution. UV and FTIR (FTIR, Shimadzu, 8900-FT-IR spectrometer Tokyo Japan) were also taken for further confirmation. Dye photodegradation was examined using a Hitachi UV–vis spectrophotometer (UV-2700, Shimadzu, Japan) at a wavelength from 200–700 UV-visible spectra of the methylene blue (MB). The proposed sample's electrical resistance was examined using a resistive test instrument of a typical four-

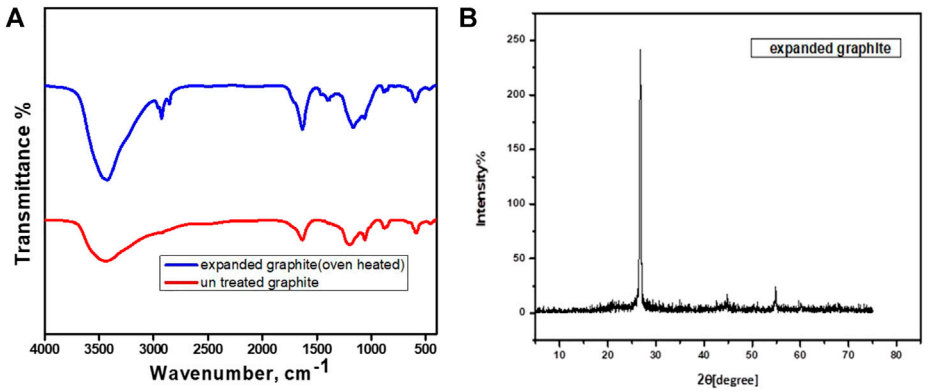

FIGURE 2
(A) FTIR of pristine graphite and expanded graphite. **(B)** XRD graph of GO (graphite oxide).

probe head system, and the thickness of layers was examined with an FTO glass using a micrometer. Using the electrochemical impedance spectroscopy (EIS) method, the charge transfer resistance (RCT) at the DSSC cathodes was examined by using the electrochemical impedance spectroscopy (EIS) technique. The efficiency of a TC-DSSC prepared by expanded graphite stacked with CQDs/PAN nanomaterials was measured using a device (Mac science CO) equipped with a solar simulator with a 160 W xenon arc lamp as a solar simulator.

Result and discussion

Schematic illustration Characterization of expanded graphite oxide

The FITR spectra of expanded graphite were obtained using Fourier transform infrared spectroscopy (FTIR), as illustrated in Figure 2A. Peaks that signify the presence of O-H stretching C-O carboxyl may be detected on 3,436 cm^{-1}, 2,921 cm^{-1}, 1,285 cm^{-1}, 164 cm^{-1}, 1,394 cm^{-1}, and 1,164 cm^{-1}. Treated graphite with OH groups improved mild to strong C=C stretching and peak definition and height. The existence of C=C is indicated by a minor absorption at 2,116 cm^{-1} in pure graphite in comparison. The O-H group is present, as indicated by the maximum wavelength of 3,438 cm^{-1} in expanded graphite. Additionally, a solid wave number of 870 cm^{-1} produced by C-H bending vibrations and the presence of weak C=C at a wavelength of 2,116 cm^{-1} were found, while pure graphite was discovered to be less absorbent and to have fewer hydroxyl groups.

On the other side, Figure 2B shows the XRD pattern for synthesized expanded GO. Here, the very strong and very sharp diffraction peak around 26.5° is assigned to the (002) diffraction peak of the plane reflection. It is confirmed that the (002) diffraction peak of the expanded graphite corresponds to the characteristic peak. This peak shows the highly active site availability in graphite structure because of thermal decomposition of intercalation compounds of graphite made highly oxidized.

Characterization of CQDs

The nano size particles and size distribution of the CQDs samples were examined by using the Zeta sizer. The CQDs with a typical size of 340 nm were uniformly distributed and monodispersed, as shown in Figures 3A and B. CQDs were discovered to be formed by oxidative cleavage into the homogeneous size of particles that have been widely dispersed. The size distribution of CQDs was in the range of 400–500 nm, with the content of CQDs reaching up to 35%. On the other hand, for structure understanding, of synthesized CQDs, as prepared by citric acid and urea, ultimately form strong carbon-based materials. Because of a strong chain of sp^2 bond present in urea, which is utilized for doping of N-doped CQDs, and a further citric acid is also a basic form of C=C/C-C, which is present in CQDs main structure, and all these bonds after thermal heating reach to the surface of the nucleus of CQDs. To confirm these functional groups, the presence of (-OH), carboxyl (-COOH), and carbonyl (-C=O) in the primary structure of CQDs was established by FTIR analysis. The FTIR spectrum validates the oxygen functionalities of different types by distinguishing different peaks. 3,450 cm^{-1} (O-H stretching vibrations), 2,902 cm^{-1}, 2,852 cm^{-1} (C-H stretching vibrations), 1,625 cm^{-1} (C-Stretching), and 3,219 cm^{-1} (peak) (N-H stretching). These findings suggest that CQDs arise by the breakdown of epoxy groups and the underlying C–C bonds. Based on these findings, we can conclude that formed CQDs are N-doped and C=C/C-C

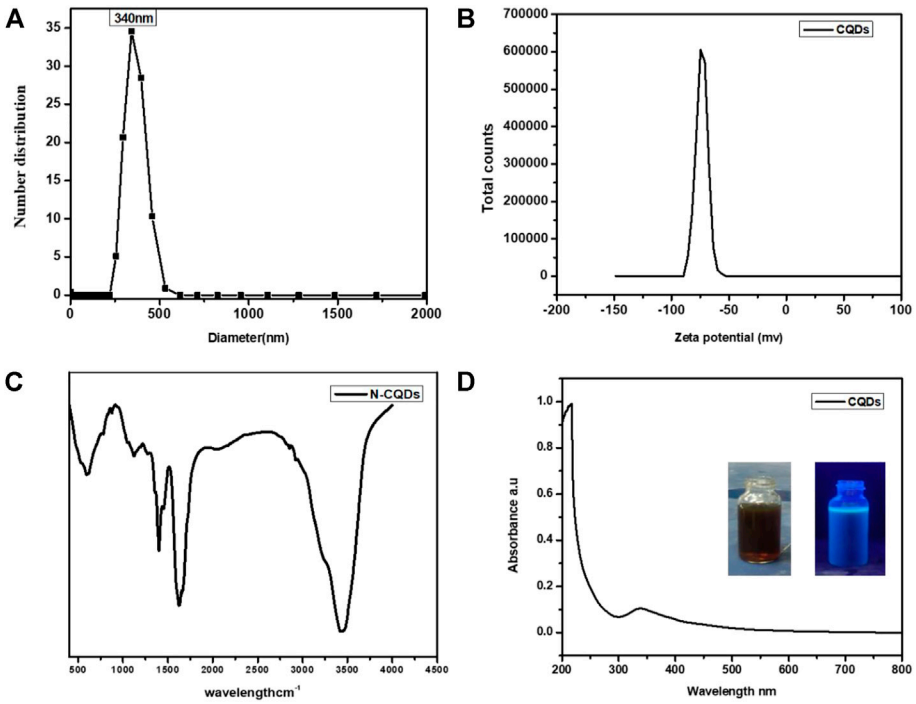

FIGURE 3
(A) Size analyzer of CQDs 3. **(B)** Zeta Potential of CQDs 3. **(C)** U-V light of CQDs3. **(D)** FTIR of CQDs.

with hydrogen bonding and that all these bonds fluctuate with hydrothermal temperature and time. Because of the carbonyl and hydroxyl groups, it is readily soluble. Furthermore, when UV-vis absorbance was used to analyze optical properties, it was discovered that the maximum absorption was seen at 340 nm (Figure 3C), which was the aromatic system's absorption and had previously been reported to have a high PL on this wavelength, and the water-soluble CQD had fine optical properties that were observed under UV-light. They emit a light brown tint throughout the day and a blue color when exposed to UV light, making them nontoxic and environmentally acceptable and considering them as alternatives for semiconductor quantum dots to be applied in the photocatalytic application. The hydrophilic nature made this a more suitable candidate for absorbency base photodegradation of MB. Moreover, N-doped CQDs, for their photoexcitation performance, enhanced the efficiency of solar cells by increasing dye electron density accelerating photovoltaic properties and the microstructure of CQDs on solar cell and on CE. This symmetrical study reveals the influence of CQDs on the efficiency of the cell.

Characterization of composite

Figure 4 summarizes several characterizations, including SEM, EDX, and TEM images of expanded graphite, PAN, and PAN/GO/CQDs composite nanofibers. SEM in Figure 4A verified the highly expanded and porous structure of graphite. After chemical treatment and thermal heating, it collapsed the graphite layer and deformed the structure randomly, resulting in high porosity and smoothness in the structure. Figures 4B and C show SEM of PAN nanofibers (b) without coating and (c) with coating, demonstrating fine, smooth, and uniform composite nanofibers with an average diameter in nm and clear difference with pristine PAN and treated PAN with CQDs. The morphology of TC-DSSC composite nonwoven complete electrode by the cross-sectional view, as displayed in Figure 4D, also demonstrates that the fine layering of graphite containing PAN with CQDs is smoothly pasted on the nonwoven structure. Figure 4E demonstrates the cross-sectional and top view PAN nanofibers loaded with CQDs taken after making a complete electrode of samples; the obtained product changed into a counter electrode shape.

Furthermore, the presence of CQDs on PAN nanofibers was investigated using a TEM image. Figure 4F confirms that nano-sized particles dispersed smoothly on the surface. In addition, the microstructure and morphology of the nanofibers were analyzed using an EDX analyzer. It was discovered that the presence of highly expanded graphite oxide and CQDs increased conductivity and photovoltaic and made the nanofiber surface highly porous, which helped to increase the active surface area

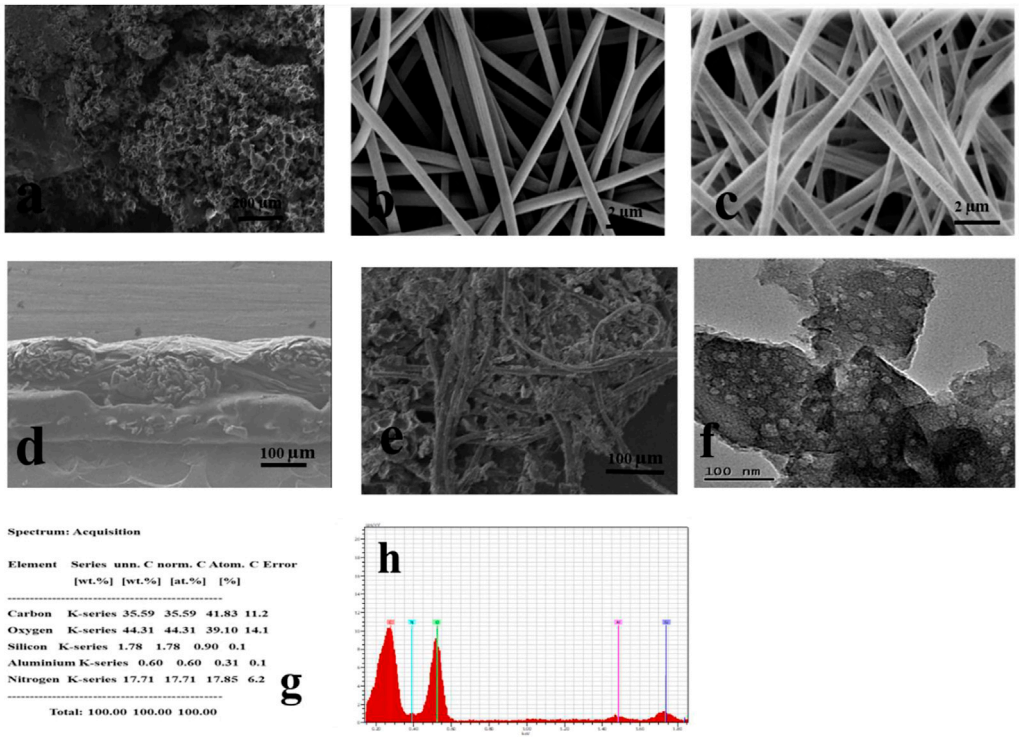

FIGURE 4
Morphology of composite **(A).** SEM of expanded graphite **(B and C).** SEM of PAN nanofibers **(D and E).** Cross-sectional and front view of composite **(F).** TEM image of CQDs with PAN **(G and H).** X-ray (EDX) of composite.

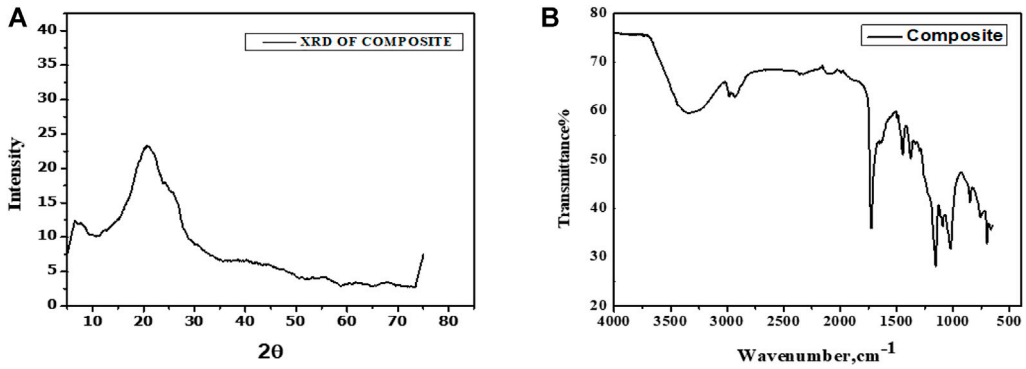

FIGURE 5
(A) XRD of composite. **(B)** FTIR of composite.

and improve the efficiency of DSSC. The layers of GO and CQDs are seen to be smooth. This cross-linked network forms a fibrous web with a wide surface area for dye absorption. To confirm the distinct elements present in the composite nonwoven sheet, an energy dispersive X-ray (EDX) examination of the composite was performed. The acquired EDX spectra are shown in Figures 4G and H, revealing the basic elements carbon (C), nitrogen (N), and oxygen (O) atoms.

In addition, X-ray diffraction was used to study the crystalline structure of the PAN/GO-CQDs nonwoven film, as shown in Figure 5A. The crystalline character of the composite was confirmed by the strong peaks at 2Θ values of 22.55°.

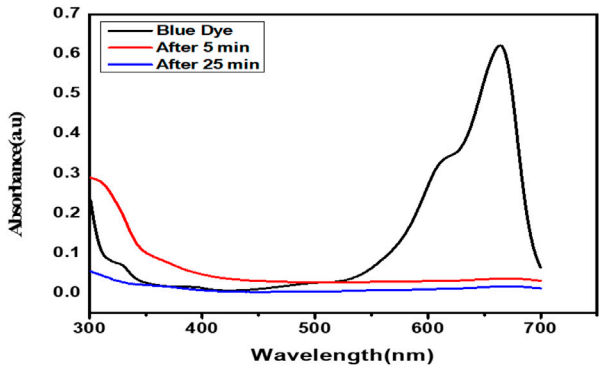

FIGURE 6
UV light of photodegradation of methylene blue.

Furthermore, one notable peak at 2Θ of 30° indicates the presence of a C-C bond, indicating that the film is substantially rich in carbon (Othman et al., 2016). On the other hand, Figure 5B shows the FTIR spectra of CQDs/PAN nanofiber coated expanded graphite/nonwoven composite. The band at 1,050 cm^{-1}, which is attributable to the symmetric stretching of CQDs and GO on PAN, can be observed in a composite. While the peak at 3,252 cm^{-1} is caused by the aromatic rings' C-H stretching vibration in GO, the peak at 1,551 cm^{-1} is caused by the -C, N, and O groups in a composite. Peaks at 2,921 cm^{-1} and 2,850 cm^{-1} correspond to strong stretching of N-H, while peaks at 1968 cm^{-1} and 2000 cm^{-1}, respectively, represent medium stretching C=C=C. Due to C-N stretching in aromatic amines, which is an indication of crosslinking, the peak at 1,149 cm^{-1} confirms the existence of aromatic amine groups in expanded graphite/PAN nanofibers. The wide band vibrates when stretched. It is possible to attribute the peak at 1,551 cm^{-1}. Because of the existence of CQDs, the peak at 1,551 cm^{-1} can be attributed to N-O asymmetric stretching.

Fabrication of expanded graphite nonwoven photocatalyst

A spectroscopy absorption approach was used to analyze the photocatalytic degradation of MB dye. A 250 ml cylindrical quartz vessel was filled with aqueous solutions of the catalyst support counter flexible electrode FTO free and the MB dyes (0.10 g/L, 100 ml). Additionally, the solution was added and stirred continuously for various time ratios to mix and mobilize the dye on the surface of the nanofibers with different time ratios. To accomplish the adsorption–desorption equilibrium of MB on the composite surface, the suspension was stirred mildly without visible light illumination. A 300 W Xenon light with a frequency from 400 to 700 nm served as a light source (Alley et al., 2012; Khalid et al., 2017; Qu et al., 2018). The separation from the light source to the fluid surface was set to 15 cm. The change in dye concentration was studied and analyzed using dye absorbance of color in UV spectra photometer after 5 min and 25 min, as shown in Figure 6. To evaluate the photocatalytic degradation of methylene blue under visible light and UV light irradiation in a photocatalytic reactor, CQDs/PAN/GO nanofibers were used. An orbital shaker, a beaker with dye solution, and a light source positioned as shown make up the photoreactor. The UV lamp was turned on to start the photocatalytic reaction, and any other lights were shielded throughout the process. A UV-visible spectrophotometer was used to record changes in the absorbance band of the MB spectrum at the specified time intervals and analyze the photo-reacted solution.

Washable textile-embedded flexible carbon-based solar cell

The light weight, flexibility, shatter resistance, and stability of textile-based solar cells with high specific power voltage are their key characteristics (Fu et al., 2018; Heo et al., 2018; Lv et al., 2022; Singh and Shougaijam, 2022). Here, in this work, we produced a combination of inexpensive and essentially usable carbon nanomaterials combined with flexible textile apparel for comfortable use on textiles. Researchers are looking for more flexible materials to replace the hard glass in the part of the light-blocking layer in order to get electrodes with greater transparency and higher efficiency (Li et al., 2019). It is anticipated that flexible energy materials would fundamentally alter how we use energy, transforming our way of life. A significant component is the fabrication of the cell process. Among several techniques, dye-sensitized solar cells stacked with fabric coated with CQDs were thought to be a hot study issue. With the addition of N and S, the photoexcitation and photovoltaic performance of DSCC are improved (Yang et al., 2014).

Without the need for battery maintenance or recharging, solar cells might make textile-based wearable devices energy-independent; however, their washing resistance, which is a requirement for consumer adoption of e-textiles, has rarely been explored. The purpose of this research is to present a thorough investigation of the launder ability of solar cells incorporated into fabrics. Because of their soft, flexible, light, air-permeable, elastic, and stretchable qualities, which are adaptable to human body forms and movements, textiles offer a natural substrate for wearable technology. Textiles are resilient to a variety of environmental factors and weather conditions, as well as rigorous handling, folding, bending, and processing. Additionally, clothing and textiles are subjected to prolonged, densely packed storage, spilling onto the ground, exposure to sunshine, chemicals, and the most demanding conditions. Textiles and clothing also resist prolonged, densely packed

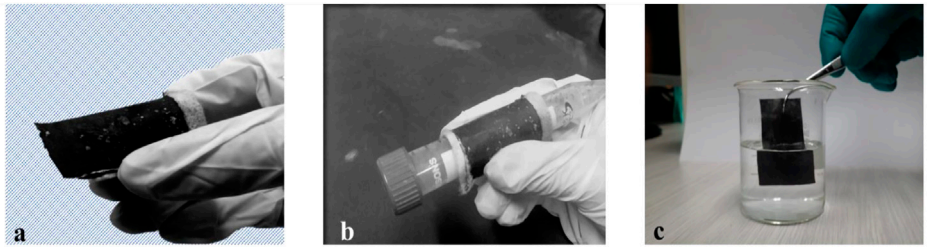

FIGURE 7
(A) Complete flexible counter electrode **(B).** Flexibility checked by wrapping on cylinder **(C).** Washing durability testing.

storage, falling to the ground, exposure to sunshine, chemicals, and the most difficult laundry washing.

E-textile do not follow standard testing of washing, hence, ISO 6330:2012 (SFS-EN ISO 6330:2012, 2012) must be followed (Rotzler et al., 2021), but these methods are difficult to follow; according to standards on our samples, the testing technique was followed by soaking electrodes in detergent water for 72 h at room temperature. As a result, it revealed good washing durability and found no material bleeding in the water. Martindale abrasion test and pilling test were carried out as suggested by different authors (Fu et al., 2018; Tao et al., 2019; Rotzler et al., 2021). These tests may be useful from the perspective of the textile industry to forecast the robustness against mechanical stress and water tightness of individual electrical components or sensor materials. While for flexibility checking wrapped electrode on a cylindrical tube, both methods were chosen to prove washing durability and flexibility of electrode as shown in Figure 7.

Photovoltaic testing

In this work, a brand-new and simple method for creating wearable dye-sensitized solar cells has been proposed. The CCE cathode of the metal-free solar panel was separated by membrane spacers that had been hydrated with polymer electrolytes. To assess the compatibility of manufactured electrodes for C-DSSC, a photo anode and cathode's ability was estimated before the complete C-DSSC was made. Different comparison studies of solar cells were created. The solar cell fabrications include (1) full TC-DSSC (with CQDs), (2) TG-DSSC (without the addition of CQDs) graphite coated on nonwoven, and (3) symmetrical cells comparison with CQDs and without CQDs. Nyquist plots were plotted using the Z-view software (Fu et al., 2018; Tao et al., 2019; Ahmed et al., 2020; Rotzler et al., 2021; Saberi Motlagh et al., 2022), and electrochemical testing was determined by calculating using an equivalent circuit. The improved photoelectric conversion efficiencies in the counter electrode front, that are predominantly attributed to the increased electron concentration from photo exciting N-CQDs and, consequently, photovoltaic performances of light-inducing CEs, are confirmed by results that show TC-DSSC impedance at CCE/CQDs. The maximum efficiency for TC-DSSC is 11.84% for CQD solar cells and 8.84% for TG-DSSC without CQDs, respectively. However, DSSC without addition of CQDs layer on cathode layer, it was coated with graphite sheet staked with nonwoven sheet, reduction of CQDs from both electrode was also analyzed and showed higher impedance, while with addition of CQDs on both electrodes in a shape of complete cell was examined, its analyzed by comparing lower impedance of due to higher electron excitation as shown in Figures 8A–C which confirms high current voltage with low impedance for CQDs containing solar cell, because the incident light passed through CQDs generate high electrons and increase absorbency of dye molecules and regulate this process fast to excite electron towards conduction band and CQDs with its photo luminous sufficiently energize to excite and hindered the electron recombine with holes during the light strikes on the surface and further more due to highly expanded and porous structure of graphite and nonwoven as a base, interfaces rapidly transfer of electron in its conductive porous structure increase the load of current density and hold for longer time because of high intake ability of nonwoven structure, as shown in I-V curve image of Figure 8D (d), which represents improved efficiency of solar cell, which confirmed the strong chemistry have been developed while without CQDs solar cell showed I-V curve with less efficient.

Higher impedance values are validated, and the generating mechanism is hampered by the CFE substrate's decreased transparency. The incoming light was absorbed by the dye molecules in the nonwoven fiber network made of expanded graphite and excited electrons that were then injected into the conduction band. Some incident photons decay and are insufficiently excited to transport electrons toward the photo anode conduction band. Due to the recombination of these decaying and lower energy electrons with holes at the electrolyte, V_{OC} has diminished. On the other hand, in the photo anode, which enhances the current density of C-DSSC as indicated in I-V findings, the charges that have been

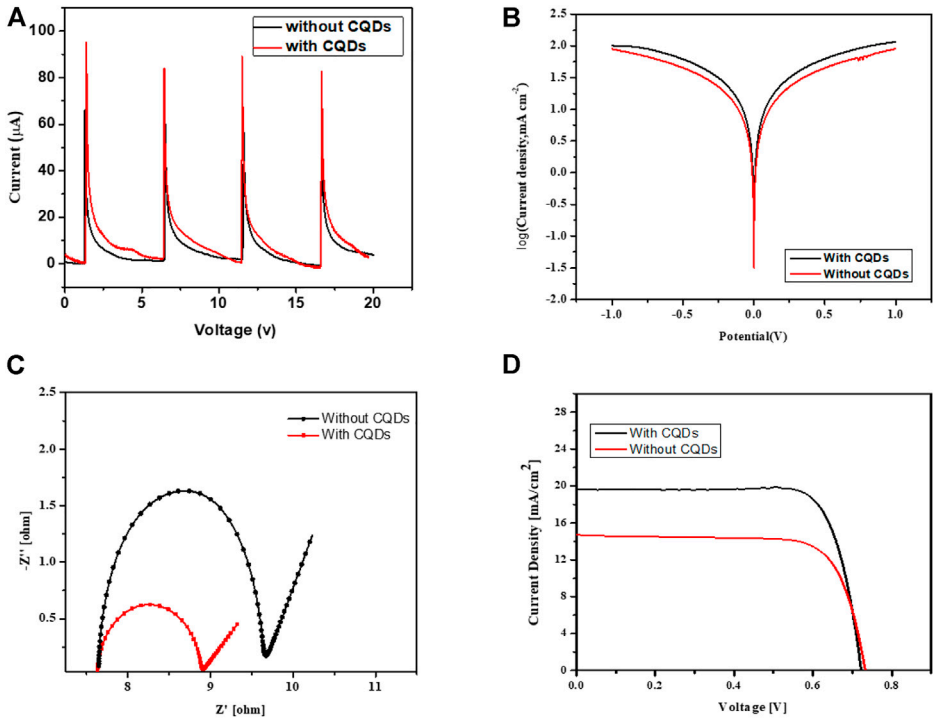

FIGURE 8
(A) Current signal produced while dropping electrolyte on electrode. **(B)** Tafel polarization curves of symmetric cell. **(C)** NY Quist plot for solar cell. **(D)** I-V curve of solar cells with CQDs and without CQDs.

TABLE 1 Comparison of electrochemical and photovoltaic performance of cells fabricated by expanded graphite nonwoven with CQDs and without CQDs electrodes.

Types of DSSC	Symmetrical cells	DSSC				
	R_S [Ω]	R_{CT} [Ω]	Jsc (mA.cm^{-2})	Voc (V)	Fill factor	η% (%)
Expanded graphite with CQDs (TC-DSSC)	7.4	1.25	19.60	0.72	78.94	11.84
Expanded graphite without CQDs (TG-DSSC)	7.6	4.69	14.74	0.73	74.63	8.06

accumulated at the TC-DSSC/CQDs interfaces quickly move towards the load. The I-V curve shows increased cell performance. The I-V curve makes it clear that the photovoltaic performance of solar cells with photo anodes that dip in CQDs with dye is on the rise. The DSSC's total effectiveness increased from 8.06% to 11.84%.

Furthermore, N-CQDs tailored cell photovoltaic performance increased as an increment of TiO_2 coating thickness on an electrode; the coating varied from 6 μm to 10 μm. The increment enabled carrying more CQD particles, increased path voltage, and even overall efficiency of the cell was observed with highly improved efficiency. Here, when N-CQDs tailored light-inducing CEOs are exposed to radiation, both the exchange current density (J0) and the limiting diffusion current density (Jim) increase. J0 = RT/nFRct and Jim = 2nFCDn/l (Guo et al., 2017; Singh and Shougaijam, 2022), where *R* is gas constant, *Ts* absolute temperature, *F* is Faraday's constant, and *l* is the spacer thickness of two electrodes; these light-inducing CEs have enhanced photovoltaic performances in TC-DSSCs (as clearly shown in Table 1). Another comparison was made using a symmetrical solar cell with layers of cathode layer covering both sides (schematic illustration shown in Figure 9) and being at the same level as modern DSSCs (Bai et al., 2014; Guo et al., 2017; Haider et al., 2019; Gao et al., 2021; Singh and Shougaijam, 2022). Overall observation cleared that electron generation and efficiency of the device were enhanced by

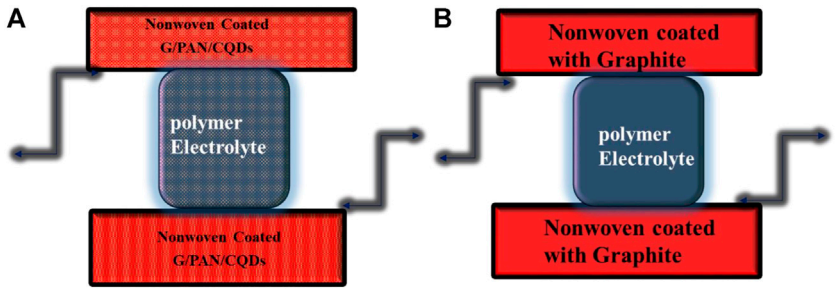

FIGURE 9
Schematic Symmetrical cell comparison **(A)** with CQDs and **(B)** without CQDs.

the right combination of composite with substrate selection. This is one of the approaches to tailor metal-free flexible electrodes. Precursor properties is a key role to improve photovoltaic properties. CQD's characteristic is more identical because of their photo excitation power; however, their stability after 15 days was tested, and their efficiency decreased over time. Further research on this work is required to extend experiments for achieving device more stability and make it applicable on a large scale.

Conclusion

Expanded graphite with CQDs incorporation possesses a high surface area, which enables electrochemical enhanced properties, which is confirmed by morphological and structure analysis. The metal-free device exhibits excellent electrochemical characteristics and more electronic and charge transfer enhancement. Electrochemical results show that, in comparison to TC-DSSC, TG-DSSC exhibits higher electronic and charge transfer efficiency. High charge transfer on a very porous structure demonstrated outstanding electrochemical capabilities, allowing for the proposal of increased solar cell efficiency. Additionally, the comparative study of symmetrical cells was examined by the incorporation of CQDs; the device with CQDs produces high efficiency in comparison to the device without CQDs, and it was discovered that the CQDs' properties are more similar and depend upon their effectiveness in attracting photons. The photoexcitation power of CQDs makes their characteristics more suitable, and, in order for them to be standardized as textile solar cells, the device's flexibility, durability, and washing fastness were tested. The results show that the device is highly flexible and stable in terms of washing fastness. The conductivity is confirmed by highly enlarged porous graphite on nonwoven, which was further improved by the addition of CQDs in photovoltaic testing. The photocatalytic performance revealed 100% photo destruction of methylene blue dye in 25 min.

Data availability statement

The original contributions presented in the study are included in the article/Supplementary Material; further inquiries can be directed to the corresponding author.

Author contributions

All authors listed have made a substantial, direct, and intellectual contribution to the work and approved it for publication.

Funding

This work was supported by the National Natural Science Foundation of China (Nos. 52073166 and 52072226), the Xi'an Key Laboratory of Green Manufacture of Ceramic Materials Foundation (No. 2019220214SYS017CG039), the Key Program for International S&T Cooperation Projects of Shaanxi Province (2020KW-038 and 2020GHJD04), the Science and Technology Program of Xi'an, China (2020KJRC0009), the Scientific Research Program Funded by Shaanxi Provincial Education Department (No. 20JY001), the Science and Technology Resource Sharing Platform of Shaanxi Province (2020 PT-022), and the Science and Technology Plan of Weiyang District, Xi'an (202009).

Acknowledgments

The authors thank the Shaanxi Key Laboratory of Green Preparation and Functionalization for inorganic materials for their experimental platform and testing conditions. Y. Q. Feng was grateful for the support from the Science and

Technology Youth Stars Project of Shaanxi Province (2021KJXX-35).

Conflict of interest

The authors declare that the research was conducted in the absence of any commercial or financial relationships that could be construed as a potential conflict of interest.

Publisher's note

All claims expressed in this article are solely those of the authors and do not necessarily represent those of their affiliated organizations, or those of the publisher, the editors, and the reviewers. Any product that may be evaluated in this article, or claim that may be made by its manufacturer, is not guaranteed or endorsed by the publisher.

References

Ahmed, D. S., Mohammed, M. K. A., and Majeed, S. M. (2020). Green synthesis of eco-friendly graphene quantum dots for highly efficient perovskite solar cells. *ACS Appl. Energy Mat.* 3, 10863–10871. doi:10.1021/acsaem.0c01896

Alley, N. J., Liao, K. S., Andreoli, E., Dias, S., Dillon, E. P., Orbaek, A. W., et al. (2012). Effect of carbon nanotube-fullerene hybrid additive on P3HT:PCBM bulk-heterojunction organic photovoltaics. *Synth. Mater.* 162, 95–101. doi:10.1016/j.synthmet.2011.11.017

Bai, X., Wang, L., Wang, Y., Yao, W., and Zhu, Y. (2014). Enhanced oxidation ability of g-C3N4 photocatalyst via C60 modification. *Appl. Catal. B Environ.* 152–153, 262–270. doi:10.1016/j.apcatb.2014.01.046

Brown, T. M., De Rossi, F., Di Giacomo, F., Mincuzzi, G., Zardetto, V., Reale, A., et al. (2014). Progress in flexible dye solar cell materials, processes and devices. *J. Mat. Chem. A* 2, 10788–10817. doi:10.1039/c4ta00902a

Cao, S., and Yu, J. (2016). Carbon-based H2-production photocatalytic materials. *J. Photochem. Photobiol. C Photochem. Rev.* 27, 72–99. doi:10.1016/j.jphotochemrev.2016.04.002

Fu, X., Xu, L., Li, J., Sun, X., and Peng, H. (2018). Flexible solar cells based on carbon nanomaterials. *Carbon N. Y.* 139, 1063–1073. doi:10.1016/j.carbon.2018.08.017

Gao, K., Gao, X., Zhu, W., Wang, C., Yan, T., Fu, F., et al. (2021). The hierarchical layered microsphere of BiOI x Br 1-x solid solution decorated with N-doped CQDs with enhanced visible light photocatalytic oxidation pollutants. *Chem. Eng. J.* 406, 127155. doi:10.1016/j.cej.2020.127155

Guo, X., Zhang, H., Sun, H., Tade, M. O., and Wang, S. (2017). Green synthesis of carbon quantum dots for sensitized solar cells. *ChemPhotoChem* 1, 116–119. doi:10.1002/cptc.201600038

Haider, Z., Cho, H., Moon, G. hee, and Kim, H. il (2019). Minireview: Selective production of hydrogen peroxide as a clean oxidant over structurally tailored carbon nitride photocatalysts. *Catal. Today* 335, 55–64. doi:10.1016/j.cattod.2018.11.067

He, B., Feng, M., Chen, X., and Sun, J. (2020). Multidimensional (0D-3D) functional nanocarbon: Promising material to strengthen the photocatalytic activity of graphitic carbon nitride. *Green Energy & Environ.* 6, 823–845. doi:10.1016/j.gee.2020.07.011

Heo, J. S., Eom, J., Kim, Y., and Park, S. K. (2018). Recent progress of textile-based wearable electronics: A comprehensive review of materials, devices, and applications. *Small* 14, 1703034. doi:10.1002/smll.201703034

Jiao, Y., Huang, Q., Wang, J., He, Z., and Li, Z. (2019). A novel MoS2 quantum dots (QDs) decorated Z-scheme g-C3N4 nanosheet/N-doped carbon dots heterostructure photocatalyst for photocatalytic hydrogen evolution. *Appl. Catal. B Environ.* 247, 124–132. doi:10.1016/j.apcatb.2019.01.073

Kandi, D., Martha, S., and Parida, K. M. (2017). Quantum dots as enhancer in photocatalytic hydrogen evolution: A review. *Int. J. Hydrogen Energy* 42, 9467–9481. doi:10.1016/j.ijhydene.2017.02.166

Khalid, N. R., Majid, A., Tahir, M. B., Niaz, N. A., and Khalid, S. (2017). Carbonaceous-TiO2 nanomaterials for photocatalytic degradation of pollutants: A review. *Ceram. Int.* 43, 14552–14571. doi:10.1016/j.ceramint.2017.08.143

Khan, M. W., Zuo, X., Yang, Q., Tang, H., Rehman, K. M. U., Wu, M., et al. (2020). Quantum dot embedded N-doped functionalized multiwall carbon nanotubes boost the short-circuit current of Ru (ii) based dye-sensitized solar cells. *Nanoscale* 12, 1046–1060. doi:10.1039/c9nr09227g

Kong, D., Zheng, Y., Kobielusz, M., Wang, Y., Bai, Z., Macyk, W., et al. (2018). Recent advances in visible light-driven water oxidation and reduction in suspension systems. *Mat. TodayKidlingt.* 21, 897–924. doi:10.1016/j.mattod.2018.04.009

Li, K., Su, F., and Zhang, W. (2016). Modification of g-C 3 N 4 nanosheets by carbon quantum dots for highly efficient photocatalytic generation of hydrogen. *Appl. Surf. Sci.* 375, 110–117. doi:10.1016/j.apsusc.2016.03.025

Li, Y., Arumugam, S., Krishnan, C., Charlton, M. D. B., and Beeby, S. P. (2019). Encapsulated textile organic solar cells fabricated by spray coating. *ChemistrySelect* 4, 407–412. doi:10.1002/slct.201803929

Lu, L., Lv, Z., Si, Y., Liu, M., and Zhang, S. (2018). Recent progress on band and surface engineering of graphitic carbon nitride for artificial photosynthesis. *Appl. Surf. Sci.* 462, 693–712. doi:10.1016/j.apsusc.2018.08.131

Lv, B., Feng, X., Lu, L., Xia, L., Yang, Y., Wang, X., et al. (2021). Facile synthesis of g-C3N4/TiO2/CQDs/Au Z-scheme heterojunction composites for solar-driven efficient photocatalytic hydrogen. *Diam. Relat. Mat.* 111, 108212. doi:10.1016/j.diamond.2020.108212

Lv, D., Jiang, Q., Shang, Y., and Liu, D. (2022). Highly efficient fiber-shaped organic solar cells toward wearable flexible electronics. *npj Flex. Electron.* 6, 38–39. doi:10.1038/s41528-022-00172-w

Mahala, C., Sharma, M. D., and Basu, M. (2020). ZnO nanosheets decorated with graphite-like carbon nitride quantum dots as photoanodes in photoelectrochemical water splitting. *ACS Appl. Nano Mat.* 3, 1999–2007. doi:10.1021/acsanm.0c00081

Mousa, S. A., Noby, S. Z., and Shalan, A. E. (2022). "Graphene and its nanocomposites derivatives: Synthesis, properties, and their applications in water treatment, gas sensor, and solar cell fields," in *Advances in nanocomposite materials for environmental and energy harvesting applications* (Springer), 95–128.

Othman, F. E. C., Yusof, N., Jaafar, J., Ismail, A., Hasbullah, H., Abdullah, N., et al. (2016). Preparation and characterization of polyacrylonitrile/manganese dioxides-based carbon nanofibers via electrospinning process. *IOP Conf. Ser. Earth Environ. Sci.* 36, 012006. doi:10.1088/1755-1315/36/1/012006

Peerakiatkhajohn, P., Yun, J.-H., Wang, S., and Wang, L. (2016). Review of recent progress in unassisted photoelectrochemical water splitting: From material modification to configuration design. *J. Photonics Energy* 7, 012006. doi:10.1117/1.jpe.7.012006

Qu, X., Yi, Y., Qiao, F., Liu, M., Wang, X., Yang, R., et al. (2018). TiO2/BiOI/CQDs: Enhanced photocatalytic properties under visible-light irradiation. *Ceram. Int.* 44, 1348–1355. doi:10.1016/j.ceramint.2017.08.185

Ramanujam, J., Bishop, D. M., Todorov, T. K., Gunawan, O., Rath, J., Nekovei, R., et al. (2020). Flexible cigs, CdTe and a-Si: H based thin film solar cells: A review. *Prog. Mat. Sci.* 110, 100619. doi:10.1016/j.pmatsci.2019.100619

Ren, Y., Zeng, D., and Ong, W. J. (2019). Interfacial engineering of graphitic carbon nitride (g-C3N4)-based metal sulfide heterojunction photocatalysts for energy conversion: A review. *Chin. J. Catal.* 40, 289–319. doi:10.1016/s1872-2067(19)63293-6

Riaz, R., Ali, M., Sahito, I. A., Arbab, A. A., Maiyalagan, T., Anjum, A. S., et al. (2019). Self-assembled nitrogen-doped graphene quantum dots (N-GQDs) over graphene sheets for superb electro-photocatalytic activity. *Appl. Surf. Sci.* 480, 1035–1046. doi:10.1016/j.apsusc.2019.02.228

Rotzler, S., Krshiwoblozki, M. von, and Schneider-Ramelow, M. (2021). Washability of e-textiles: Current testing practices and the need for standardization. *Text. Res. J.* 91, 2401–2417. doi:10.1177/0040517521996727

Saberi Motlagh, M., Mottaghitalab, V., Rismanchi, A., Rafieepoor Chirani, M., and Hasanzadeh, M. (2022). Performance modelling of textile solar cell developed by carbon fabric/polypyrrole flexible counter electrode. *Int. J. Sustain. Energy*, 1–21.

Sadasivuni, K. K., Deshmukh, K., Ahipa, T. N., Muzaffar, A., Ahamed, M. B., Pasha, S. K., et al. (2019). Flexible, biodegradable and recyclable solar cells: A review. *J. Mat. Sci. Mat. Electron.* 30, 951–974. doi:10.1007/s10854-018-0397-y

Sahito, I. A., Ahmed, F., Khatri, Z., Sun, K. C., and Jeong, S. H. (2017). Enhanced ionic mobility and increased efficiency of dye-sensitized solar cell by adding lithium

chloride in poly(vinylidene fluoride) nanofiber as electrolyte medium. *J. Mat. Sci.* 52, 13920–13929. doi:10.1007/s10853-017-1473-z

Sahito, I. A., Sun, K. C., Arbab, A. A., Qadir, M. B., Choi, Y. S., and Jeong, S. H. (2016). Flexible and conductive cotton fabric counter electrode coated with graphene nanosheets for high efficiency dye sensitized solar cell. *J. Power Sources* 319, 90–98. doi:10.1016/j.jpowsour.2016.04.025

Sahito, I. A., Sun, K. C., Arbab, A. A., Qadir, M. B., and Jeong, S. H. (2015a). Graphene coated cotton fabric as textile structured counter electrode for DSSC. *Electrochimica Acta* 173, 164–171. doi:10.1016/j.electacta.2015.05.035

Sahito, I. A., Sun, K. C., Arbab, A. A., Qadir, M. B., and Jeong, S. H. (2015b). Integrating high electrical conductivity and photocatalytic activity in cotton fabric by cationizing for enriched coating of negatively charged graphene oxide. *Carbohydr. Polym.* 130, 299–306. doi:10.1016/j.carbpol.2015.05.010

Saravanan, S., Kato, R., Balamurugan, M., Kaushik, S., and Soga, T. (2017). Efficiency improvement in dye sensitized solar cells by the plasmonic effect of green synthesized silver nanoparticles. *J. Sci. Adv. Mater. Devices* 2, 418–424. doi:10.1016/j.jsamd.2017.10.004

Sharif, N. F. M., Shafie, S., Ab Kadir, M. Z. A., Md Din, M. F., Yusuf, Y., and Shaban, S. (2022). TiO2 photoelectrode band gap modification using carbon quantum dots (CQDs) for dye-sensitised solar cells (DSSCs). *Key Engineering Materials* 908, 265–270. doi:10.4028/p-577y33

Singh, S. S., and Shougaijam, B. (2022). Recent development and future prospects of rigid and flexible dye-sensitized solar cell: A review. *Contemp. Trends Semicond. Devices*, 85–109.

Tao, X., Cochrane, C., and Koncar, V. (2019). Launderability of conductive polymer yarns used for connections of e-textile modules: Mechanical stresses. *Fibers Polym.* 20, 2355–2366. doi:10.1007/s12221-019-9325-x

Yang, S., Sun, J., Li, X., Zhou, W., Wang, Z., He, P., et al. (2014). Large-scale fabrication of heavy doped carbon quantum dots with tunable-photoluminescence and sensitive fluorescence detection. *J. Mat. Chem. A* 2, 8660–8667. doi:10.1039/c4ta00860j

Yang, Z., Peng, H., Wang, W., and Liu, T. (2010). Crystallization behavior of poly(ε-caprolactone)/layered double hydroxide nanocomposites. *J. Appl. Polym. Sci.* 116, 2658–2667. doi:10.1002/app.31787

Zhang, Z., Yang, Y., Gao, J., Xiao, S., Zhou, C., Pan, D., et al. (2018). Highly efficient Ag2Se quantum dots blocking layer for solid-state dye-sensitized solar cells: Size effects on device performances. *Mat. Today Energy* 7, 27–36. doi:10.1016/j.mtener.2017.11.005

frontiers | Frontiers in Environmental Science

TYPE Original Research
PUBLISHED 13 January 2023
DOI 10.3389/fenvs.2022.1028793

OPEN ACCESS

EDITED BY
Chuanbao Wu,
Shandong University of Science and Technology, China

REVIEWED BY
Muhammad Aftab Akram,
Pak-Austria Fachhochschule Institute of Applied Sciences and Technology, Pakistan
Faraz Fazal,
University of Edinburgh, United Kingdom

*CORRESPONDENCE
Muhammad Amjad,
amjad9002@uet.edu.pk

SPECIALTY SECTION
This article was submitted to Interdisciplinary Climate Studies, a section of the journal Frontiers in Environmental Science

RECEIVED 26 August 2022
ACCEPTED 28 December 2022
PUBLISHED 13 January 2023

CITATION
Razzaq I, Amjad M, Qamar A, Asim M, Ishfaq K, Razzaq A and Mawra K (2023), Reduction in energy consumption and CO_2 emissions by retrofitting an existing building to a net zero energy building for the implementation of SDGs 7 and 13. *Front. Environ. Sci.* 10:1028793. doi: 10.3389/fenvs.2022.1028793

Reduction in energy consumption and CO_2 emissions by retrofitting an existing building to a net zero energy building for the implementation of SDGs 7 and 13

Ibtisam Razzaq[1], Muhammad Amjad[1,2]*, Adnan Qamar[2], Muhammad Asim[2], Kashif Ishfaq[2], Afia Razzaq[3] and Khadija Mawra[3]

[1]Centre for Energy Research and Development, University of Engineering and Technology, Lahore, Pakistan, [2]Faculty of Mechanical Engineering, University of Engineering and Technology, Lahore, Pakistan, [3]Faculty of Architectural Engineering and Design, University of Engineering and Technology, Lahore, Pakistan

This work aims to reduce the energy consumption of existing buildings through retrofitting and converting them into net zero energy buildings (NZEBs). Various retrofits for an existing academic building were modeled and analyzed using REVIT software. Energy consumption was reduced to approximately 34% through retrofits, and a Solar System of 41.6 kW was integrated to meet the reduced energy demand, consequently converting the building into an net zero energy building (NZEB). Furthermore, environmental and economic analyses were conducted, and the results show a reduction of 32.8 metric tons of CO_2 emissions per year as a result of retrofitting the building, converting it into an net zero energy building. The building envelope retrofits and electrical appliances have a payback period of 2.96 and 2.62 years, respectively, whereas the proposed Solar System has a payback period of only 2.3 years. Moreover, the building was rated using the Leadership in Energy and Environmental Design (LEED) rating tool, and it qualifies for silver certification after retrofits and the integration of renewable energy sources (RES). The reduction in energy consumption and integration of renewable energy sources contribute to achieving Sustainable Development Goal (SDG) 7, and reduced CO_2 emissions save climate variations, which leads to achieving Sustainable Development Goal 13.

KEYWORDS

retrofitting, building information modeling (BIM), net zero energy building (NZEB), renewable energy integration, RIVET

1 Introduction

Net zero energy building (NZEB) is an emerging reform in building construction, which addresses the increasing energy demands around the world, especially in developing and energy-deficient countries (Valasai et al., 2017) (Yousuf et al., 2014). Due to the speedy growth of urbanization and infrastructure change, the energy crisis has become a major issue, not only in developing countries but across the globe (Raheem et al., 2016). To meet the ever-increasing energy demands, fossil fuels are depleting at a much higher rate. Moreover, they are also responsible for greenhouse gas emissions (GHG) in the atmosphere, which is a serious environmental concern (Pervez et al., 2021). Since the energy deficit and GHG emissions have become a global concern, the World Health Organization (WHO) has recently issued a set of Sustainable Development Goals (SDGs) and has set a target of 2030 to transform the world

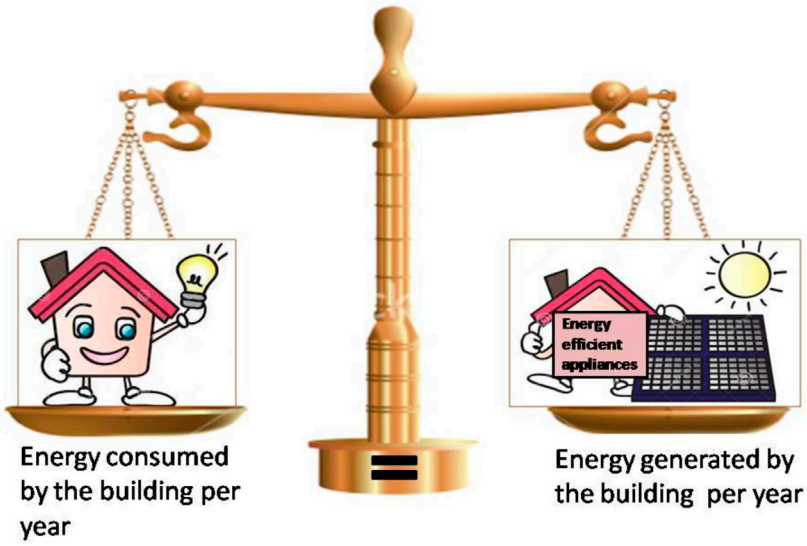

GRAPHICAL ABSTRACT

into a better place for all (Pradhan et al., 2017). There are 17 SDGs that aim to remove poverty, protect our environment, and make this planet safer and more reliable for humanity (Chirambo, 2018). SDG 7"Affordable and Clean Energy" and SDG 13"Climate Action" are primarily related to the energy reforms required globally that ensure a reduction in energy scarcity and carbon emissions for a better climate (Röck et al., 2020). The retrofitting of an existing structure is one way of contributing to the achievement of SDGs 7 and 13 (Allen et al., 2016). All over the world, construction industries have started to adopt novel technologies to overcome the energy deficit, among which, the NZEB has gained prime importance (McCollum et al., 2018).

Over the past few decades, the concept of the NZEB has been adopted by many countries. Its refined definition is a building that generates an equal or greater amount of emission-free renewable energy than its emission-producing, non-renewable energy consumption (Soni & Bhagat Singh, 2020). Many researchers have emphasized reducing energy usage rather than renewable energy production through different methods, such as passive designing (Hasan & Mohamed, 2015), energy-efficient building services (Torcellini et al., 2006), thermal resistive construction materials (Aized et al., 2017), building envelope insulation strategies to gain maximum daylight and ventilation benefits, and the integration of renewable energy generation systems (Purbantoro & Siregar, 2019). Design-related strategies are, however, to be considered for a new building yet to be constructed where the implementation of other techniques has been considered in the design phase and operation phase retrofits as well.

New buildings have the potential for the application of all energy-efficient strategies, but improvement in the energy performance of existing buildings is also extremely important, along with the need of the hour: to save energy (Maheshwari et al., 2017). For existing buildings, retrofitting (after initial construction and occupation) is the most efficient way to reduce energy consumption, and integrating a renewable energy source fulfills the purpose of enhancing the building's energy performance (Ma et al., 2012; Farooqui, 2014). Building retrofits have helped to reduce global greenhouse gas emissions significantly (Li et al., 2019). In developing nations, retrofitting existing buildings to increase their energy saving and reduce the environmental burden is now a critical component of modern building sector strategies (Aman et al., 2017). Building energy retrofit measures have shown the potential to reduce energy loads by 30% (Aydin And Mihlayanlar, 2020), and a deeper retrofit can even reach 72% in some developed countries (Xiao, 2014).

Various studies have shown that energy-efficient retrofitting measures include the replacement of conventional lighting fixtures with energy-efficient ones (Kaewunruen et al., 2019), applying window shading (Ahmed & Asif, 2020), the use of glazed glass, and improving airtightness (Urbikain, 2020). The use of an energy-efficient air conditioning system (She et al., 2018) and adding building envelope insulation are also among the eight energy efficiency measures (EEMs) that can reduce energy use by up to 60% (Pohoryles et al., 2020) and CO_2 emissions by up to 30% (Kamal et al., 2019). Among these retrofit measures, replacing inefficient equipment with more energy-efficient options can save up to 27.4% of energy consumption (Luddeni et al., 2018).

In recent times, the replacement of conventional lights with energy-efficient LEDs has been proven to be an effective retrofit measure (Hayter Kandt, 2011). Furthermore, reflecting daylight off indoor surfaces inside a building is a way of using renewable energy sources, i.e., using sunlight for lighting purposes (Mughal et al., 2018). As lighting fixtures release heat, minimizing the use of artificial lights and replacing them with daylight or LED lights (Dubois et al., 2015) will not only reduce the impact of lighting on energy consumption (Vogiatzi et al., 2020) but also results in the reduced thermal effect on a building, which consequently reduces cooling loads from the overall energy consumption, thus lowering energy costs (Winkler et al., 2018). However, sunlight may be a good source of renewable energy, but a location with good sunlight reception also faces the challenge of an increase in building temperature in hot climates and thus an increase in cooling loads on energy consumption (Sharaf, 2014). By providing building envelope insulation, using glazed windows for blocking out the heat of sunlight and only allowing useful light to enter, and

TABLE 1 Details of the selected building.

Building parameters	Description
Location	University of Engineering and Technology, New campus
Building Type	Academic building
Timing	8:00 a.m. to 4:00 p.m.
Stories	2
Longitude	74.24°
Latitude	31.69°
Building Area	50,424 ft^2

insulating the roofs and walls with heat repellants like epoxy (Wong, 2021), calcium silicate, or polythene, the cooling loads can also be controlled for the reduction of the overall energy consumption (Annibaldi et al., 2020). It is considered important to assess the extent of achievement in converting any construction to a net zero energy building, and in the past few decades, it has become an essential practice to rate buildings on their energy performance (Doan et al., 2017).

With different scenarios, building types, climatic conditions, and norms of the construction industries, there is vast diversity in retrofitting techniques and their effectiveness. This work represents a step further toward the achievement of SDG 7 and SDG 13 by converting an academic building to a net zero energy building through indigenous retrofitting and integrating renewable energy sources. The building under consideration is rated under a standard building rating tool: Leadership in Energy and Environmental Design (LEED). Furthermore, a comparison is made in terms of energy consumption and CO_2 emissions before and after indigenous retrofitting solutions.

2 Methodology

Buildings such as residential apartments, academic blocks, hospitals, *etc.*, and most importantly, multi-purpose buildings, which are used throughout the day, are the targeted buildings for this study. This study focuses on the conversion of the academic block of the University of Engineering and Technology (UET), which is predicted to save energy and provide financial support to the institution. Details of the selected academic building are given in Table 1. The architectural plans of the first and second floors of the building are given in Supplementary Figures S1, S2, respectively, in the supplementary information file.

The methodology involves the collection of pre-existing information, like the manual counting of appliances with their power rating, the material used in the building, the building elevation, and full details of all other appliances that contribute to the energy consumption of the building. Table 2 shows the details of existing fixtures. Figure 1A shows the 3D model of the building, and Figure 1B represents the energy model of the building on REVIT.

2.1 Retrofitting measures and renewable integration

Different retrofitting measures were adopted to make the building an NZEB. After the collection of the existing data, it was analyzed that the existing appliances were obsolete and not energy efficient and led to energy wastage. Similarly, the building envelope was not thermally resistive, with single-glazed windows and an uninsulated roof and walls, which significantly affected the cooling load of the internal space of the building. Existing appliances were replaced by energy-efficient appliances; for example, conventional fluorescent lights were replaced with energy-efficient lights such as LEDs, old, conventional fans were replaced with new, energy-efficient fans, and conventional air conditioners were replaced with the latest inverter technology-based air conditioners.

The building envelope is a major contributor to raising the cooling requirements of the building due to heat transfer through windows, doors, walls, and the roof. Therefore, to reduce the cooling requirements, different retrofitting measures were used in the building. The retrofitting measures include the replacement of single-glazed windows with double-glazed windows, roof coating with reflective paint, and the addition of a wall insulation layer. All

TABLE 2 Details of existing fixtures.

Appliances	Quantity	Rated power of each appliance (W)	Peak power (kW)
Tube Light (4 ft)	272	45	12.24
Fans	114	110	12.54
Compact fluorescent lamp	12	45	.54
Compact fluorescent lamp	7	25	.18
Compact fluorescent lamp	10	18	.18
LED Panels	173	36	6.23
Air Conditioner (1.5 tons)	3	1800	5.40
Air Conditioner (2 tons)	2	2,400	9.60
HVAC	-	55,000	55.00

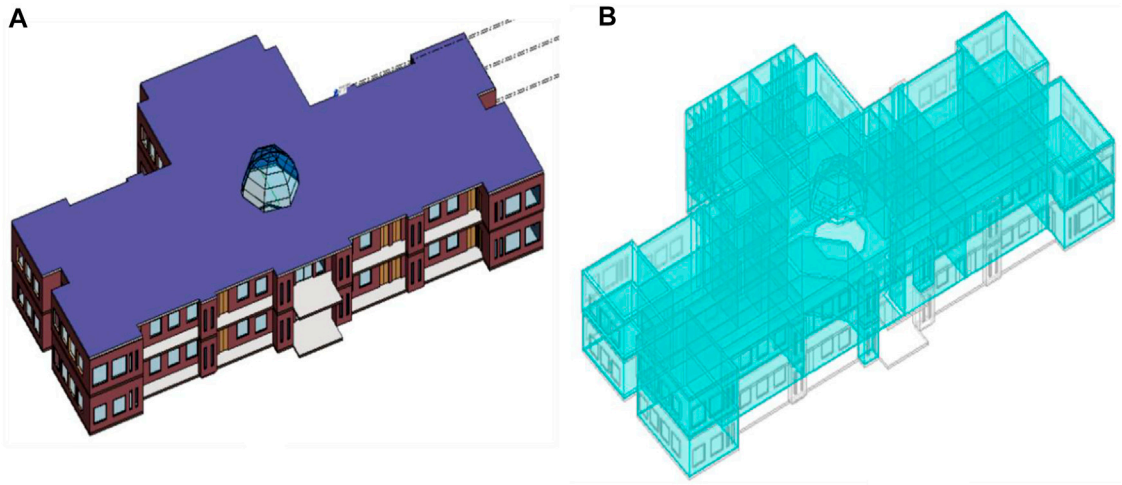

FIGURE 1
(A) Existing 3D BIM model, **(B)** Energy model visualization of the building.

the above cases, including the existing data and after retrofitting measures, were analyzed using REVIT, a building information modeling (BIM) tool.

After performing electrical retrofitting and making improvements in the building envelope, the reduction in energy consumption was calculated through BIM analysis. After minimizing the total energy consumption of the building through various retrofitting measures, solar photovoltaic-based energy was integrated to compensate for the remaining energy needs to make the building an NZEB. Solar panels were integrated because enough space was available on the rooftop of the building for their installation and because of their economic gain and environmentally friendly behavior. PV installation on the rooftop has multiple benefits, including the provision of insulation in the roof to prevent excessive heat penetration into the building. This, in turn, reduces the cooling requirements of the building. The Solar System containing 80 PV panels was applied with an intra-row spacing of 3.3 ft. The Helioscope tool was used for the integration of solar panels with the building system. The power of the system is 41.6 kW, with an annual production of 63.15 MWh.

An analysis of CO_2 emissions was conducted using electrical energy consumption (kWh) and the emission factor (EF) as per the available literature (Latif et al., 2022) relevant to the selected location. An economic analysis of all retrofitting measures was conducted based on the payback period. The payback period was based on the energy saving resulting from retrofitting measures and the integration of the solar PV system. Annual energy savings based on the electricity consumption tariff in Pakistan were evaluated and the resulting reduction in CO_2 emissions was calculated. Eventually, the completion of all these analyses enabled the achievement of SDG 7, ensuring access to affordable, reliable, sustainable, and modern energy for all, and SDG 13, contributing to combatting climate change.

3 Results and analysis

For electrical retrofitting, the first step is to collect the existing electricity consumption data of the building through an energy audit. It is found that the existing fixture in the building consumes extra energy and needs to be replaced with energy-efficient ones. Based on the electrical audit results, electrical fixtures that consume less energy and deliver the same output were selected. The difference in the power of the existing and proposed fixtures is shown in Table 3.

The comparison of existing and proposed fixtures for each electrical appliance is shown in Figures 2, 3.

Figure 4 shows the reduction in energy loads through retrofitting. The electrical load of the building is reduced by 34% by adopting various retrofitting measures. The lighting load of the building is reduced by 39.60% from the existing loads. Similarly, the fan load and the air conditioning load are reduced by 40.90% and 15.19%, respectively.

For the retrofitting of the building envelope, various options were selected, including the addition of insulation in walls, the replacement of windows glass, and the coating of the roof with reflective paint. Energy Analysis of the building for various retrofitting measures was done through a building information modeling (BIM) tool, i.e., REVIT. The main aim of energy analysis of a building is to check for its cost-effective and sustainable alternatives at the design and planning stage. BIM gives many such opportunities, of which, creating insights and energy analysis through REVIT is one of the most effective. To determine the cooling loads of the selected building for different retrofitting measures, it was required to run an energy simulation through REVIT.

For wall insulation, an insulation sheet of 1-inch thickness was applied, which reduced the building temperature by 8–10°. The existing window glass was replaced with double-glazed glass, which impacted the cooling loads. For the roof retrofitting, epoxy paint was applied to reflect most of the incoming solar heat.

TABLE 3 Details of the existing and proposed fixtures.

Existing appliances	Power (W) of existing appliance	Proposed energy efficient appliances	Power (W) of the proposed appliance (W)
Tube light 4 ft	45	LED tube rod 4 ft	18
Fan	110	Energy-efficient fan	65
Compact fluorescent lamp	45	LED Bulb	27
Compact Fluorescent lamp	25	LED Bulb	18
Compact fluorescent lamp	18	LED Bulb	12
Air Conditioner	1,800	Inverter Tech split AC	1,640
Air Conditioner	2,400	Inverter Tech split AC	1,950

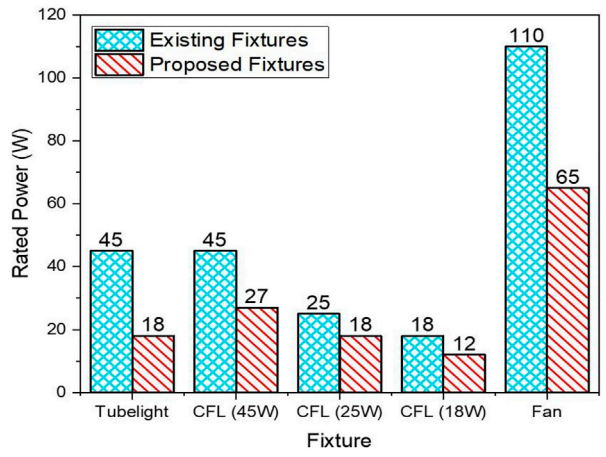

FIGURE 2
Comparison of energy consumption in tube light, compact fluorescent lamp (CFL), and fan.

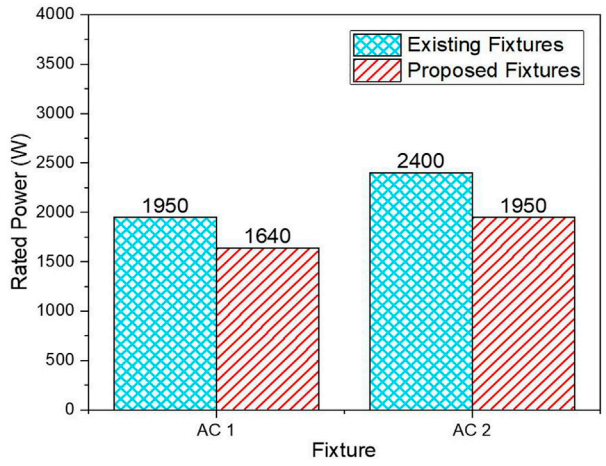

FIGURE 3
Comparison of energy consumption in the existing and proposed air conditioners.

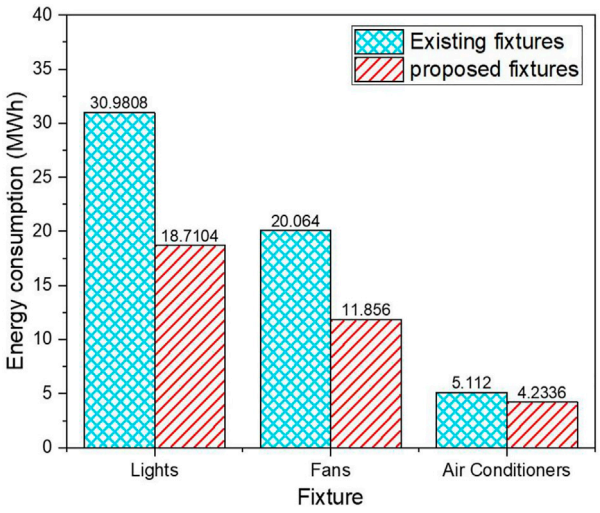

FIGURE 4
Difference in energy consumption of existing and proposed electrical fixtures of the selected building.

3.1 Reduction in cooling load

The spaces generated in the architectural model are considered for heating and cooling load calculation. After updating the weather details of the selected location, reports of heating and cooling load are generated for the existing and proposed fixtures. For the existing building, the peak cooling load was found to be 124.1 tons at 2:00 p.m. in June, whereas the peak cooling load for all combined retrofit cases was found to be 87.5 tons at 2:00 p.m. in June, a decrease of 30% from existing loads.

The prominent reductions in the cooling loads attained through the implementation of various retrofitting measures are shown in Figure 5, and a maximum reduction of 13% in cooling load was achieved through the use of double-glazed windows. The application of epoxy resins on the roof resulted in an 8% reduction. However, the value for all combined cases indicates a 30% decrease in cooling loads, which ultimately leads to significant energy savings.

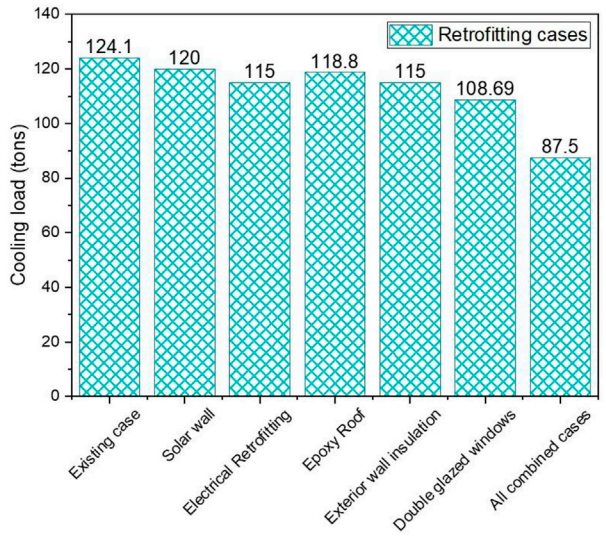

FIGURE 5
Reduction in cooling loads through various retrofitting measures.

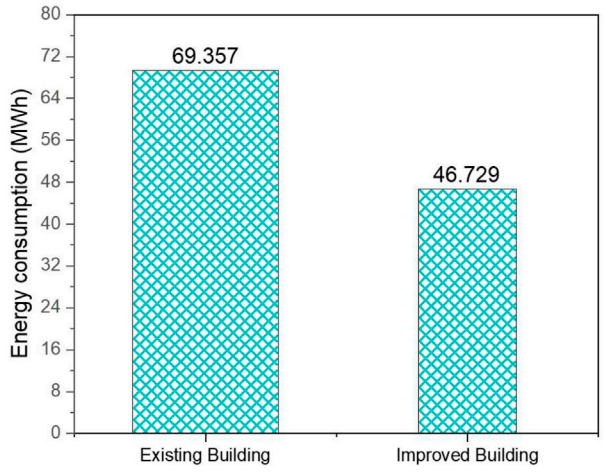

FIGURE 6
Energy consumption in the selected building before and after retrofitting.

3.2 Reduction in overall energy consumption of the building

Firstly, the building is retrofitted using different measures, and energy consumption is reduced. Then, according to the energy demand, a Solar System is installed to generate energy to meet the requirement of the building. The energy consumption of the building is reduced by applying all measures in the building, as discussed in Section 3.1. By implementing all the retrofitting measures, the annual energy consumption is reduced from 69,356.0 kWh to 46,729.5 kWh, which is approximately a 34% reduction, as shown in Figure 6.

The main objective of this study is the conversion of the selected building to an NZEB, so there was a need to integrate renewable energy to meet the remaining energy demand. A solar energy system was installed, the generation of which would be beneficial in net metering, and ultimately, the building would be converted into an NZEB.

As the building energy usage was reduced by implementing different retrofitting measures, the next step was to design a Solar System to meet the remaining energy demand, which was approximately 46 MWh (46,729 kWh). Therefore, a Solar System was designed using Helioscope software. It consisted of 80 panels with an inter-row spacing of 3.3 ft and was installed on the roof with a tilt angle of 32°. Figure 7 shows the detailed layout of the Solar System design. The system's installed capacity was 41.6 kW, with an annual production of 63.15 MWh.

3.3 Environmental analysis

Carbon dioxide emissions are harmful gases released into the atmosphere by different human activities. Therefore, it was important to analyze carbon dioxide emissions in the selected building, CERAD, before and after the retrofitting measures. The analysis was conducted by Eq. 1, as reported in (Latif et al., 2022).

$$CO_2\ Emissions = EC \times EF \quad (1)$$

where 'EC' is the electrical energy consumption (kWh) and 'EF' represents the emission factor. The carbon dioxide reduction was calculated based on an emission factor of .405 kg CO_2/kWh, as per the IGCEP (Indicative Generation Capacity Expansion Plan) report by NTDC (National Transmission and Dispatch Company) per kWh energy generation (Latif et al., 2022).

Figure 8A illustrates the carbon dioxide emissions of electrical fixtures such as lights, fans, and air conditioners. The energy-based carbon dioxide emissions are further reduced by improving the building envelope with different techniques. The reduction in cooling loads lowers the use of electrical appliances to cool the building. Consequently, the carbon dioxide emissions are reduced from 26.5 metric tons to 17.9 metric tons through the integration of all retrofitting measures. In the retrofitted building, the CO_2 emissions are reduced by approximately 33% as compared to the existing building emissions, as shown in Figure 8B. The integration of solar systems also has an environmental impact. Therefore, the installed system of 41.6 kW eliminates 25.2 metric tons of carbon dioxide per year. Table 4 depicts a clear reduction in emissions of retrofitted electrical fixtures that can be observed from the results.

3.4 SDGs and economic assessment

The assessment of SDGs is related to the energy consumption of the building and its influence on the climate. The reduction in energy consumption and the integration of renewable energy resources contribute to the achievement of SDG 7, and carbon dioxide emissions lessen the frequent climate variations that facilitate the attainment of SDG 13. Therefore, this analysis can act as one of the important steps in attaining SDG 7 and SDG 13 through retrofitting.

Economic analysis of all retrofitting measures is determined based on the payback period. The simple payback period was calculated for

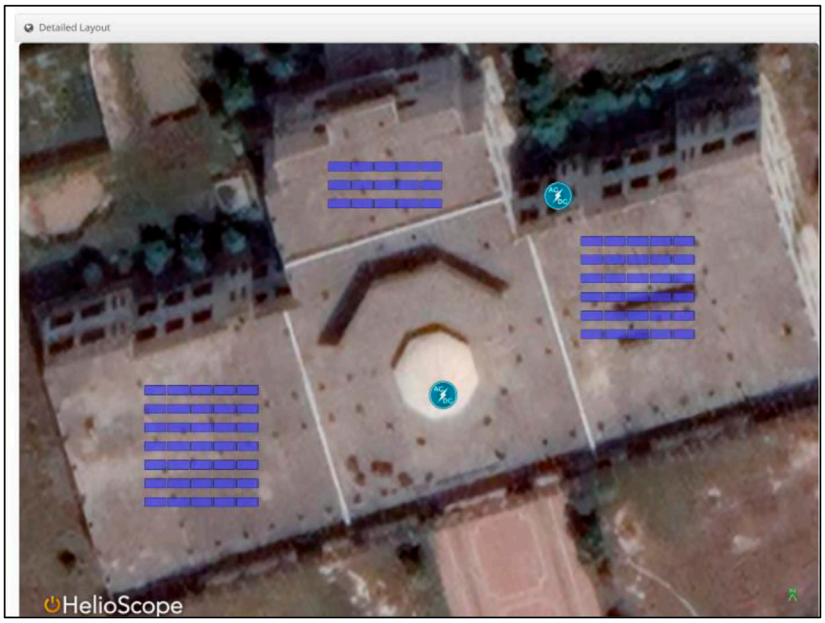

FIGURE 7
Detailed layout of solar system design.

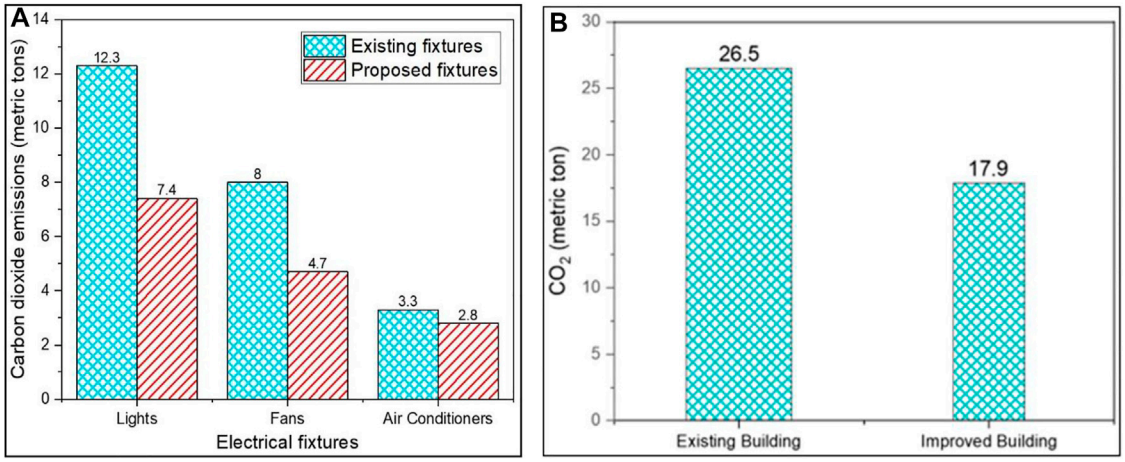

FIGURE 8
(A) Comparison of reduction in CO_2 emissions before and after retrofitting measures in electrical fixtures and **(B)** overall reduction in CO_2 emission of the building after retrofitting.

TABLE 4 CO_2 emissions reduced by electrical retrofitting.

Type of fixture	CO_2 emissions (metric tons) by existing fixtures	CO_2 emissions (metric tons) by proposed fixtures
Lights	12.3	7.4
Fans	8.0	4.7
Air conditioners	3.3	2.8

the implementation of all energy-efficient retrofitting measures using the relation expressed in Eq. 2

$$PP = \frac{C_i}{S_a} \tag{2}$$

Where 'PP' is the payback period in years, 'C_i' is the initial cost (USD) of energy-efficient retrofitting measures, and 'S_a' is the resulting annual energy savings (USD/year). The annual energy saving was calculated by multiplying the amount of energy saved (kWh) by the

TABLE 5 Payback period for electrical fixtures.

Electrical fixture	Load reduction (kW)	Percentage load reduction (%)	Expected retrofitting cost (USD)	Expected payback period (Years)
Lights	7.4	38.9	1,257.88	.71
Fans	5.1	40.8	3,058.12	2.58
Air Conditioner	1.2	17.1	333.80	4.57
Combined effect	13.7	31.8	7,654.30	2.62

TABLE 6 Payback period for building envelope.

Cases	Cooling load (kW)	Percentage load reduction (%)	Expected retrofitting cost (USD)	Payback period (Years)
Existing case	436.71	—	—	—
Epoxy roof	418.36	2.00	2,859.02	3.14
Exterior wall insulation	405.14	7.25	2010.30	1.52
Double-glazed windows	382.24	12.4	10,062.00	4.22
Combined effect	332.04	23.95	14,931.30	2.96

TABLE 7 Comparative rating of the building before and after retrofitting.

Sr No.	Aspects	Before retrofitting	After retrofitting
1	Location and Transportation	6	6
2	Sustainable Sites	2	2
3	Water Efficiency	6	6
4	Energy and Atmosphere	13	34
5	Material and Resources	3	3
6	Indoor Environmental Quality	8	8
7	Innovation	0	0
	Total Score	**38**	**59**

energy tariff in Pakistan, which is approximately .14 USD/kWh (Latif et al., 2022).

The cost estimates of all materials and components used for retrofitting were taken from the local market to evaluate the payback period. For the wall insulation, epoxy roof, and double-glazed windows, the area of application, and cost per square foot were determined. The cost of the energy saved through these retrofitting measures and solar energy integration was evaluated and thus, the payback period was calculated. The payback period of electrical retrofitting is shown in Table 5. It can be observed that the combined amount required for electrical retrofitting is approximately 8,000 USD, with an expected payback period of 2.62 years.

Table 6 enlists the payback periods for each retrofit measure of the building envelope. The combined cost required for the improvement in the building envelope was almost 15,000 USD and their payback period was observed to be 2.96 years. Moreover, the installation of the Solar System on the roof of the building cost approximately 20,000 USD, and the payback period for this system was 2.3 years.

3.5 Results of the LEED application on building

The building was rated according to LEED v4.1 O + M (details are available in Supplementary Table S1 in supplementary information) for the existing building before and after retrofitting. The precondition points are required by the building and have no credit value. They are assessed using a "Yes or No" system. Other points are received for achievement, and the point for "yes" counts for the building rating while "no" indicates the absence of that aspect/factor. Such ratings vary from certified to platinum.

Upon assessment of the building, it was found that the building scored 38 points before retrofitting and lies in the range of non-certified buildings, as per LEED standards. For this study, a minimum score was given to the transportation performance, water performance, waste performance, and indoor environmental quality performance as the focus of this study is only on energy performance (Elsorady & Rizk, 2020) (Khan et al., 2020). The scorecards for existing and improved buildings are

attached in Supplementary Figures S3, S4, in the supplementary information file. However, after the electrical and building envelope retrofitting, the energy performance level, which lies under the "energy and atmosphere" credit category, was improved. Along with this, under the same credit category, the building gained a point for "grid harmonization" as, after the installation of solar panels, the building was capable of generating energy. It was found that the building could be a candidate for silver certification as it gained 59 points after electrical and building envelope retrofitting. A prominent difference in the energy and atmosphere aspects can be observed as it improved from 13 points for the existing building to 33 points with the installation of the Solar System of 41.6 kW. Table 7 shows the comparative rating of the building.

4 Conclusion

This work presents an analysis of the conversion of an existing academic building to a net zero energy building through retrofitting measures and the integration of solar energy to reduce the CO_2 emissions. The study concludes that:

1. The electrical retrofitting measures for lighting fixtures reduced energy consumption by 26%. The combined impact of applying all retrofitting measures resulted in a 30% reduction in the cooling load of the building and the results are aligned with that of the existing literature (Al-Mofeez, 2006; Patel et al., 2019).
2. A reduction in the energy load of the retrofitted building resulted in a 32% reduction in carbon dioxide emissions. The integration of solar photovoltaic panels on the rooftop resulted in a further reduction of 25.2 metric tons of CO_2 emissions per year.
3. The cost of retrofitting the building envelope with double-glazed windows, epoxy coating, and wall insulation was approximated to be 15,000 USD, with a payback period of 2.96 years. Electrical retrofitting required around 8,000 USD, with an expected payback period of 2.62 years, while the integration of the Solar System required 20,000 USD, with an expected payback of 2.3 years.
4. The energy-efficient building is a way forward in the achievement of SDGs 7 and 13. The building was capable of achieving a silver rating in LEED v4.1 O + M after retrofitting measures, whereas, with the previous conditions, it did not qualify to be certified.
5. Buildings that consume more energy must be converted into NZEBs, and this concept should be included in the rules and regulations of the planning and construction of residential buildings. Besides the integration of the photovoltaic system, the building's waste-to-energy concept can make the buildings more sustainable.

Data availability statement

The original contributions presented in the study are included in the article/Supplementary Material, further inquiries can be directed to the corresponding author.

Author contributions

IR and MAM conceived the concept. IR executed the work and drafted the manuscript in coordination with MAM and AQ. MAM and MAS supervised the work. AQ and KI reviewed and refined the draft with AR and KM. All authors contributed equally to the preparation and revision of this manuscript and have no conflict of interest.

Acknowledgments

The authors are thankful to the Director, CERAD, and UET Lahore for facilitating and supporting this work.

Conflict of interest

The authors declare that the research was conducted in the absence of any commercial or financial relationships that could be construed as a potential conflict of interest.

Publisher's note

Supplementary material

The Supplementary Material for this article can be found online at: https://www.frontiersin.org/articles/10.3389/fenvs.2022.1028793/full#supplementary-material

References

Ahmed, W., and Asif, M. (2020). BIM-based techno-economic assessment of energy retrofitting residential buildings in hot humid climate. *Energy and Build.* 227, 110406. doi:10.1016/j.enbuild.2020.110406

Aized, T., Mehmood, S., and Anwar, Z. (2017). Building energy consumption analysis, energy saving measurements and verification by applying HAP software. *Pak. J. Engg. Appl. Sci* 21.

Al-Mofeez, I. A. (2006). Predicted vs. long-term electrical energy consumption pre and post energy conservation measures: A case study of one-story house in dhahran, Saudi arabia.Proceedings of the 4th International Energy Conversion Engineering Conference and Exhibit (IECEC) June 2006. San Diego, CA, USA 1 (2), 388–397. doi:10.2514/6.2006-4044

Allen, C., Metternicht, G., and Wiedmann, T. (2016). National pathways to the sustainable development goals (SDGs): A comparative review of scenario modelling tools. *Environ. Sci. Policy* 66, 199–207. doi:10.1016/j.envsci.2016.09.008

Aman, M. A., Ahmad, S., Munir, M., and Ali, M. (2017). Solutions of current energy crisis for Pakistan. *Int. J. Comput. Sci. Inf. Secur.* 15 (5), 145–149.

Annibaldi, V., Cucchiella, F., De Berardinis, P., Gastaldi, M., and Rotilio, M. (2020). An integrated sustainable and profitable approach of energy efficiency in heritage buildings. *J. Clean. Prod.* 251, 119516. doi:10.1016/j.jclepro.2019.119516

Aydin, D., and Mihlayanlar, E. (2020). A case study on the impact of building envelope on energy efficiency in high-rise residential buildings. *Archit. Civ. Eng. Environ.* 13 (1), 5–18. doi:10.21307/acee-2020-001

Chirambo, D. (2018). Towards the achievement of SDG 7 in sub-Saharan Africa: Creating synergies between Power Africa, Sustainable Energy for All and climate finance in-order to achieve universal energy access before 2030. *Renew. Sustain. Energy Rev.* 94, 600–608. doi:10.1016/j.rser.2018.06.025

Doan, D. T., Ghaffarianhoseini, A., Naismith, N., Zhang, T., Ghaffarianhoseini, A., and Tookey, J. (2017). A critical comparison of green building rating systems. *Build. Environ.* 123, 243–260. doi:10.1016/j.buildenv.2017.07.007

Dubois, M., Bisegna, F., Gentile, N., Knoop, M., Matusiak, B., Osterhaus, W., et al. (2015). Retrofitting the electric lighting and daylighting systems to reduce energy use in buildings: A literature review. *Energy Res. J.* 6 (1), 25–41. doi:10.3844/erjsp.2015.25.41

Elsorady, D. A., and Rizk, S. M. (2020). LEED v4.1 operations and maintenance for existing buildings and compliance assessment: Bayt Al-Suhaymi, Historic Cairo. *Alexandria Eng. J.* 59 (1), 519–531. doi:10.1016/j.aej.2020.01.027

Farooqui, S. Z. (2014). Prospects of renewables penetration in the energy mix of Pakistan. *Renew. Sustain. Energy Rev.* 29, 693–700. doi:10.1016/j.rser.2013.08.083

Hasan, A., and Mohamed, A. (2015). "Net- and nearly- zero energy buildings: A review of the definitions and case studies," in Proceedings of the 6th International Conference on Heating, Ventilation and Air-Conditioning, Tehran, Iran, May 2015.

Hayter, S. J., and Kandt, A. (2011). "Renewable energy applications for existing buildings preprint,". NREL/CP-7A40-52172 (Colorado, CO, USA: National Renewable Energy Lab).

Kaewunruen, S., Sresakoolchai, J., and Kerinnonta, L. (2019). Potential reconstruction design of an existing townhouse in Washington DC for approaching net zero energy building goal. *Sustain. Switz.* 11 (23), 6631–6715. doi:10.3390/su11236631

Kamal, A., Al-ghamdi, S. G., and Koç, M. (2019). Role of energy ef fi ciency policies on energy consumption and CO 2 emissions for building stock in Qatar. *J. Clean. Prod.* 235, 1409–1424. doi:10.1016/j.jclepro.2019.06.296

Khan, A. A., Zaheer, M. U., Asghar, S., and Gardezi, S. S. (2020). Green rating assessment of a residential building in Pakistan using LEED'S. *Open J. Sci.* 3 (2), 126–139. doi:10.31580/ojst.v3i2.1474

Latif, M. H., Amjad, M., Tahir, Z. ur R., Qamar, A., Asim, M., Mahmood, W., et al. (2022). Nexus implementation of sustainable development goals (SDGs) for sustainable public sector buildings in Pakistan. *J. Build. Eng.* 52, 104415. doi:10.1016/j.jobe.2022.104415

Li, Y. L., Han, M. Y., Liu, S. Y., and Chen, G. Q. (2019). Energy consumption and greenhouse gas emissions by buildings: A multi-scale perspective. *Build. Environ.* 151, 240–250. doi:10.1016/j.buildenv.2018.11.003

Luddeni, G., Krarti, M., Pernigotto, G., and Gasparella, A. (2018). An analysis methodology for large-scale deep energy retrofits of existing building stocks: Case study of the Italian office building. *Sustain. Cities Soc.* 41, 296–311. doi:10.1016/j.scs.2018.05.038

Ma, Z., Cooper, P., Daly, D., and Ledo, L. (2012). Existing building retrofits: Methodology and state-of-the-art. *Energy Build.* 55, 889–902. doi:10.1016/j.enbuild.2012.08.018

Maheshwari, S., Chauhan, P., Tandon, S., and Sagar, S. (2017). A review study on net zero energy building. *Int. Res. J. Eng. Technol. (IRJET)* 4, 1567–1570.

McCollum, D. L., Echeverri, L. G., Busch, S., Pachauri, S., Parkinson, S., Rogelj, J., et al. (2018). Connecting the sustainable development goals by their energy inter-linkages. *Environ. Res. Lett.* 13 (3), 033006. doi:10.1088/1748-9326/aaafe3

Mughal, S., Sood, Y. R., and Jarial, R. K. (2018). A review on solar photovoltaic technology and future trends. *Int. J. Sci. Res. Comput. Sci.* 4 (1), 227–235.

Patel, A., Ghodasara, D., Bhatt, N., and Kandya, A. (2019). "Energy retrofitting of a commercial building towards a" net zero energy building" by simulation model," in *Creative construction conference* (Budapest, Hungary: Budapest University of Technology and Economics), 699–712. doi:10.3311/ccc2019-096

Pervez, H., Ali, Y., and Petrillo, A. (2021). A quantitative assessment of greenhouse gas (GHG) emissions from conventional and modular construction: A case of developing country. *J. Clean. Prod.* 294, 126210. doi:10.1016/j.jclepro.2021.126210

Pohoryles, D. A., Maduta, C., Bournas, D. A., and Kouris, L. A. (2020). Energy performance of existing residential buildings in europe: A novel approach combining energy with seismic retrofitting. *A Nov. approach Comb. energy seismic Retrofit.* 223, 110024. doi:10.1016/j.enbuild.2020.110024

Pradhan, P., Costa, L., Rybski, D., Lucht, W., and Kropp, J. P. (2017). A systematic study of sustainable development goal (SDG) interactions. *Earth's Future* 5 (11), 1169–1179. doi:10.1002/2017EF000632

Purbantoro, F., and Siregar, M. (2019). Design of net zero energy building (NZEB) for existing building in jakarta. *IOP Conf. Ser. Earth Environ. Sci.* 399 (1), 012076. doi:10.1088/1755-1315/399/1/012076

Raheem, A., Abbasi, S. A., Memon, A., Samo, S. R., Taufiq-Yap, Y. H., Danquah, M. K., et al. (2016). Renewable energy deployment to combat energy crisis in Pakistan. *Energy, Sustain. Soc.* 6 (1), 16. doi:10.1186/s13705-016-0082-z

Röck, M., Ruschi, M., Saade, M., Balouktsi, M., Nygaard, F., Birgisdottir, H., et al. (2020). Embodied GHG emissions of buildings – the hidden challenge for e ff ective climate change mitigation. *Appl. Energy* 258, 114107. doi:10.1016/j.apenergy.2019.114107

Sharaf, F. M. (2014). Daylighting: An alternative approach to lighting buildings. *J. Am. Sci.* 10 (4), 1–5.

She, X., Cong, L., Nie, B., Leng, G., Peng, H., Chen, Y., et al. (2018). Energy-efficient and -economic technologies for air conditioning with vapor compression refrigeration: A comprehensive review. *Appl. Energy* 232, 157–186. doi:10.1016/j.apenergy.2018.09.067

Soni, K. M., and Bhagat Singh, P. (2020). First onsite net zero energy green building of India. *Int. J. Environ. Sci. Technol.* 17 (4), 2197–2204. doi:10.1007/s13762-019-02514-0

Torcellini, P., Pless, S., Deru, M., and Crawley, D. (2006). Zero energy buildings: A critical look at the definition. *ACEEE Summer Study Pac. Grove* 15.

Urbikain, M. K. (2020). Energy efficient solutions for retrofitting a residential multi-storey building with vacuum insulation panels and low-E windows in two European climates. *J. Clean. Prod.* 269, 121459. doi:10.1016/j.jclepro.2020.121459

Valasai, G. Das, Uqaili, M. A., Memon, H. U. R., Samoo, S. R., Mirjat, N. H., and Harijan, K. (2017). Overcoming electricity crisis in Pakistan: A review of sustainable electricity options. *Renew. Sustain. Energy Rev.* 72, 734–745. doi:10.1016/j.rser.2017.01.097

Vogiatzi, C., Gemenetzi, G., Massou, L., Poulopoulos, S., Papaef, S., and Zervas, E. (2018). Energy use and saving in residential sector and occupant behavior: A case study in athens. *Energy Build.* 181, 1–9. doi:10.1016/j.enbuild.2018.09.039

Winkler, J., Munk, J., and Woods, J. (2018). Effect of occupant behavior and air-conditioner controls on humidity in typical and high-efficiency homes. *Energy and Build.* 165, 364–378. doi:10.1016/j.enbuild.2018.01.032

Wong, I. L. (2021). A review of daylighting design and implementation in buildings. *Renew. Sustain. Energy Rev.* 74, 959–968. doi:10.1016/j.rser.2017.03.061

Xiao, N. (2014). Energy-efficiency building envelope technologies Naiyuan. Thesis. Gävle, Sweden: University of Gävle, 1–34.

Yousuf, I., Ghumman, A. R., Hashmi, H. N., and Kamal, M. A. (2014). Carbon emissions from power sector in Pakistan and opportunities to mitigate those. *Renew. Sustain. Energy Rev.* 34, 71–77. doi:10.1016/j.rser.2014.03.003

Nomenclature

BIM Building Information Modeling

BREEAM Building Research Establishment Environmental Assessment Method

BTU British Thermal Unit

CASBEE Comprehensive Assessment System for Built Environment Efficiency

EEM Energy Efficiency Measure

EISA Energy Independence and Security Act

EPA Environmental Protection Agency

GBRT Green Building Rating Tool

GHG Greenhouse Gas

GS Green Star

IGCEP Indicative Generation Capacity Expansion Plan

kWh Kilowatt hour

LBC Living Building Challenge

LEED Leadership in Energy and Environmental

NZEB Net Zero Energy Building

NTDC National Transmission and Dispatch Company

PEC Pakistan Engineering Council

RES Renewable Energy Sources

SDG Sustainable Development Goal

USD United States Dollar

USGBC US Green Building Council

WHO World Health Organization

frontiers | Frontiers in Energy Research

TYPE Original Research
PUBLISHED 10 March 2023
DOI 10.3389/fenrg.2023.1017943

OPEN ACCESS

EDITED BY
Haris Ishaq,
University of Victoria, Canada

REVIEWED BY
Yunus Emre Yuksel,
Afyon Kocatepe University, Türkiye
Paulo Smith Schneider,
Federal University of Rio Grande do Sul, Brazil
Gustavo R. Anjos,
Federal University of Rio de Janeiro, Brazil

*CORRESPONDENCE
Gleyzer Martins,
gmartins@ufu.br
Enio Pedone Bandarra Filho,
bandarra@ufu.br

SPECIALTY SECTION
This article was submitted to Solar Energy, a section of the journal Frontiers in Energy Research

RECEIVED 12 August 2022
ACCEPTED 27 February 2023
PUBLISHED 10 March 2023

CITATION
Martins G, Mendoza OSH, Amjad M and Bandarra Filho EP (2023), Analysis of the generation potential of hybrid solar power plants.
Front. Energy Res. 11:1017943.
doi: 10.3389/fenrg.2023.1017943

Analysis of the generation potential of hybrid solar power plants

Gleyzer Martins[1]*, Oscar Saul Hernandez Mendoza[1], Muhammad Amjad[2] and Enio Pedone Bandarra Filho[1]*

[1]School of Mechanical Engineering, Federal University of Uberlandia, Uberlandia, Brazil, [2]Department of Mechanical, Mechatronics and Manufacturing Engineering, New Campus, University of Engineering and Technology Lahore, Lahore, Pakistan

Photovoltaic solar energy has emerged in Brazil in distributed generation due to affordable costs and its application in different segments of the market. However, the electric energy storage in the photovoltaic systems is only viable for certain conditions in which the installation does not have access to the electricity network and the thermal portion of the solar energy is lost to the ambient. Heliothermic power plant represents another system available for solar electricity generation, which has higher costs, but takes better advantage of the portion of thermal energy and allows energy storage efficiently to meet the demands during periods without incident solar radiation. Heliothermic and photovoltaic generation have great potential in the Southeast and Northeast regions of Brazil, but the costs of both technologies cannot meet the demands during periods without solar radiation. This work presents a conceptual analysis of compound parabolic solar concentrators along with hybrid of photovoltaic and thermal collector systems to meet both the demand during sunlight hours and without solar radiation. The investigation consisted of implementing an organic Rankine cycle with different heliothermic plant configurations and the analysis of the diode model to examine different commercial photovoltaic cells operated in the Rankine cycle evaporation region. The results showed that the best working fluid for the application is R245fa with Urea-NaCl as molten salt for the thermal energy storage. The expected electrical power for the hydride cycle is 1580W at 2600 rpm and at 80°C of evaporation temperature, enabling a power generation for 1 hour and 20 min without solar radiation.

KEYWORDS

photovoltaic, heliothermic, heat storage, molten salt, hybrid power plant

1 Introduction

The use of solar concentration in monocrystalline photovoltaic modules results in significant improvements in electricity generation, as long as the effects of operating temperature on cell performance are considered (O'Gallagher, 2008). Notably, the amount solar energy that is not converted in these applications can reach more than 80% of the incident energy.

Studies of hybrid photovoltaic-thermal systems for heat and electricity generation have shown promising results in the existing literature (Khelifa et al., 2015; Tae-Hyeon et al. (2017). Hybrid power plants are described in the literature in practically three ways: photovoltaic/thermal hybrid solar systems for heat extraction (Tripanagnostopoulos et al., 2002; Coventry, 2005; Rosell et al., 2005; Chow, 2010); photovoltaic plants and

thermoelectric materials for electricity generation (Vorobiev et al., 2006); and photovoltaic systems and organic Rankine cycles for power production (Manolakos and Papadakis, 2011; Tourkov and Schaefer, 2015; Hosseini and Butler, 2021).

Organic Rankine cycles operate in low temperature using an organic working fluid. According to Tourkov and Schaefer (2015), this cycle can operate with dry fluids (n-Pentane), wet fluids (Ammonia), and isentropic fluids (R11). These categories are associated to the vapor saturation curve, where dry fluids have a positive slope, wet fluids a negative one and isentropic nearly vertical one. It is important to highlight that for low-temperature organic Rankine cycles the dry fluids are recommended, since the outlet of the turbine is guaranteed to be in the superheated vapor region (Tourkov and Schaefer, 2015).

Different working fluids, several configurations of organic Rankine cycle and photovoltaic cell types were evaluated to improve photovoltaic thermal/organic Rankine cycle systems (Tourkov and Schaefer, 2015). The findings revealed that alkanes (n-butane) performed best in terms of efficiency, and the advanced configuration using internal heat exchanger (IHE) and a closed feed organic fluid heater (CFOH) was the best match for these operating fluids. Additionally, the CdS photovoltaic cells were the least affected by increasing operating temperature on the photovoltaic system.

Experimental investigation and simulation developed by Kosmadakis, Manolakos and Papadakis (2011) also demonstrated that the efficiency of hybrid power plants can reach up to 12%, with emphasis for R-245fa as a working fluid, in addition to pointing out that hybrid systems have better economic feasibility than concentrating photovoltaic systems.

With hybrid power plants, it is possible to use both direct photovoltaic energy and fraction of the heat rejected for thermoelectric power generation. Another valuable aspect is the development of heliothermic power plants that, despite the remarkable potential, is still little explored in Brazil, as described in the online platform Heliothermic, supported by the Brazilian Institute of Information in Science and Technology.

Heliothermic power plants convert solar energy into thermal energy, producing mechanical power for electricity generation through a thermal cycle. Usually, thermal cycles are based on the organic Rankine cycle, that uses solar energy to vaporize and superheat the working fluid (synthetic oils, molten salt or water vapor) (Tolmasquim, 2016), which when expanding in a turbine or expander coupled to an electrical generator, produces electricity. To close the cycle, a heat exchanger, condenser (to condense the working fluid) and a pump are used.

Heliothermic power plant's net electrical energy output represents just 16% of the incident solar energy, owing to low temperatures and efficiency of heat transfer to the fluid in the receiver (Schmalensee et al. (2015)).

The arrangements for concentrating solar energy in the heliothermic power plants are classified in point-focus or line-focus designs, in which the receiving fluid can be fixed or mobile, allowing four types of configurations: linear Fresnel (line-focus design and fixed fluid); solar tower (point-focus design and fixed fluid; parabolic trough (line-focus design and mobile fluid) and parabolic receiver system (point-focus design and mobile fluid).

The photovoltaic systems available on the market can be differentiated according to the absorption spectrum of solar radiation, in single-junction and multi-junction photovoltaic cells. The absorption spectrum of single-junction solar cells is smaller, with silicon monocrystalline cells being the most commercially efficient, although the market offers other technologies, including thin-film polycrystalline cadmium telluride (CdTe) solar cells, copper-indium-gallium diselenide (CIGS) and hydrogenated amorphous silicon (a-Si:H). In general, the efficiency of commercial single-junction cells is below 21%, with acquisition costs increasingly accessible to end consumers. The absorption spectrum of multi-junction cells is broader, allowing better efficiency, in the order of 40%, requiring solar cell under high light concentration to maximize conversion into electrical energy (Dambhare, Butey, Moharil, 2021). The solar concentration associated with the solar tracking system increases the costs of installing multi-junction cells, thereby limiting the economic feasibility of this technology.

The application of concentrating photovoltaic cells, despite increasing the electrical generation per cell and reducing costs with expensive materials, such as high-purity silicon, can be negatively affected, as solar concentration can reduce its life span.

The research problem is to evaluate what is the configuration for the photovoltaic system and for the organic Rankine cycle with thermal storage that enhances the application of a hybrid solar plant. The present work seeks to evaluate the best types of commercial photovoltaic cells and the configuration of the Organic Rankine cycle, where different working fluids, operating conditions and different fusible salts of the thermal reservoir that enhance the electrical generation of a hybrid solar plant are studied. Thus, the theoretical electrical generation of the organic Rankine cycle was modeled with the scroll expander model defined by Lemort et al. (2006) and the diode modeling was carried out to quantify the electrical generation of photovoltaic cells.

The use of the hybrid cycle will improve the electrical generation of photovoltaic cells by using solar concentration and by reducing the operating temperature of these cells due to the use of the saturation region of the Organic Rankine cycle. The Organic Rankine cycle will also increase electrical generation, in addition to enabling the thermal storage of energy to be used in electrical generation outside the period of insolation.

2 Methodology

The photovoltaic and heliothermal plant consists of parabolic concentrators that concentrate solar energy 4.5 times under a linear array of photovoltaic cells. This cell arrangement was installed on an aluminum plate in the saturation region of the organic Rankine cycle, an additional cellless collector area was employed to superheat the working fluid entering the thermal storage tank. In the storage tank, part of the thermal energy is stored using fusible salts and another part directed to the scroll expander for electrical generation. This working fluid at the outlet of the expander is condensed in the heat exchanger for subsequent pumping, closing the organic Rankine cycle. Figure 1 presents the proposed hybrid solar plant.

For the photovoltaic analysis and determination of the solar collector areas, the standard irradiation of 1000 W/m^2 was considered. The power generation performance of photovoltaic cells was evaluated using the diode model for the photovoltaic cells

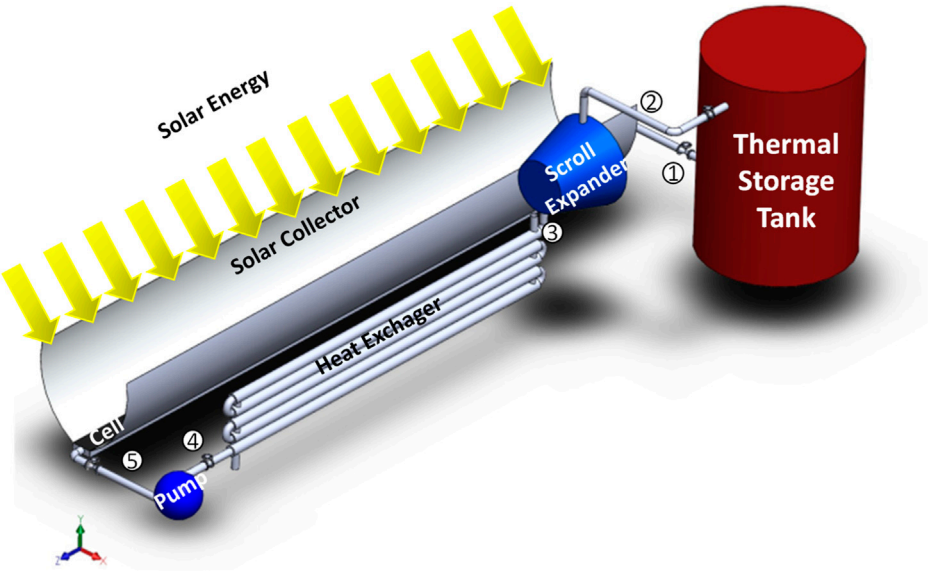

FIGURE 1
Schematic representation of the proposed hybrid solar system.

and electricity data of the single-junction cells, since it is necessary to calculate the effect of temperature on the efficiency of cells.

For the analysis of the organic Rankine plant, the operating pressures were defined according to the different temperatures in the evaporator, keeping the temperature in the condenser at 35°C, and the temperature at the outlet of the evaporator and at the inlet of the storage tank is equal to 150°C. A scroll expander derived was implemented from the scroll compressor with 36.54 cc and the parameters defined by Lemort et al. (2009).

The modeling of hybrid power plant was divided into models for simulating the heliothermic power plant, especially the expander model, and for simulating photovoltaic electricity generation. An analysis of the hybrid plants available in the literature was also performed. The modeling of the heliothermic power plant used the conservation of mass and energy applied to the basic equipment of the organic Rankine cycle, pump, expander and heat exchangers, according to Landellea et al. (2017) and Equations 1, 2:

$$0 = \frac{d}{dt}\int_{cv} \rho dv + \int_{cs} \rho\left(\vec{V}\cdot\vec{n}\right)dA \tag{1}$$

$$\dot{Q} - \dot{W} = \frac{d}{dt}\int_{cv} \rho\left(u + \frac{V^2}{2} + z\right)dv + \int_{cs} \rho\left(h + \frac{V^2}{2} + z\right)\left(\vec{V}\cdot\vec{n}\right)dA \tag{2}$$

The system's simulation was performed at a steady-state condition, and the equipment was modeled theoretically at a constant performance, except for the expander. The model proposed by Lemort et al. (2006) and Lemort, Declaye and Quoilin (2011) was used to simulate the expander, which consists of determining the power developed by the expander considering the heat exchanges with the environment and the expansion process in two stages, one isentropic and another isovolumetric, considering that total power is theoretical power plus losses, as illustrated in Figure 2.

The mass flow rate is a function of the expander swept volume V_s, the compressor rotational speed N, and leakages $\dot{M_{leak}}$ (Equation 3):

$$\dot{M} = \frac{N \cdot V_S}{v_{su,2}} + M_{leak} \tag{3}$$

The internal expansion power $\dot{W}_{in}$, is calculated using an isentropic expansion and a constant-volume evolution, according to Eq. 4:

$$\dot{W}_{in} = \dot{M}_{in}\left[\left(h_{su,2} - h_{ad}\right) + r_{v,in}\cdot v_{su,2}\left(P_{ad} - P_{ex,2}\right)\right] \tag{4}$$

where $h_{su,2}$ and h_{ad} are the enthalpies of the fluid at the supply of the expander and of the isentropic expansion, respectively, and $P_{ex,2}$ and P_{ad} represent the exhaust pressure and isentropic expansion pressures. $r_{v,in}$ is the internal volume ratio.

The total power $\dot{W}$ is computed considering the power losses due to mechanical losses $\dot{W}_{loss,1}$ and electromechanical losses $\dot{W}_{loss,2}$ as defined by Eq. 5.

$$\dot{W} = \dot{W}_{in} - \dot{W}_{loss,1} - W_{loss,2} \tag{5}$$

Internal heat transfers are lumped into equivalent supply $\dot{Q}_{su}$ and exhaust $\dot{Q}_{ex}$ heat rates, based on overall heat transfer coefficients, while external heat transfer is also defined by a global heat transfer coefficient AU_{amb}, and the energy balance can be given by Eq. 6:

$$Q_{su} + \dot{Q}_{ex} - AU_{amb}\cdot\left(T_{Shell} - T_{amb}\right) + \dot{W}_{loss,1} + \dot{W}_{loss,2} = 0 \tag{6}$$

where T_{Shell} and T_{amb} represent the temperatures associated to the expander shell and the ambient, respectively.

To estimate the generation of photovoltaic cells, the effect of temperature on the efficiency of solar cells must be calculated, which, according to Gow and Manning, (1999), is given by the diode model, as defined below:

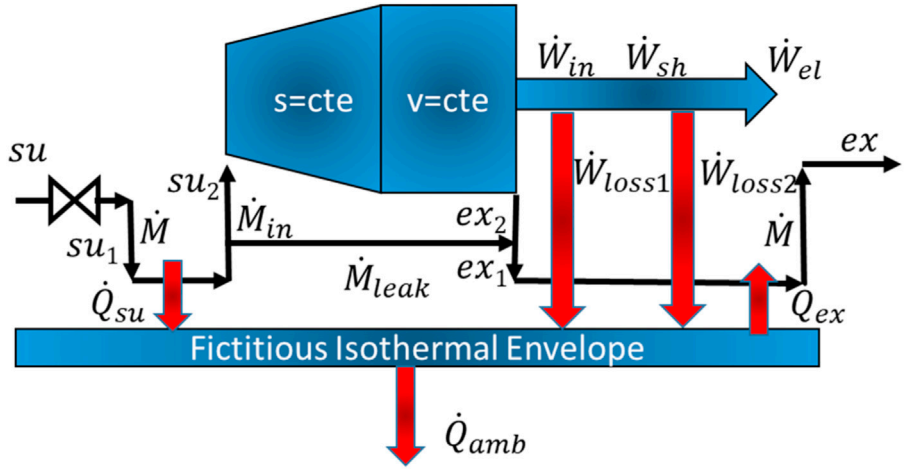

FIGURE 2
Schematic representation of the scroll expander proposed by Lemort et al., 2011.

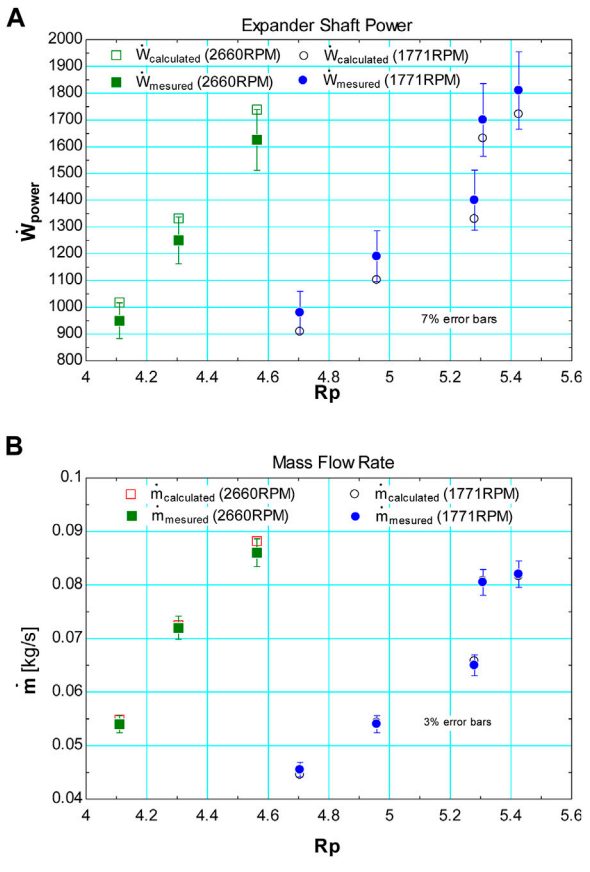

FIGURE 3
Results of the validation of the expander model: Expander Shaft Power **(A)** and Mass flow rate **(B)**. Hybrid power plant simulation for different rotations using the R245fa.

$$I = I_{fg} - I_0 \times \left[\exp\left(\frac{(V + R_s \times I)}{n \times k \times T}\right) - 1\right] \tag{7}$$

$$I_{fg} = [I_{cc} + \alpha \times (T - T_r)] \times \frac{S}{S_r} \tag{8}$$

$$I_0 = \frac{I_{fg}}{\left(\exp\left(\frac{V_{ca} \times q}{n \times k \times T}\right) - 1\right)} \exp\left(\frac{q \times EG}{n \times k} \times \left(\frac{1}{T_r} - \frac{1}{T}\right)\right) \tag{9}$$

In these equations, I_{fg}, I_0 and I_{cc} represent the output, photogenerated, diode saturation and short-circuit currents, respectively; V and V_{Ca} are the terminal and open-circuit voltages; T and T_r are the module and standard module temperatures; S and S_r are the intensities of solar radiation and standard solar radiation. The model constants are α, k, n, q and EG, which represent the temperature coefficient, the Boltzmann constant, the diode ideality factor, the elementary charge and the energy band-gap, respectively. The series resistance, R_s, is a parameter that adjusts the model to the modules used. The effects of temperature and variation of solar irradiation are considered in the photogenerated current and in the diode saturation current (GOW AND MANNING, 1999).

3 Results and discussions

Initially, the results of mass flow and shaft power of the scroll expander were validated for different pressure ratios and rotational speeds, according to data from Lemort et al. (2009), as shown in Figure 3.

Figure 3A illustrates that the scroll expander model predicts, satisfactorily, the mass flow rate with errors smaller than 3%. However, Figure 3B shows the increment of errors in the shaft power expander simulation approximately of 7%. The Lemort et al. (2009) presents similar errors in the prediction experimental mass flow and shaft power for scroll expander.

To evaluate the effect of the working fluid on the hybrid power plant, a simulation of the operating conditions of the heliothermal and photovoltaic power plant was performed, considering a standard Rankine cycle and temperature conditions of 75°C in

TABLE 1 Results for different refrigerants as working fluid.

	R11	R123	R245fa	R134A	R1234yf	R423A
$\dot{m}_{ref}$ [KG/S]	0.02551	0.0264	0.03837	0.114	0.1239	0.1253
$Area_{colector}$ [M^2]	6.819	7.332	12.4	34.07	33.89	32.68
$Area_{Phovoltaic}$ [M^2]	4.891	4.812	7.691	20.65	18.37	18.49
$Pressure_{Evaporator}$ [BAR]	1.479	1.307	2.11	8.875	8.952	7.965
$Pressure_{Condenser}$ [BAR]	4.594	4.31	6.958	23.66	22.72	21.42
$Power_{photovoltaic}$ [W]	409	402.4	643.2	1,727.4	1,536.6	1,546.8
$Power_{Rankine}$ [W]	110.7	174.9	335.1	378.1	317.3	569.7
$Power_{Total}$ [W]	510.6	568.1	954.7	1,865.0	1,584.1	1,889.6
η_{total} [%]	10.13	10.96	11.31	9.575	9.385	10.27

the evaporator tube and 30 °C in the condenser tube. The results are depicted in Table 1.

Table 1 shows that the choice of operating fluid is important for defining the areas of solar capture and application of solar cells and for determining the power generation performance of the thermal plant. The working fluids R134a, R1234yf and R423A, in other words, high pressure fluids, require the largest areas of solar energy collection, as these larger areas provide a greater power of the hybrid system, mainly the photovoltaic portion. In turn, the working fluids R11, R123 and R245fa (low pressure fluids) have the smallest areas of solar energy collection and, consequently, the smallest photovoltaic power. However, these fluids demonstrate the best thermal efficiencies for the hybrid system, especially R245fa, which showed better thermal efficiency with heliothermal power similar to the fluids with large energy collection area. As the photovoltaic-cell operating temperatures are constant for the different fluids, a result of the photovoltaic efficiency of 8.364% was achieved.

In terms of pressures in the cycles, it can be observed that the fluids with smaller areas of solar capture have the lowest pressures, which reduces the thickness of pipes and pressure vessels, hence reducing costs.

Thus, analyzing in detail the simulations of the thermal fluid R245fa for different rotations, it is possible to obtain Figure 3.

Figure 3B illustrates that the power and efficiency in the hybrid cycle increase significantly with increasing rotation, showing a clear trend of efficiency stabilization. Particularly, in Figure 3A, it is possible to observe the increase of collector area and mass flow rate.

Figure 4 shows the simulation of the hybrid power plant, evaluating the effect of molted salt type in accordance of thermo-physical properties defined by Sabour and Dorca (2019).

Figure 4 also shows that best molted-salts efficiency and solar collect area is the KNO_3NaNO_2, since this salt present the lowest electric power and operation time of power plant without incident solar radiation. The Urea-$NaNO_3$ represents the molted salt with high electric power, however lowest efficiency and high solar collect area. The Urea-NaCl and Urea-KCl show moderate solar collect area with satisfactory electric power, efficiency and operation time, although the efficiency of Urea-KCl is better than Urea-NaCl, the cost and commercial availability is favorable in the Urea-NaCl choice.

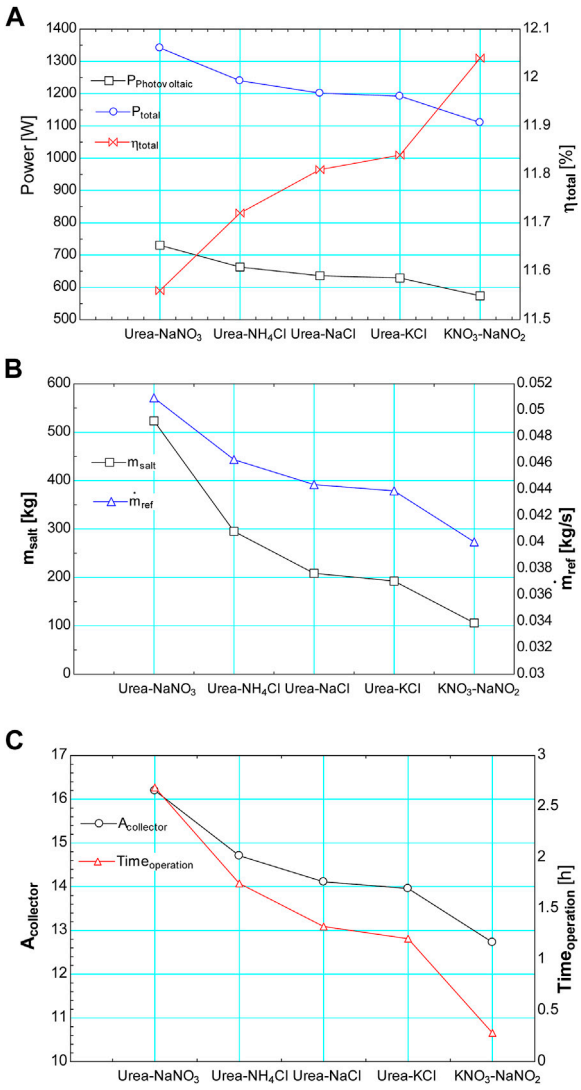

FIGURE 4
Hybrid power plant simulation for different molted salt, in terms of power **(A)** salt mass **(B)**, Solar collector Area **(C)** Panel 5 Hybrid power plant simulation for different temperatures, in terms of Solar collector Area **(A)** and power **(B)**the R245fa.

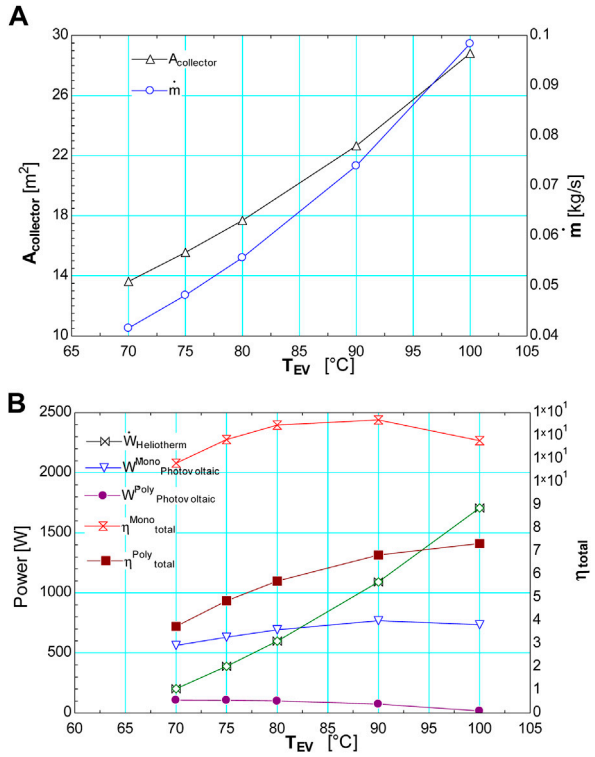

FIGURE 5
Hybrid power plant simulation for different temperatures, in terms of Solar collector Area **(A)** and power **(B)** the R245fa.

To determine the influence of the evaporation temperature, that is, the operating temperature of the two different commercial photovoltaic cells, it was possible to obtain Figure 5.

Figure 5 shows that the increment in evaporation temperature increases the solar collector area and the mass flow rate, as well as the heliothermic power. However, it can be noted a marked reduction of the photovoltaic power and a peak of efficiency at 80 °C for monocrystalline cells. The polycrystalline cells, in turn, present results of low photovoltaic energy generation and consequent low efficiency of the hybrid cycle.

Based on experimental results, the optimum operating point of the system is with a rotation of 2600 rpm and an evaporation temperature of 80 °C, with a hybrid cycle performance of 12% and a total power of 1580W. The cycle also achieved higher powers using monocrystalline cells, at the expense of photovoltaic power and cycle efficiency. Thus, a solar collector area of 17.68 m^2 is recommended, which requires a salt storage of 261.3 kg and an operating time without incident solar radiation of 1h20min.

4 Conclusion

Photovoltaic solar energy is widespread due to the affordable costs of installations and abundant availability. Non-etheless, this system presents problems with its storage, both due to the direct and indirect costs of batteries. In turn, the proposal of a hybrid heliothermic and photovoltaic plant represents a way to extend the use of solar energy to periods without solar radiation with the storage of thermal energy in fusible salts. Further, the heliothermic system allows thermal protection of concentrating solar cells in the biphasic heat exchange region. In this sense, different working fluids were evaluated for a heliothermic power plant operating with an organic Rankine cycle, using a scroll expander to generate electricity. Moreover, different media for solar thermal energy storage including fusible salts, urea and common salt were investigated for extended periods without solar radiation. As per the numerical results, the best working fluid for the installation of the hybrid solar plant was R245fa, using monocrystalline cells and Urea-NaCl molted salt as storage material with a recommended solar concentration area of 17.7 m^2. An increased operation time of 1 h and 20min for power generation was observed thus making the system a viable solution for operation in the absence of the solar flux.

Data availability statement

The raw data supporting the conclusion of this article will be made available by the authors, without undue reservation.

Author contributions

GM conducted all the simulations and analyses, OM contributed with the simulation as well as the results analyses. MA performed the revision and revision the manuscript and EB organized the material, written and participes the discussion.

Acknowledgments

The authors acknowledge the financial support provided for this research by CAPES, CNPq and FAPEMIG.

Conflict of interest

The authors declare that the research was conducted in the absence of any commercial or financial relationships that could be construed as a potential conflict of interest.

Publisher's note

References

Chow, T. T. (2010). A review on photovoltaic/thermal hybrid solar technology. *Appl. Energy* 87, 365–379. doi:10.1016/j.apenergy.2009.06.037

Coventry, J. S. (2005). Performance of a concentrating photovoltaic/thermal solar collector. *Sol. Energy* 78, 211–222. doi:10.1016/j.solener.2004.03.014

Dambhare, M. V., Butey, B., and Moharil, S. V. (2021). Solar photovoltaic technology: A review of different types of solar cells and its future trends. *J. Phys. Conf. Ser.* 1913, 012053. doi:10.1088/1742-6596/1913/1/012053

Gow, J. A., and Manning, C. D. (1999). Development of a photovoltaic array model for use in power-electronics simulation studies. *IEE Proc.* 146, 193. doi:10.1049/ip-epa:19990116

Hosseini, S. E., and Butler, B. (2021). Design and analysis of a hybrid concentrated photovoltaic thermal system integrated with an organic Rankine cycle for hydrogen production. *J. Therm. Analysis Calorim.* 144, 763–778. doi:10.1007/s10973-020-09556-4

Khelifa, A., Touafek, K., Ben Moussa, H., Tabet, I., Ben cheikh El hocine, H., and Haloui, H. (2015). Analysis of a hybrid solar collector photovoltaic thermal (PVT). *Energy Procedia* 74, 835–843. doi:10.1016/j.egypro.2015.07.819

Landellea, A., Tauverona, N., Haberschillc, P., Revellinc, R., and Colassona, S. (2017). Performance evaluation and comparison of experimental organic rankine cycle prototypes from published data. *Procedia* 105, 1706–1711. doi:10.1016/j.egypro.2017.03.555

Lemort, V., Declaye, S., and Quoilin, S. (2011). Experimental characterization of a hermetic scroll expander for use in a micro-scale Rankine cycle. *Part A J. Power Energy* 226, 126–136. doi:10.1177/0957650911413840

Lemort, V., Quoilin, S., Cuevas, C., and Lebrun, J. (2009). Testing and modeling a scroll expander integrated into an organic Rankine cycle. *Appl. Therm. Eng.* 29, 3094–3102. doi:10.1016/j.applthermaleng.2009.04.013

Lemort, V., Teodorese, I. V., and Lebrun, J. (2006). *Experimental study of the integration of a scroll expander into a heat recovery rankine cycle*. International Compressor Engineering Conference.

Manolakos, D., and Papadakis, G. (2011). Simulation and economic analysis of a CPV/thermal system coupled with an organic Rankine cycle for increased power generation. *Sol. Energy* 85, 308–324. doi:10.1016/j.solener.2010.11.019

O'Gallagher, J. J. (2008). "Practical design of CPC PV concentrators," in *Nonimaging optics in solar energy. Synthesis lectures on energy and the environment: Technology, science, and society* (Cham: Springer). doi:10.1007/978-3-031-79420-9_4

Rosell, J. I., Vallverdú, X., Lechón, M. A., and Ibánez, M. (2005). Design and simulation of a low concentrating photovoltaic/thermal system. *Energy Convers. Manag.* 46, 3034–3046. doi:10.1016/j.enconman.2005.01.012

Sabour, I., and Dorca, A. (2019). Review on heat transfer analysis in thermal energy storage using latent heat storage systems and phase change materials. *Int. J. Energy Res.* 43, 29–64. doi:10.1002/er.4196

Schmalensee, R., Bulovic, V., Armstrong, R., Batlle, C., Brown, P., Deutch, J., et al. (2015). *The future of solar energy: An interdisciplinary MIT study*. Massachusetts Institute of Technology, MIT Energy Initiative.

Tae-Hyeon, K., Kim, S., Jeong, D. H., Geum, D. M., Lee, S., Junga, S. J., et al. (2017). A highly-efficient, concentrating-photovoltaic/thermoelectric hybrid generator. *Nano Energy* 37, 242–247. doi:10.1016/j.nanoen.2017.05.023

Tolmasquim, M. T. (2016). *Energia renovável: Hidráulica, biomassa, eólica, solar, oceânica*. Rio de Janeiro: EPE.

Tourkov, T., and Schaefer, L. (2015). Performance evaluation of a PVT/ORC (photovoltaic thermal/organic Rankine cycle) system with optimization of the ORC and evaluation of several PV (photovoltaic) materials. *Energy* 82, 839–849. doi:10.1016/j.energy.2015.01.094

Tripanagnostopoulos, Y., Nousia, Th., Souliotis, M., and Yianoulis, P. (2002). Hybrid photovoltaic/thermal solar systems. *Sol. Energy* 72, 217–234. doi:10.1016/s0038-092x(01)00096-2

Vorobiev, Yu., González-Hernández, J., Vorobiev, P., and Bulat, L. (2006). Thermal-photovoltaic solar hybrid system for efficient solar energy conversion. *Sol. Energy* 80, 170–176. doi:10.1016/j.solener.2005.04.022

Nomenclature

A Area [m^2]
E energy band-gap [eV]
k Boltzmann constant [J/K]
$\dot{M}$ Mass flow [kg/s]
$\vec{n}$ Unit Vector
n diode ideality factor
$\dot{Q}$ Heat transfer [W]
R_s Series resistance [Ω]
T Temperature [K]
V Voltages [V]
v Specific Volume [m^3/kg]
z Elevation [m]
AU Global heat transfer coefficient [W/m^2-K]
h Enthalpy [kJ/kg]
I Circuit current [A]
N Rotation [rpm]
P Pressure [Bar]
r_v Internal volume ration
S Solar radiation Intensity [W/m^2]
u Internal energy[kJ/kg]
$\vec{V}$ Velocity [m/s]
V_s Swept volume [m^3]
$\dot{W}$ Power [W]

Subscribed

ad Adiabatic
ca Open-circuit t
cv Control volume
ex Exhaust
f g Photogenerated
leak Leakages
o Diode saturation
shell Shell
amb Ambient
cc Circuit curren
cs Control surface
el Electric
in Internal
loss Losses
r Standard
su Supply

Greek Symbols

ρ Density [kg/m^3]
α Temperature Coefficient [1/K]

Frontiers in
Energy Research

Advances and innovation in sustainable, reliable and affordable energy

Explores sustainable and environmental developments in energy. It focuses on technological advances supporting Sustainable Development Goal 7: access to affordable, reliable, sustainable and modern energy for all.

Discover the latest Research Topics

See more →

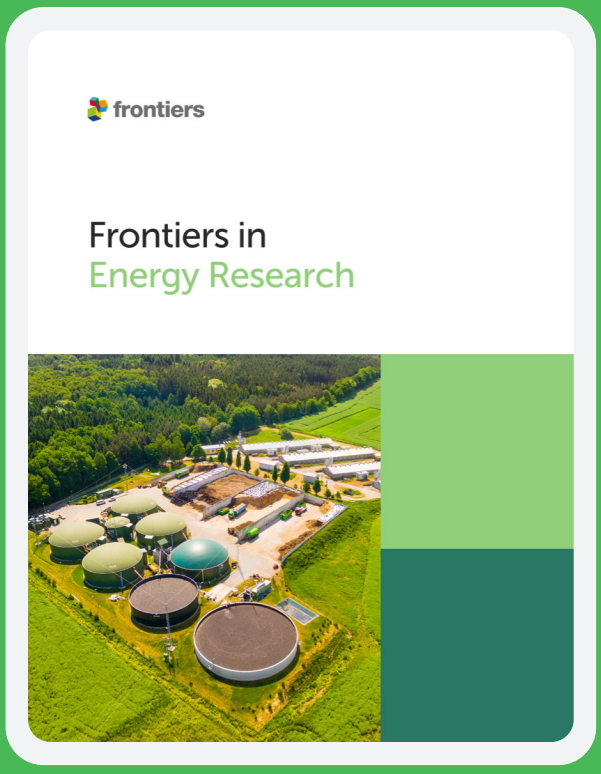

Frontiers

Avenue du Tribunal-Fédéral 34
1005 Lausanne, Switzerland
frontiersin.org

Contact us

+41 (0)21 510 17 00
frontiersin.org/about/contact